1-18-2019

Study on microstructure, corrosion performance and mechanical properties of hypereutectic Zn-Al alloy

Xingyuan Wei
University of Windsor

Study on microstructure, corrosion performance and mechanical properties of hypereutectic Zn-Al alloy

By

Xingyuan Wei

A Thesis

Submitted to the Faculty of Graduate Studies

Through the Department of Mechanical, Automotive and Materials Engineering

In Partial Fulfillment of the Requirements for

The Degree of Master of Applied Science

At the University of Windsor

Windsor, Ontario, Canada

2019

Study on microstructure, corrosion performance and mechanical properties of hypereutectic Zn-Al alloy

By

Xingyuan Wei

APPROVED BY:

_____

J. Ahamed

Department of Mechanical, Automotive and Materials Engineering

_____

V. Stoilov

Department of Mechanical, Automotive and Materials Engineering

_____

X. Nie, Co-Advisor

Department of Mechanical, Automotive and Materials Engineering

_____

H. Hu, Co-Advisor

Department of Mechanical, Automotive and Materials Engineering

December 13, 2018

DECLARATION OF CO-AUTHORSHIP / PREVIOUS PUBLICATION

I. Co-Authorship

I hereby declare that this thesis incorporates material that is result of joint research. In all cases, the key ideas, primary contributions, experimental designs, data analysis and interpretation, were performed by the author and Dr. H. Hu and Dr. X. Nie as advisors. Chapter 3 was co-authored with Luyang Ren, Xinyu Geng, Zixi Sun and Anindya Banerji who assisted in bulk samples preparations. Chapter 4 and 5 were co-authored with Dr. Hu and Dr. Nie who contributed to characterization. I am aware of the University of Windsor Senate Policy on Authorship and I certify that I have properly acknowledged the contribution of other researchers to my thesis, and have obtained written permission from each of the co-author(s) to include the above material(s) in my thesis. I certify that, with the above qualification, this thesis, and the research to which it refers, is the product of my own work.

II. Previous Publication

This thesis includes 3 original papers that have been previously published/submitted for publication in peer reviewed journals, as follows:

Thesis Chapter	Publication title/full citation	Publication status
Chapter 3	Wei, X., Ren, L., Geng, X., Sun, Z., Hu, H., Nie, X., & Banerji, A. (2019). Nano microstructure development and solidification of Zn-6 wt% Al hypereutectic alloy. Materials Characterization. Vol 147, 295-302	Published
Chapter 4	Xingyuan Wei, Henry Hu, Xueyuan Nie, Influence of Galfan coating on tensile properties of CRS 1018 steel	2nd International Conference on Advances in Materials and Processing Technology, Taipei, Taiwan Oct 24-29. 2019, submitted
Chapter 5	Xingyuan Wei, Henry Hu, Xueyuan Nie, Corrosion and Microstructure of hypereutectic Zn-Al alloy.	Prepared

I certify that I have obtained a written permission from the copyright owner(s) to include the above published material(s) in my thesis. I certify that the above material describes work completed during my registration as a graduate student at the University of Windsor.

III. General

I declare that, to the best of my knowledge, my thesis does not infringe upon anyone's copyright nor violate any proprietary rights and that any ideas, techniques, quotations, or any other material from the work of other people included in my thesis, published or otherwise, are fully acknowledged in accordance with the standard referencing practices. Furthermore, to the extent that I have included copyrighted material that surpasses the bounds of fair dealing within the meaning of the Canada Copyright Act, I certify that I have obtained a written permission from the copyright owner(s) to include such material(s) in my thesis.

I declare that this is a true copy of my thesis, including any final revisions, as approved by my thesis committee and the Graduate Studies office, and that this thesis has not been submitted for a higher degree to any other University or Institution.

ABSTRACT

Hypereutectic Zn-Al alloys with different cooling rates and their coatings on mild steel were successfully prepared and characterized. Zn - 6 wt. % Al alloy was cast into different moulds to obtain various cooling rates. It was found that the increasing cooling rates reduced the average grain size. High cooling rate also decreased the decomposition rate of primary γ-ZnAl phase. When the cooling rate increased to 10℃/s, a large number of nano-size eutectic grains were formed in the alloy. Through hot-dipping technique, Zn - 6 wt. % Al was coated on tensile bars made of ASTM CRS 1018 steel in order to study the effect of Zn alloy-based coatings on tensile properties of mild steel. By comparing the same types of steel which experienced the same thermal process without coating, it was found that the yield strength and ultimate tensile strength of CRS 1018 were reduced but the elongation was significantly improved. The change of tensile properties might result from the decrease in dislocation densities, which were estimated by nano hardness measurements. Furthermore, the hypereutectic Zn-Al alloys with various Al contents from 6 to 10 wt.% were prepared to study the Al influence on their corrosion behaviors. In the low voltage corrosion, higher Al content was beneficial to the alloys due to passivity whereas Al increased the risk of pitting corrosion in the high voltage test after passive layers were broken down. The microstructure observed by scanning electron microscopy (SEM) of tested samples also supported the obtained corrosion data.

DEDICATION

To My Parents,

Mr. and Mrs. Wei

For their unconditional love and support

S. D. G.

ACKNOWLEDGEMENT

I would like to thank Dr. Henry Hu and Dr. Xueyuan Nie, for their hard working, appreciation and care on me in my master program, and for their kindly suggestions, encouragement and excellent supervision of this research work. Great thanks to Dr. Vesselin Stoilov and Dr. Mohammed Jalal Ahamed for the time given for my research thesis and presentations as my committee members, and providing valuable suggestions for this project. I am very grateful to U Windsor technical support center and other technicians for the technical support, Dr. Xuezhi Zhang, Dr. Li Fang, Mr. Chen Zhao, Mr. Junxiang Zhou and all other group members for their assistance in this research. Most of all I would like to express my deepest gratitude to my family: my parents for their love, and support.

TABLE OF CONTENTS

LIST OF TABLES

LIST OF FIGURES

CHAPTER 1 Introduction

1.1 Background

Zn alloys and their advantage in anti-corrosion usage had long been noticed in ancient Greece where the ornaments and statuettes were made of alloys zinc based alloy 2500 years ago. In the 18th centary, P.J. Malouin, a French chemist, reported to the Royal Academy of Sciences some researches involving iron with molten zinc, which is sometimes considered as the beginning of modern galvanizing technique. Despite the long history, Zn-Al alloys can still be found in modern world in variety kinds of occasions. In recent three decades, eutectic and hypereutectic Zn-Al alloys, also known as Galfan, has been widely used in the automotive industry, construction, marine environment, electrical communication etc. as anti-corrosion coating material. The hot-dipping (HD) method was officially reported for the first time in 1980s after which it was accepted commonly by many manufactures thank to its remarkable controllability in production, excellent durability in different environments, strong adhesion and low cost. However, some vital properties of Galfan alloy and coating are rarely reported.

1.2 Motivation

Although Zn-Al alloys have been widely used, there are some issues that have not been systematically studied yet. For example, most factories using HDG technology only cool the products with air in room temperature. However, the microstructure of Zn-Al alloys can be influenced by many factors in solidification including cooling rates. As an essential aspect, microstructure determines the mechanical properties, electrochemical

performance, adhesion etc. Another example is the influence of the entire HDG process. Steel substrate is usually dipped into molten Zn-Al at around 400℃ to 500℃ in which there are no phase transformation for Fe-C alloy under equilibrium condition. In reality, it is uncertain if the mechanical properties changed. Furthermore, it is found that some commercial Zn-based coating have Al content higher than eutectic composition. The effect of hypereutectic Zn-Al alloys with different Al contents on their microstructure mechanical properties, and corrosion behavior are seldom studied.

1.3 Research objectives

The objectives of this research are:

- To study the microstructure of hyper eutectic Zn-Al alloys prepared with different cooling conditions and their thermal histories.
- To simulate the entire coating process in the lab environment i.e. surface cleaning, pickling, fluxing; hot dipping in a certain temperature with a certain speed; quenching after coating;
- To evaluate the tensile properties of hypereutectic Zn-Al alloys coated mild steel.
- To vary the Al content between 6% to 10% and study the corrosion performance. Investigate the effect of the Al content in hypereutectic Zn-Al alloys on their corrosion behaviors.

1.4 Thesis layout

The thesis contains seven chapters. Chapter 1 provides the general background about Zn-Al alloys and the motivation of this research. Chapter 2 is the literature review on the

fundamental knowledge of Zn-Al alloys. Chapter 3 studies the relationship between the thermal history and the microstructure of Zn-6 wt% Al alloy. Chapter 4 reveals the influence of hot-dipping technique on tensile properties using Zn-6 wt% Al. Chapter 5 shows the different electrochemical performance of Zn-Al alloys with Al content from 6% to 10%. Chapter 6 concludes the all the experiments shown in this thesis. Chapter 7 predicts some possibilities of future studies related to the current work.

CHAPTER 2 Literature review

2.1 Introduction to Zn-Al alloy

2.1.1 Basic knowledge about Zn

Zinc is the 30th element in the periodic table located in the period 4 and the group 12. In some respects, zinc shares the similar chemical properties with magnesium e.g. both elements have only one normal oxidation state (+2); Zn^{2+} and Mg^{2+} ions are in the similar size. Zinc is the 24th most abundant element on Earth with five stable isotopes. The most common zinc ore is sphalerite which is a zinc sulfide mineral. The largest workable lodes are in Australia, Asia, and the United States[1].

Pure Zn in the room temperature has hexagonal close packing structure with 134 pm of atomic radius. Due to the the typical metal electron configuration, $3d^{10}$ $4s^2$, the oxidation state has 0, +1, +2. The Young's modulus of Zn is 108 GPa making it into a relative soft metal compared with pure Fe (211 GPa) and its alloys. Zn has a high thermal expansion i.e. 30.2 μm/(m·K) at 25℃. This value is higher than both Fe (11.8 μm/(m·K))and Al (23.1 μm/(m·K))[2].

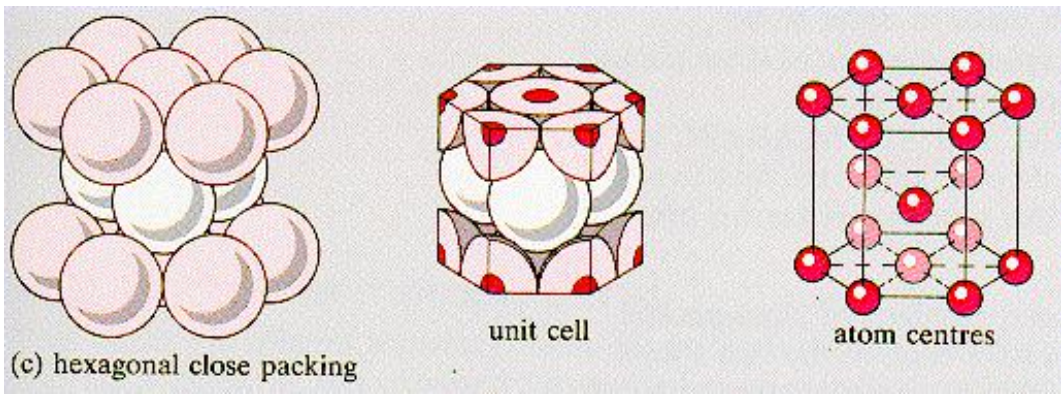

Figure 2.1 Structure of hexagonal close packing lattice[3].

2.1.2 Basic knowledge about Al

Aluminum is a silvery-white, soft, ductile metal in boron group. It is the most abundant metal in the Earth crust occupying 8% of the total mass. Bauxite is the main existence form of Al on Earth. Due to the high reactivity, aluminum metal can hardly exist in the natural environment. However, 270 different minerals were found containing Al[4]. The passivation of aluminum brings excellent corrosion resistance. Together with the low density, Al has become one of the best options in aerospace, automotive, and building industries[5].

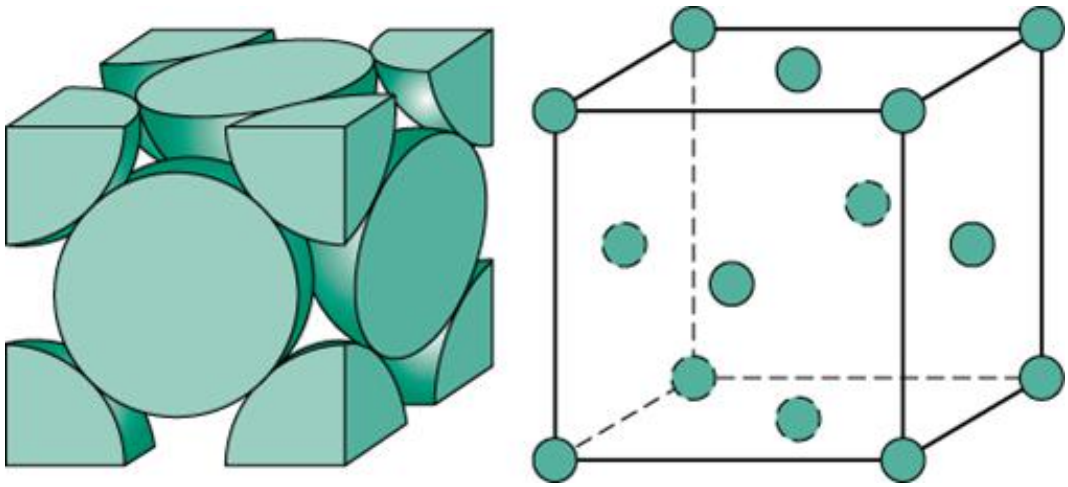

Figure 2.2 Structure of face-centered cubic lattice[6].

Normally, aluminum has face-centered cubic lattice structure. Although the atomic number is only 13, the atomic radius of Al reaches 143 pm. 13 electrons are arranged as $[Ne]3s^2 3p^1$. Three outermost electrons can be easily lost providing this element most properties of metals. However, the unique structure electron shell also maintains some

features of non-metal such as the high reactivity with alkaline.

2.1.3 Zn-Al phase diagram

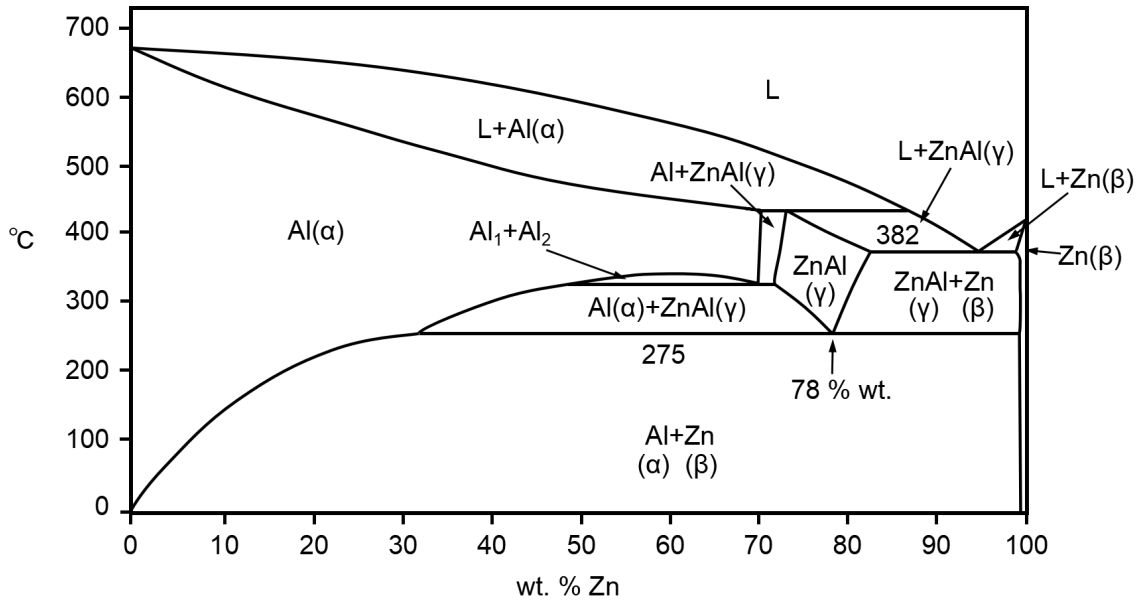

Figure 2.3 Zn-Al phase diagram[7].

Figure 2.3 is the Zn-Al phase diagram where the eutectic point is found around 95wt.% of Zn. The eutectic Zn-Al alloy often called Galfan alloy. Three phases are found around the eutectic point which are α-Al, β-Zn, and γ-ZnAl. According to Skoko et al., α-Al (fcc, the matrix, M) contains 99 at% Al and 1 at% Zn approximately, and β-Zn (hexagonal, the precipitates), has about 99.5 at% Zn and 0.5 at% Al[8].

Hypereutectic and hypoeutectic alloys in this area would experience three phase reactions. The primary reaction, which produces primary γ-ZnAl alone, happens at the liquidus line depending on the different percentage of Al. A slight variation of eutectic temperature is found in literature where the value changes between 381℃ to 385℃[9]. This reaction transforms most liquid metal into solid and introduces massive eutectic

γ-ZnAl and and eutectic β-Zn. Eutectoid reaction occurs between 275℃ to 278℃ [10, 11] in which the γ-ZnAl decompose into β-Zn and α-Al. In the real situation, the third reaction does not fully happen to leave γ-ZnAl even to the room temperature.

2.1.4 Microstructure of eutectic Zn-Al alloy

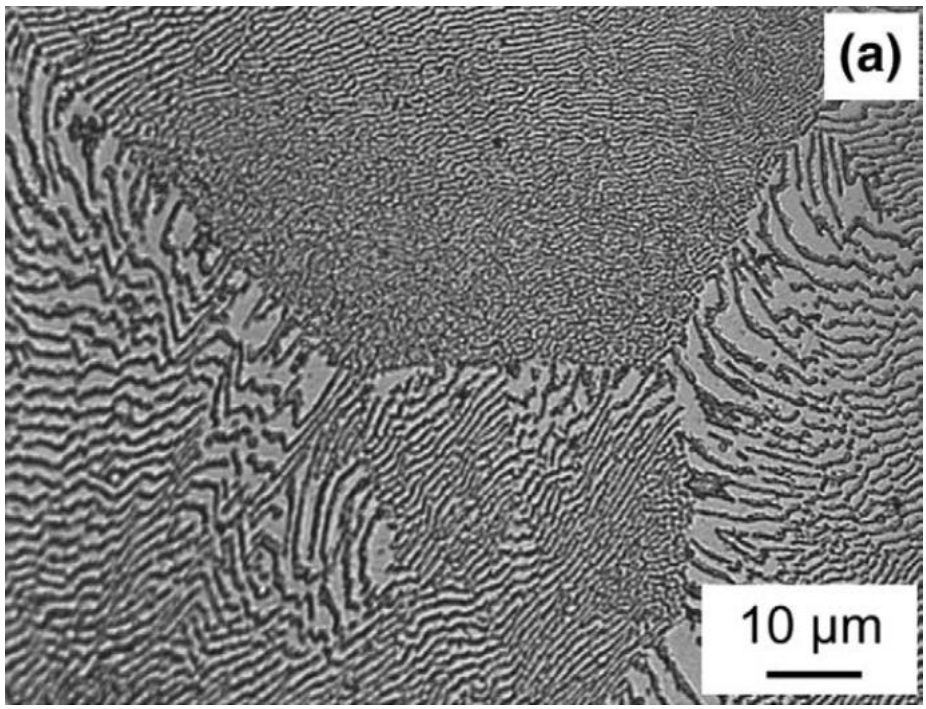

(a)

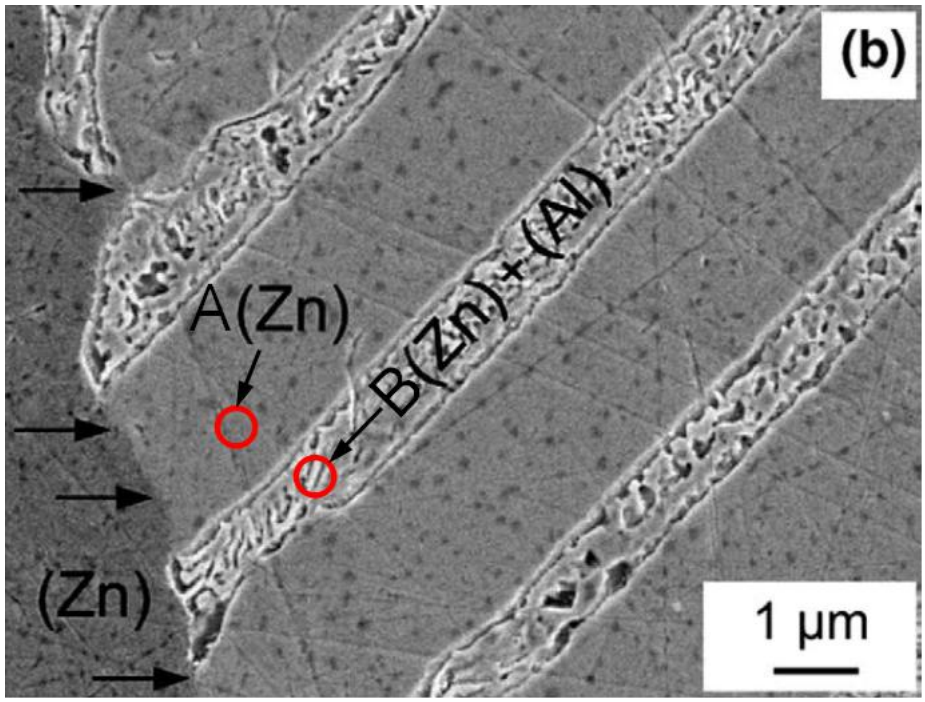

(b)

Figure 2.4 Optical (a) and secondary-electron (b) micrographs of cross sections of the as-cast Zn-5 wt% Al alloy after cooling down to room temperature. A Zn-rich phase/Zn-rich phase GB is marked by arrows (b)[12].

Figure 2.4 demonstrate the microstructure of eutectic Zn-Al alloy. According to the phase diagram, point A is the eutectic β-Zn phase in which Zn is the dominant element. This phase is formed in eutectic reaction together with eutectic γ-phase. However, γ-phase decomposes in the eutectoid reaction which eventually generates the island-like eutectoid α-Al and eutectoid β-Zn as in Figure 2.4 (b).

2.2 Hot dipping

2.2.1 History of hot dipping

Hot dipping is a technology where the substrate (usually Fe) is dipped into a tank of molten liquid to get the coating. Record of zinc usage in construction began in 79AD, which could be considered the origination of galvanizing. The first recorded history of galvanizing dates back to when Malouin, a French chemist, presented to the Royal Academy of Sciences several experiments involving coating iron with molten zinc in 1742. Over a century later, the British galvanizing industry was consuming 10,000 tons of zinc annually for the production of galvanized steel. The United States, in the 1870s, had its first galvanizing plant open. At the time, the steel was hand dipped in the zinc bath. Today, more than 600,000 tons of zinc is consumed annually in North America to produce hot-dip galvanized steel - 200,000 tons for after fabrication (batch) process and 400,000 for the continuous galvanizing process. Galvanizing is found in almost every major application and industry where iron or steel is used. The utilities, chemical process, pulp and paper, automotive, and transportation industries etc. Hot-dip galvanizing has a proven and growing history of success in myriad applications worldwide[13].

2.2.2 The process of hot dipping Galfan (HDG)

2.2.2.1 Surface prepare

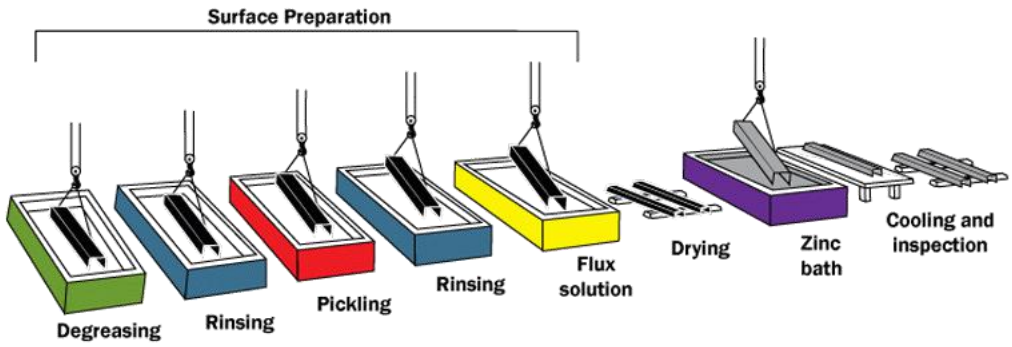

Figure 2.5 The process of hot dipping[14].

Generally speaking, there are three stages: Surface preparation, Galvanizing, and Inspection. For mild steel, the surface preparation includes: degreasing, pickling, and fluxing. Degreasing is a process to remove the organic pollution on the surface such as such as dirt, paint markings, and oil. A hot alkali solution, mild acidic bath, or biological cleaning bath are all suitable options for this process. 7 Pickling process is designed to desolve the oxidized layer by hydrochloric acid or sulfuric acid. It is also reported that pickling and degreasing could be replace by air sand blast or other similar technologies. In fluxing, the substrate immerses into zinc-ammonium solution for two purpose: (1) to remove the remaining oxides and (2) to form a protective layer to prevent further oxides until galvanizing[14].

2.2.2.2 Hot dipping bath

In galvanizing, the coating material is molten in a bath tank with the protective gas if

needed. When the substrate is dipped into the liquid metal, Fe and Zn forms the chemical and physical bonds producing the intermatelic layer with the coating-metal layer on the top as shown in Figure 2.5.

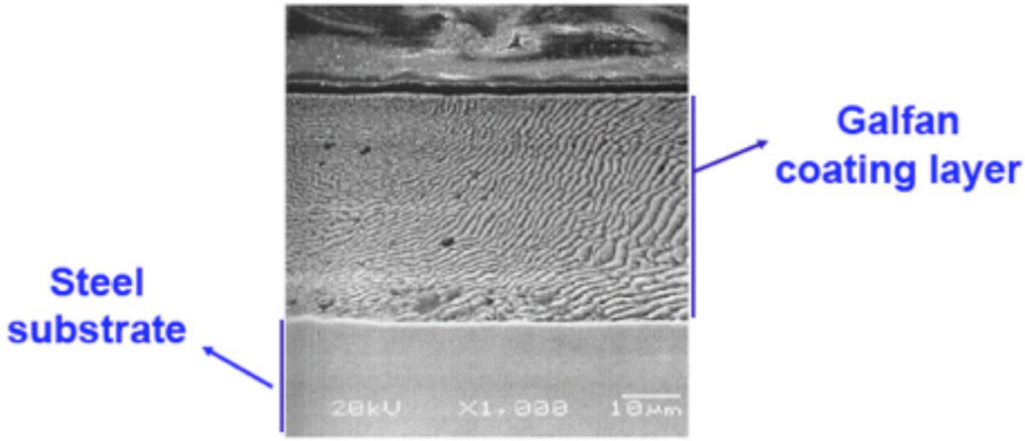

Figure 2.5 Microstructure of Zn-5% Al Coating [15].

2.2.2.3 Inspection

Inspection of galvanzing coating mainly focuses on coating thickness and surface condition. Products are galvanized according to long-established, accepted, and approved standards of ASTM, the International Standards Organization (ISO), the Canadian Standards Association (CSA), and the American Association of State Highway and Transportation Officials (AASHTO). These standards cover everything from the minimum coating thicknesses required for various categories of galvanized items to the composition of the zinc metal used in the process[14].

2.3 Introduction of Galfan corrosion

2.3.1 Chemical properties of Zn and ZnAl

As an element in group 12 of the periodic table, Zn is a moderately reactive metal and a reducing agent. Pure Zn tarnish quickly in the air. However, with the presence of carbon dioxide, a protective passivation layer is form consisting zinc carbonate.[16] Zinc reacts readily with acids, alkalis and other non-metals[17]. Strong acids, such as hydrochloric or sulfuric acid, can remove the passivating layer and subsequent reaction with water releases hydrogen gas[18].

2.3.2 Corrosion types

2.3.2.1 Uniform corrosion

Uniform corrosion, also known as general corrosion, is the most common form of corrosion. It is usually happens with a uniform chemical or electrochemical reaction over the whole surface. The metal would become thinner as the reaction proceed until it fails. Figure 2.6 is a schematic diagram of uniform corrosion.

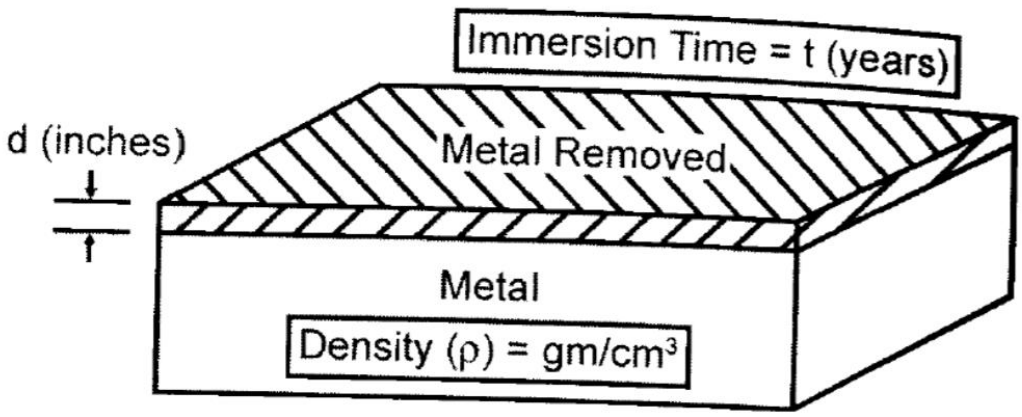

Figure 2.6 Schematic diagram of uniform corrosion[19].

2.3.2.2 Pitting corrosion

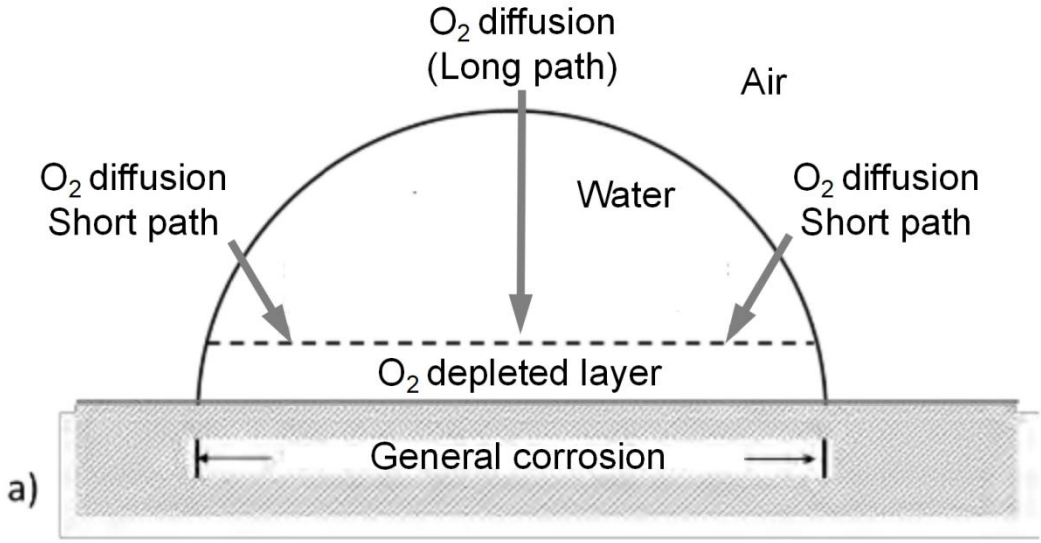

(a)

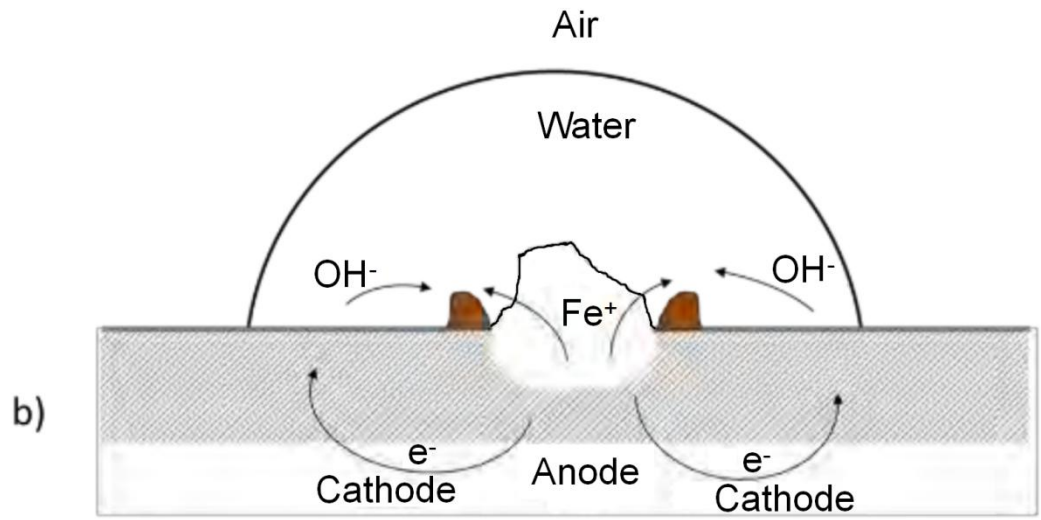

(b)

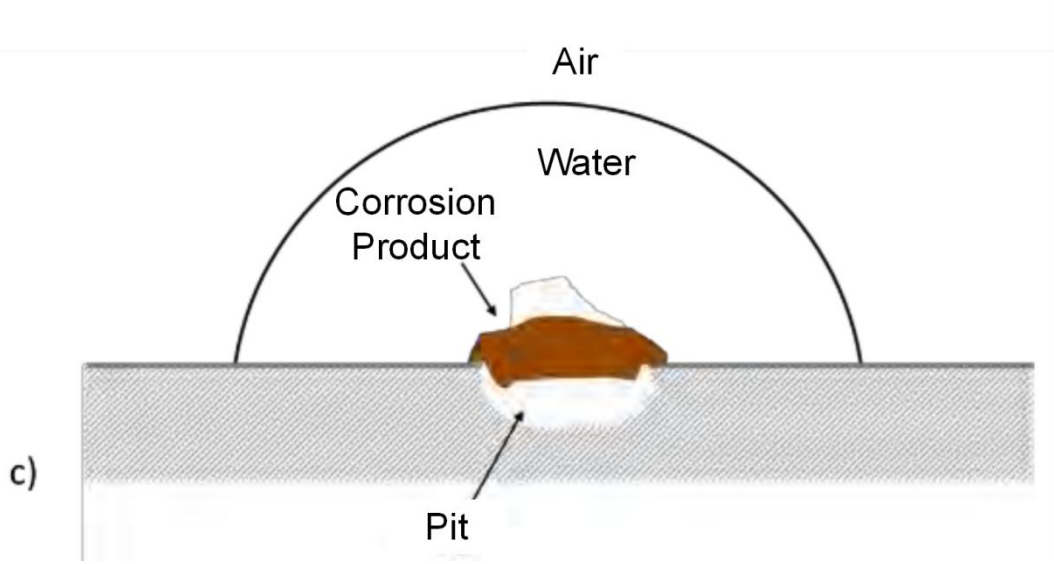

(c)

Figure 2.7 Simple illustration of pitting corrosion mechanism. (a) General corrosion over wetted area results in oxygen depletion in adjacent electrolyte to steel surface. (b) Metal dissolution leads to corrosion product formation around the newly formed pit. (c) Corrosion products accumulate with time to cover the pit[20].

Pitting corrosion happens as some points and eventually forms holes in the metal. Pits are sometimes close with each other making the surface rough. Pitting is highly destructive to the metal. Despite the weight loss caused by pitting corrosion is small, it may result serious fail. It takes several month or even years to reveal its severity. This type of corrosion is also difficult to detect due to the small size and the covered unnoticed surface.

General corrosion starts from an area of the wet surface as in Figure 2.7 (a). An oxygen concentration gradient in the liquid is then formed because the normal cathode reaction consumes more oxygen through the short path on the side. Once this happens,

hydroxyl ions are dissolved and accelerate the cathode reaction with iron in the center. Gradually, the insoluble reaction products deposits on the top of the pit gradually making a hole in the substrate. It is found that the present of chloride ions can increase the risk of pitting corrosion[21].

2.3.3.3 Galvanic corrosion

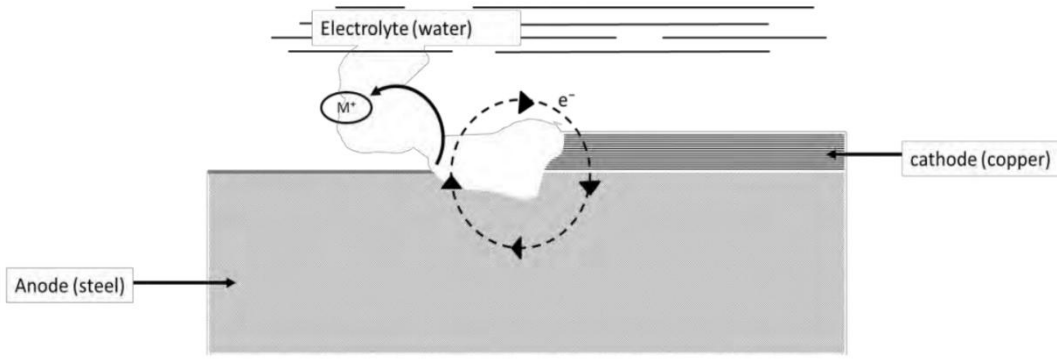

Figure 2.8 Galvanic couple formed between steel and copper whereby steel is corroded in preference to copper[22].

A electrochemical potential difference usually exists between different kinds of metals. With the a conductive media, usually corrosive electrolyte, the electrons started to move which produces a galvanic corrosion reaction. Since the reaction happens on cathode (nobler material) metal only provides electrons in the metal, the main mass loss is on the anode where the electrons flow to cathode and the metal ions are dissolved in the electrolyte. Figure 2.8 demonstrates the mechanism of galvanic corrosion of Cu-Fe couple. Standard electrode potential is defined to measure the individual potential of reversible electrode at standard state with ions at an effective concentration of 1mol/dm^3

at the pressure of 1 atm. From Table 2.1, it is found that iron (potential is -0.44V), would become cathode with any element having a lower potential such as zinc and aluminum.

Table 2.1 Standard electrode potential of metals[23]

Element	Electrode Potential (V)	Element	Electrode Potential (V)	Element	Electrode Potential (V)
Lithium	-3.04	Zinc	-0.76	Antimony	0.1
Rubidium	-2.92	Chromium	-0.74	Copper	0.34
Potassium	-2.92	Tungsten	-0.58	Iodine	0.54
Calcium	-2.87	Iron	-0.44	Silver	0.8
Barium	-2.8	Cadmium	-0.4	Mercury	0.85
Sodium	-2.71	Cobalt	-0.28	Bromine	1.07
Magnesium	-2.37	Nickel	-0.24	Platinum	1.2
Beryllium	-1.85	Tin	-0.14	Chlorine	1.36
Aluminum	-1.67	Lead	-0.13	Gold	1.5
Manganese	-1.19	Hydrogen	0	Fluorine	2.87

2.3.3.4 Intergranular corrosion

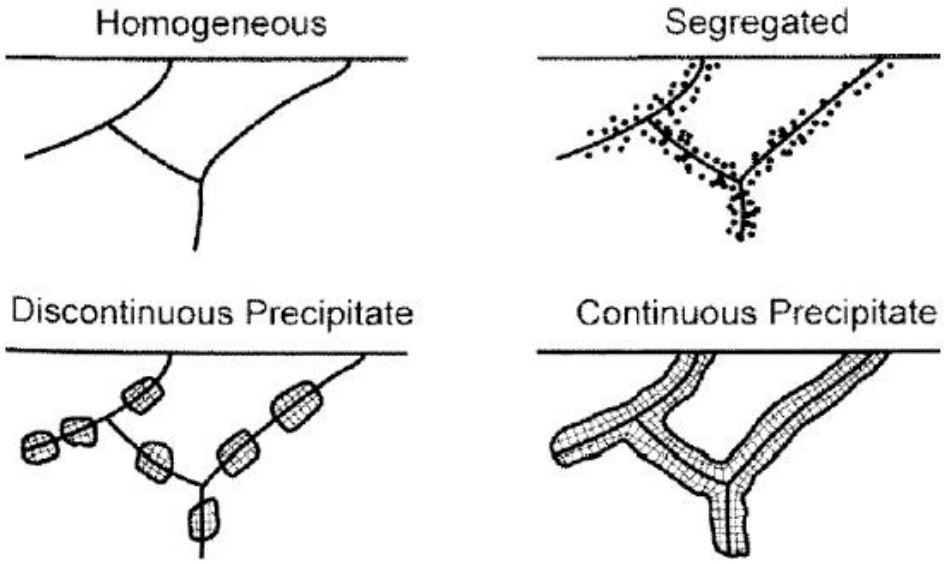

Figure 2.9 Intergranular corrosion takes place when elements segregating or precipitating atgrain boundaries cause the area to become anodic in relation to the interior of the grain[21].

Figure 2.9 shows the process of intergranular corrosion. Grain boundaries usually have more defect than the center part of the grains. Therefore, the are more reactive in corrosion. For most metals, this difference is so little that the general uniform corrosion can overwhelm it. However, under some conditions, the interface could become more reactive very obviously enhancing the grain boundary corrosion. There are several reasons to explain this phenomenon including the impurities on the boundary, enrichment of alloy element, and depletion of element. Intergranular corrosion is common on Austenitic stainless steel at 510-780℃[24].

2.4 Reference

[1] Lehto, R. S. (1968). "Zinc". In Clifford A. Hampel. The Encyclopedia of the Chemical Elements. New York: Reinhold Book Corporation. pp. 822–830.

[2] Weast, Robert (1984). CRC, Handbook of Chemistry and Physics. Boca Raton, Florida: Chemical Rubber Company Publishing. pp. E110.

[3] Nglos324 - hcp. (n.d.). Retrieved from https://www.princeton.edu/~maelabs/mae324/glos324/hcp.htm

[4] Shakhashiri, B. Z. (17 March 2008). "Chemical of the Week: Aluminum" (PDF). SciFun.org. University of Wisconsin. Archived from the original (PDF) on 9 May 2012. Retrieved 4 March 2012.

[5] Singh, B. J. (2014). RSM: A Key to Optimize Machining: Multi-Response Optimization of CNC Turning with Al-7020 Alloy.

[6] Iron crystallizes in a face-centered cubic system. | Socratic. (n.d.). Retrieved from https://socratic.org/questions/iron-crystallizes-in-a-face-centered-cubic-system-if-the-radius-of-an-iron-atom-

[7] Ares AE, Gassa LM. Corrosion susceptibility of Zn‐Al alloys with different grains and dendritic microstructures in NaCl solutions. Corrosion Science. 2012 Jun 1;59:290-306.

[8] Skoko, Ž., Popović, S., & Štefanić, G. (2009). Microstructure of Al-Zn and Zn-Al Alloys. Croatica chemica acta, 82(2), 405-420.

[9] Cao, R., Sun, J. H., Chen, J. H., & Wang, P. C. (2014). Cold metal transfer joining of aluminum AA6061-T6-to-galvanized boron steel. Journal of Manufacturing Science and Engineering, 136(5), 051015.

[10] Rettenmayr, M., Lambracht, P., Kempf, B., & Tschudin, C. (2002). Zn-Al based alloys as Pb-free solders for die attach. Journal of electronic materials, 31(4), 278-285.

[11] Agapie, M., Peter, I., & Varga, B. (2015). Structure of cooled Zn-Al eutectoid based alloys in biphasic domain. JOURNAL OF OPTOELECTRONICS AND ADVANCED MATERIALS, 17(11-12), 1842-1848.

[12] López, G. A., Mittemeijer, E. J., & Straumal, B. B. (2004). Grain boundary wetting by a solid phase; microstructural development in a Zn–5 wt% Al alloy. Acta Materialia, 52(15), 4537-4545.

[13] What is Galvanizing? (n.d.). Retrieved from https://galvanizeit.org/hot-dip-galvanizing/what-is-galvanizing

[14] HDG Process. (n.d.). Retrieved from https://galvanizeit.org/hot-dip-galvanizing/what-is-galvanizing/hdg-process

[15] Zinc-5% Aluminum Alloy-Coated Steel Sheet. (n.d.). doi:http://www.galvinfo.com/ginotes/GalvInfoNote_1_9.pdf

[16] Porter, F. C. (1994). Corrosion resistance of zinc and zinc alloys. CRC Press.

[17] Hinds, J. I. D. (1902). Inorganic chemistry: with the elements of physical and theoretical chemistry. J. Wiley & sons.

[18] Zinc. (2018, August 16). Retrieved from https://en.wikipedia.org/wiki/Zinc

[19] Tevera, T. (2014). Evaluation of corrosion behaviour of hot dip Zn and Zn-Al alloy coatings on steel wire using laboratory and field tests (Doctoral dissertation, University of Cape Town).

[20] Trethewey KR, Chamberlain J. Corrosion for science and engineering. 2nd ed. Harlow, Essex: Longman;

1995.

[21] Tevera, T. (2014). Evaluation of corrosion behaviour of hot dip Zn and Zn-Al alloy coatings on steel wire using laboratory and field tests (Doctoral dissertation, University of Cape Town).

[22] Schweitzer, P. A. (1989). Corrosion and corrosion protection handbook (Vol. 1). CRC Press.

[23] (n.d.). Retrieved from https://www.engineeringtoolbox.com/electrode-potential-d_482.html

[24] Fontana, M. (1990). Corrosion engineering. New York: Mc Graw-Hill.

CHAPTER 3 Nano Microstructure Development and Solidification of Zn-6 wt.% Al Hypereutectic Alloy

3.1 Introduction

Zn alloys have been extensively used as a protective coating on steel and other metals in consideration of stable quality, mature manufacturing processes and low costs. Their engineering applications are present in the electronic, transportation and construction industries [1-9]. Among the Zn-based alloys, the eutectic Zn-Al alloy with an aluminum content of 5 wt.%, named Galfan, is one of the most widely used coating material due to its excellent long-term durability and flexibility, and low cost. To produce the good quality of the Galfan coating, the hot-dipping technology is usually employed as a primary manufacturing process because of its high production rate and microstructural controllablity and stability. During the hot dipping, substrates following surface modification are immersed in the molten Galfan bath and the coated substrates are cooled consequently. The cooling process plays an important role in the engineering performance of Galfan coatings including mechanical properties and corrosion resistance. Since its first report in 1981, extensive studies on Galfan-relevant coatings have been carried out, which focus on issues such as corrosion performance, optimization of hot dipping processes, and microstructure evolution, etc [8-13]. The study by Elvins et al [11] indicated that variation in microstructure of the Galfan alloy due to different cooling rates affected its corrosion resistance. But, no precise measurements of temperatures were performed to directly determine cooling rates.

Also, it has been reported [12] that a high aluminum content improves the corrosion

resistance of the Galfan, although additional Al increases the processing cost due to its high liquidus temperature. Nevertheless, the relation between the microstructure development and measured cooling rates for the eutectic and hypereutectic Zn-Al alloys is still unclear.

In the present work, the development of microstructure was investigated during the solidification of a hypereutectic Zn–6wt.% Al alloy. Computer-based thermal analysis, and scanning electron microscopy (SEM) techniques with energy dispersive X-ray spectroscopy (EDS) were employed to examine the characteristic temperatures of microstructural constituents and their evolution of the alloy. The obtained results are beneficial for understanding the microstructure development and the design of manufacturing processes for Zn-Al alloys.

3.2 Experimental procedure

3.2.1 Material

The base material selected was the hypereutectic Zn-6 wt.% Al alloy with its chemical composition listed in Table 3.1. In each test, about 0.6 kg of the alloy melt was prepared in an electric resistance furnace using a mild steel crucible. The melt was held at 550℃±10℃ for about 20 min, stirred for 20 s, and then poured into the corresponding molds installed for different cooling conditions.

Table 3.1 Chemical composition of hypereutectic Zn - 6 wt.% Al alloy

Elements	Al	Fe	Si	Pb	Cd	Sn	Zn
wt.%	6.08	0.02	0.002	0.002	0.005	0.001	Balance

3.2.2 Cooling conditions

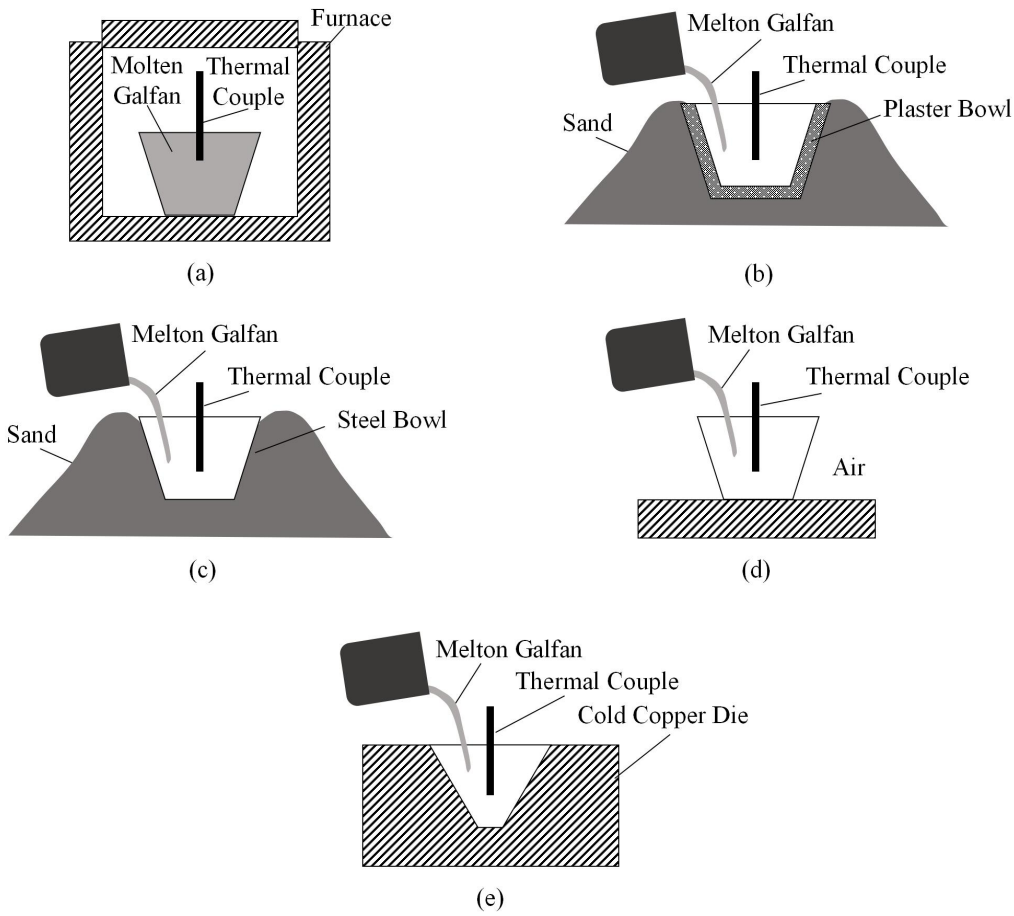

Figure 3.1 Schematic diagram of different cooling conditions used for measuring the thermal history of Galfan alloy (a) furnace cooling. (b) plaster cooling. (c) sand cooling. (d) air cooling. (e) copper die cooling.

To achieve five different cooling rates, the prepared molten alloy was poured into a mold with a height of 30 mm and a diameter of 30 mm. For furnace cooling, the filled mold was cooled inside the furnace from 550 ℃ to room temperature. The plaster mold was employed for simulating a cooling rate of 0.10 ℃/s. The sand cooling condition was obtained for the melted alloy for being buried in silica sand. By leaving the molten

alloy in the air, the air cooling occurred to the alloy. To maximize the cooling, a copper die was used for the molten alloy during its solidification. For each test, about 0.2 kg of melt sample was taken from the well-stirred alloys for casting. The cooling rates of the furnace, plaster, sand, air and copper die cooling are given in Table 3.2.

Table 3.2 Cooling rates of furnace, sand, air and copper die cooling

Cooling method	Furnace	Plaster	Sand	Air	Copper die
Cooling rate (℃/s)	0.04	0.10	0.22	0.40	10.00

3.2.3 Thermal Analysis

A chromel-alumel (K type) thermocouple protected by a thin steel sheath was positioned at a distance of 15 mm from the bottom of the mold center, and was connected to a computer-based data acquisition system to measure the temperature variation. In thermal analyses, the temperatures of solidifying alloy samples were recorded by the data acquisition system at a regular interval of 100 ms as they cooled from the completely liquid state, through the solidification range, to become fully solid. The acquired temperature (T) vs time (t) data from 500 to 200 ℃ were processed, and cooling curves (T vs. t) were plotted using the Microsoft Excel spreadsheet software. The corresponding first and second derivative curves (dT/dt and d^2T/dt^2) were also derived and plotted to reveal detailed characteristics of solidification that cannot be detected on the cooling curves alone. Several duplicate runs on each melt were conducted to ensure an uncertainty of ±0.1%.

3.2.4 Microstructural Analysis

Specimens were sectioned, mounted, and polished from the center of the cast cylindrical coupons, and prepared following the standard metallographic procedures. The detailed features of the microstructure were characterized at high magnifications by a scanning electron microscope (SEM), i.e., Hitachi Tabletop Microscope TM3000, in backscattered electrons (BSE) mode. To maximize composition reading of the energy dispersive spectroscopy (EDS) data, an etchant of 5% nitric acid was applied to polished specimens for microscopic examination.

3.3 Result and discussion

3.3.1 Cooling curve

Figure 3.2 represents a cooling curves recorded during solidification of the Zn-6 wt.% Al alloy along with the corresponding first derivative and second derivative curves. The presence of peaks and transition points on a dT/dt derivative curve indicates that a phase transformation occurs due to releasing latent heat at an increased rate. The peaks on a second derivative curve are considered as the accurate indicator of nucleation temperatures, when the d^2T/dt^2 curve varies considerably. The temperature at which the very first crystal nucleates, stabilizes and starts to grow can be determined. Furthermore, the peak on the second derivative curve indicates a minimum temperature, at which the nucleated crystals have grown in such a way that the liberated latent heat of fusion balances the heat extracted from the samples.

Examination of the cooling curve illustrated in Figure 3.2 (a) manifests three distinguished stages during the solidification process of the Zn-6 wt.% Al alloy with a cooling rate of 0.04 ℃/s. The nucleation of the primary γ-ZnAl phase happens in stage

I, from which the non-equilibrium liquidus temperature is recorded as 390.3 ℃. Stage II at 381.5 ℃ is the nucleation of the eutectic γ-ZnAl and eutectic β-Zn phase, which has no obvious undercooling detected on the cooling curves. Stage III is the occurrence of the eutectoid reaction at 277.6 ℃, i.e., γ-ZnAl → α-Al + β-Zn, where no undercooling phenomena are observed for the decomposition of the primary and eutectic γ-ZnAl phase. According to the Zn-Al phase diagram [13] given in Figure 3.3, the equilibrium temperatures for the phase changes of the Zn- 6 wt.% Al alloy are 382 and 275 ℃ for the eutectic and eutectoid reactions, respectively. Rettenmayr et al [14] reported the liquidus and eutectic temperatures for alloy Zn-6wt.% computed by using ChemSage were 391 and 381 ^{o}C, respectively. Agapie et al [15] and Yang et al [16] showed the eutectoid temperature was 278 and 277 ^{0}C, respectively. The phase change temperatures resulting from the 0.04 ℃/s cooling are in very good agreement with the data existing in the literature, since the furnace cooling gives an extremely slow cooling rate which is very close to the equilibrium, named near-equilibrium. The cooling or solidification rate of the alloy is calculated by the division of the temperature difference between the liquidus and eutectic temperatures with the corresponding time interval from the commencement of the primary reaction to the onset of the eutectic reaction, because the cooling rate is near zero during the eutectic solidification. The effect of cooling rates on the phase change and transformation temperatures for the alloy is summarized in Table 3.3. An increase in cooling rate reduces the liquidus temperature. As the cooling rate increases from 0.04 to 10.00 ℃/s, the liquidus temperature decreases from 390.3 to 382.9 ℃.

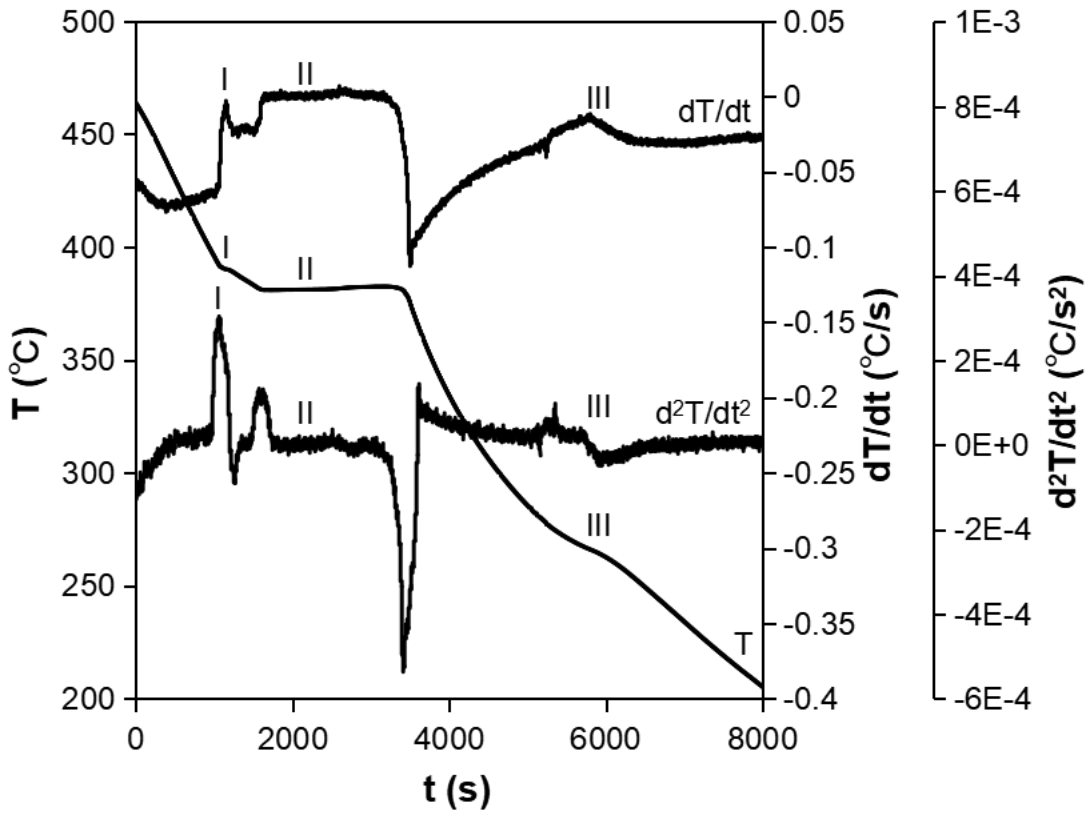

(a)

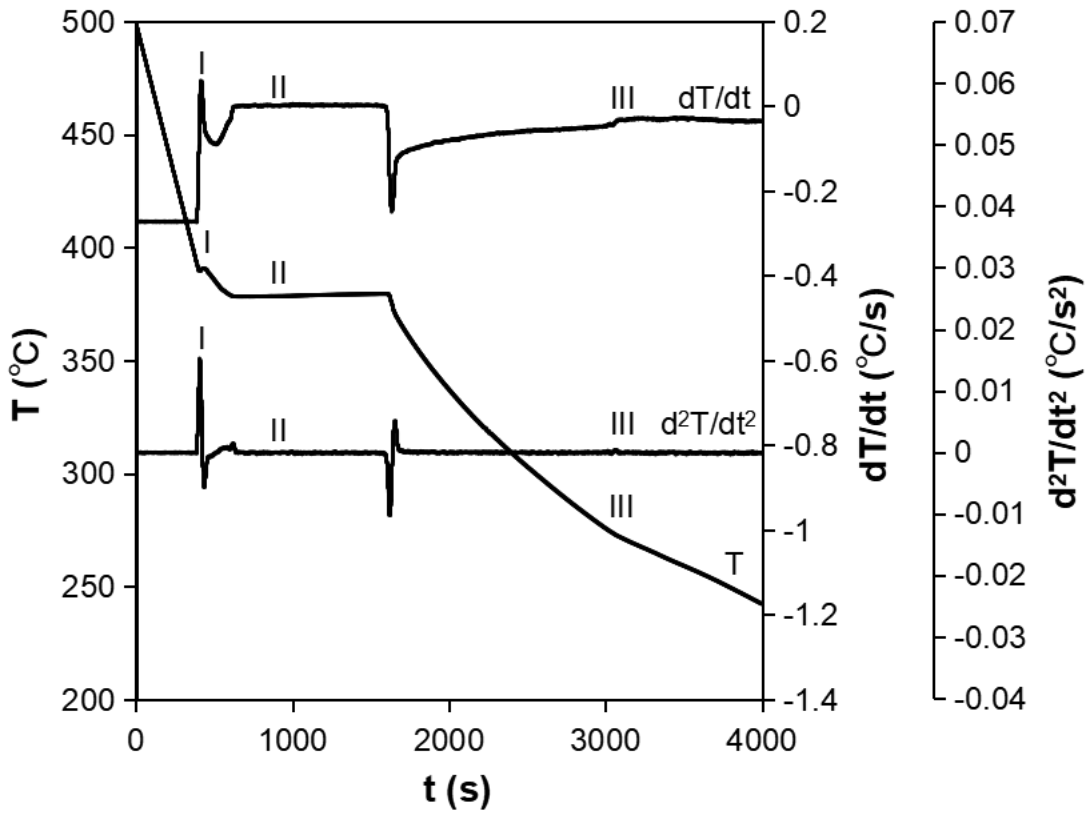

(b)

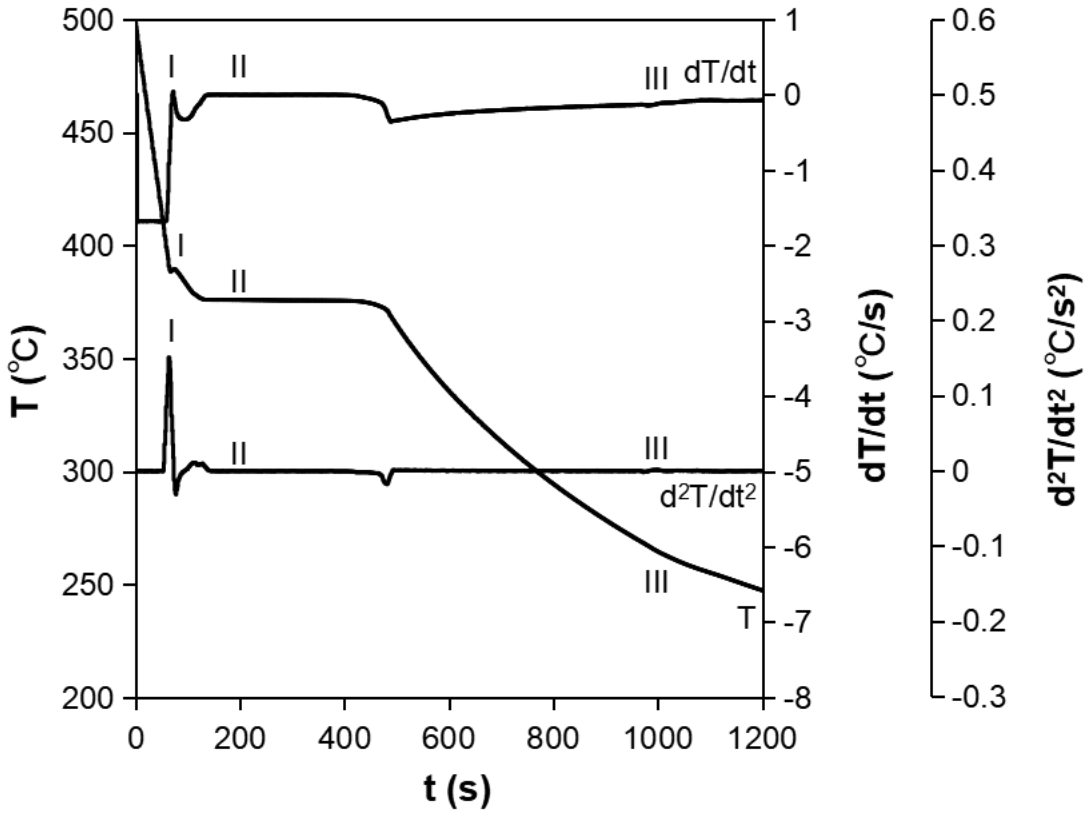

(c)

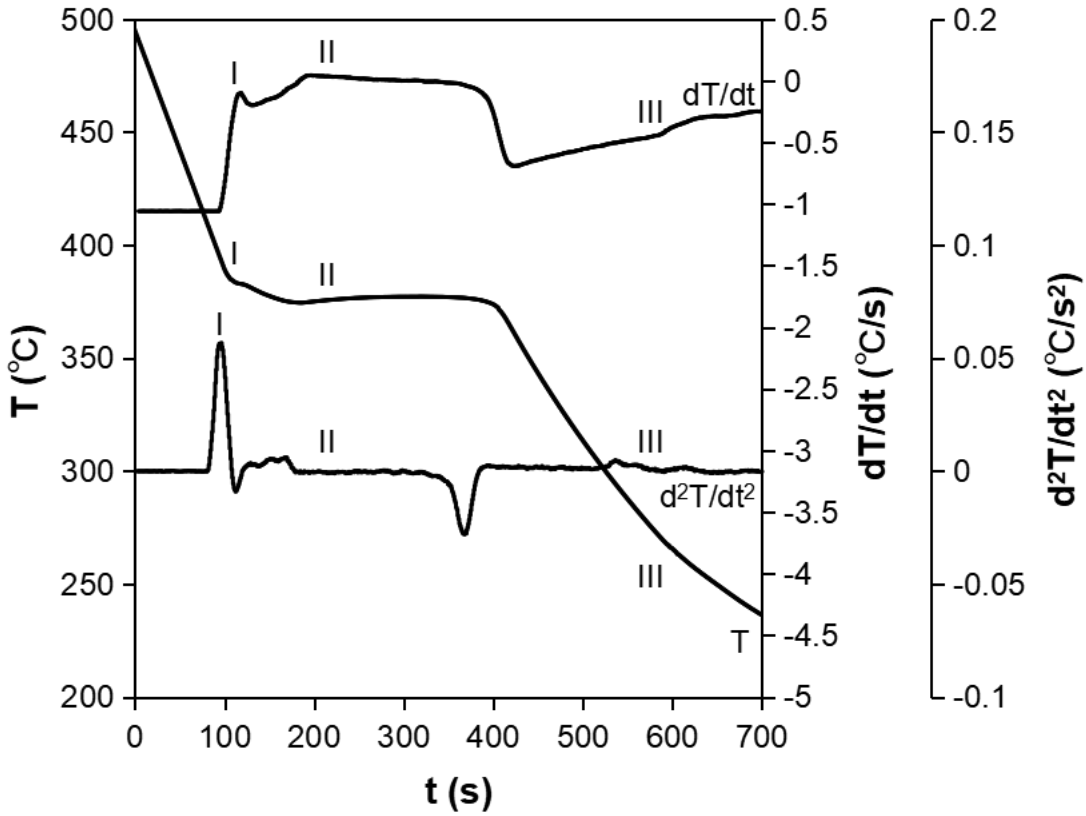

(d)

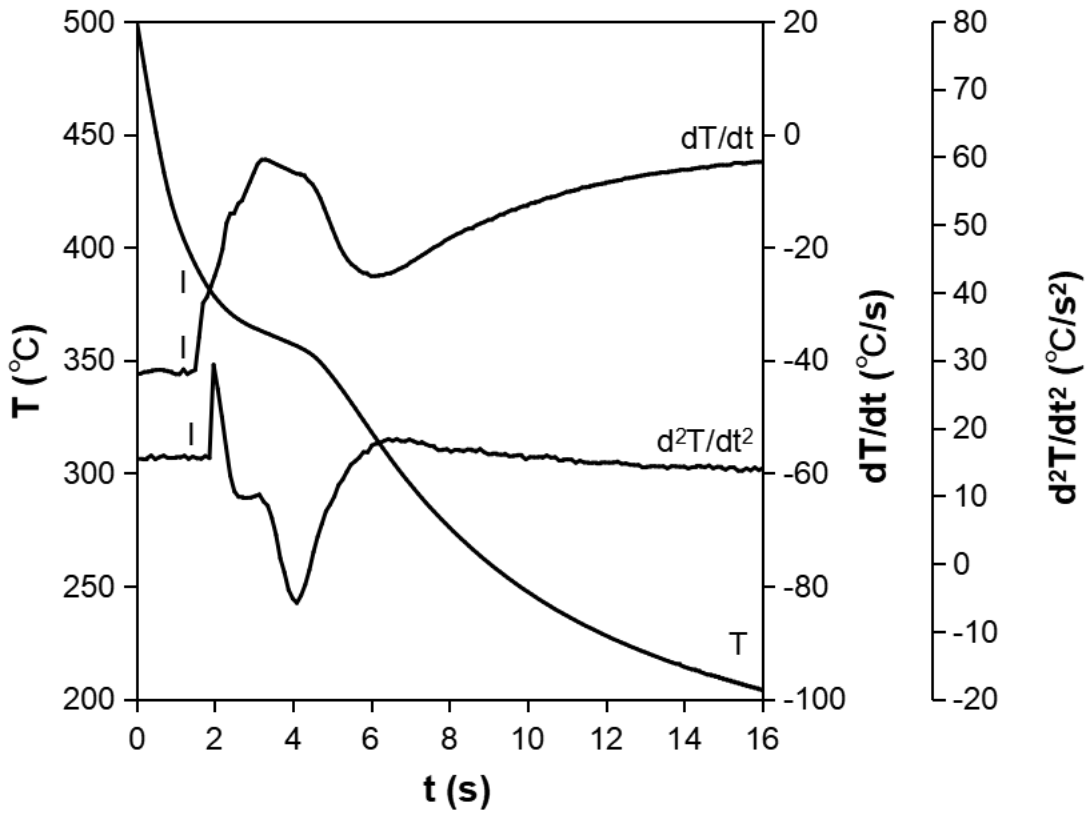

(e)

Figure 3.2 Cooling curves, and first and second order differentials of the Zn - 6 wt.% Al alloy under the cooling rates of (a) 0.04, (b) 0.10, (c) 0.22, (d) 0.40 and (e) 10.00 °C/s.

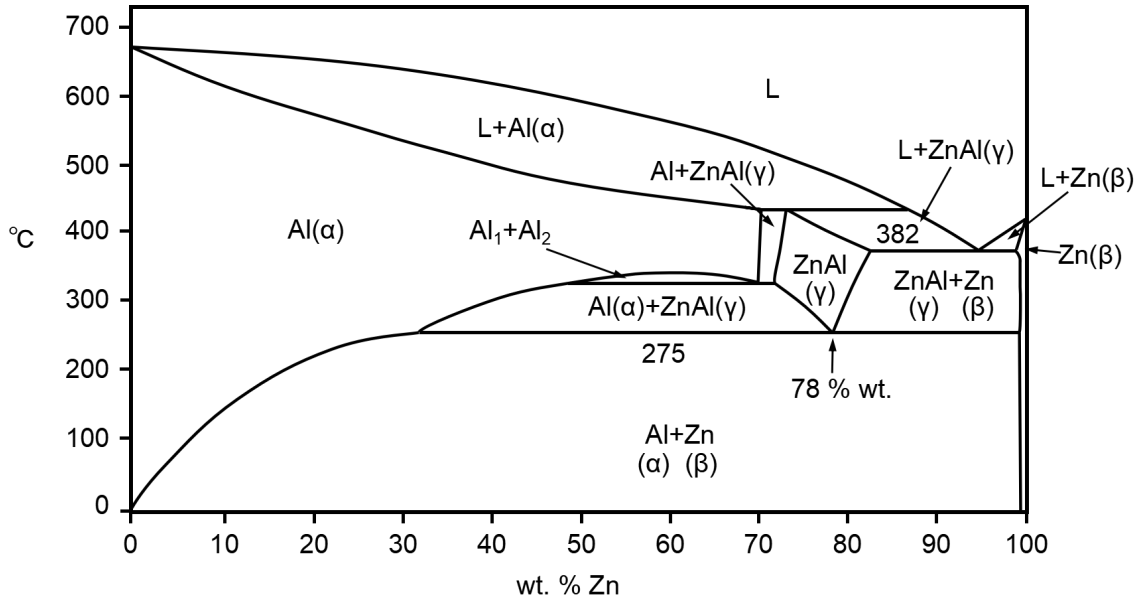

Figure 3.3 Zn-Al phase diagram [13].

Table 3.3 Liquidus, eutectic and eutectoid temperatures for Zn-6wt.% Al alloy at different cooling rates

Cooling Rate (°C/s)	0.04	0.10	0.22	0.40	10
Liquidus Tl (°C)	390.3	389.9	389.4	389.2	382.9
Eutectic Teutectic (°C)	381.5	378.7	377.2	375.6	-
Eutectoid Teutectoid (°C)	277.7	273.7	270.2	267.6	-

The cooling curve of the Zn-6 wt.% Al alloy with the relatively high cooling rates

are given in Figure 3.2 (b), (c) and (d), which reveal the similar three-stage solidification behavior. The formation of primary γ-ZnAl phase begins around 389 ℃ in stage I. But, moving to the second stage, the main difference is that the durations of the eutectic solidification for the plaster, sand and air cooling are shortened to 997 s, 355 s and 215 s from 1776 s for the furnace cooling, respectively. The eutectic temperature for the alloy decreases with the cooling rates, which is 378.7, 377.2 and 375.6 ℃ for the cooling rate of 0.10, 0.22 and 0.40 ℃/s, respectively. Stage three (eutectoid reaction) from the first and second derivatives of the cooling curves in Figure 3.2 (b), (c) and (d) is also observed which begins at 273.7, 270.2 and 267.6 ℃, respectively. Although Figure 1(e) is obtained with the same alloy, there are almost no clearly distinguished stages found on the cooling curve even with significant temporal enlargement. The first derivative curve reveals a transition point present at 382.9 ℃, which indicates the occurrence of the primary reaction. There is no plateau near zero on the first derivative curve, which implies the eutectic reaction is suppressed. But, 4 seconds after the commence of the primary solidification, a trough on the first order differential curve indicates the completion of the entire solidification and/or phase transformation process, including the primary, eutectic and/or eutectoid reactions, which takes place rapidly within only 5 s, since there are no visible transition points afterwards. The absence of transition points around the eutectoid temperature suggests the suppression and rapidity of the eutectoid reaction.

3.3.2 Determination of equilibrium liquidus and eutectoid temperatures

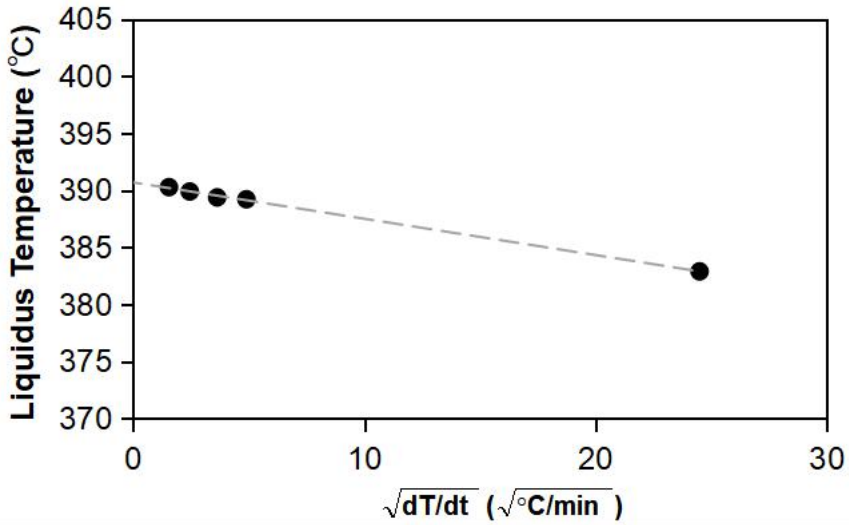

Figure 3.4 Calculation of equilibrium liquidus temperature for Zn-6wt.% Al alloy.

The determination of the equilibrium temperature is often vital for the scientific understanding of solidification. The thermal analysis enables to determine the non-equilibrium liquidus temperature from the plateau temperatures on the cooling curve and the derivate changes on the differential curve [17]. To calculate the equilibrium temperature (T_{eq}), the extrapolation of the linear function between the non-equilibrium liquidus temperature (T_{noneq}) and the square root of the cooling rate (dT/dt) to the zero cooling rate needs to be performed. Equation 1 which correlates the non-equilibrium liquidus temperature and the cooling rate can be used to determine the equilibrium temperature

$$T_{noneq} = T_{eq} + k\,(dT/dt)^{1/2} \qquad (1)$$

where k is a material-related empirical constant. For the Zn-6 wt.% Al alloy, Figure 3 presents the linear relation between the non-equilibrium liquidus temperature (T_{noneq}) and the square root of the cooling rate (dT/dt) with a correlation coefficient of 0.999. By

applying Equiation (1) to the data given in Table 3.3, the equilibrium temperature for the alloy is calculated to be 390.7 ℃.

It can be seen from Figure 3.2 (e) that, as the cooling rate increases to be very high, the eutectoid temperature at the end of the cooling process became unobvious, which is caused by serious microsegregation. Fredriksson[17] suggested that this temperature could be determined only by analyzing the corresponding phase transformation stage on the heating curve, although it is almost impossible to accurately determine the equilibrium eutectoid temperature by performing thermal analysis on cooling curves. Figure 3.5 presents a heating curve and its derivative for the Zn-6 wt.% Al alloy. From Figure 3.5, the eutectoid temperature is determined at stage III as 275.0 ℃. Despite that the determined temperature of 275.0 ℃ is a near-equilibrium eutectoid, it is comparable to the equilibrium one (275-278 ℃) given in the literature present in the preceding section.

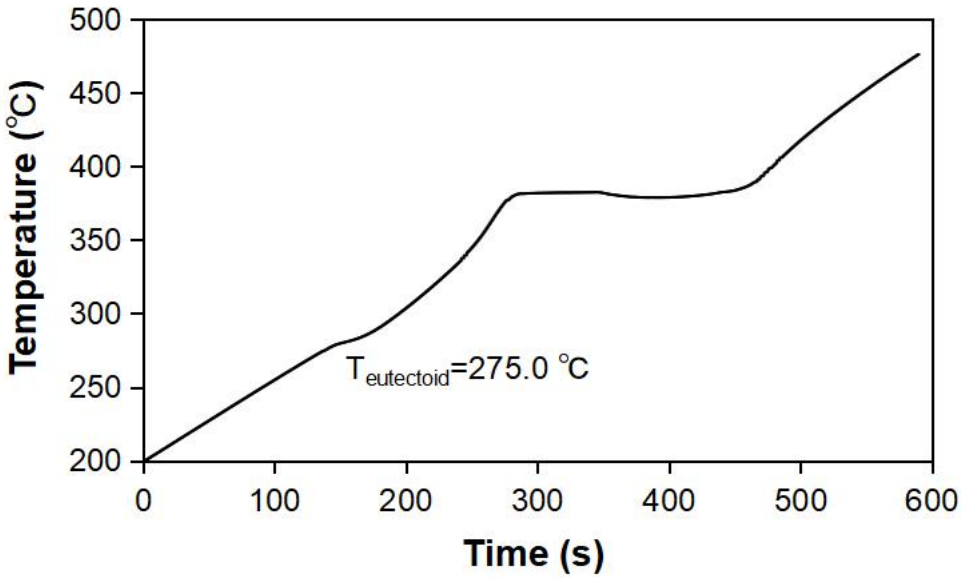

Figure 3.5 Heating curve and derivative for the Zn-6 wt.% Al alloy.

3.3.3 Microstructural constituents and phase identification

The SEM and EDS results for the Zn - 6 wt.% Al alloy solidified under a cooling rate of 0.04 °C/s are shown in Figures 3.6 to 3.8. Figures 3.6 presents the SEM micrographs showing the microstructural constituents of the alloy. Table 3.4 gives the weight percent and atomic percent of elements Zn and Al detected by the EDS in areas A and B. The EDS element analyses indicate that area A contains almost 100% Zn, while the ratio of Zn (45.80%) and Al (54.20%) in terms of atomic percentages in area B is 0.85 close to 1. The observation on the element distribution in areas A and B implies the presence of the eutectic β-Zn phase which contains mostly Zn as well as the primary γ-ZnAl phase. The presence of the eutectic β-Zn phase should be responsible for the evident appearance of the second stage on the first (dT/dt) derivative curve of the alloy. In contrast to that of area A, the formation of the γ-ZnAl phase in the primary reaction results in the appearance of stage I in both the first (dT/dt) and second (dT^2/dt^2) derivative curves of the alloy. Figures 3.7 presents SEM micrograph in BSE mode presenting enlarged zone I in Figures 3.6, showing the microstructural constituents, i.e., eutectoid phases in the Zn - 6 wt.% Al alloy solidified.

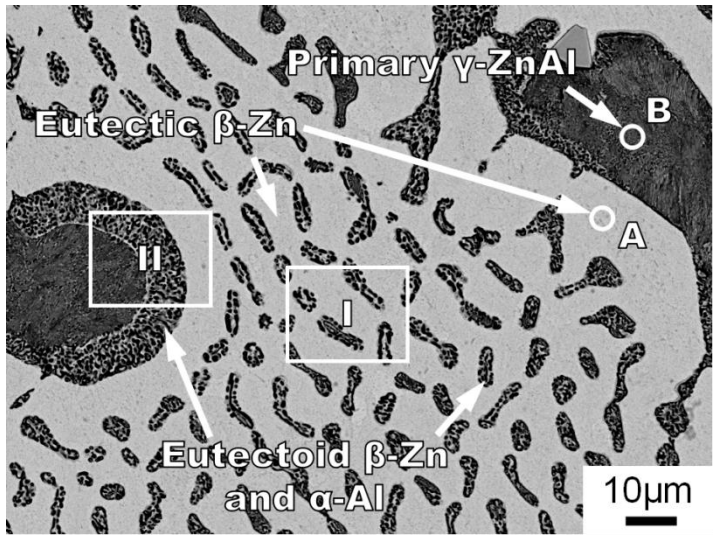
Primary γ-ZnAl
B
Eutectic β-Zn
A
II
I
Eutectoid β-Zn
and α-Al
10μm

(a)

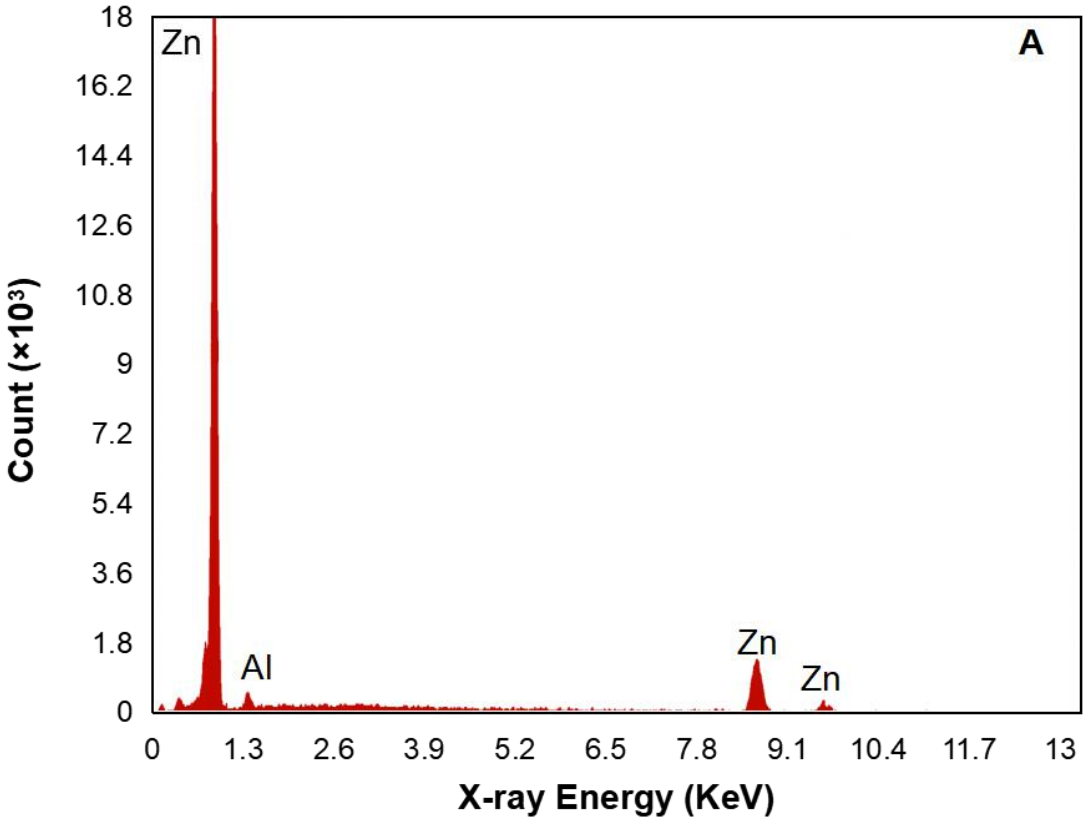
Zn
A
Al
Zn
Zn
Count (×10³)
X-ray Energy (KeV)
0
1.8
3.6
5.4
7.2
9
10.8
12.6
14.4
16.2
18
0
1.3
2.6
3.9
5.2
6.5
7.8
9.1
10.4
11.7
13

(b)

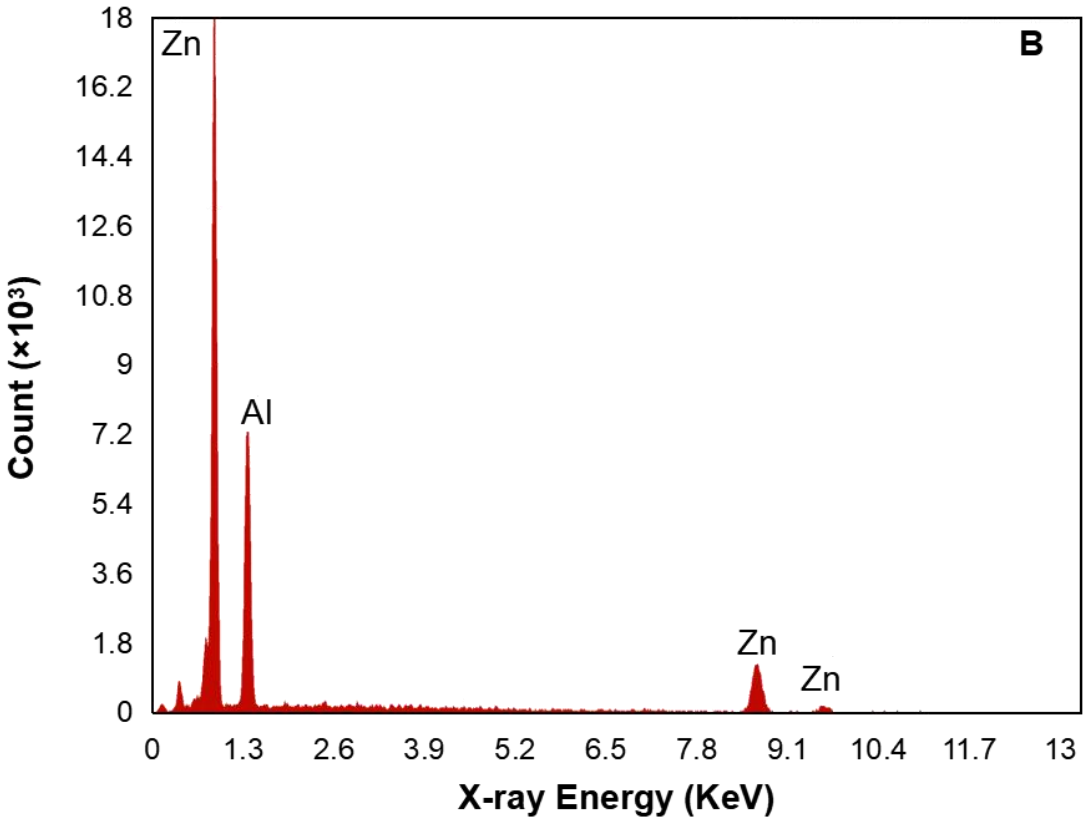

(c)

Figure 3.6 (a) SEM micrograph in BSE mode showing microstructural constituents, and EDS spectra showing (b) eutectic β-Zn phase and (c) primary γ-ZnAl phases of the Zn - 6 wt.% Al alloy solidified under a cooling rate of 0.04 ℃/s.

Table 3.4 Chemical composition of areas A and B in Figure 3.6 (a)

Area	Element	Weight Percent [wt.%]	Atomic Percent [at.%]
A	Zn	97.36	93.83
	Al	2.64	6.17
B	Zn	67.19	45.80

	Al	32.81	54.20

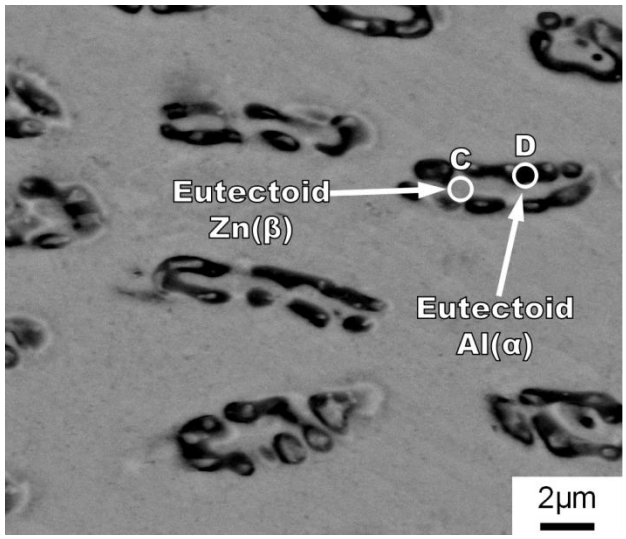

(a)

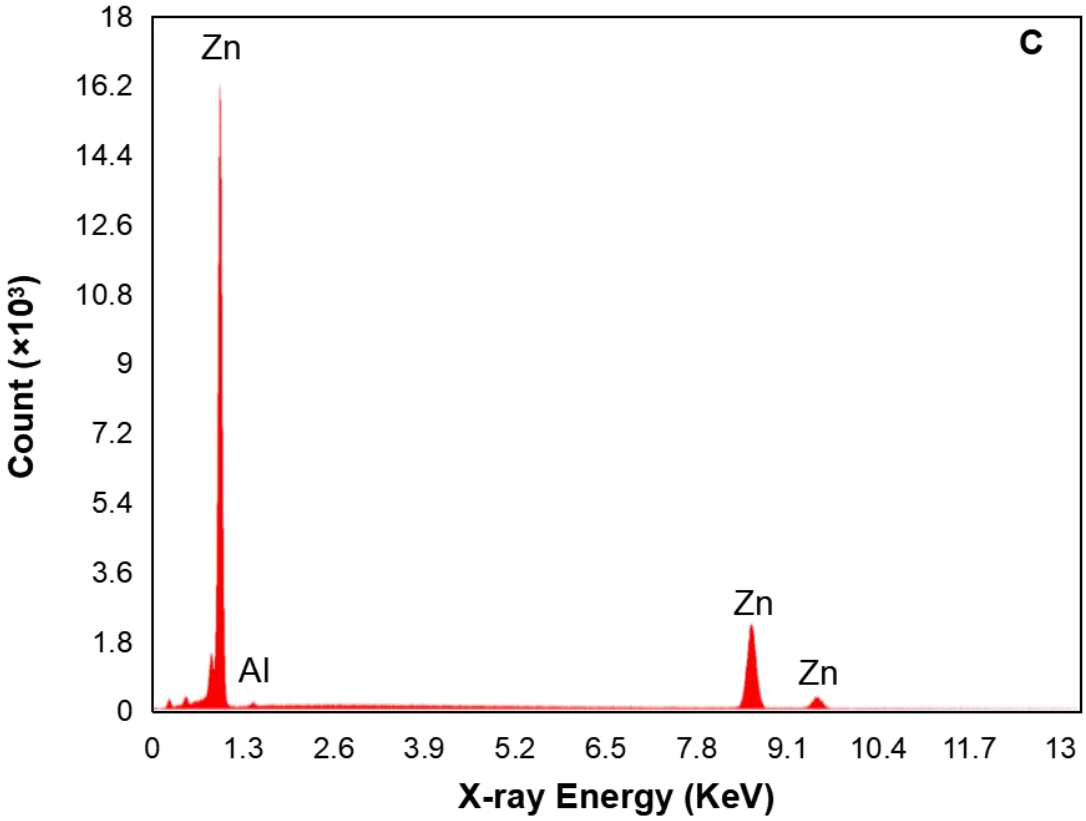

(b)

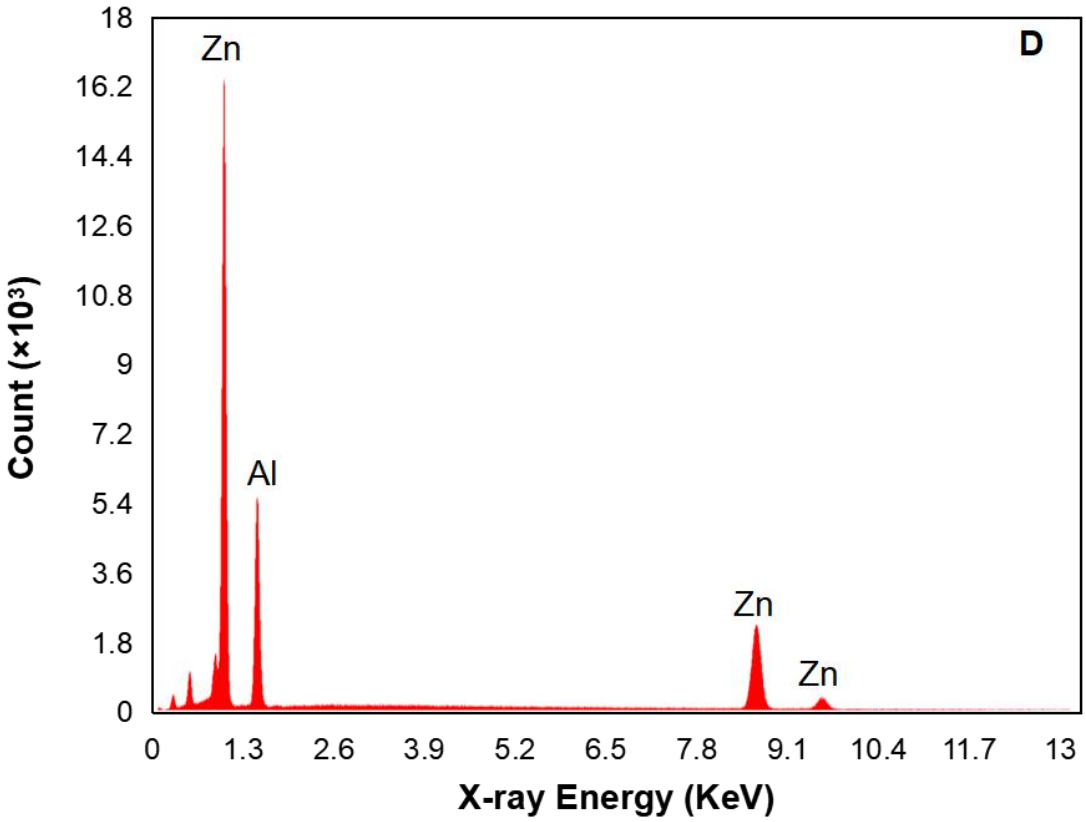

(c)

Figure 3.7 (a) SEM micrograph in BSE mode presenting enlarged zone I in Figures 3.6, showing microstructural constituents, and EDS spectra showing (b) eutectoid β-Zn and (c) eutectoid α-Al phases in the shape of footprints decomposed from the eutectic γ-ZnAl phase in the Zn - 6 wt.% Al alloy solidified under a cooling rate of 0.04 ℃/s.

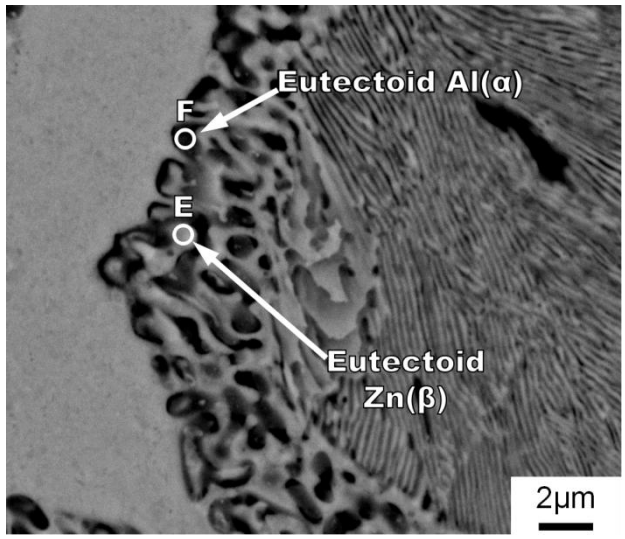
Eutectoid Al(α)
F
E
Eutectoid
Zn(β)
2μm

(a)

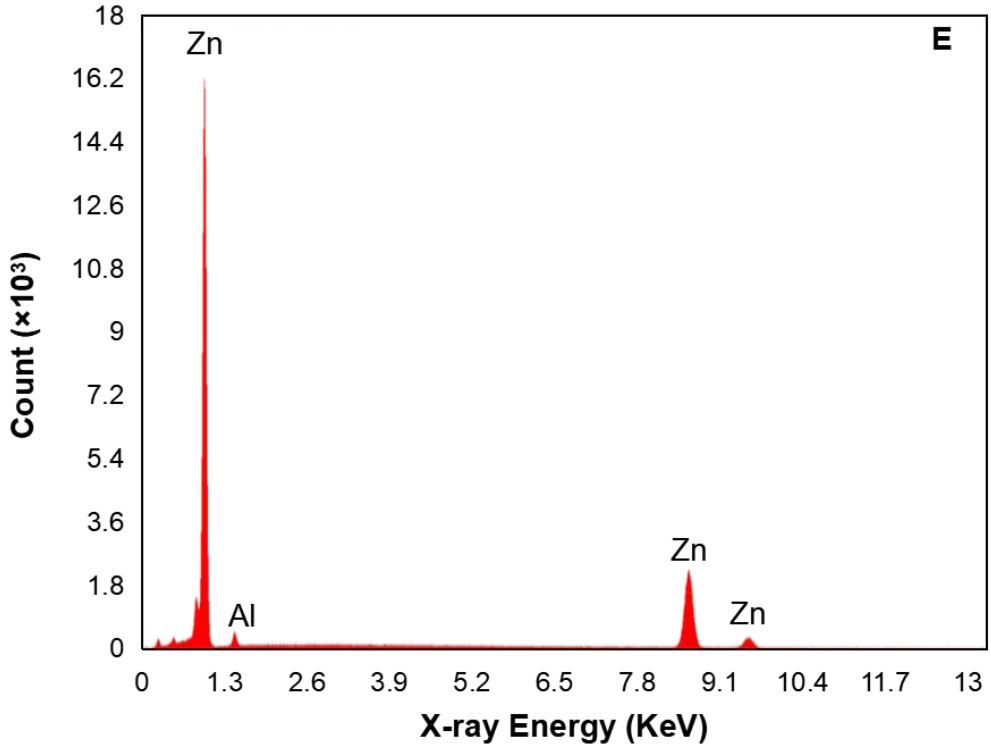
Zn
E
Al
Zn
Zn
Count (×10³)
X-ray Energy (KeV)
18
16.2
14.4
12.6
10.8
9
7.2
5.4
3.6
1.8
0
0
1.3
2.6
3.9
5.2
6.5
7.8
9.1
10.4
11.7
13

(b)

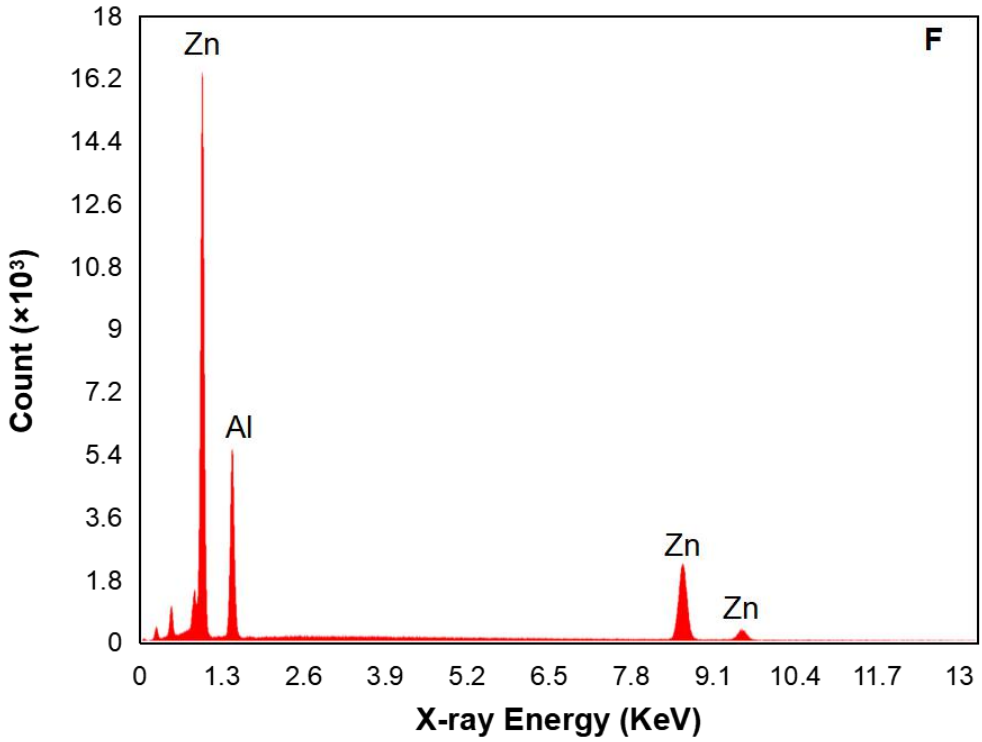

(c)

Figure 3.8 (a) SEM micrograph in BSE mode presenting enlarged zone II in Figures 3.6, showing microstructural constituents, and EDS spectra showing (b) eutectoid β-Zn and (c) eutectoid α-Al phases in the shape of islands decomposed from the primary γ-ZnAl phase, in the Zn-6 wt.% Al alloy solidified under a cooling rate of 0.04 °C/s.

The EDS spectra identify the presence of the eutectoid β-Zn and eutectoid α-Al phases in areas C (gray) and D (black), respectively. The eutectoid β-Zn and eutectoid α-Al phases forming a shape of individual footprints are decomposed from the eutectic γ-ZnAl phase. Figures 3.8 illustrates the identification of the eutectoid β-Zn (area E in gray) and eutectoid α-Al (area F in black) phases surrounding the primary γ-ZnAl phase present in the enlarged zone II of Figures 3.6. The existence of the eutectoid β-Zn (area E) and eutectoid α-Al (area F) should be attributed to the decomposition of the primary

γ-ZnAl phase.

3.3.3 Variation of microstructure with cooling rates

Figures 3.9 shows the variation of the microstructures revealed by SEM with the applied cooling rates. Examination of the samples solidified under the five cooling conditions indicates that all of them contain the primary γ-ZnAl phase in large irregular shapes and dark gray color, while the small well-distributed footprints were the eutectic γ-ZnAl phase. Due to the presence of a eutectoid reaction in the solidification of the Zn-6 wt.% Al alloy based on the Zn-Al phase diagram (Figure 3.3), there are the footprint-shaped eutectoid α-Al and β-Zn phases decomposed completely from the eutectic γ-ZnAl phase in all the observed samples despite their difference in sizes. The primary γ-ZnAl phase is partially decomposed and the resultant eutectoid α-Al and β-Zn phases as islands distributed around the boundaries between the primary γ-ZnAl and eutectic β-Zn. The comparison of the five cooling cases manifests that the cooling rate has a significant influence on the morphology and size of the microstructural constituents including the primary, eutectic and eutectoid phases.

In order to quantitatively characterize microstructures, a public domain image processing system is employed [18]. With ImageJ, different microstructural constituents can be identified through image contrast. To determine the differences in microstructures of the samples resulting from the five cooling rates, the decomposition rate (R_{dcp}) of the primary phase is defined as Equation (2):

$$R_{dcp} = 1 - S_{remaining\ \gamma} / S_{primary\ \gamma} \quad (2)$$

where $S_{remaining\ \gamma}$ is the remaining area of the primary γ-ZnAl phase after decomposition; $S_{primary\ \gamma}$ is the original area of the primary γ-ZnAl phase including both the decomposed

and remaining areas as shown in Figures 3.10 (a). Meanwhile, the average size of the eutectic phase (D_{etc}) is calculated by

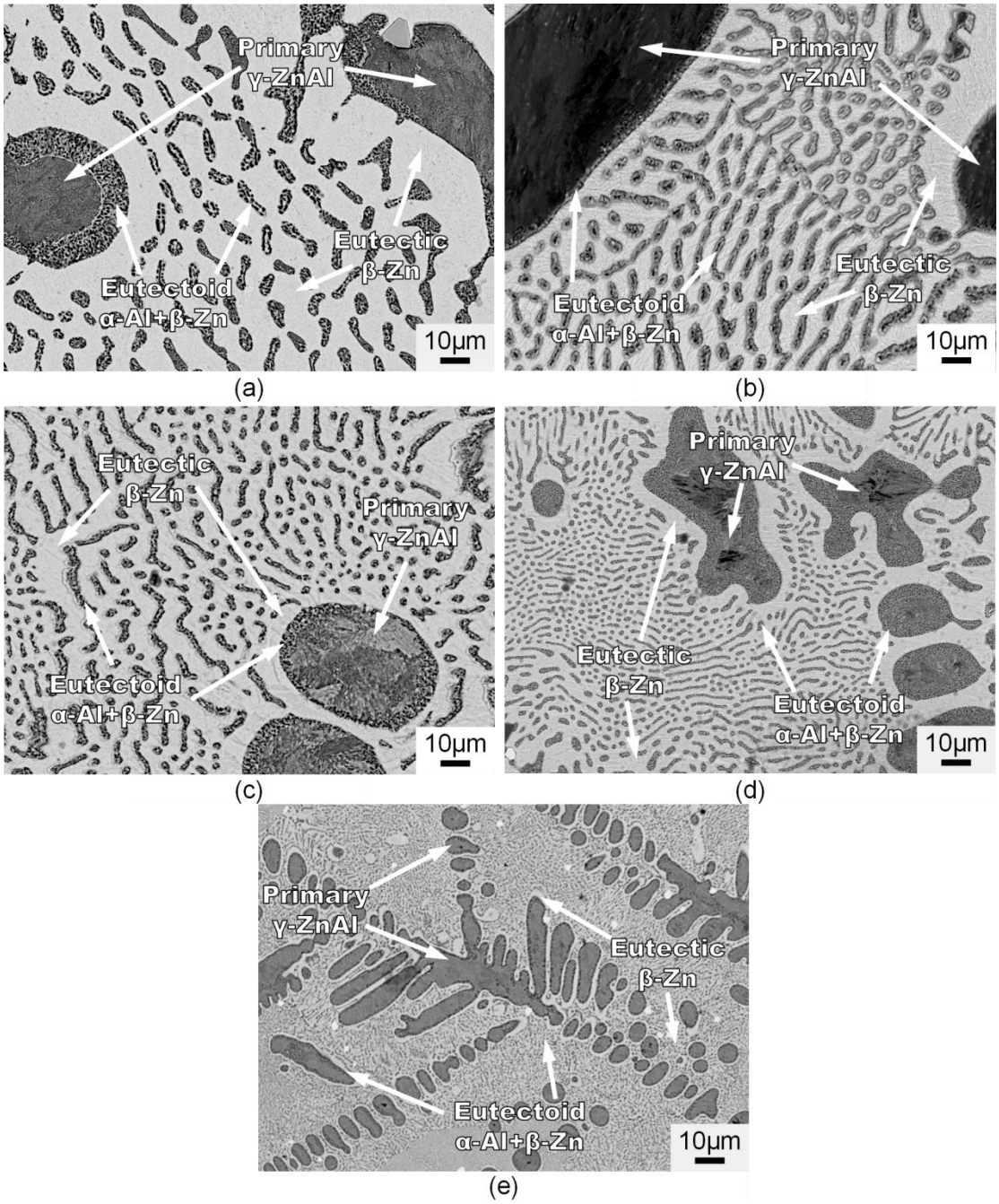

Figure 3.9 SEM micrographs in BSE mode showing the microstructure of the Zn - 6 wt.% Al alloy solidified under four different cooling rates, (a) 0.04 ℃/s, (b) 0.1 ℃/s, (c) 0.22 ℃/s, (d) 0.4 ℃/s, and (e) 20 ℃/s.

$$D_{etc} = (D_l + D_s)/2 \qquad (3)$$

where D_l is the longest diameter, and D_s is the shortest diameter as illustrated in Figures 3.10 (b). In the present analyses, for each microstructural constituent, at least 50 regions were randomly selected from each specimen to ensure an uncertainty less than 5%.

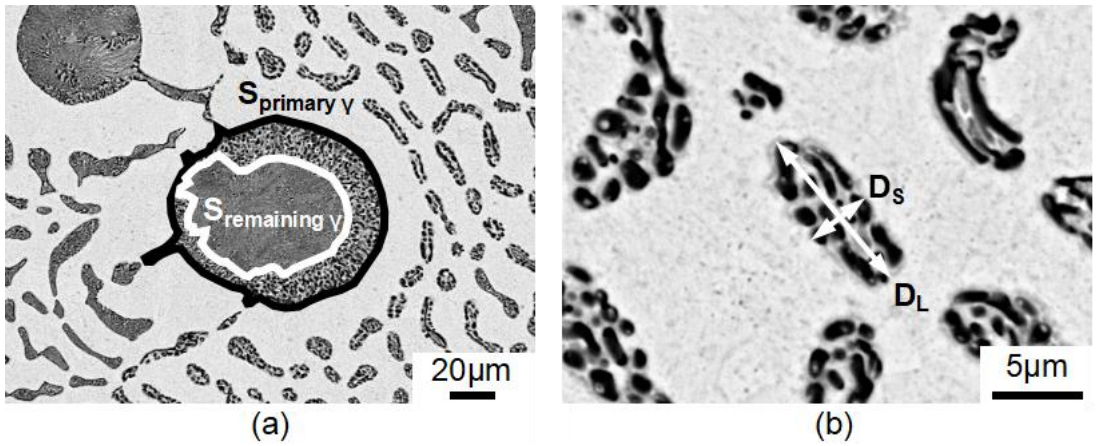

Figure 3.10 SEM micrographs in BSE mode illustrating definitions of (a) the remaining area of the primary γ-ZnAl phase after decomposition ($S_{remaining\ \gamma}$) and the original area of the primary γ-ZnAl phase ($S_{primary\ \gamma}$) for calculation of the decomposition rate (R_{dcp}) of the primary phase, and (b) the longest diameter (D_l) and the shortest diameter (D_s) for calculation of the average size of the eutectic phase (D_{etc}).

Table 3.5 Decomposition rate of the primary phase and average size of the eutectic phase

Cooling rate (℃ /s)	0.04	0.10	0.22	0.4	10.00
Decomposition rate (%)	54±15	43±10	38±9	32±7	27±4
Average size of eutectic (μm)	7.58±1.68	3.2±1.18	2.2±0.62	1.93±0.59	0.58±0.11

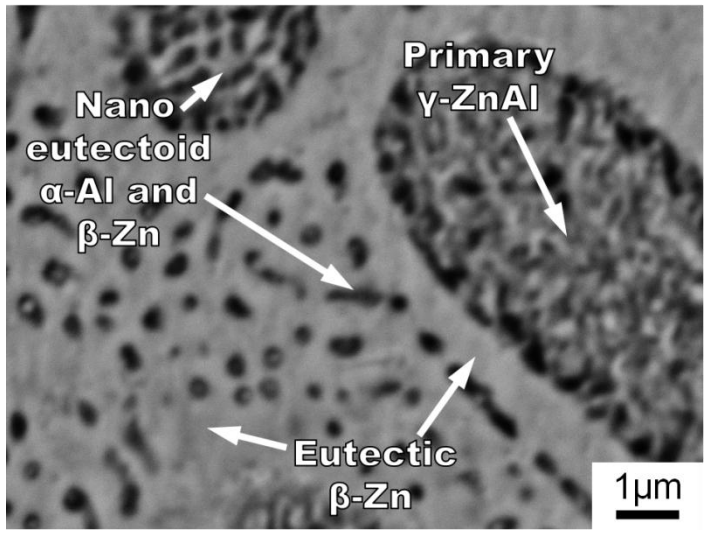

Figure 3.11 SEM micrograph in BSE mode showing the presence of nano-sized eutectoid phases in the Zn - 6 wt.% Al alloy solidified under a cooling rate of 10.00℃/s.

Table 3.5 shows the variation of the decomposition rates of the primary phases and the average sizes of the eutectic phases for the alloys solidified under different cooling rates. The calculated results listed in Table 3.5 show that the cooling rates affect the

development of the microstructure of the Zn-6wt.% Al hypereutectic alloy considerably. The decomposition rate of the primary phases for the cooling rate of 10.00 ℃/s is 27 %, which is only a half of that for the cooling rate of 0.04 ℃/s. The average size of the eutectic phase is significantly reduced by more than an order of magnitude from the micron size (7.58 μm) for the cooling rate of 0.04 ℃/s to the nano size (0.58 μm = 580 nm) for the cooling rate of 10.00 ℃/s. The SEM micrograph given in Figure 3.11 evidently shows the presence of nano-sized eutectoid phases in the Zn-6 wt.% Al alloy solidified under a cooling rate of 10.00 ℃/s. Also, the primary phase is refined considerably as shown in Figures 3.11. This is because the high cooling rate could result in a large undercooling instantaneously, and consequently a high nucleation rate for the development of the refined microstructure and the creation of the nano-sized eutectic phase which forms the nano eutectoid phases subsequently. Moreover, the high cooling rate offers a minimum time to suppress the decomposition of the primary phase and the eutectic reaction. It is expected that the resultant fine microstructural constituents, i.e., primary γ-ZnAl and eutectic β-Zn, as well as the nano-sized eutectoid α-Al and β-Zn phases should be beneficial to the engineering performance of the Zn-6 wt.% Al hypereutectic alloy such as corrosion resistance and mechanical properties. As an on-going research project, the corrosion and mechanical behaviors of the alloy are being evaluated and will be reported later elsewhere.

3.4 Conclusions

The solidification and microstructure development of the Zn-6 wt.% Al hypereutectic alloy are investigated by the thermal analysis. With the slow cooling

rates of 0.04, 0.10, 0.22 and 0.40 ℃/s, three stages for phase changes on the cooling curves are determined by the first and second order differentiation. The nucleation of the primary γ-ZnAl phase happens in stage I in a near-equilibrium condition of cooling (0.04 ℃/s), from which the liquidus temperature is recorded as 390.3 ℃. Stage II at 381.5 ℃ is the nucleation of the eutectic γ-ZnAl and eutectic β-Zn phase. Stage III is the occurrence of the eutectoid reaction at 277.7 ℃, i.e., γ-ZnAl → α-Al + β-Zn. As the cooling rate increases from 0.04 to 10.00 ℃/s, the liquidus temperature decreases from 390.3 to 382.9 ℃. The equilibrium liquidus temperature is calculated to be 390.7 ℃ by extrapolating the linear function between the non-equilibrium liquidus temperature and the square root of the cooling rate (dT/dt) to the zero cooling rate. The temperature recording on a heating curve is analyzed for determination of the equilibrium eutectoid temperature, which is 275.0 ℃.

The SEM and EDS results for the Zn-6wt.% Al alloy solidified under the cooling rates of 0.04, 0.10, 0.22 and 0.40 ℃/s reveal the presence of the primary γ-ZnAl phase, the eutectic β-Zn phase, and the eutectoid α-Al and eutectoid β-Zn phases. As the cooling rate increases to 10.00 ℃/s, which suppresses the eutectic and eutectoid reactions, the average size of the eutectic phase is significantly reduced by more than an order of magnitude from the micron size (7.58 μm) for the cooling rate of 0.04 ℃/s to the nano size (0.58 μm = 580 nm) for the cooling rate of 10.00 ℃/s. Compared to those of the other three cooling rates, the microstructural constituents in the alloy solidified under the cooling rate of 10.00 ℃/s are refined considerably, despite the existence of the primary γ-ZnAl phase and the eutectic β-Zn phase.

3.5 References

[1] Green A, van Wesemael J. Zinc die casting alloys and sustainability. Die Casting Engineer. 2009:56.

[2] Apelian D, Paliwal M, Herrschaft DC. Casting with zinc alloys. JOM. 1981 Nov 1;33(11):12-20.

[3] Porter FC. Corrosion resistance of zinc and zinc alloys. CRC Press; 1994 Jun 29.

[4] Azizan FM, Purwanto H, Mustafa MY, et al.. Effect of Adding Ag on Tensile and Microstructure Properties of Zinc Alloy. International Journal of Engineering & Technology. 2012;12:78-84.

[5] Ares AE, Schvezov CE. The effect of structure on tensile properties of directionally solidified Zn-based alloys. Journal of Crystal Growth. 2011 Mar 1;318(1):59-65.

[6] Gueijman SF, Schvezov CE, Ares AE. Vertical and horizontal directional solidification of Zn-Al and Zn-Ag diluted alloys. Materials transactions. 2010 Oct 1;51(10):1861-70.

[7] Rosenberger MR, Ares AE, Gatti IP, et al. Wear resistance of dilute Zn–Al alloys. Wear. 2010 May 12;268(11-12):1533-6.

[8] Ares AE, Gassa LM, Schvezov CE, Rosenberger MR. Corrosion and wear resistance of hypoeutectic Zn–Al alloys as a function of structural features. Materials Chemistry and Physics. 2012 Oct 15;136(2-3):394-414.

[9] Smith WF. 1993. Structure and properties of engineering alloys, McGraw-Hill Inc., US, 2 edition.

[10] Prosek T, Hagström J, Persson D, et al. Effect of the microstructure of Zn-Al and Zn-Al-Mg model alloys on corrosion stability. Corrosion Science. 2016 Sep

1;110:71-81.

[11] Elvins J, Spittle JA, Worsley DA. Microstructural changes in zinc aluminium alloy galvanising as a function of processing parameters and their influence on corrosion. Corrosion Science. 2005 Nov 1;47(11):2740-59.

[12] International Zinc Association. https://www.galvinfo.com/wp-content/uploads/sites/8/2017/05/GalvInfoNote_1_9.pdf

[13] Ares AE, Gassa LM. Corrosion susceptibility of Zn–Al alloys with different grains and dendritic microstructures in NaCl solutions. Corrosion Science. 2012 Jun 1;59:290-306.

[14] Rettenmayr M, Lambracht P, Kempf B, Tschudin C. Zn-Al based alloys as Pb-free solders for die attach. Journal of electronic materials. 2002 Apr 1;31(4):278-85.

[15] Agapie M, Peter I, Varga B. Structure of cooled Zn-Al eutectoid based alloys in biphasic domain. Journal of Optoelectronics and Advanced Materials. 2015 Nov 1;17(11-12):1842-8.

[16] Yang L, Zhang Y, Zeng X, et al. Corrosion behaviour of superplastic Zn–Al alloys in simulated acid rain. Corrosion Science. 2012 Jun 1;59:229-37.

[17] Fredriksson H. Interpretation and use of cooling curves(thermal analysis). ASM Handbook.. 1988;15:182-5.

[18] Collins TJ. Image J for Microscopy. BioTechniques, 43, S25-S30.

CHAPTER 4 Influence of Galfan coating on tensile properties of CRS 1018 steel

4.1 Introduction

Zinc alloys with aluminum as a major alloying element consist of a class of alloys, which provides the most significant part of all coating manufactured, and have been widespread use for commercial application, especially in the aerospace and automotive industries. Recently, major attention is focused on the hypereutectic Zn-Al alloys such as Galfan hot-dipping coating (GHD) especially aiming at its influence on mechanical properties. This is because the GHD is one of the most cost-effective processes compared to other coating processes such as spray and electrodeposited coatings, and also the hypereutectic Zn-Al alloys offer enhanced corrosion resistance[1].

Generally speaking, the GHD process has three main stages which are surface treatment (e.g. degreasing, pickling, fluxing etc.), coating, and inspection. Depending on specific process, the substrate, which is mostly steel, is heated to a temperature over 400℃ for one or several times. Thermal energy input into the substrate during heating plays a very significant role in varying its mechanical properties, since holding the substrate at such a high temperature could result in the change of phase contents, dislocation arrangement and densities, and internal stresses in the substrate, and consequently alter mechanical properties. Tsuji et al[2] reported that the nominal UTS of ultrafine low carbon steel decreased by about 350 MPa after annealed at 489.85℃ for 1.8ks due to recrystallization. Similarly, Park et al[3] showed, a reduction of

approximately 100 MPa in the UTS of the angular pressed nano-grain low carbon steel, after annealing for one hour at 479.85℃, due to the significant change of grain sizes. Besides the recrystallization, the study by Shin et al[4] depicted dislocation rearrangement by heating as researched. Song et al[5] found that the dislocation density in 0.2 wt.%C – Mn steel reduced after annealing. in. Panagopoulos et al[6] discovered that Zn-Fe coating had a negative effect on the strengths of the mild steel. However, the effect of the GHD coating on the mechanical properties such as strengths and ductility are rarely reported in the open literature.

The objective of the present study was to investigate the change of mechanical properties of cold-rolled low carbon steel subjected to the GHD coating. The optical and electron scanning microscopies (SEM) were applied to analyze the microstructure of both the coated and uncoated cold rolled CRS 1018 steel. The mechanical properties of the coated and uncoated steel were determined by tensile testing. For the purpose comparison, the heated CRS 1018 steel was also analyzed and evaluated. Nano indentation testing was employed to understand the variation of dislocation densities in the tested specimens.The fracture behaviors of the GHD coated and uncoated samples were analyzed by fractography using the SEM. The mechanism responsible for the resulted tensile and fracture behaviors was discussed based on the optical and SEM microstructural characterization.

4.2 Experimental Procedure

4.2.1 Materials.

Two types of metallic alloys, CRS 1018 steel and Zn - 6% wt. Al (Galfan) alloy, were used in this study. Serving as the substrate, commercially-available CRS 1018 strips

were received in the cold rolled condition. The CRS 1018 is a general purpose low carbon steel with the chemical composition (wt.%) of Fe-0.2C-0.8Mn.

Figure 4.1 An electric resistance furnace Hardin HD-2344SS and accessories.

An electric resistance furnace, Hardin HD-2344SS, was chosen in this experiment due to its small size, which could be installed in a glove box. The furnace was originally designed for jewelry casting. Therefore, the maximum temprature can reach 1200℃. A graphite crucible was employed to contain 1.4 kg of Galfan alloy at the maximum

capacity. Since the lid could be fully open to horizontal position upwards, a large space above the furnace become available for other attachments.

4.2.2 Surface pretreatment

A safe and effective surface treatment process was employed involving 3 steps, degreasing, pickling, and fluxing. Firstly, the steel substrate was immersed into with 8% wt. NaOH solution for 2 min. Then, repeat the same process in 9% wt. hydrochloride acid. Both pickling and degreasing are finished with an ultrasonic cleaner. The fluxing solution contained 40% wt. zinc chloride and 10% of ammonium chloride in which samples stayed for 10 min. To dry the substrate completely, samples were heated up to 300 ℃ for 10 min before dipped into molten Galfan.

4.2.3 Dipping motion control

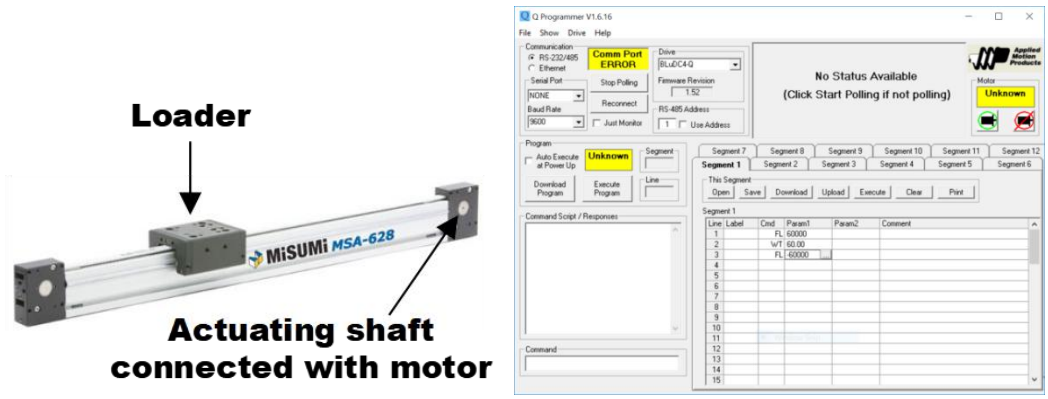

(a) (b)

Figure 4.2 (a) Misumi MSA-62B actuator. (b)Q programmer.

Considering the instability of manual dipping, a Misumi MSA-62B actuator and Applied Motion MMK-A58 motor with other accessories were used to move the sample smoothly with pre-coded motion and parameter. Q programmer provided an excellent

and accessible platform for this task. After connecting and modulating the computer to the motor, some basic commands were given such as FL (move the holder for a certain length), WT (wait for a certain time), AC (accelerate to a certain speed) etc. A customized sample holder was designed and installed onto the loader of the actuator. Then, the actuator is fixed vertically on a movable shelf above the furnace as shown in Figure 4.3.

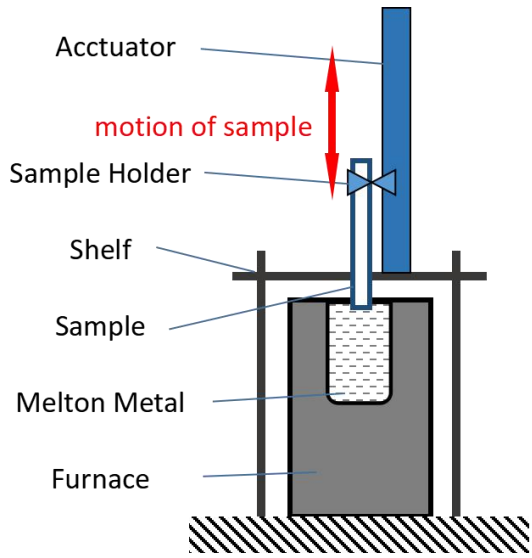

Figure 4.3 Schematic diagram of the dipping system.

4.2.4 Protective atomsphere

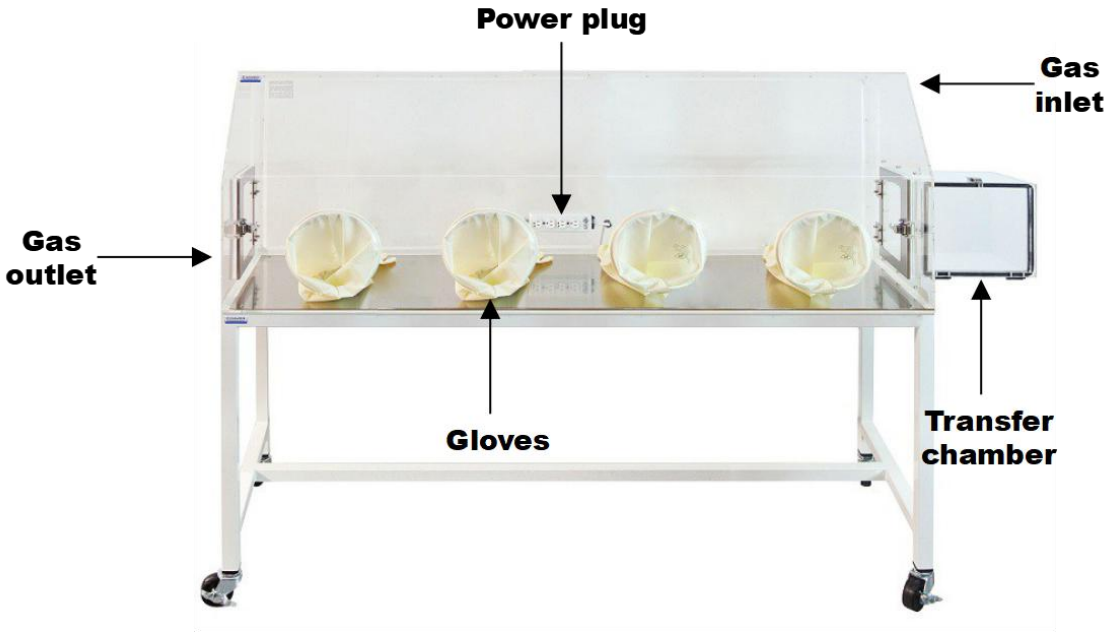

Figure 4.4 A customized glove box manufactured by Cleatech Inc for the HDG simulation.

Through the literature review, it is found that protective gases are needed sometimes to replace the fluxing process because it is less toxic and simplifies the production process. Thus, a customized glove box was designed and employed to improve and coating quality and to vary the experiments. Figure 4.4 shows a customized glove box made by Cleatech in Santa Ana, California, USA. The main chamber of the glove box is 120cm in height. Figure 4.5 schematically shows the protective gas supply system. A safe hydrogen (mixture of hydrogen (5%) and nitrogen (95%)) and ultra pure nitrogen were both supplied to the glove box controlled by the regulator on the gas value.

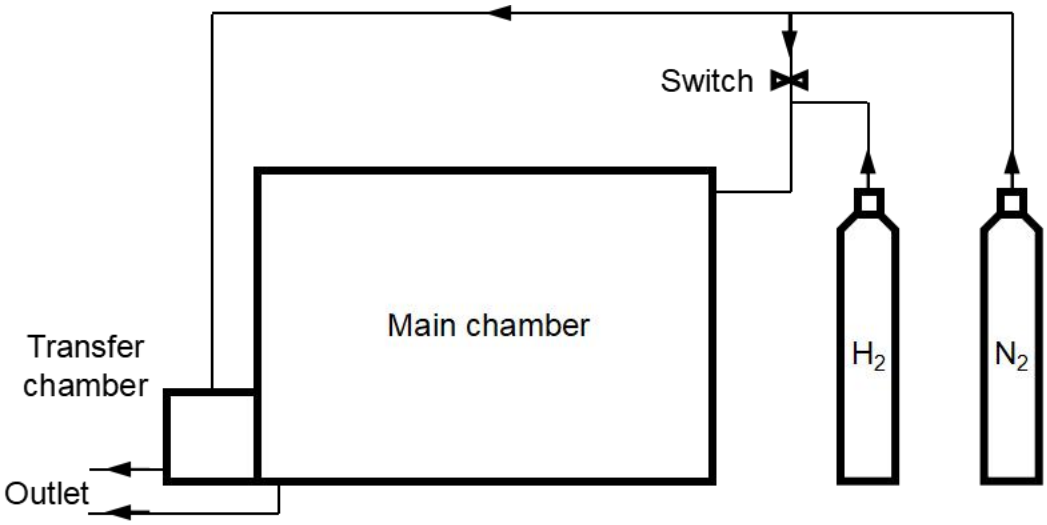

Figure 4.5 Schematic diagram of the protective gas system.

4.2.5 Parameter control and detection

Temperature is one of the most vital parameters during the HDG simulation experiment work. An Omega HH509 thermometer and Matlab temperature recording program are used to detect the real-time temperatures and to record the thermal history, respectively. Both systems used chromel-alumel (K type) thermocouples. As to other detectors, environmental temperature and humidity are measured by a monitor while the oxygen concentration was detected by an analyzer provided by Analytical Industries Inc.

Figure 4.6 Omega HH509 thermometer.

4.2.6 Coating Process.

Commercial Galfan ingots were cut into small pieces and molten in a graphite crucible at 450 ℃ for hot dipping. There were several stages involved in the coating of the steel tensile bars for high quality surface treatment. First, to clean the organic contamination, 8.0 % NaOH aquatic solution was used for degreasing CRS 1018 tensile specimens. Then, the CRS 1018 substrate was pickled in a 9.0 % HCl solution to remove the oxide layer. An 80.0 % solution of zinc chloride and ammonium chloride mixturewith a ratio of 4:1 was used for the final cleaning step, in which the tensile specimens were immersed for 10 min[7]. After drying, the cleaned specimens were dipped into the bath of hot liquid Galfan at 450℃ for 2 minutes. Finally, the coated specimens were lifted out of the bath and cooled to room temperature. The entire coating process was performed under an purge gas blender of nitrogen and 5% hydrogen

to avoid oxidization of substrate surface.

4.2.7 Tensile Test.

Tensile specimens was sectioned and machined from the CRS 1018 steel strips. according to ASTM To reveal the heating effect, a group of specimens without coating were also prepared and subjected to a heating process at 450 ℃ for 2 minutes for tensile testing. For clarification, three groups of specimens were designed as S1 (as-machined), S2 (heated, uncoated), and S3 (heated, coated). The tensile testing of each group included five repeated tests to ensure the reliability and repeatability of the results. According to the ASTM standard E8 [8], subsize tensile specimens with the dimensions of 3 mm in thickness, 6 mm in width and 25 mm in gauge length were prepared. The specimens were tested at room temperature on an Instron 30 kN Materials Test System equipped with a data acquisition system. The load cell and test speed were set up at 10 kN and 2 mm/min. The output data, including the displacement measured by an extensometer, and tensile load, were analyzed. The ultimate tensile strength (UTS), 2% offset yield strength (YS) and elongation (e_f) were determined for all tested specimens based on the average of five tests.

4.2.8 Nano Indentation Testing

The indentation analysis was performed using a Hysitron Ubi® 1 Nanomechanical Test Instrument. There is a program in the instrument, which can be set up to carry out indentations along a straight line, a circle or a rectangle. Such equipment allows the application of loads from 0.01 mN to 8 mN and the recording of penetration depths as a function of applied loads with high load resolution (1nN) and high displacement resolution (0.04 nm). A Berkovich diamond indenter was used with a maximum load of

8 mN at room temperature. Ten indentations were precisely performed within the ferrite at the center area of the cross-section of each sample.

4.2.9 Microstructure Analysis.

Following the standard metallographic procedure including: sectioning, mounting, grinding and polishing, the specimens were prepared. First of all, the specimens were grounded using 120, 600, 800, and 1200 grit silicon carbide papers and polished using 0.5μm and 1μm alumina suspension. The etchant used was 5% of nital solution (5ml fuming nitric acid and 95ml ethanol). After etching the specimens for 15s, the detailed microstructure characteristics were observed by using an optical microscope, and a scanning electron microscope (SEM), Hitachi Tabletop Microscope TM3000, with a maximum resolution of 30 nm in a backscattered mode/1 μm in x-ray diffraction mapping mode, and useful magnification of 15–30,000.. The fractured surfaces of tensile specimens were observed by SEM.

Figure 4.7 Buehler optical image analyzer models 2002 used for low magnification microstructure analysis.

Figure 4.8 FEI Quanta 200 FEG Scanning electron microscopy used for high magnification microstructure analysis and EDS test for chemical composition analysis.

4.3 Result and Discussion

4.3.1 Tensile Properties

The typical engineering stress-strain curves of samples S1, S2 and S3 are shown in Figure 4.9. The tensile curve for sample S1 exhibited a much lower strain than those of samples S2 and S3, which had a similar trend with an extended strain and low strengths. Table 4.2 summarized the average tensile properties extracted from Figure 4.9, including UTS, YS and ef . It can be seen that the unheated samples S1 had the average UTS, YS and ef of 833.1 ± 7.9 MPa, 821.4 ± 7.1 MPa, 2.5 ± 0.21%, respectively. For the heated samples including the uncoated (S2) and coated(S3) with the similar tensile

curves, their YS values were 682.4 ± 6.5 MPa and 681.6 ± 5.1 MPa, while their UTS values were 703.6 ± 7.2 MPa and 700.2 ± 9.5 MPa, respectively. In comparison with the elongation of 2.5±0.21% for unheated group S1, the elongation of groups S2 and S3 increased significantly to 12.9 ± 2.9% and 12.1 ± 2.8%, respectively . This observation implied that, rather than coating itself, the thermal energy received by sampless S2 and S3 from heating might play a role in sustaining large strains during tensile loading. The heat input could lead to recovery in which dislocation rearrangement and densities might occur, and even recrystallization and phase transformation.

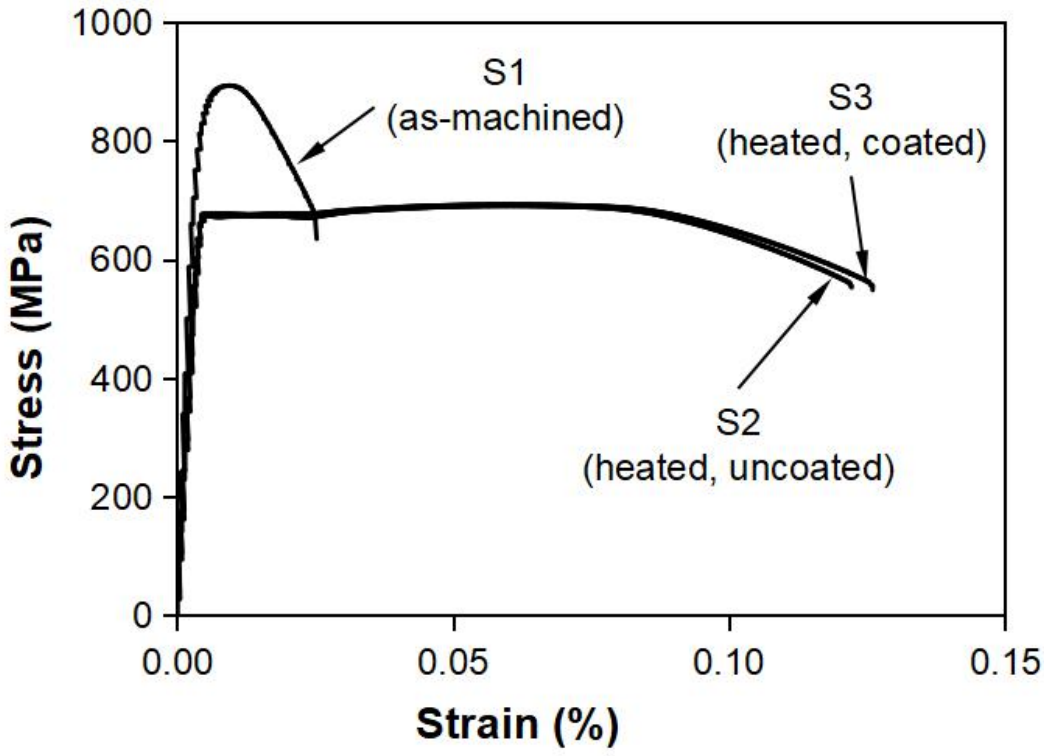

Figure 4.9 Typical engineering tensile curves of samples S1 (as-machined), S2 (heated, uncoated), and S3 (heated, coated) of CRS 1018 steel.

Table 4.1 Tensile properties of samples S1, S2, and S3

Materials	UTS (MPa)	YS (MPa)	Elongation (%)
S1 (As-machined)	833.1±7.9	821.4±7.1	2.5±0.21
S2 (Heated, Uncoated)	703.6±7.2	682.4±6.5	12.9±2.9
S3 (Heated, Coated)	700.2±9.5	681.6±5.1	12.1±2.8

4.3.2 Microstructure

Figure 4.10 presents the OM micrographs of the S1, S2, and S3 samples. Due to the anisotropy induced by cold rolling on the CRS 1018 steel strips, the microstructure was viewed from three rectangular axis directions as illustrated in Figure 2(a). The rolling direction, the direction normal to the strip width, the direction perpendicular to the strip thickness were named the longitudinal direction (LD), the short transverse direction (ST) and the long transverse direction (LT), respectively. The planes comprised of the LD and LT directions, the LT and ST directions, and the LD and ST directions was referred to as the LD-LT, LT-ST, and LD-ST planes. As can be seen from Figure 4.10, all the microstructures consisted of two phase constituents, characterized by the white and black areas. Visually, the white areas in all micrographs appeared to occupy a larger portion of the observed microstructures. These areas represented the α-iron phase, ferrite. This phase is characterized as relatively soft and ductile, and is the primary phase in most low carbon steels [9]. From the high magnification SEM micrographs given in Figure 4.11, it can be seen that the relatively bright region (black area observed in OM) consisted of a lamellar (layered) type structure.

This is the typical microstructure of pearlite. The layers were thin phases of ferrite, and cementite, the two phases alternatively present in low-carbon steels. The pearlite microstructure was much stronger and harder than the ferrite phase. By comparing Figure 4.10 (b) and (c) to Figure 4.10(a), there were almost no visible microstructure changes between samples S1, S2 and S3.

The microstructure of sample S1 was highly elongated in the LD and LT direction, although the ferrite phase were rounded in the ST direction. The length and width of the ferrite phases were close to each other on the LD-LT plane. The length in the LT direction was much greater than the width in the ST direction on the LT-ST plane, while the length in the LD direction was much greater than the width in the ST direction on the LD-ST plane. The measured dimensions of the ferrite phase on the three different planes for samples S1, S2 and S3 are summarized in Table 2. The difference in ferrite sizes between samples S1, S2 and S3 on the designated plane appeared very limited. This observation suggested that no recrystallization took place in heating since only a very short period of time was applied for heating. Just based on the OM and SEM microstructure analyses, hence, it seems hard to explain the variation in tensile properties of the CRS 1018 steel with and without the Galfan coating.

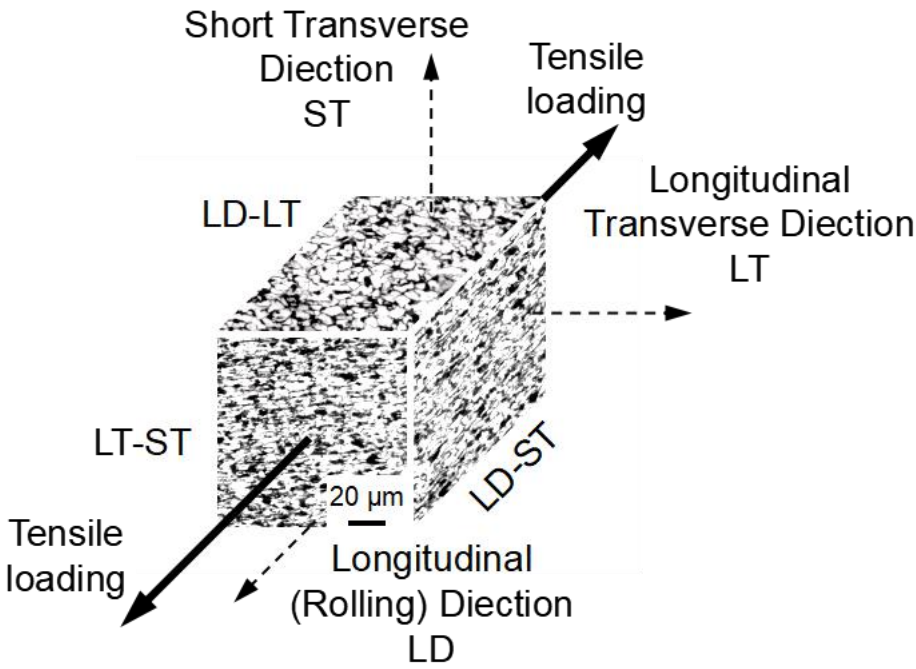
Short Transverse
Diection
ST
Tensile
loading
Longitudinal
Transverse Diection
LT
LD-LT
LT-ST
LD-ST
20 μm
Tensile
loading
Longitudinal
(Rolling) Diection
LD

(a)

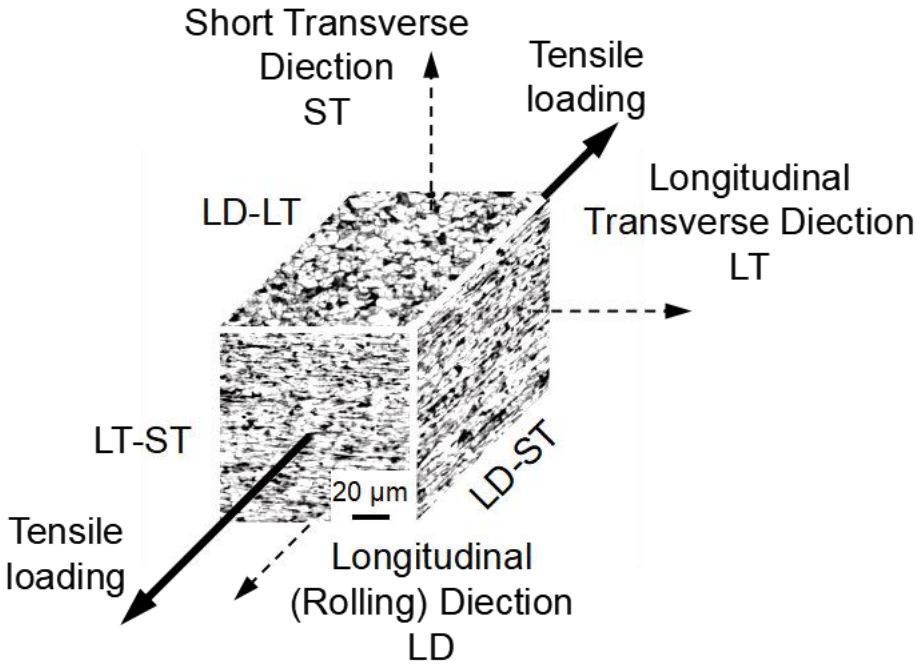
Short Transverse
Diection
ST
Tensile
loading
Longitudinal
Transverse Diection
LT
LD-LT
LT-ST
LD-ST
20 μm
Tensile
loading
Longitudinal
(Rolling) Diection
LD

(b)

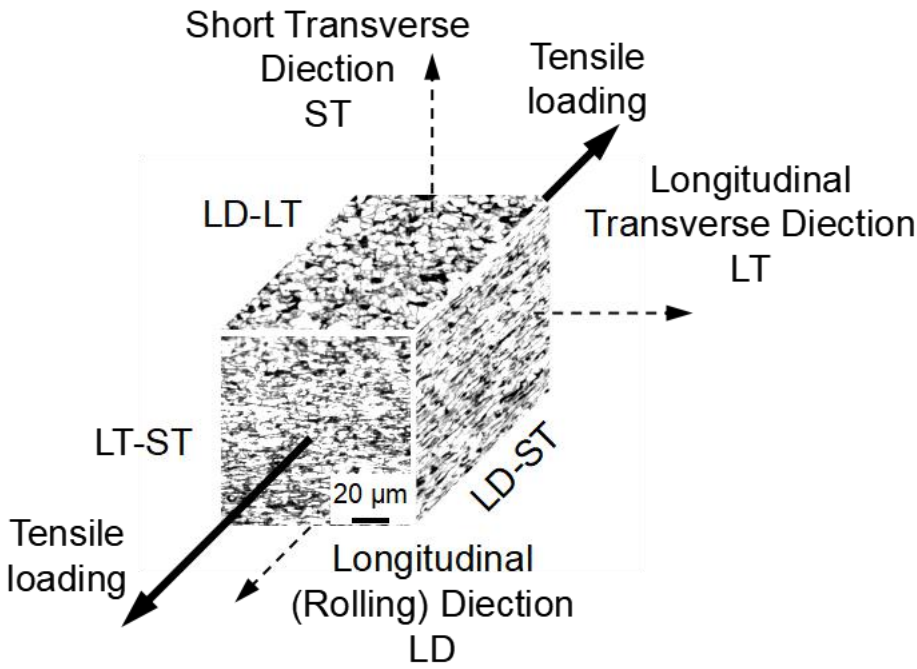

(c)

Figure 4.10 (a) illustration showing anisotropy in a rectangular coordinating system; optical micrographs showing microstructures of (b) S1 (as-machined), (c) S2 (heated uncoated), (d)S3 (heated coated) samples.

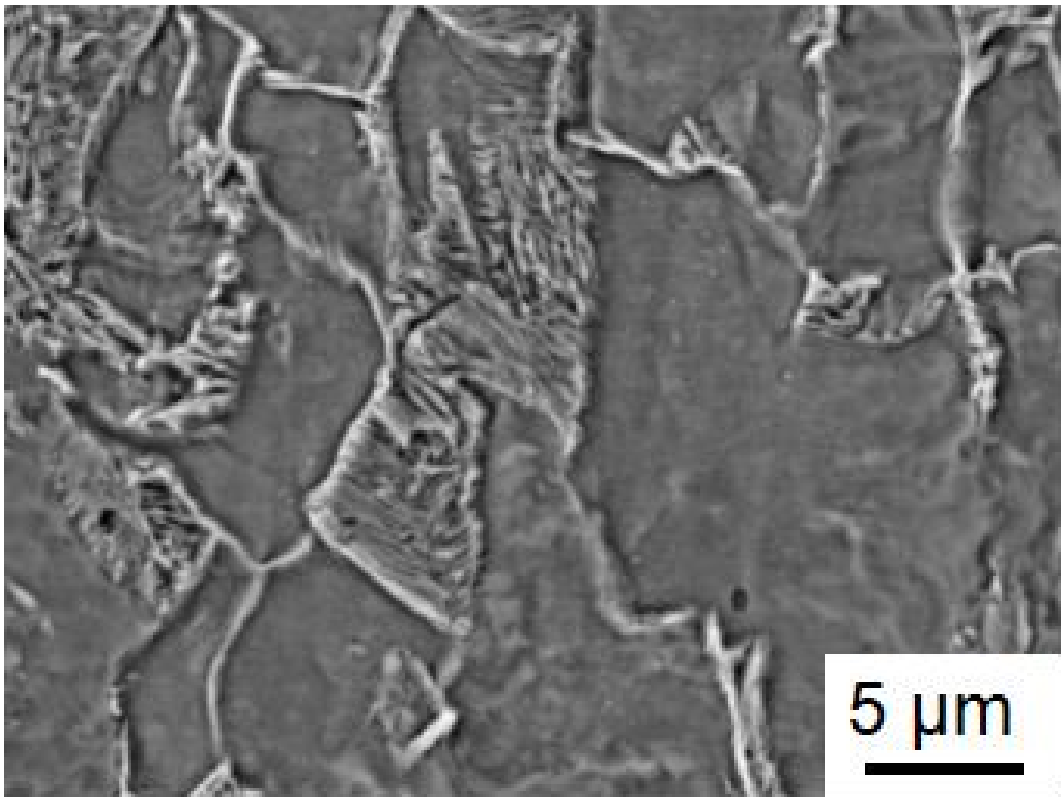

Figure 4.11 SEM micrograph showing the presence of pearlite in the microstructure of the CRS 1018 steel.

Table 4.2 Dimensions of ferrite phase on three different planes for samples S1, S2 and S3

Sample	Plane	Length (μm)	Width (μm)
S1	LT-ST	7.58±2.86	2.13±0.41
	LD-ST	9.26±3.44	2.06±0.50
	LD-LT	10.84±3.31	7.65±1.37
S2	LT-ST	7.26±2.62	2.53±0.62
	LD-ST	9.54±3.62	2.46±0.85
	LD-LT	10.54±3.27	7.30±1.28
S3	LT-ST	7.15±2.48	2.44±0.60
	LD-ST	9.38±3.45	2.39±0.84
	LD-LT	10.38±3.15	7.21±1.27

4.3.3 Nanoindentation

Ubi ® 1 Nanomechanical Test Instrument is also capable of Scanning Probe Microscopy (SPM) imaging. In this type of imaging, a sharp probe tip was moved in a raster scan pattern across a sample surface using a three-axis piezo positioner. A SPM image of the residual indent impression left by a typical Berkovich indentation on the polished surface of the CRS 1018 steel is shown in Figure 4.12. Figure 4.13 shows averaged load–unload curves obtained within the ferrite phase of the S1, S2 and S3 samples as well as the Galfan coating using a Berkovich indenter with a maximum load of 6 mN. Each curve in Figure 4.13 gives an averaged value of a number of homologous load–unload curves chosen from the 10 individual curves for each sample.

To truly represent the local mechanical deformation behavior within the ferrite phase of the three steel samples as well as the Galfan coating, it was necessary to choose only those curves that have homologous characteristics so that microdefects, such as porosity and microcracks, have the least effect on the deformation behavior.

The hardness (H) value was calculated using the following equation [10]:

$$H = \frac{P_{max}}{A} \quad (1)$$

where P_{max} is the maximum load, A is projected area of the indentation, and hp is the indentation depth.

Figure 4.14 shows the hardness (H) values versus penetration depth (h) curves for samples S1, S2 and S3 at room temperature. The hardness values versus penetration depth curves for all the three samples and the coating at room temperature were very similar and consisted of two segments. The initial segment, for which the penetration depth was very small, mainly involved elastic deformations. During this initial segment, the hardness increased rapidly and reached a peak value of around 5.6GPa. As the indenter further penetrated into the materials, the contact area between the indenter and the samples increased. Since the hardness was inversely proportional to the contact area, the hardness values dropped rapidly from the peak value to about 5.2 GPa as the penetration depth increased from 42.9 to 69.7 nm. As the penetration depth further increased to 251.8 nm and beyond, the hardness gradually decreased, and tended to reach a steady value of around 4.5 GPa. This observation can, in part, be attributed to the fact that, once the penetration reached a certain depth, any further increase in penetration depth had a limited influence on the contact area.

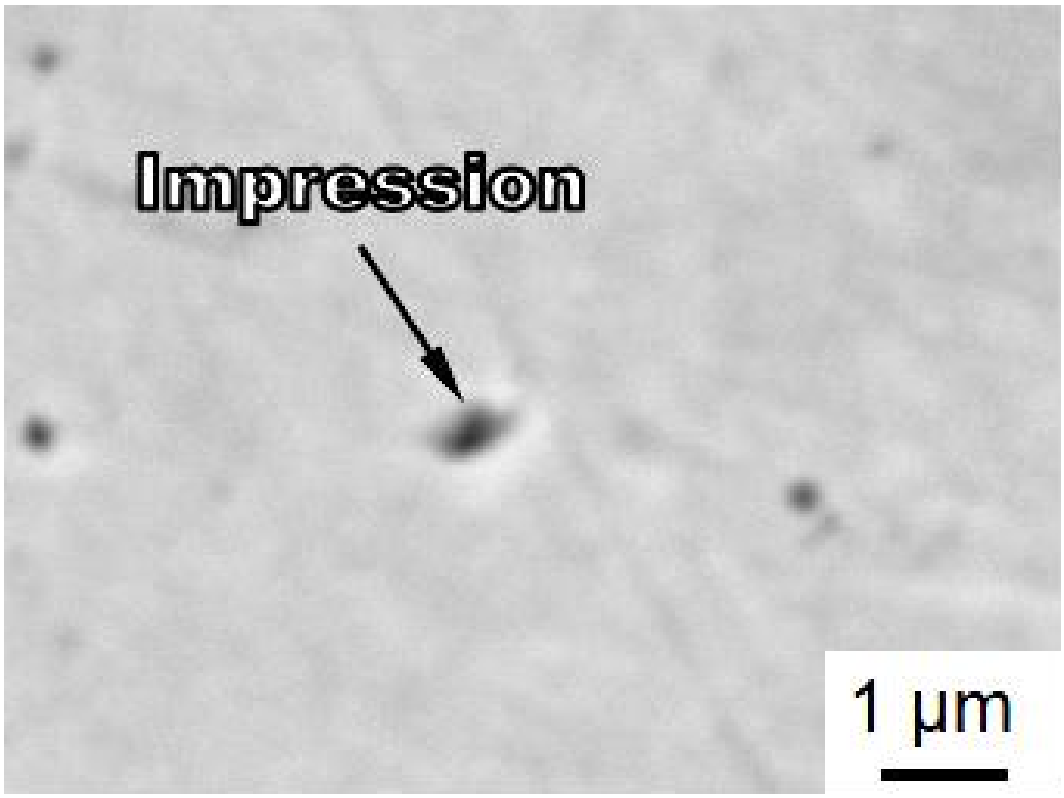

Figure 4.12 A image of the residual indent impression left by a typical Berkovich on the polished surface of the CRS 1018 steel.

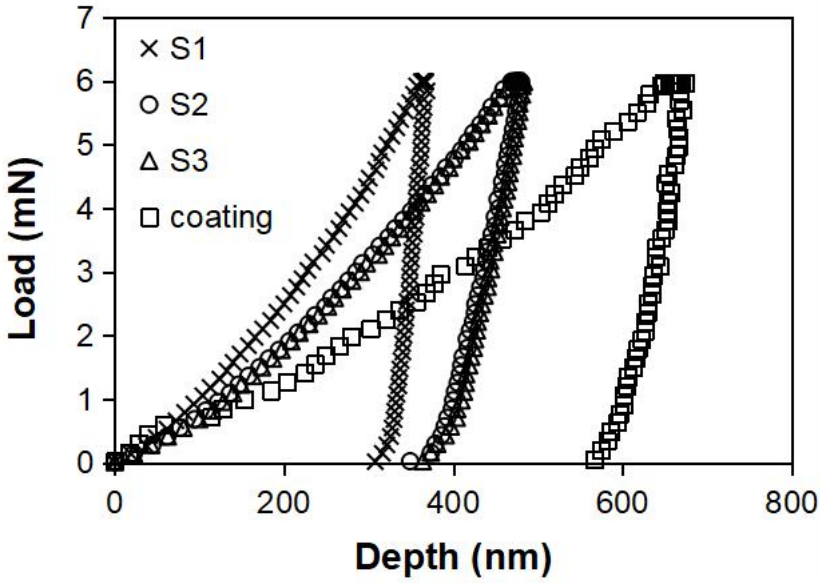

Figure 4.13 Typical averaged load – unload curves for the indentation within the ferrite phases of samples S1, S2 and S3 as well as the Galfan coating. A Berkovich indenter with a maximum load of 6mN was used for the tests.

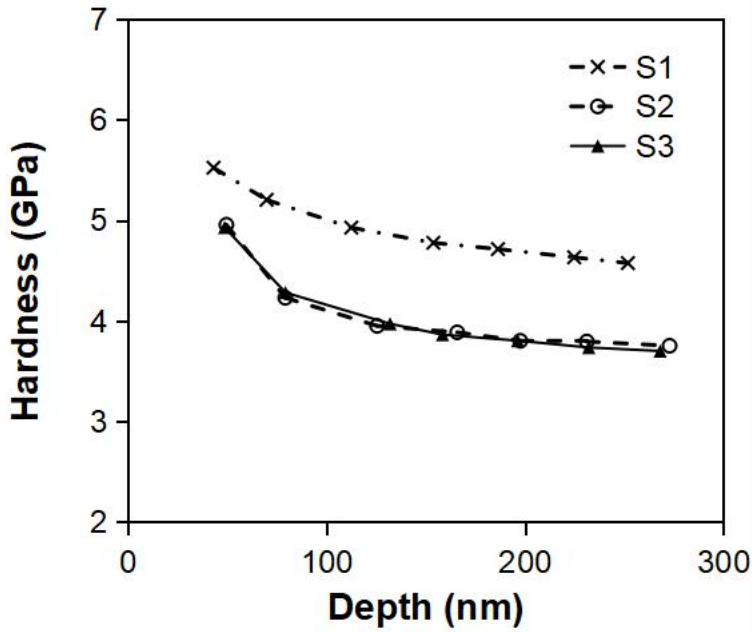

Figure 4.14 Hardness values vs. penetration depth curves for the ferrite phases of samples S1, S2 and S3 as well as the Galfan coating at room temperature.

4.3.4 Determination of Dislocation Density

As can be seen from Figure 4.14, the hardness values decreased as the indentation depth increased. Nix and Gao [11] developed a model by using a simple equation expressing that the square of the normalized hardness should be a linear function of the reciprocal of the indentation depth:

$$\left(\frac{H}{H_0}\right)^2 = 1 + h^* \bullet \left(\frac{1}{h}\right) \tag{2}$$

where H_0 is the hardness in the limitation of infinite depth, and h^* is a characteristic length which depends on types of materials and indenter geometry. The Nix-Gao model directly related the characteristic length (h^*) to the dislocation density with the following equation:

$$\rho_s = \frac{3\tan^2\theta}{2f^3bh^*} \tag{3}$$

where ρ^s is the density of dislocations statistically stored in the lattice (SSDs), θ is the angle between the surface of the material and the surface of the indenter, b is the Burgers vector of the dislocations, f is a correction factor for the size of the plastic zone. The model has been extensively verified by TEM and SEM observations and XRD measurements on various metals and alloy with different crystal structures such as Face-Centred Cubic (FCC) for Ag [11], Cu [11, 12],Ni [13, 14] and austenite in stainless steel [15], Body-Centered Cubic (BCC) for ferrite in stainless steel [15] and tungsten [16], as well as HCP for Co.

Figure 4.15 presents a plot of the square of the normalized hardness as a function of the reciprocal of the indentation depth. The data in Figure 4.15 were fit to a line having slopes of 24.782, 52.004 and 53.103, intercepts of 0.985, 0.953 and 0.953, a correlation

coefficients of 0.986, 0.965 and 0.992, which gave the h^* values of 24.782, 52.004 and 53.103 for samples S1, S2 and S3, respectively. θ, f and b were 20o, 1.9 and 0.25 nm, cited from references 13 and 15. The values of Ho , which were determined based on the regression analyses of the H vs h relations, were 4.445, 3.444, andd 3.420 GPa for samples S1, S2 and S3, respectively. By inputting these parameter values into Equation (3), the dislocation densities of samples S1, S2 and S3 were 4.676×10^{15}, 2.228×10^{15} and 2.182×10^{15} m^{-2}, respectively. Ameri et al [15] estimated the dislocation density from microhardness measurements in hot rolled stainless steel 2101. The estimated dislocation densities were 5.54×10^{14} and 1.71×10^{15} m^{-2} in the BCC-structured ferrite and FCC-structured austenite phases, respectively. Their results were verified with X-ray diffraction (XRD) profiles. The minor discrepancy between the determined dislocation densities in the present study and those given in reference 15 might result from the fact that the cold rolling was applied to the samples instead of hot rolling and annealing. In general, the dislocation density estimated based on indentation hardness measurements under different loads was in agreement with the results reported in reference 15. It has been pointed out [17] that the yield stress is a linear function of the square root of dislocation density. Expectedly, the low dislocation densities in samples S2 and S3 due to recovery caused by heating should be responsible for the reduction in their tensile properties.

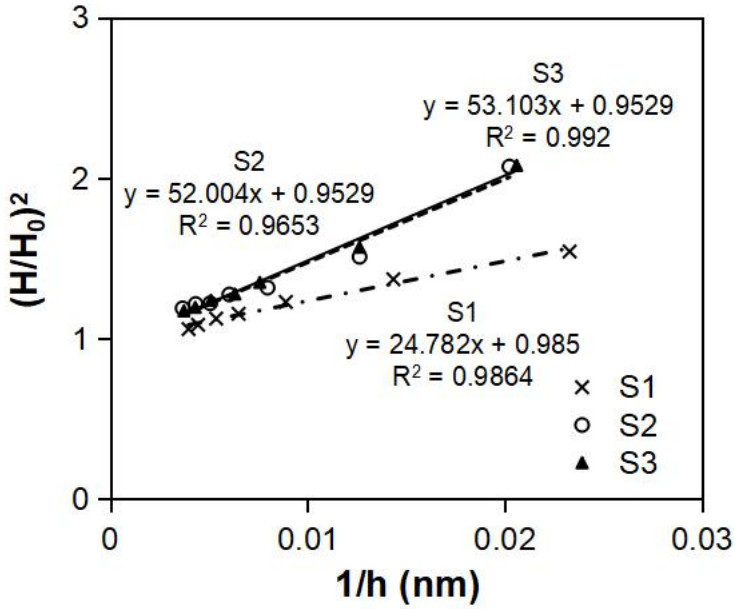

Figure 4.15 A plot of the square of the normalized hardness as a function of the reciprocal of the indentation depth for samples S1, S2 and S3.

4.3.4 Fracture Behavior

Figures 16-18 give SEM fractographs which reveal the fracture behaviors of samples S1, S2 and S3. The observed fracture mode of all three samples appeared quasi-cleavage as illustrated in Figs. 8(a), 9(a) and 10(a), although the direct comparison of SEM fractographs under low magnification showed that there was almost little difference in the features of the fracture surfaces between the three samples.

With high magnification, the characteristic feature of cleavage fracture, flat facets, was observed on the fracture surface of sample S1 as shown in Figure 4.16(b). The flat facets were covered fully by river lines on the fracture surface of sample S1. The river lines were the result of the crack moving through the grain along a number of parallel planes, which formed a series of plateaus and connecting ledges. the tensile fracture surface of sample S1 was somewhat brittle in nature. However, the high-magnification

SEM fractographs, Figure 17(b) and 18(b), depicted the presence of massive deep dimples with extensive deformation marking along the walls of individual craters on the surfaces of samples S2 and S3. The dimples were caused by the localized microvoid coalescence. This feature was an indication of the energy absorption through local deformation. A considerable amount of energy was required to be consumed in the process of the formation of microvoids and microvoid-sheet, eventually leading to the creation of cracks. Thus, this type of ductile fracture failure resulted from the coalescence of microvoids under the tensile stress. The relatively low dislocation density of samples S2 and S3, which enabled further accumulation of dislocations at their large strain hardening regions in the tensile stress–strain curves, should be responsible for the resultant fracture mode. Overall, the SEM fractograph observations on the fracture surfaces were consistent with the mechanical properties of sample S1, S2 and S3 extracted from tensile testing.

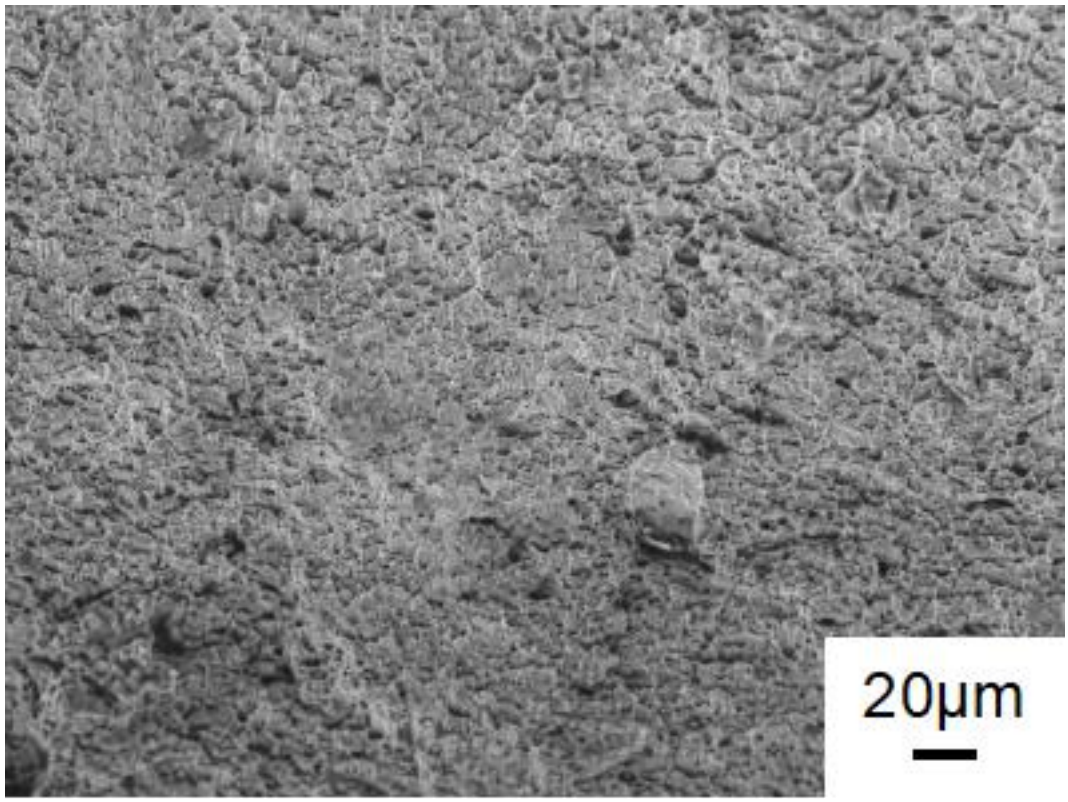

(a)

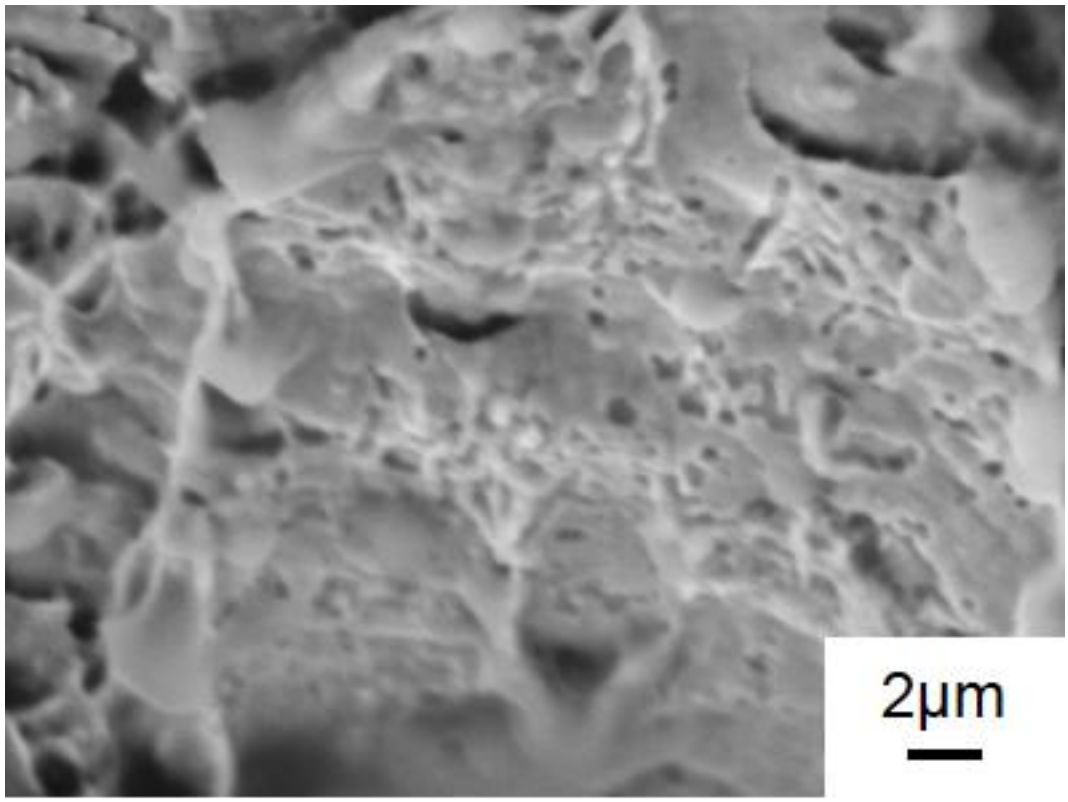

(b)

Figure 4.16 SEM fractographs of sample S1. (a) low magnification and (b) high magnification.

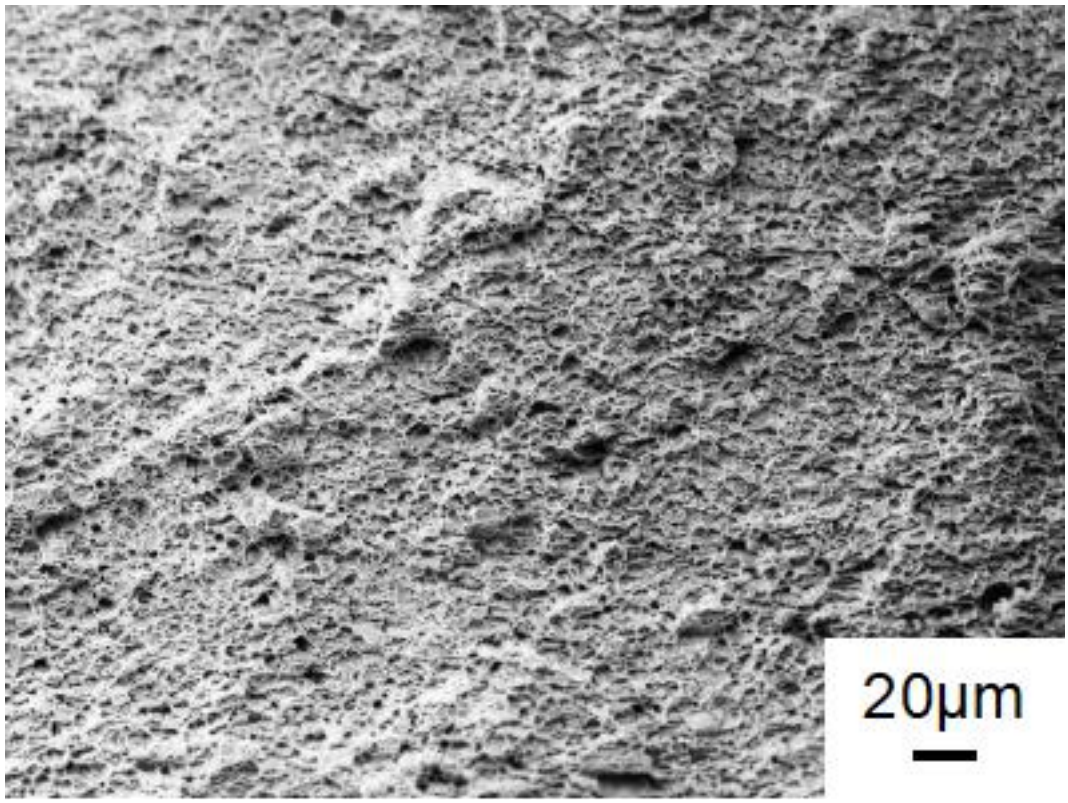

(a)

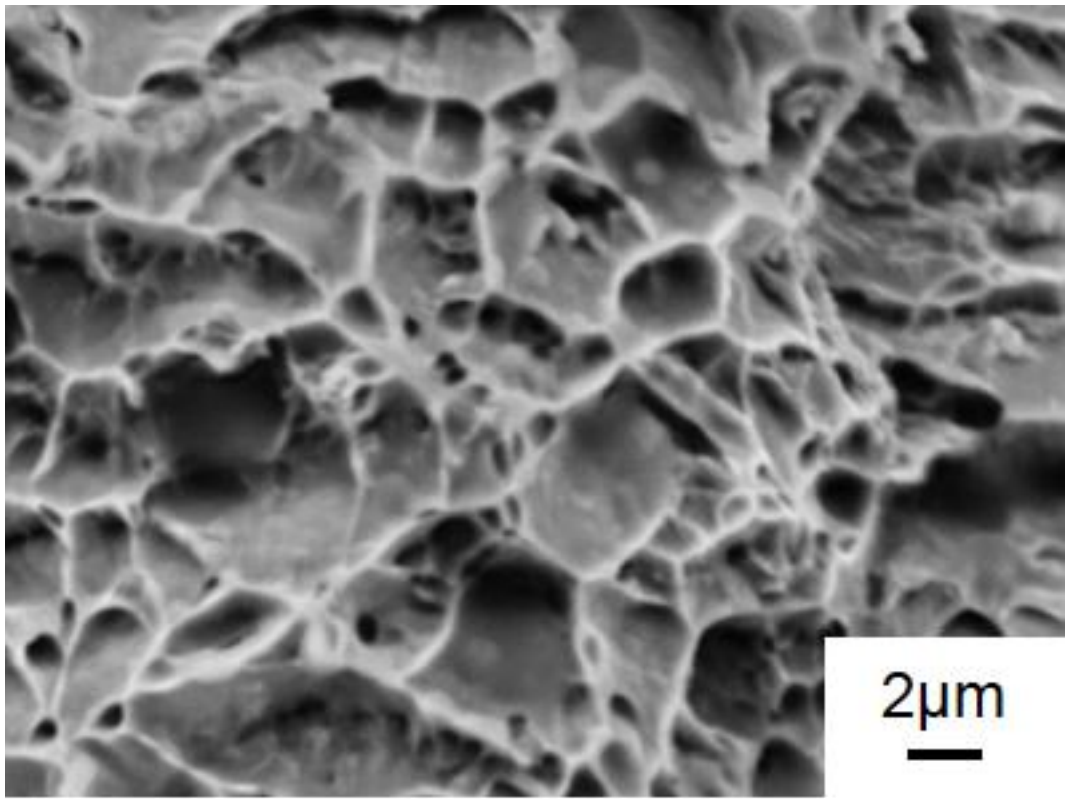

(b)

Figure 4.17 SEM fractographs of sample S2. (a) low magnification and (b) high magnification.

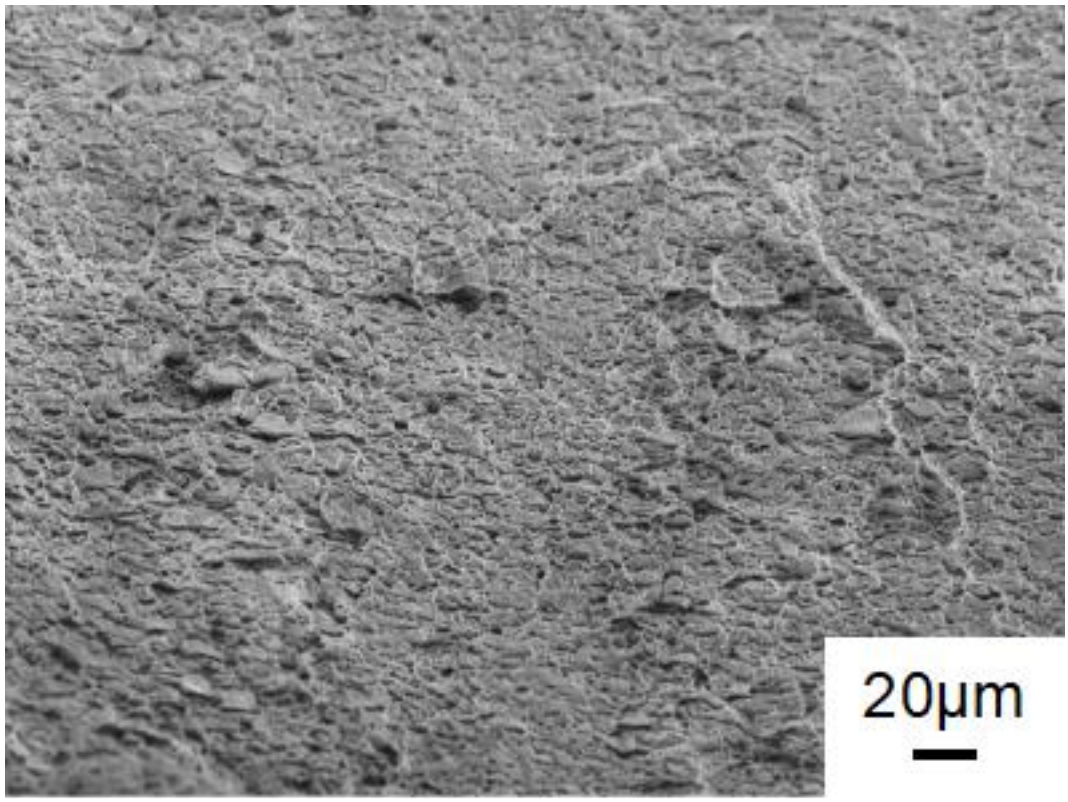

(a)

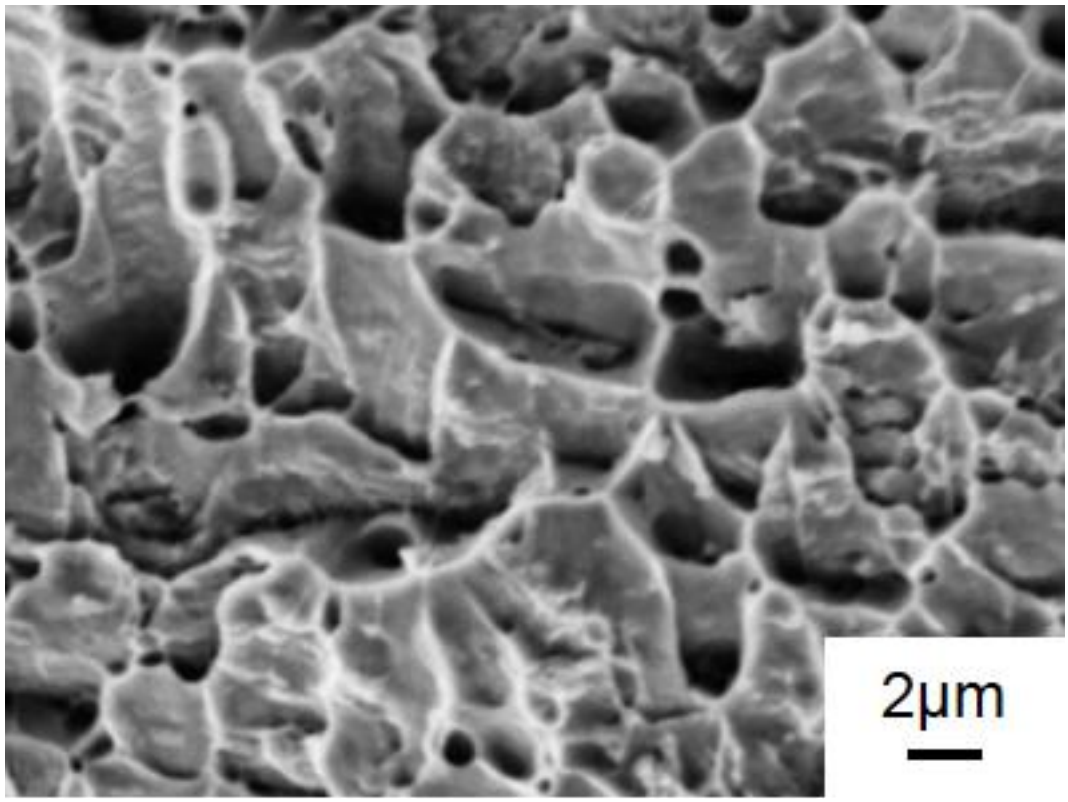

(b)

Figure 4.18 SEM fractographs of sample S3. (a) low magnification and (b) high magnification.

4.4 Conclusions

In the present work, the CRS 1018 steel was coated by the Galfan alloy via the hot dipping process. The mechanical properties of the coated and uncoated CRS 1018 steel were evaluated by tensile testing. The characterized microstructures as well as the dislocation densities of the coated and uncoated steel samples determined by nanoindentation testing were related to their tensile behaviors. The drawn conclusion are summarized below:

The uncoated CRS 1018 steel without any heating had the average UTS, YS and ef of 833.1 ± 7.9 MPa, 821.4 ± 7.1 MPa, 2.5 ± 0.21%, respectively. For the coated steel, its YS and UTS values were 681.6 ± 5.1 and 700.2 ± 9.5 MPa, respectively. In comparison with the elongation of 2.5±0.21% for the uncoated steel, the elongation of the coated steel increased significantly to 12.1 ± 2.8%. The Galfan hot dipping coating decreased the tensile strengths and increased the elongation of the steel.

The OM and SEM analyses revealed that the microstructures of both the coated and uncoated samples consisted of two phases, ferrite and pearlite. The difference in ferrite sizes between samples S1, S2 and S3 on the designated plane appeared very limited.

The dislocation density of the coated steel samples determined by nanoindentation testing was 2.182×10^{15} m^{-2} , which is lower than that (4.676×10^{15} m^{-2}) of the uncoated sample. The low dislocation density of the coated sample, which might arise from

recovery due to heating in the Galfan hot dipping coating, should be responsible for the reduction in the tensile properties.

The characteristic feature of cleavage fracture, flat facets, was observed on the fracture surface of the uncoated steel, which was somewhat brittle in nature. But, the massive deep dimples with extensive deformation marking along the walls of individual craters were present on the fracture surface of the coated sample, which suggested the ductile fracture failure resulted from the coalescence of microvoids under the tensile stress. The SEM fractograph observations on the fracture surfaces were in a good agreement with the mechanical properties of the coated and uncoated steels extracted from tensile testing.

4.5 References

[1] Surface Preparation. (n.d.). Retrieved from https://galvanizeit.org/inspection-course/galvanizing-process/surface-preparation

[2] Tsuji, N., Ueji, R., Minamino, Y., & Saito, Y. (2002). A new and simple process to obtain nano-structured bulk low-carbon steel with superior mechanical property. Scripta Materialia, 46(4), 305-310.

[3] Park, K. T., Kim, Y. S., Lee, J. G., & Shin, D. H. (2000). Thermal stability and mechanical properties of ultrafine grained low carbon steel. Materials Science and Engineering: A, 293(1-2), 165-172.

[4] Shin, D. H., Kim, B. C., Park, K. T., & Choo, W. Y. (2000). Microstructural changes in equal channel angular pressed low carbon steel by static annealing. Acta Materialia, 48(12), 3245-3252.

[5] Song, R., Ponge, D., Raabe, D., & Kaspar, R. (2005). Microstructure and crystallographic texture of an ultrafine grained C–Mn steel and their evolution during warm deformation and annealing. Acta Materialia, 53(3), 845-858.

[6] Panagopoulos, C. N., Georgiou, E. P., Agathocleous, P. E., & Giannakopoulos, K. I. (2009). Mechanical behaviour of Zn–Fe alloy coated mild steel. Materials & Design, 30(10), 4267-4272.

[7] Warichet, D., Van Herck, K., Van Lierde, A., Gerain, N., & Matthijs, E. (2005). U.S. Patent No. 6,921,439. Washington, DC: U.S. Patent and Trademark Office.

[8] Standard Test Methods for Tension Testing of Metallic Materials, (2016), ASTM E8/E8M − 16a, ASTM International, West Conshohocken, PA, United States.

[9] Sante Dicecco, William Altenhof, Henry Hu, and Richard Banting. (2017). High Cycle Fatigue of High Strength Low Alloy Steel Q345 Subjected to Immersion Corrosion for Mining Wheel Applications. Journal of Materials Engineering and Performance. 26(4): 1758–1768.

[10] L. Han, H. Hu, D.O. Northwood, N. Li, Microstructure and nano-scale mechanical behavior of Mg-Al and Mg-Al-Ca alloys. (2008). Materials Science and Engineering A, 473, 16-27.

[11] Nix, W. D., & Gao, H. (1998). Indentation size effects in crystalline materials: a law for strain gradient plasticity. Journal of the Mechanics and Physics of Solids, 46(3), 411-425.

[12] Barmouz, M., & Abrinia, K. (2013). Using hardness measurement for dislocation densities determination in FSPed metal in order to evaluation of strain rate effect on the tensile behavior. Materials Science and Engineering: A, 559, 917-919.

[13] Graça, S., Colaço, R., Carvalho, P. A., & Vilar, R. (2008). Determination of dislocation density from hardness measurements in metals. Materials Letters, 62(23), 3812-3814.

[14] Graça, S., Colaço, R., and Vilar, R. (2007). Indentation size effect in nickel and cobalt laser clad coatings, Surface & Coating Technology, 202, 538-548.

[15] Ameri, A. A., Elewa, N. N., Ashraf, M., & Escobedo-Diaz, J. P. (2017). General methodology to estimate the dislocation density from microhardness measurements. Materials Characterization, 131, 324-330.

[16] X. Qiu , Y. Huang, W. D. Nix, K. C. Hwang and H. Gao, (2001). Effect of intrinsic lattice resistance in strain gradient plasticity, Acta Mater. 49 3949–3958

[17] George E. Dieter, Mechanical Metallurgy, McGraw-Hill, New York, New York, 1986, 191.

CHAPTER 5 Corrosion and Microstructure of hypereutectic Zn-Al alloy

5.1 Introduction

Zn-Al based materials have become one of the most significant candidates for anti-corrosion applications due to their low cost, high reliability and excellent adhesion. In the automotive industry, Zn-Al alloys are widely used for the protective coating in tubing systems such as brake lines and fuel pipes. It is also proved to be effective in high humidity surroundings including marine and fresh water environment. Studies on improving the performance and decreasing the cost focus on the variation of chemical composition of the alloys, which is easy to apply technologically and economically. However, the influence of these changes are complex because of the development of different phase constituents and microstructure. Consequently, their various material properties such as molten point, viscosity, corrosion resistance, and adhesion etc are changed.

Fayomi et al[1] compared the Zn and Zn-Al film on mild steel substrate. Their experimental results showed that Zn-Al coatings had homogeneous distribution of the fine Al rich phases. Zn-Al coatings had higher corrosion and wear resistances over the Zn deposited coatings as well as the substrate. They fabricated Zn-Al coating for preventing service failure and corrosion attack in the industries[2]. Zn-Al film was developed with zinc and aluminum powder particles dissolved in nitric acid and sodium hydroxide respectively, to form solutions containing zinc and aluminum ions. Anomalous

co-deposition on mild steel resulted into surface modification attributed to the complex alloys that was developed. It was found that when Al weight percentage changes from 1% to 5%, the polarization resistance significant and corrosion current density increased from $2.89x10^3$ Ω to $1.38x10^5$ Ω and $1.5x10^{-4}$ to $3.5x10^{-7}$ A/cm^2 whereas the corrosion potential decreased for -0.563V to -0.768V. Yang et al[3] studied the corrosion performance of ZA4, ZA8, ZA12, and ZA16 in acid environment. The samples were tested through polarization and immersion. The result suggested that the overall corrosion rate trend was ZA4 > ZA8 > ZA12 > ZA16. Using cyclic voltammetry and potential scan/hold technique, Miao et al[4] studied the electrochemical properties of Zn-5Al and Zn-55 Al. The result shows with the increase of aluminum content in the coatings, the dependence of pitting potential on solution pH within the pH range from 7 to 12 became more and more sensitive.

However, the electrochemical performance of Zn alloys with 6% to 10% are rarely reported. In practical using, the researchers also found that some manufacturers provide hypereutectic Zn-Al as the hot dipping coating material instead of eutectic alloy Galfan. Moreover, the roles of Al in Galfan alloy are reported seemingly with contradiction. A few papers (e.g. reference 2 and 3) suggest that Al is constructive in corrosion test, while others show its negative influences. Therefore, the corrosion mechanism of the hypereutectic Zn-Al alloys with different Al contents needs to be clarified.

5.2 Experimental Procedure

5.2.1 Alloys Preparation

Zn and Al ingots were cut into small pieces and mixed in different ratios. Zn - 6

wt.% Al, Zn - 7 wt.% Al, Zn - 8 wt.% Al, Zn -9 wt.% Al, and Zn -10 wt.% Al samples were then prepared with each for 500g. The original materials were molten in the graphite crucibles under 550℃. All the liquid metals were well stirred before cast into steel bowls surrounded by sands with a thermal couple in it. After several hours when the samples cooled down to room temperature, the ingots were cut into 1.5cm×1.5cm×0.5cm bulks for SEM and corrosion test.

5.2.2 Electrochemical Experimentation

Alloys were machined into certain shape to fit the chemical workstation. Been polished with sand papers with grades from 200 to 1200 grit, and then with 1μm and 0.05μm alumina polisher. After cleaned in acetone and ethanol, the test surfaces were rinsed with deionized water and dried prior to potentiodynamic polarization. EC-LAB SP-150 electrochemical workstation and EC-lab software were involved for electrochemical studies. The testing alloys were arranged as the working electrode in a three-electrode cell. The reference electrode and counter electrode were chosen into Ag/AgCl/sat'd KCl and Pt, respectively. Before the scanning, specimens were immersed in the electrolyte with open circuit potential to settle to a constant value for 30 min. Then, the alloys were scanned with 10mv/s rate in a certain voltage ranges. Two groups of test were designed to study the corrosion performance under different voltages. In group A, potentiodynamic polarization scans proceeded at a rate of 3mv/s from -0.5v versus open circuit potential to 0.5v versus the reference electrode. Group B kept all the same parameters except for the stop potential which were 0.1v. The values of corrosion potential (E_{corr}) and current density (I_{corr}) were calculated automatically through the intersection of the anodic and cathodic Tafel tangent, which were determined by the

linear parts of the polarization curves. In both groups, the exposing area of the sample in the electrode was 1 cm^2. 3.5 wt% NaCl aquatic solution was chosen as the electrolyte. The ratio of the volume of NaCl solution/sample area was 300 ml/cm^2.

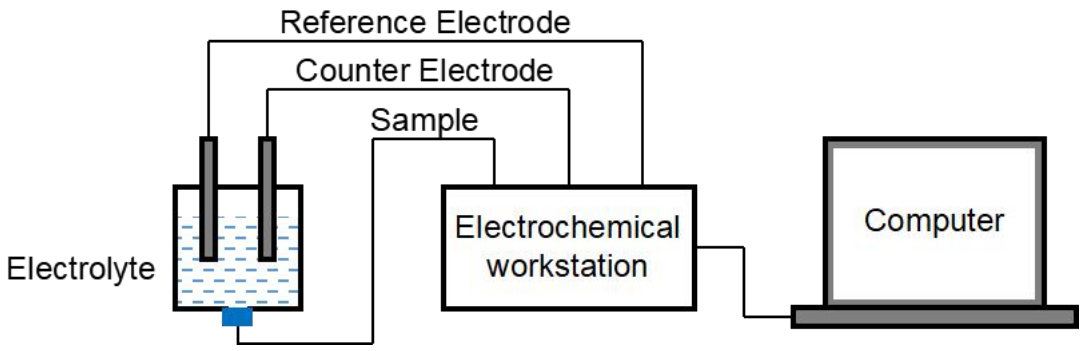

Figure 5.1 Schematic diagram of the electrochemical workstation used for polarization curve[5].

The corrosion resistance of the coatings was assessed by potentiodynamic polarization tests with a Solartron 1285 Potentiostat and Corrware software. The diagrammatic sketch of the system is illustrated in Figure 5.1. In the three-electrode cell, a tested alloy sample was used as the working electrode (WE) together with Ag/AgCl / sat KCl electrode as the reference electrode (RE), and a platinum rod as the counter electrode (CE).

5.2.3 Microstructure Analysis

Mounted samples were made into 150 mm (diameter) × 50 mm (height) cylinders. After been polished by silicon and carbide papers and alumina polisher and etched with 5% of nital, specimens were observed by FEI Quanta 200 FEG (Tokyo, Japan) scanning electron microscope (SEM) with a mixed mode of secondary electrons (SE) and backscattered electrons (BSE). To detect the chemical composition, energy dispersive

X-ray was introduced.

5.3 Results and Discussion

5.3.1 As-Cast Microstructure

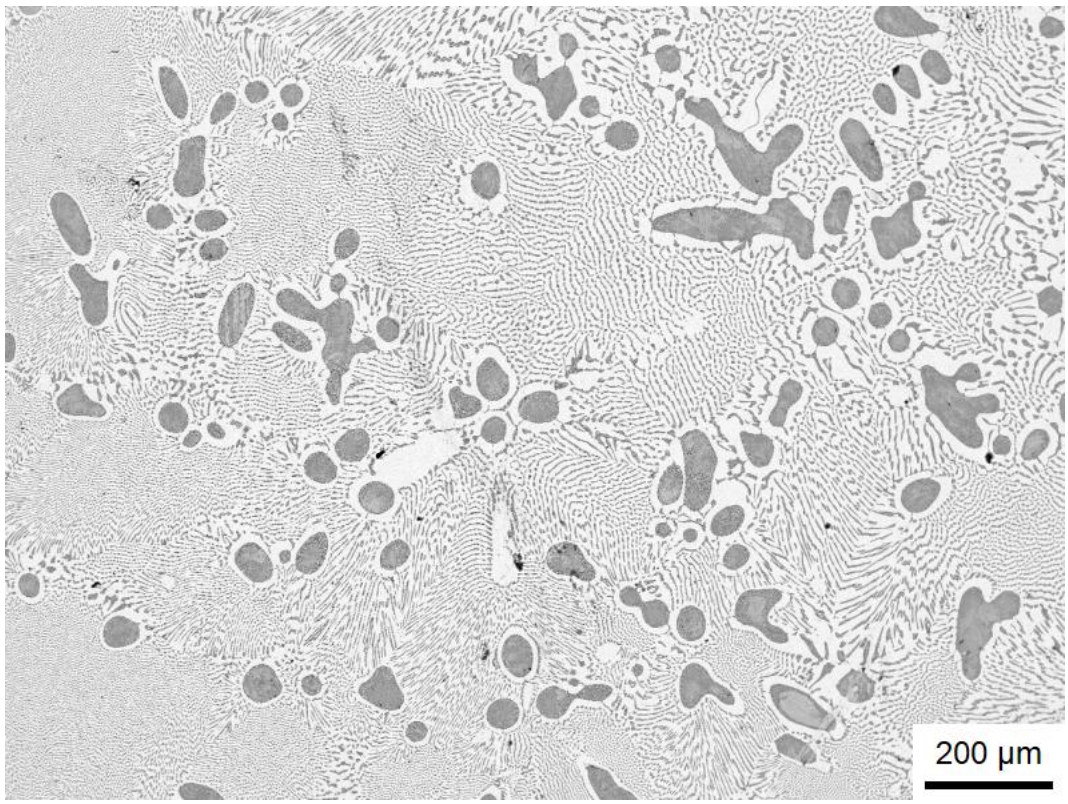

(a)

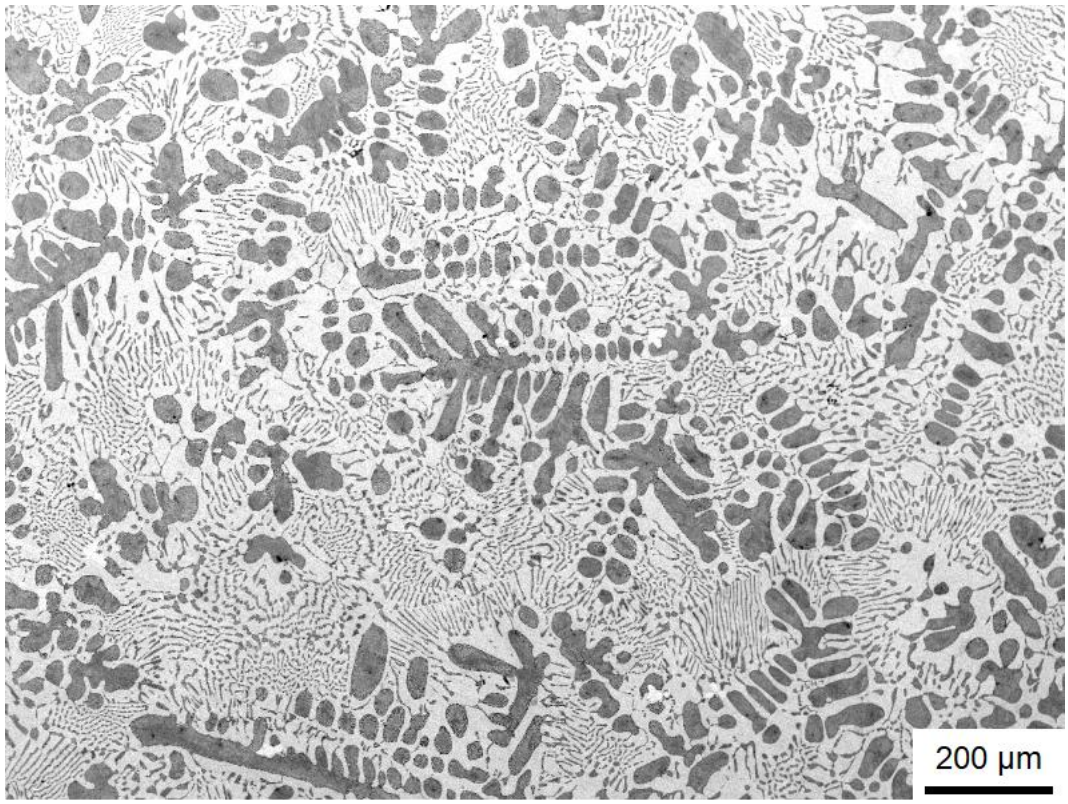

(b)

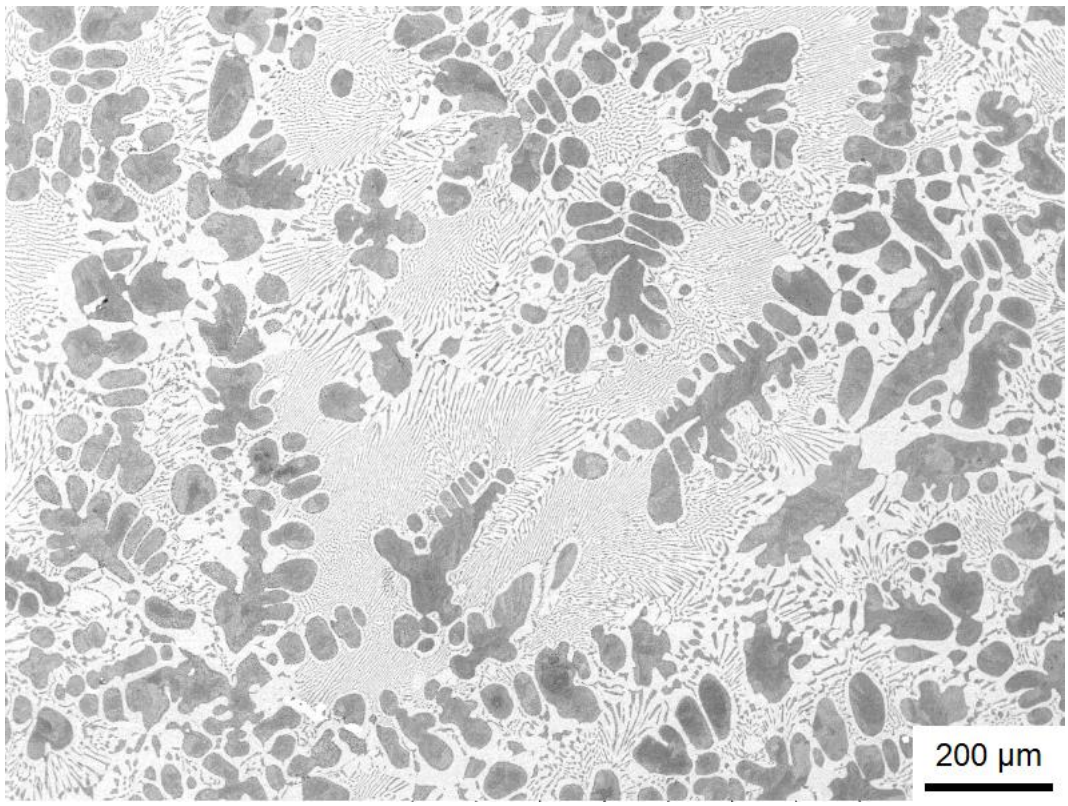

(c)

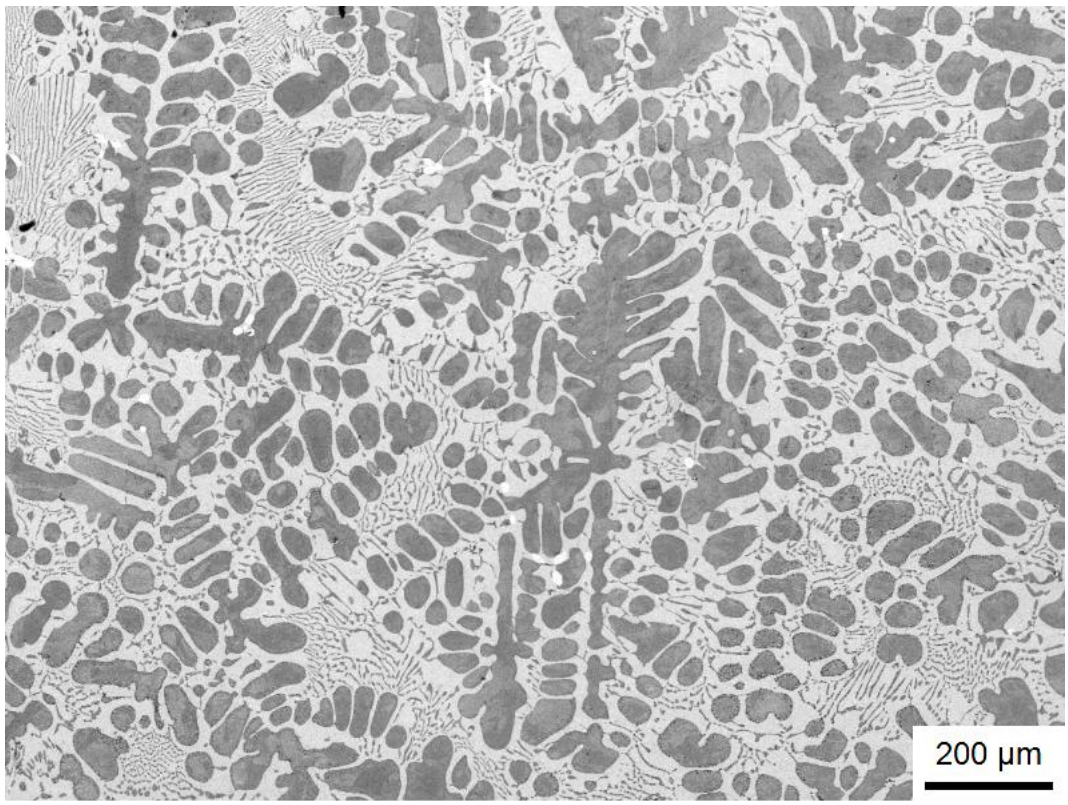

(d)

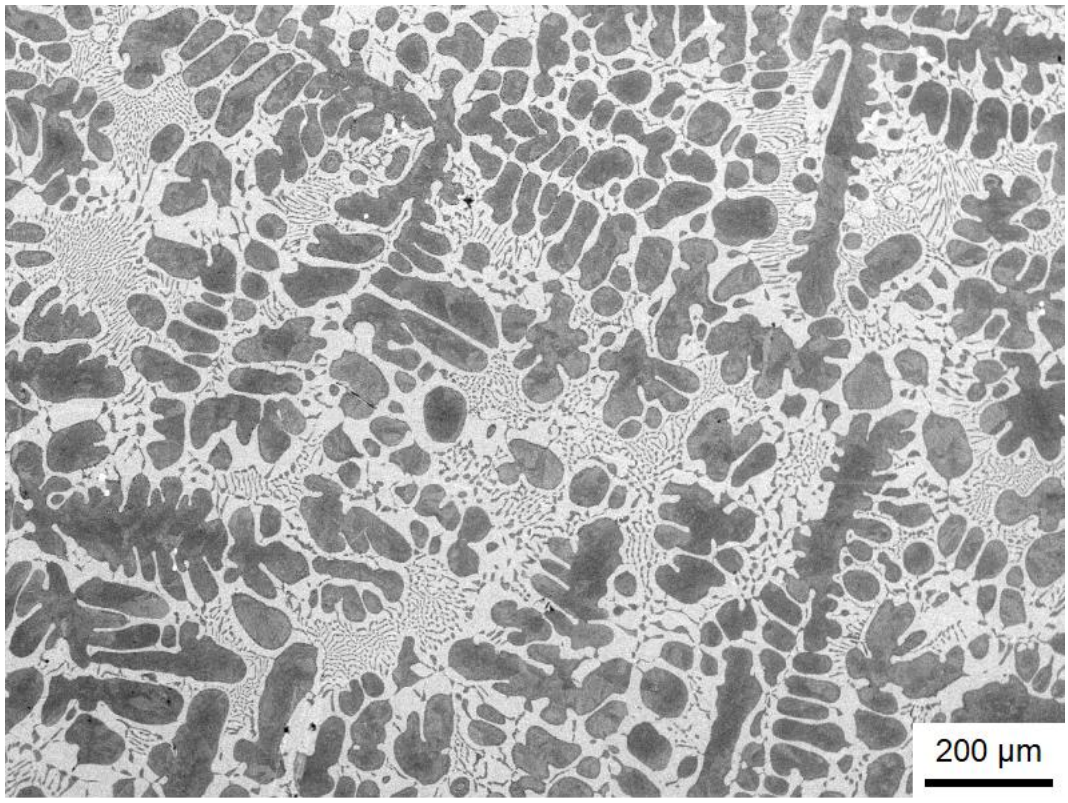

(e)

Figure 5.2 SEM pictures showing the microstructure of (a) Zn-6 wt.% Al, (b) Zn-7 wt.% Al, (c) Zn-8 wt.% Al, (d) Zn-9 wt.% Al, (e) Zn-10 wt.% Al.

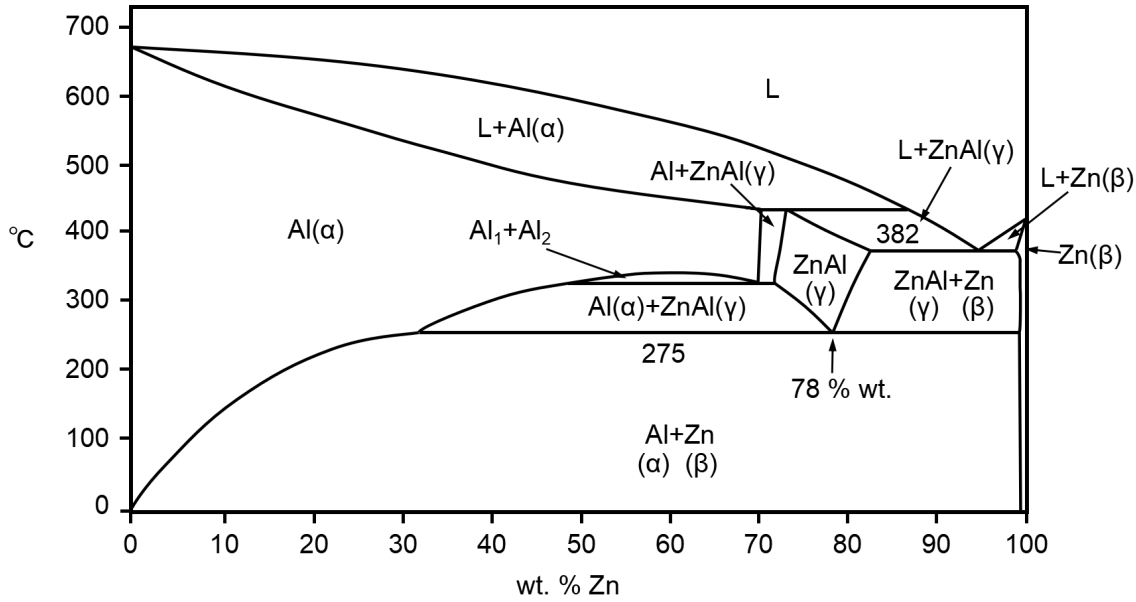

Figure 5.3 Zn-Al phase diagram [6].

The SEM analyses revealed the etched microstructure of the as-cast hypereutectic Zn - 6 wt.% Al, Zn - 7 wt.% Al, Zn - 8 wt.% Al, Zn -9 wt.% Al, and Zn -10 wt.% Al alloys before corrosion test, as shown in Figure 5.2. Theoretically, according to the phase diagram[6] in Figure 5.3, all five alloys share the similar phase composition but with different percentages. During the primary reaction, the primary of γ-ZnAl are formed with large grains. When eutectic reaction happens at 382℃, small-size well distributed eutectic grains of β-Zn and γ-ZnAl are shaped. Another eutectoid transformation occurs at 275℃ where γ-ZnAl decomposes into α-Al and β-Zn.

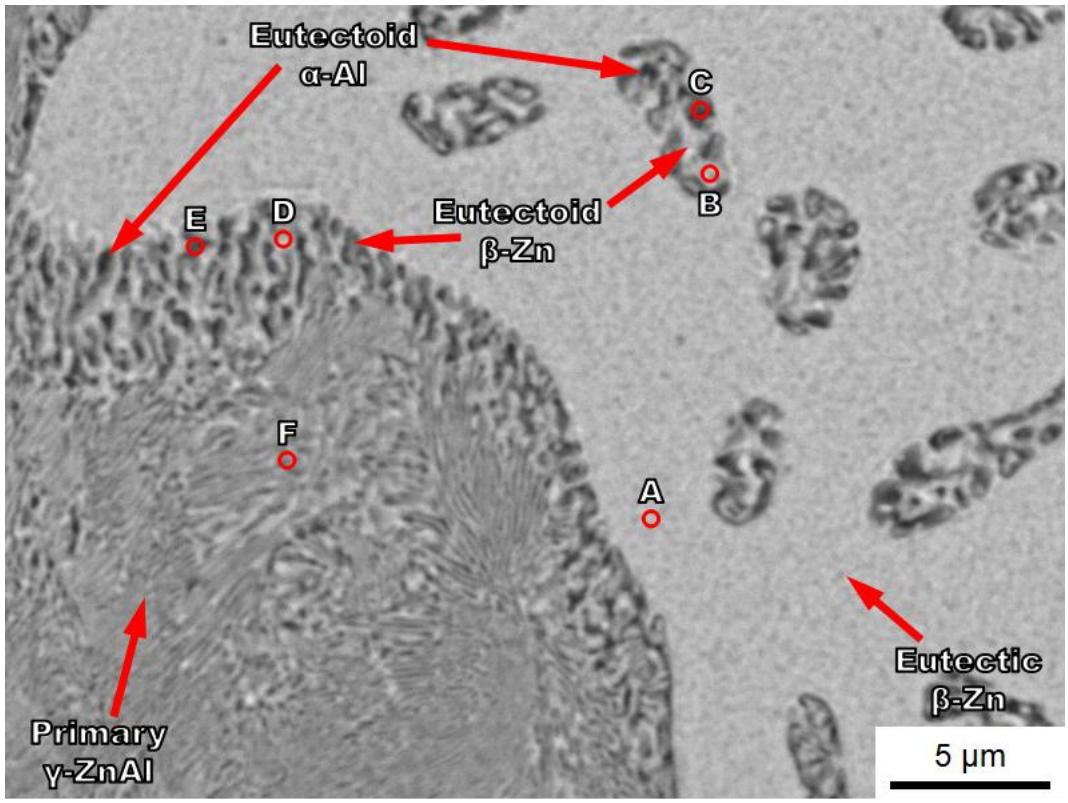

Figure 5.4 SEM micrographs in mix mode showing constituent phases in microstructure of etched Zn - 6 wt.% Al alloy.

Table 5.1 Chemical composition of the points in Figure 5.4

Point	Zn at. %	Al at. %	Phase
A	98.97	1.03	Eutectic β-Zn
B	88.75	11.25	Eutectoid β-Zn
C	25.32	74.68	Eutectoid α-Al
D	83.51	16.49	Eutectoid β-Zn
E	20.44	79.56	Eutectoid α-Al
F	48.63	51.37	Primary γ-ZnAl

Figure 5.4 presents the SEM micrograph in the mode of BSE and SE showing the etched microstructure of the as-cast Zn - 6 wt.% Al in details at a high magnification. The results of the EDS elements analysis in atomic percentage are listed in Table 5.1 indicating that the bright backgournd-like part is β-Zn. It is also found the large gray irregular grains are primary γ-ZnAl because the atomic percentage ratio of Zn and Al is close to 1:1. Since the samples were cooled in non-equilibrium condition, the center of primary γ-ZnAl grains did not completely decompose whilst the small eutectic γ-ZnAl phase was fully transformed into α-Al and β-Zn. Comparing the data of point B, C and D, E, it is found that the dark small islands are eutectoid α-Al and the bright gaps between are eutectoid β-Zn. In summary, there are four phases remained in Zn - 6 wt.% Al sample under room temperature: (1) primary γ-ZnAl; (2) eutectic β-Zn; (3) eutectoid β-Zn; (4) eutectoid α-Al;

In order to compare the difference between five samples, ImageJ was used to transform the SEM pictures into black-and-white binary image for analyzing the content of the sample. Each sample is measured multiple times to ensure the accuracy. Table 5.2 reveals the contents of different phases. As weight percentage of Al changed from 6% to 10%, the proportion Al-contained phases (namely primary γ-ZnAl and eutectoid α-Al) also increase from 40.43±0.39% to 58.00±0.58%. The data between are 45.20±0.44%, 48.85±0.47%, 53.36±0.44% for Zn - 7 wt.% Al, Zn - 8 wt.% Al, Zn -9 wt.% Al samples, respectively.

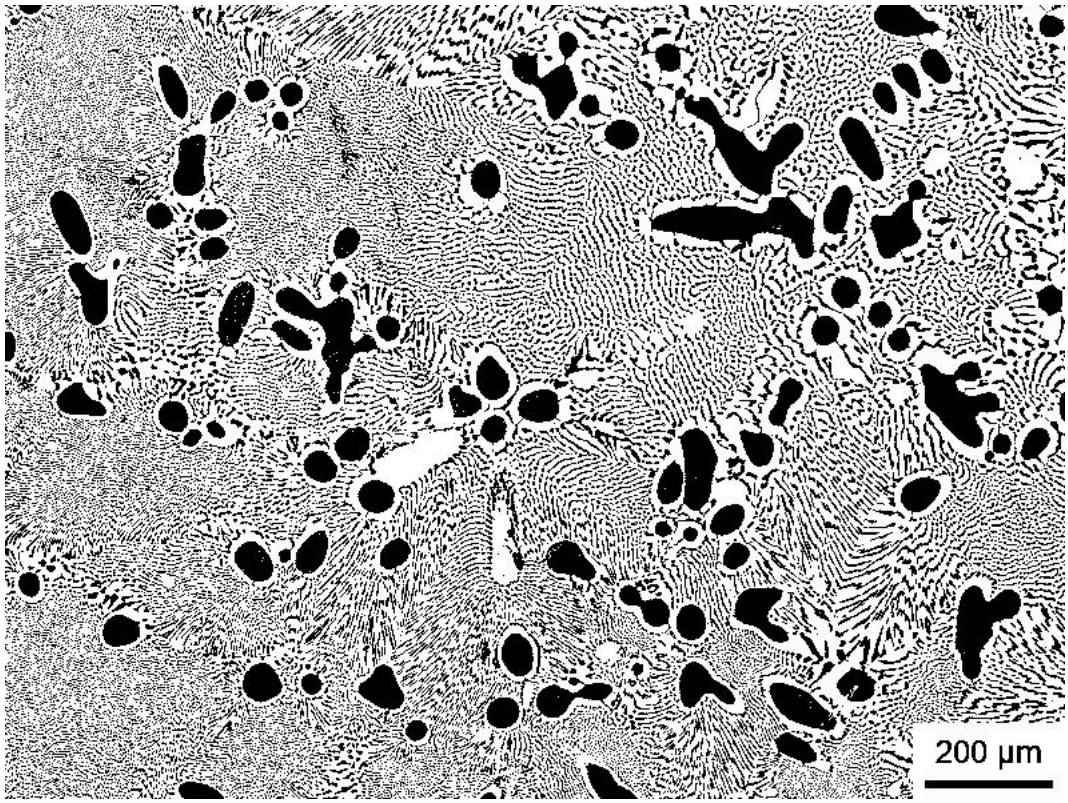

(a)

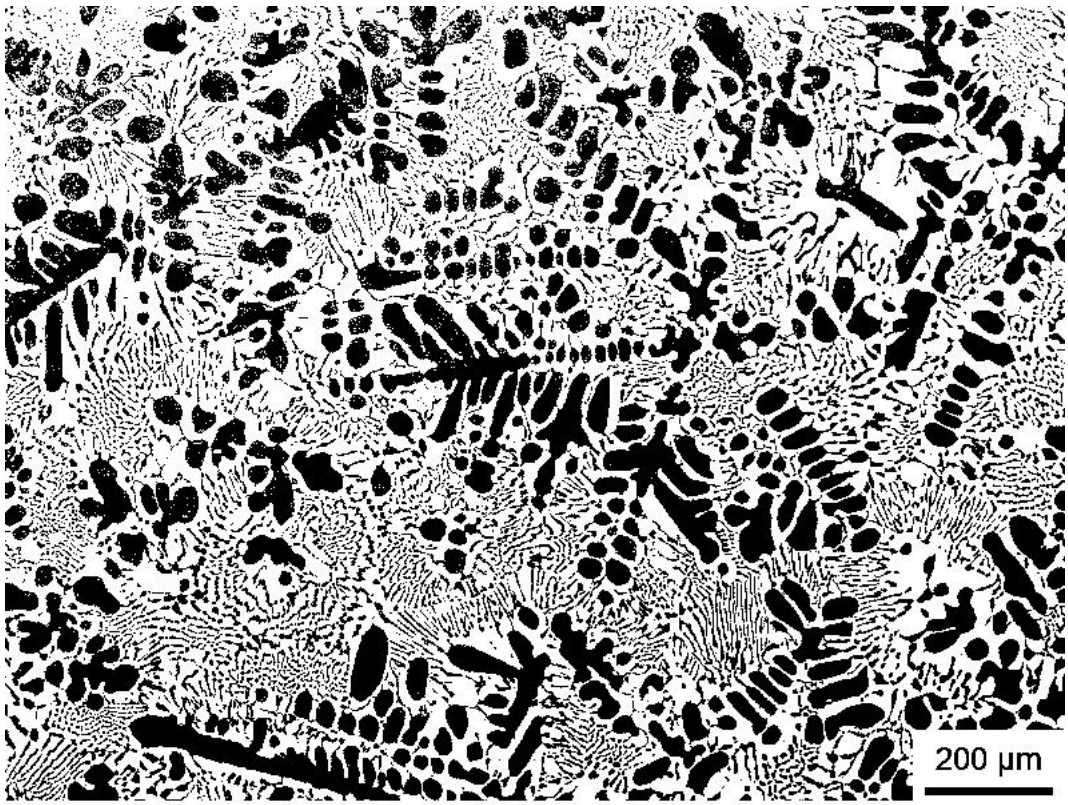

(b)

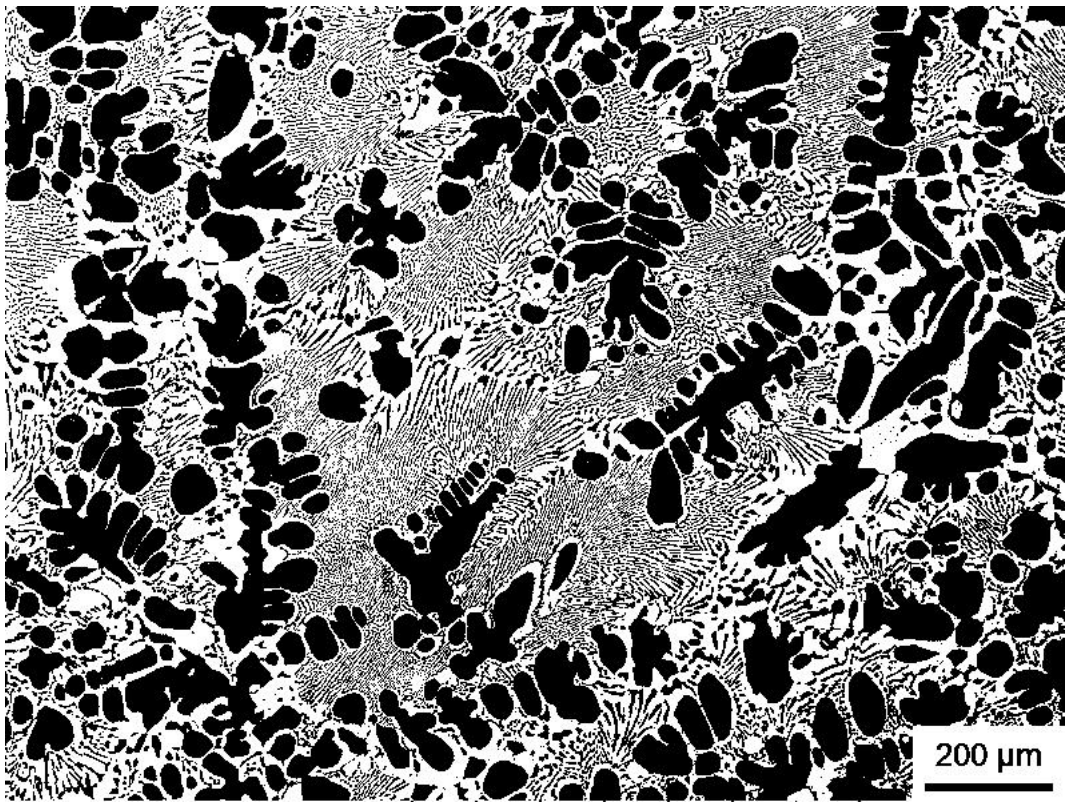

(c)

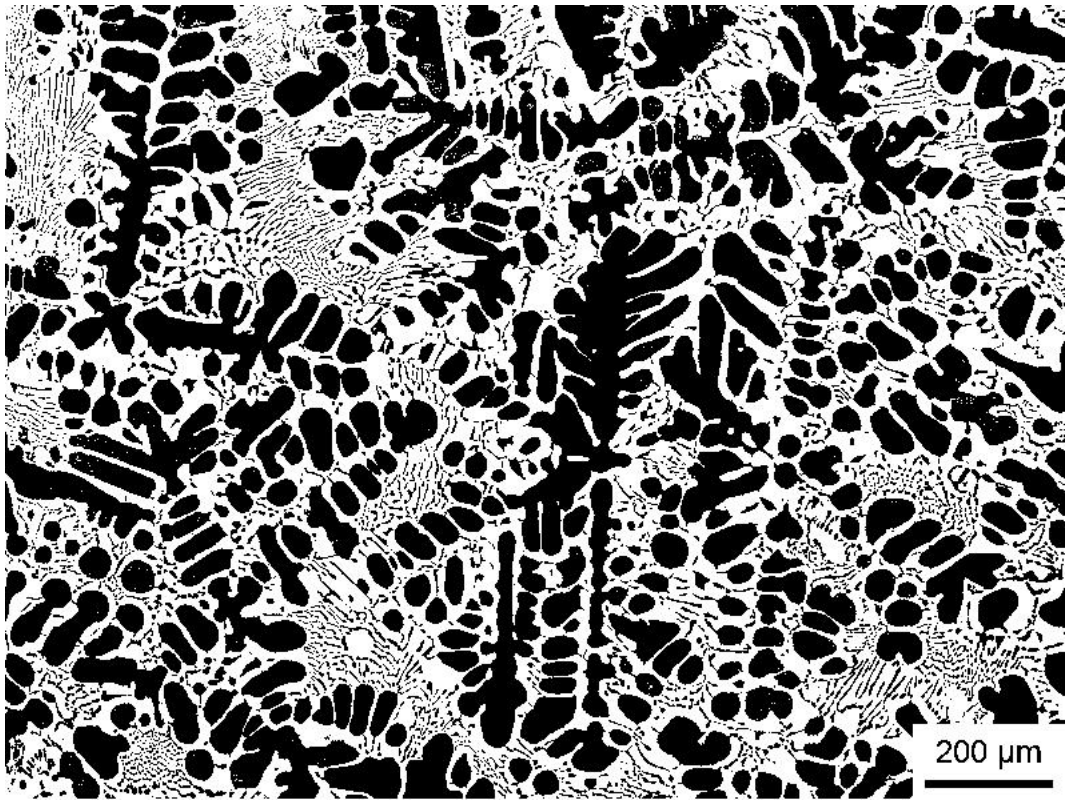

(d)

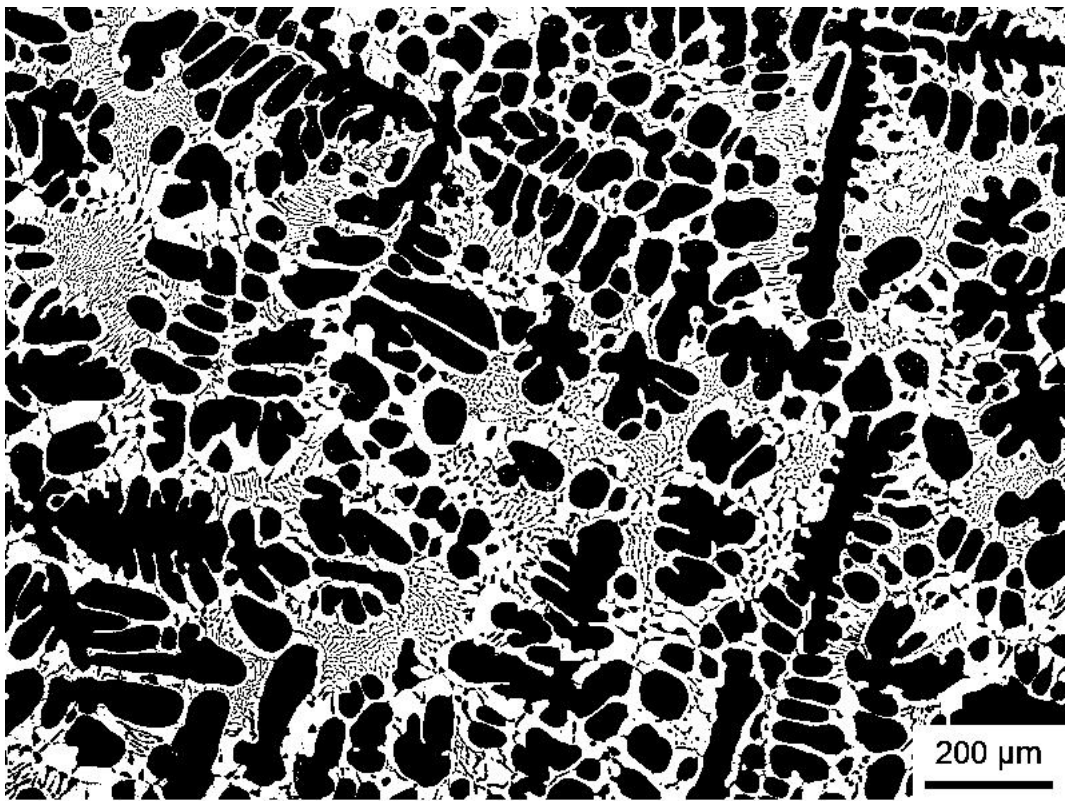

(e)

Figure 5.5 SEM pictures after binary treatment by ImageJ for calculating the phase content of (a) Zn-6 wt.% Al (b) Zn-7 wt.% Al (c) Zn-8 wt.% Al (d) Zn-9 wt.% Al (e) Zn-10 wt.% Al.

Table 5.2 Proportion of Al-contained phases with different Al content.

Alloy	Al-contained phase content (%)
Zn - 6 wt.% Al	40.43±0.39
Zn - 7 wt.% Al	45.20±0.44
Zn - 8 wt.% Al	48.85±0.47
Zn -9 wt.% Al	53.36±0.44
Zn -10 wt.% Al	58.00±0.58

5.3.2 Electrochemical Tests

5.3.2.1 General corrosion

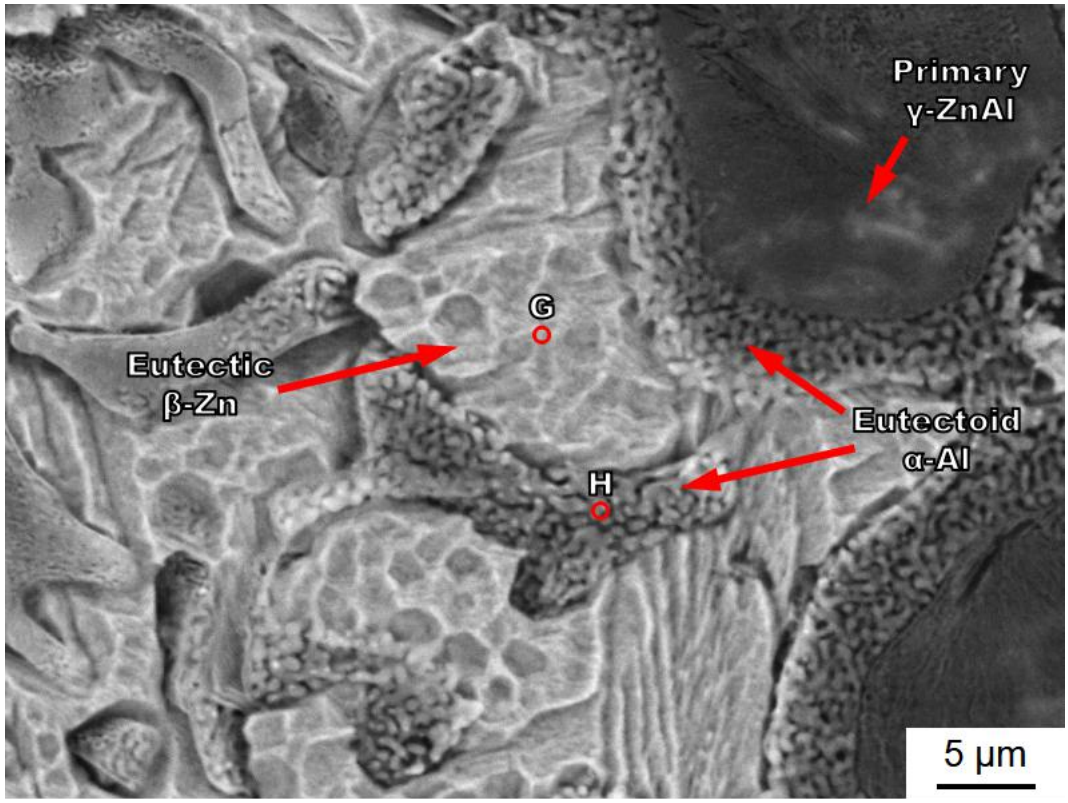

(a)

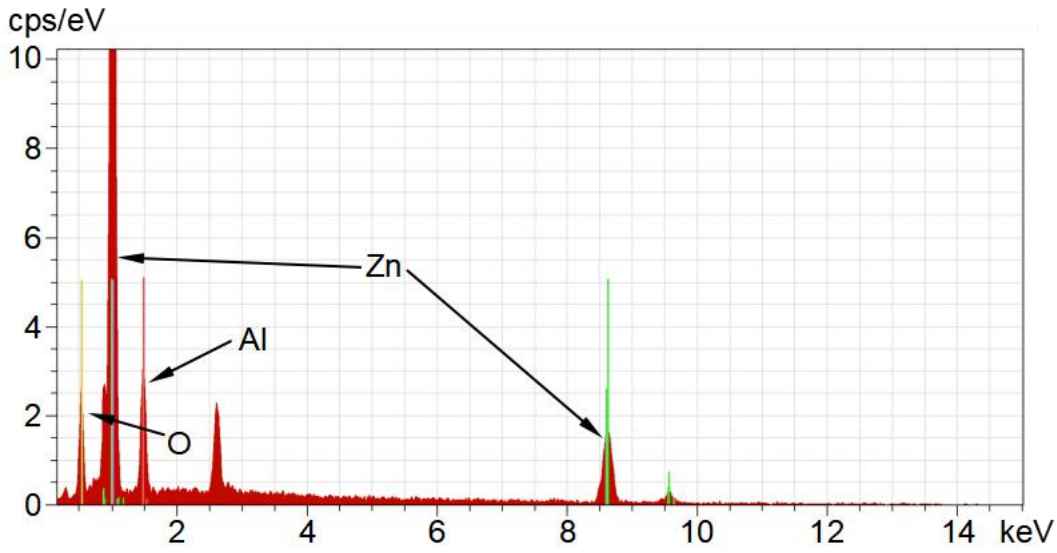

(b)

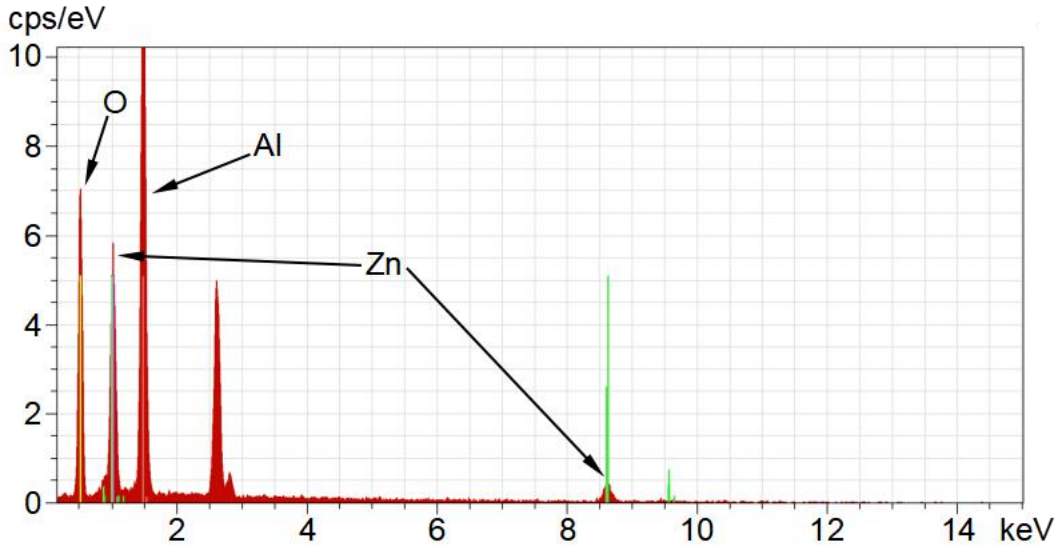

(c)

Figure 5.6 (a) SEM micrographs in mix mode showing microstructure of mirror-polished Zn - 8 wt.% Al sample after polarization test in which the scanning voltage is from -0.5V to 0.1V (b) EDS spectrum of point G with weak oxygen single (c) EDS spectrum of point H with strong oxygen single.

To study the electrochemical properties of Zn-Al alloy in low test voltage, the corrosion potentials were in the range from -0.5V to 0.1V (SCE). At the beginning of the test, due to the higher reactivity of Al compared with Zn, the Al phases reacted with water and formed a passive layer of aluminium hydroxide which prevented further reactions on Al.[7] Then, the uniform corrosion on Zn dominated this process. This can be proved by the SEM and EDS results of the tested surface shown in Figure 5.6. The reactions of Zn can be described as following[8]:

$(Zn \rightarrow Zn^{2+} + 2e^{-}) (x2)$ (1)

$$O_2 + 2H_2O + 4e^- \rightarrow 4OH^- \quad (2)$$

$$2Zn + O_2 + 2H_2O \rightarrow 2Zn^{2+} + 4OH^- \quad (3)$$

$$2Zn^{2+} + 4OH^- \rightarrow 2Zn(OH)_2 \quad (4)$$

$$2Zn(OH)_2 + CO_2 + O_2 + H_2O \rightarrow Zn_4CO_3(OH)_6 \quad (5)$$

whereas the passive reactions of Al are illustrated as[9]:

$$2Al + 6H_2O \rightarrow 2Al(OH)_3\downarrow + 3H_2 \quad (6)$$

Figure 5.7 shows the polarization curves of the as-cast alloy Zn - 6 wt.% Al, Zn - 7 wt.% Al, Zn - 8 wt.% Al, Zn -9 wt.% Al, and Zn -10 wt.% Al. Through automatic fitting in EC-lab software, the slopes of cathode reaction (β_c) and anode reaction (β_a), corrosion potential (E_{corr}), and corrosion current (i_{corr}) were computed and shown in Table 5.3. Corrosion resistance (R_p) was then calculated according to the equation (7) .

$$R_p = \frac{b_a \times b_c}{2.3 \times i_{corr} \times (b_a + b_c)} \quad (7)$$

where i_{corr} is the corrosion current density, and b_a and b_c are the slopes of the anodic and cathodic Tafel regions respectively. Figure 5.8 demonstrates the tendency of R_p. It is very clear in this diagram that the increasing Al percentage brought higher R_p, which is preferable in anti-corrosion material. This observation is in agreement with the results reported in reference 2.

On the upper part of the polarization curve, there is a point where the current gradually stops growing as the potential continuing increase. This point is the starting point of passivity where the passivity potential (E_{pp}) is determined[10]. Using Microsoft Excel, E_{pp} was found at the point with the maximum second derivative on the upper part of the curve. The results are listed in the last column in Table 5.3 and Figure 5.6. Similarly with R_p, E_{pp} also grows alone with the Al content. This means that higher Al

percentage can delay the passivity which is beneficial as protective coating material.

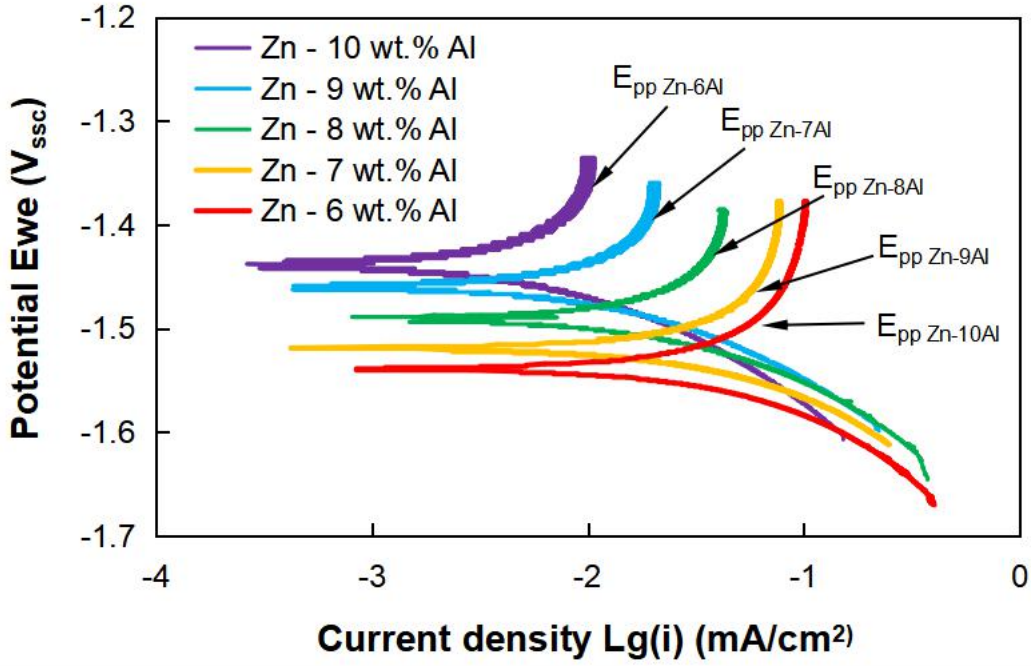

Figure 5.7 Tafel curves of Zn - 6 wt.% Al, Zn - 7 wt.% Al, Zn - 8 wt.% Al, Zn -9 wt.% Al, and Zn -10 wt.% Al alloys in low scanning voltage from -0.5V to 0.1V.

Table 5.3 Electrochemical parameters of the Zn - 6 wt.% Al, Zn - 7 wt.% Al, Zn - 8 wt.% Al, Zn -9 wt.% Al, and Zn -10 wt.% Al alloys

Sample	b_a (mV/dec)	b_c (mV/dec)	Icorr ($\mu A/cm^2$)	R_p (kΩ cm2)	E_{corr} (V)	E_{pp} (V)
Zn-6 wt.% Al	-1490.13	72.85	225.81	946.68	1.09	-1.39
Zn-7 wt.% Al	-1543.74	60.22	227.59	1385.53	1.41	-1.41
Zn-8 wt.% Al	-1540.50	39.05	227.21	1298.58	2.15	-1.43
Zn-9 wt.% Al	-1479.45	12.91	214.50	994.45	5.94	-1.47
Zn-10 wt.% Al	-1493.97	11.68	239.33	1112.21	7.33	-1.50

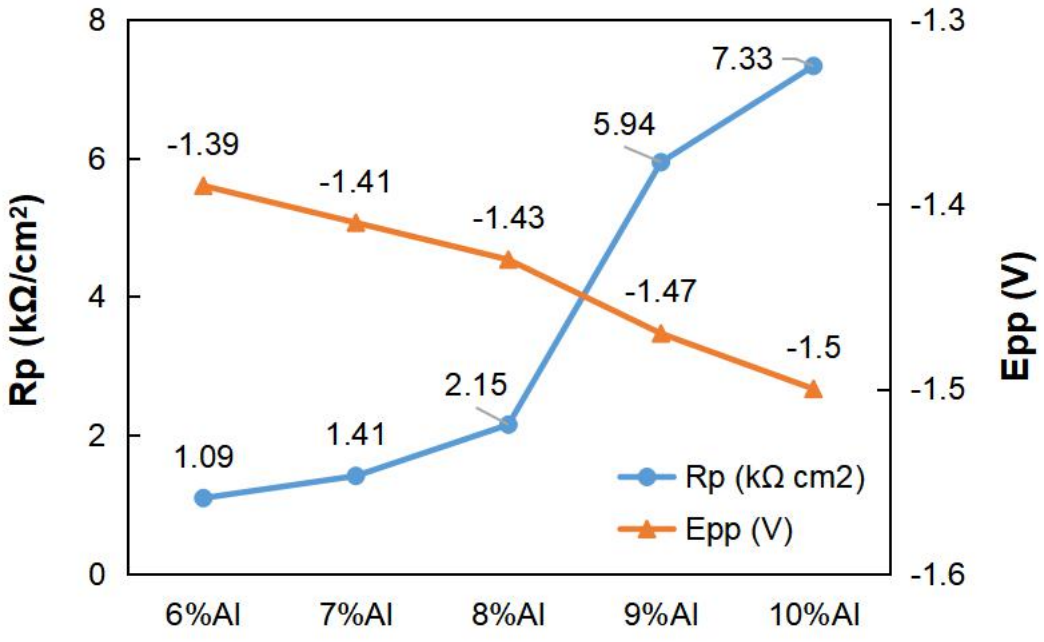

Figure 5.8 Variation tendency of corrosion resistance and passive potential.

5.3.2.2 Pitting corrosion

Pitting corrosion happens once the passivity of Al is lost[11]. The consequence of this phenomenon is that the corrosion rate of Al would dramatically increase. In order to study the ability of Zn-Al alloys resisting pitting corrosion, the scanning voltage was set from -0.5V to +0.5V. Figure 5.9 is the SEM picture and EDS spectrum of selected point. Point I, which has similar amount of Al and Zn, is identified as corrupted γ-ZnAl. The rough surface and depth of the whole also suggest the present of serious pitting corrosion. High proportion of Zn found in point J and K and curvy smooth surface indicates that these two points are β-Zn which was uniformly corrupted. Therefore, the small well-distributed holes were left by the removal of the eutectoid α-Al when pitting

corrosion occurred.

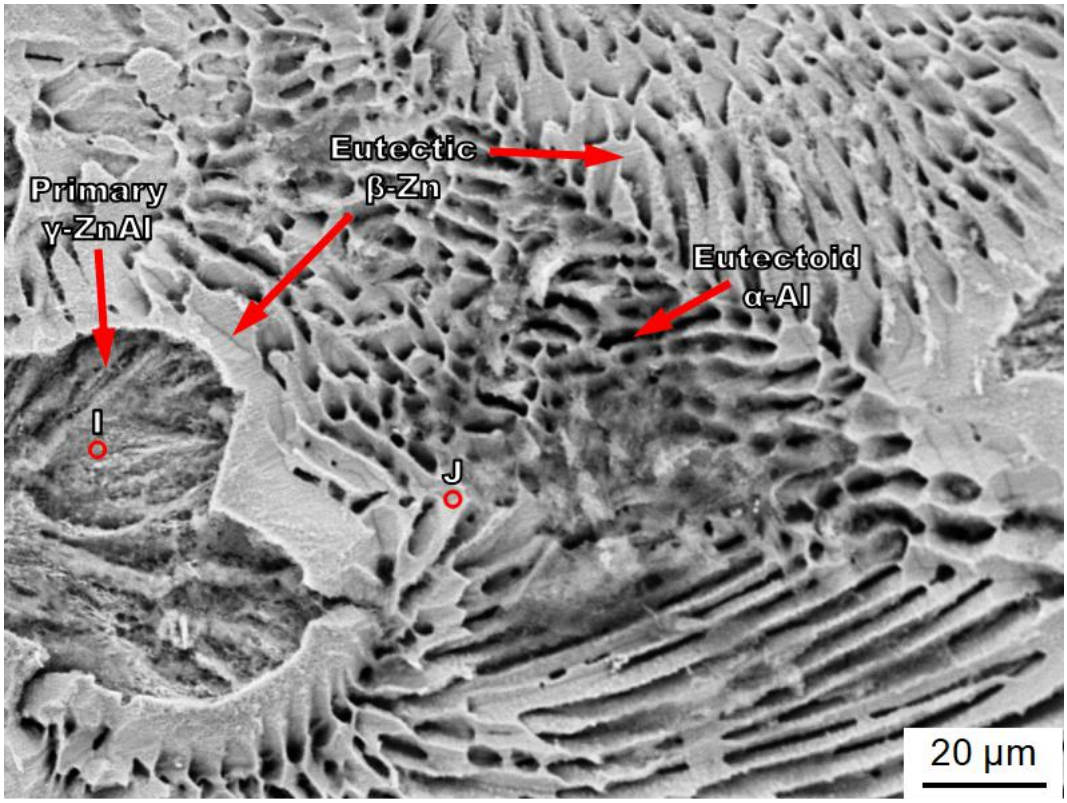

(a)

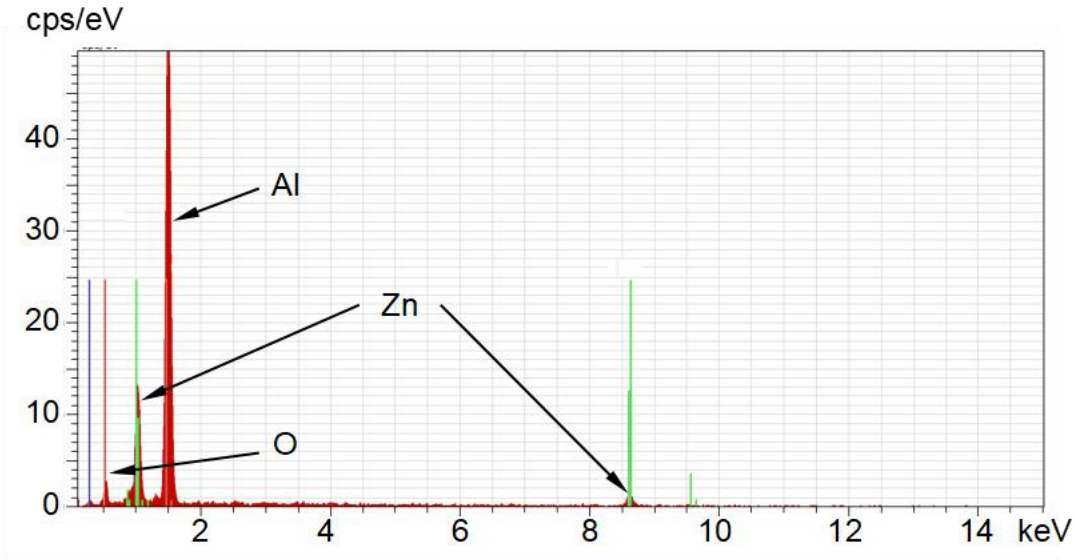

(b)

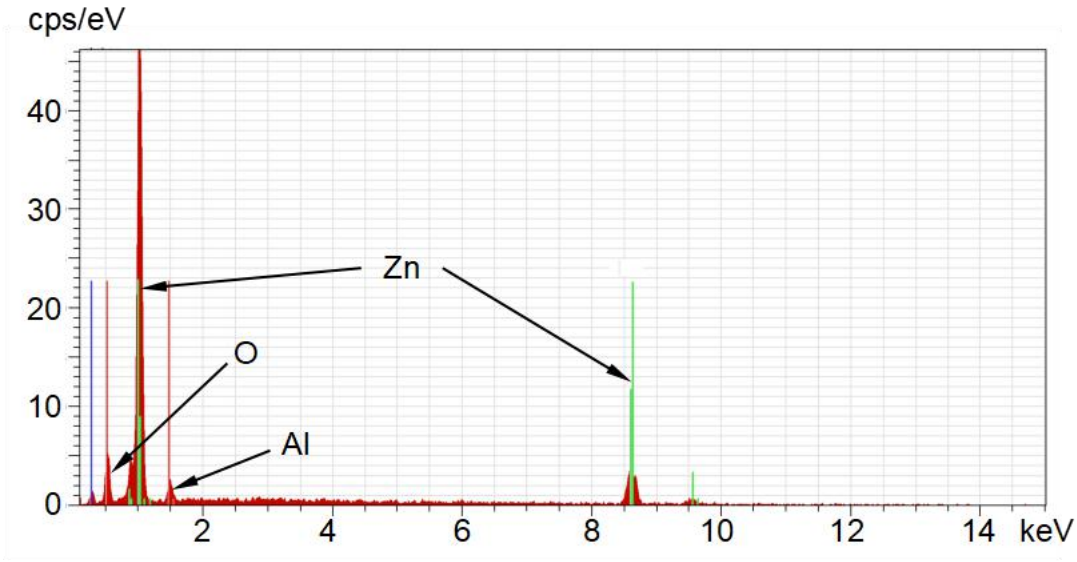

(c)

Figure 5.9 (a) SEM micrographs in mix mode showing microstructure of mirror-polished Zn - 8 wt.% Al sample after polarization test in which the scanning voltage is from -0.5V to 0.5V. (b) EDS spectrum of point I with strong Al signal. (c) EDS spectrum of point J with strong Zn signal.

On the high potential polarization curves (Figure 5.10), the current suddenly went up at the top of the curve. This occurred after the passive layer on Al was breakdown, i.e. pitting corrosion started, which led to a significant increase of current density. According to Jones[12], when the test voltage was above E_{pit} , the new pitting formed and grew. Therefore, the high E_{pit} can reduce the chance of pitting corrosion. In this study, E_{pit} was determined in the similar way with E_{pp}, the peak value of second derivative. The specific E_{pit} values of different samples are given in Table 5.4 and Figure 5.12 in which the E_{pit} decreased from -0.92V to -1.11V as the Al percentage increased from 6 wt.% to 10 wt.%. Hence, lower Al content is beneficial to prevent pitting corrosion, which is consistent

with the finding by Yang et al [3].

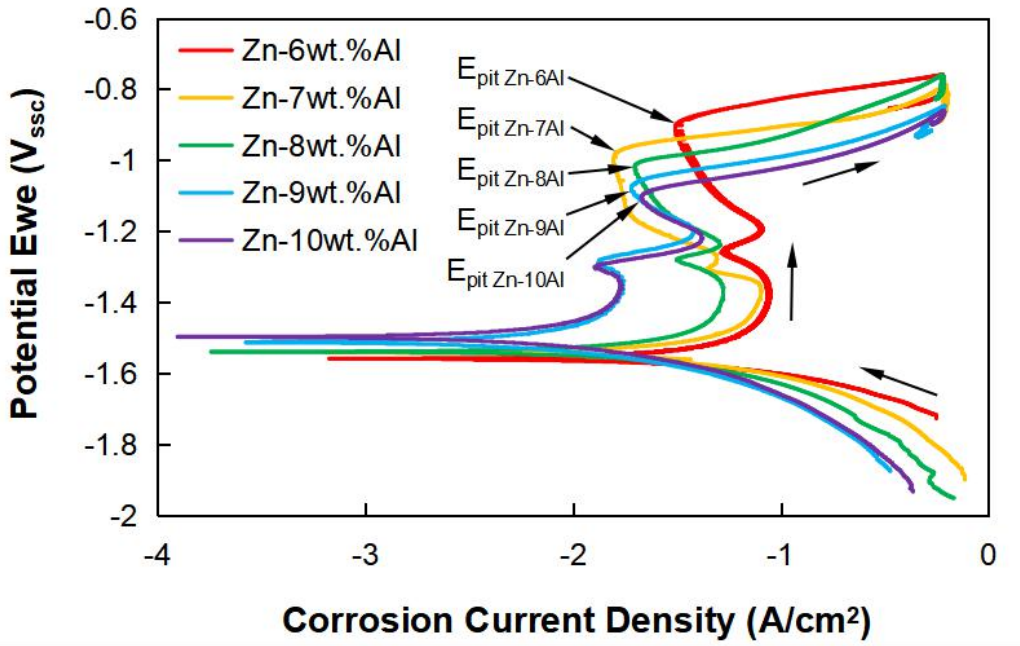

Figure 5.10 Tafel curves of Zn - 6 wt.% Al, Zn - 7 wt.% Al, Zn - 8 wt.% Al, Zn -9 wt.% Al, and Zn -10 wt.% Al alloys in low scanning voltage from -0.5V to 0.5V.

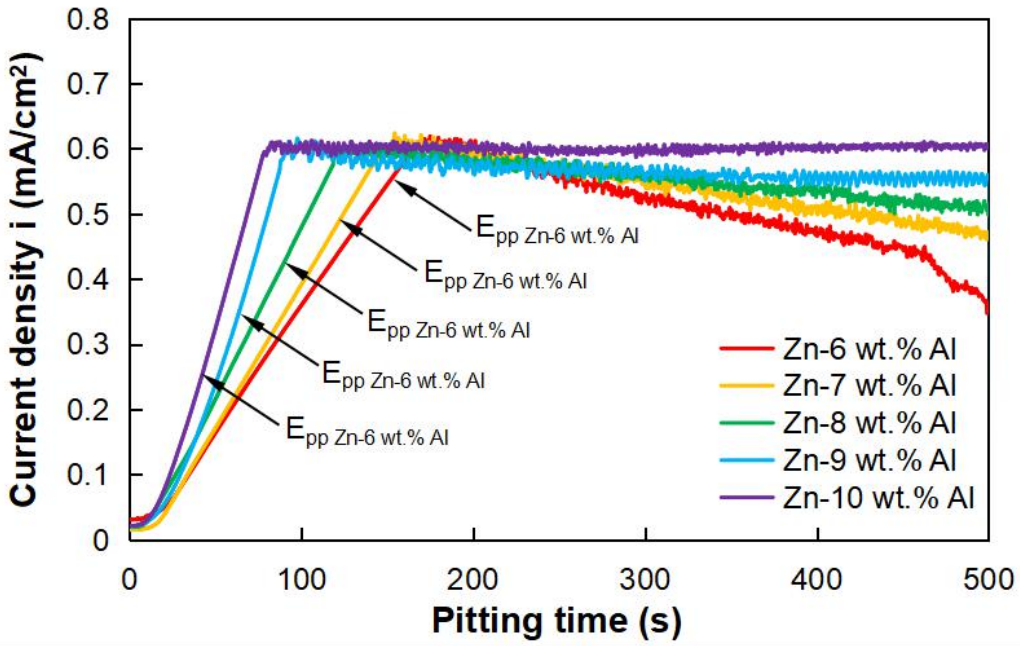

Figure 5.11 current change of Zn - 6 wt.% Al, Zn - 7 wt.% Al, Zn - 8 wt.% Al, Zn -9 wt.% Al, and Zn -10 wt.% Al alloys after pitting corrosion occurred.

Table 5.4 Calculation result of pitting potential, integral of i vs t from 0s to 500s, and slope of right side of the curve

Sample	Epit (V)	Integral of i from 0s to 500s (C/cm^2)	Slope of right part ($\mu A/cm^2/s$)
Zn - 6 wt.% Al	-0.92	216.12	-0.62
Zn - 7 wt.% Al	-1.00	230.86	-0.44
Zn - 8 wt.% Al	-1.03	239.44	-0.20
Zn -9 wt.% Al	-1.08	247.60	-0.17
Zn -10 wt.% Al	-1.11	255.83	-0.03

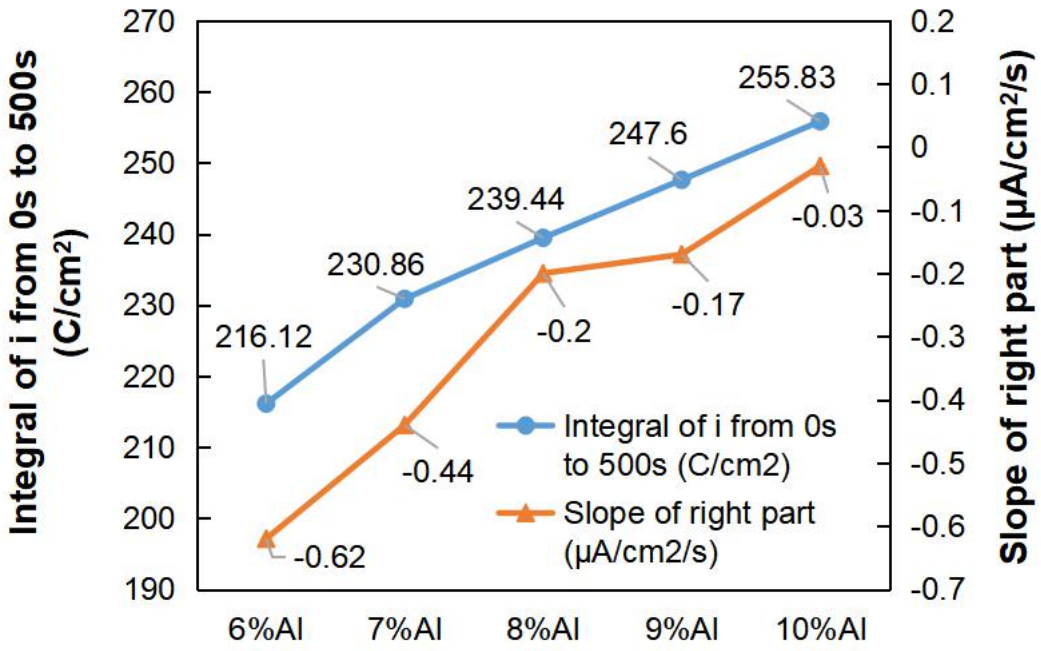

Figure 5.12 Variation tendency of corrosion resistance and passive potential.

To study the detail of pitting stages, i-t (current vs time) curve was plotted in Figure 5.11 in which the zero point of time was the moment when scanning voltage reached the E_{pit} . There were two vital values that can be obtained through it. Firstly, the integral of current is able to project the mass loss and corrosiveness of the samples. The integral of the first 500s was calculated after pitting happened. The results are listed in Table 5.4. While Zn - 6 wt.% Al lost 216.12 C/cm^2 electrons, 255.83 C/cm^2 electrons were consumed in Zn -10 wt.% Al sample. The data for Zn-7 wt.% Al, Zn-8 wt.% Al, Zn-9 wt.% Al are 230.86 C/cm^2, 239.44 C/cm^2, and 247.60 C/cm^2, respectively. This means that an increase in Al percentage increased less mass losses.

Furthermore, the hysteresis of current on polarization curves on the upper part of when voltage went down in the end decides if the alloy is pitting resistant[6]. These features are mirrored in i-t plot through the overall slopes of the curve on the right side of the peak of current. As Figure 5.11 shows the tendency of variation of the slops, Table 5.4 and Figure 5.12 present the quantified values which were determined by the linear regression of all the points between the 0s and 500s. The results suggest the low Al percentage is preferable against pitting corrosion.

5.4 Conclusions

The two groups of polarization curves with different scanning voltage have been obtained for Zn-6 wt.% Al, Zn-7 wt.% Al, Zn- wt.% Al, Zn-9 wt.% Al, and Zn-10 wt.% Al alloys. As-tested surface was observed by SEM and analyzed by EDS. The conclusions are given below:

1. Al exists in hypereutectic Zn-Al alloy in two different forms i.e. γ-ZnAl phase and

α-Al phase. When Al percentage increase, the proportion of Zn-rich phase also goes up.

2. In polarization test, general and pitting corrosion are both involved in the reaction. Due to the strong passivity of Al, the precipitate would prevent Al from reaction soon after the corrosion start. Therefore, in the low voltage scanning range from -0.5V to 0.1V, uniform attack on Zn is the major type of corrosion. The high Al content can increases the corrosion resistance, and passive potential.
3. In the high voltage scanning from -0.5 to 0.5V, pitting corrosion happens after Al loses passivity after which the current dramatically increases to the maximum limit then decreases with the potential. During this process, pits are created and grow rapidly. The integral and slope calculation on the i-t curve suggest that more Al caused more pitting damage on the alloys.

5.5 Reference

[1] Fayomi, O. S., & Popoola, M. O. (2012). Comparative studies of microstructural, tribological and corrosion properties of plated Zn and Zn-alloy coatings. International Journal of Electrochemical Science, 7, 4860-4870.

[2] Fayomi, O. S., & Popoola, M. O. (2012). Electrochemical and Mechanical Properties of Mild Steel Electro-plated with Zn-Al. International Journal of Electrochemical Science, 7, 4898-4917.

[3] Yang, L., Zhang, Y., Zeng, X., & Song, Z. (2012). Corrosion behaviour of superplastic Zn–Al alloys in simulated acid rain. Corrosion Science, 59, 229-237.

[4] Miao, W., Cole, I. S., Neufeld, A. K., & Furman, S. (2007). Pitting corrosion of Zn

and Zn-Al coated steels in pH 2 to 12 NaCl solutions. Journal of The Electrochemical Society, 154(1), C7-C15.

[5] Ma, Y. (2005). An investigation of the electrolytic plasma oxidation process for corrosion protection of pure magnesium and magnesium alloy AM50.

[6] Ares, A. E., & Gassa, L. M. (2012). Corrosion susceptibility of Zn–Al alloys with different grains and dendritic microstructures in NaCl solutions. Corrosion Science, 59, 290-306.

[7] Badawy, W. A., Al-Kharafi, F. M., & El-Azab, A. S. (1999). Electrochemical behaviour and corrosion inhibition of Al, Al-6061 and Al–Cu in neutral aqueous solutions. Corrosion Science, 41(4), 709-727.

[8] Vu, T. N. (2012). Selective dissolution from Zn-Al alloy coatings on steel (Doctoral dissertation, Université Pierre et Marie Curie-Paris VI).

[9] Badawy, W. A., Al-Kharafi, F. M., & El-Azab, A. S. (1999). Electrochemical behaviour and corrosion inhibition of Al, Al-6061 and Al–Cu in neutral aqueous solutions. Corrosion Science, 41(4), 709-727

[10] Davis, J. R. (2000). Corrosion of aluminum and aluminum alloys. Materials Park: ASM International.

[11] Fontana, M. (1990). Corrosion engineering. New York: Mc Graw-Hill.

[12] Jones, D. A. (1996). Principles and prevention of corrosion. Upper Saddle River: Prentice Hall.

CHAPTER 6 Conclusions

The conclusions drawn from this study are summarized as follows:

1. The solidification and microstructure of Zn-6wt.% Al alloy was studied by thermal analysis and SEM, respectively. By drawing the derivative and second derivative of the cooling curve, the temperature of the primary, eutectic, and eutectoid reaction were confirmed as 390.3 ℃, 381.5 ℃, and 277.7 ℃ as the alloy solidified at a cooling rate of 0.04℃/s, respectively. When cooling rate raised to 10 ℃/s, the solidification process finished within several seconds. As a result, the obvious stages diminished and the liquidus temperature decreased to 382.9 ℃. The equilibrium liquidus temperature is calculated to be 390.7 ℃ by extrapolating the linear function between the non-equilibrium liquidus temperature and the square root of the cooling rate (dT/dt) to the zero cooling rate.

The SEM and EDS results revealed the presence of four phases, i.e., the primary γ-ZnAl phase, the eutectic β-Zn phase, the eutectoid α-Al and the eutectoid β-Zn phases. The alloy solidified at the cooling rates varying from 0.04 to 10 ℃/s. The decomposition rate of the γ-ZnAl phase was highly related to cooling rate which can shorten the reaction time. It was also found that the high cooling rate (10 ℃/s) produced massive nanosize eutectic grains.

2. CRS 1018 steel was successfully coated by the Galfan alloy via the hot dipping process. It was found that the coated sample has a noticeable change in mechanical properties. Its UTS decreased from 833.1±7.9 MPa to 700.2±9.5 MPa while the YS reduced from 821.4±7.1 MPa to 681.6±5.1 MPa. However, the elongation increased

from 2.5±0.21% 12.1±2.8% after heating. The later nanoindentation test showed an obvious difference in nano-hardness and Young's model. The calculated dislocation densities by the Nix-Gao theory were 2.182×10^{15} and 4.676×10^{15} m^{-2} for the coated and uncoated samples, respectively. The reduction in dislocation density resulting from heating during coating should be responsible for the change of the mechanical properties of the substrate.

3. Zn-6 wt.% Al, Zn-7 wt.% Al, Zn-8 wt.% Al, Zn-9 wt.% Al, and Zn-10 wt.% Al alloys were prepared and observed with an optical microscope. The increased percentage of Al directly leads to a higher proportion of Zn-rich phases. Polarization tests with low voltage (-0.5V - 0.1V) show that Al improves the corrosion resistance (R_p) of samples as well as the passive potential (E_{pp}). The SEM and EDS analysis reveal that Zn was uniformly attacked while Al was protected by passive layer. This explains the relationship between the high Al content and the enhanced corrosion resistance. When the scanning voltage became high, pitting corrosion occurred after the passive layer were broken, which significantly increased the current to the limit of the test equipment. Then voltage went down automatically leaving a hysteresis of current. The start voltages of pitting corrosion were raised by the Al content due to the passivity of Al. But once pitting corrosion started, the large amount of Al-rich phase on the test area provide more spots to grow new pits. The current vs time curve was plotted, on which the integrals represented the loss of etymology of electricity and the slopes of the right part of the curve determined the pitting resistant ability. Both values were negatively affected by high Al percentage. On the SEM pictures, there were clear holes left by corrupted Al phase while Zn phase remained smooth. Hence, Al was constructive in low corrosion

potential but harmful if pitting corrosion occurred in high voltage.

CHAPTER 7 Future work

The current results reveal some factors that can change the microstructure of Zn-Al alloys such as the Al content and cooling rate. Different structures and phase contents may result in different anti-corrosion performance.

Since nano-size grains are very easy to obtain in near-eutectic alloys, it provides possibilities to commercialize nano-crystal material at a reasonable cost. Thus, the production process of low-cost nano-crystal would be an interesting field for further investigation.

APPENDIX

Microstructure Analysis Figures

Metallic coating of commercial brake line

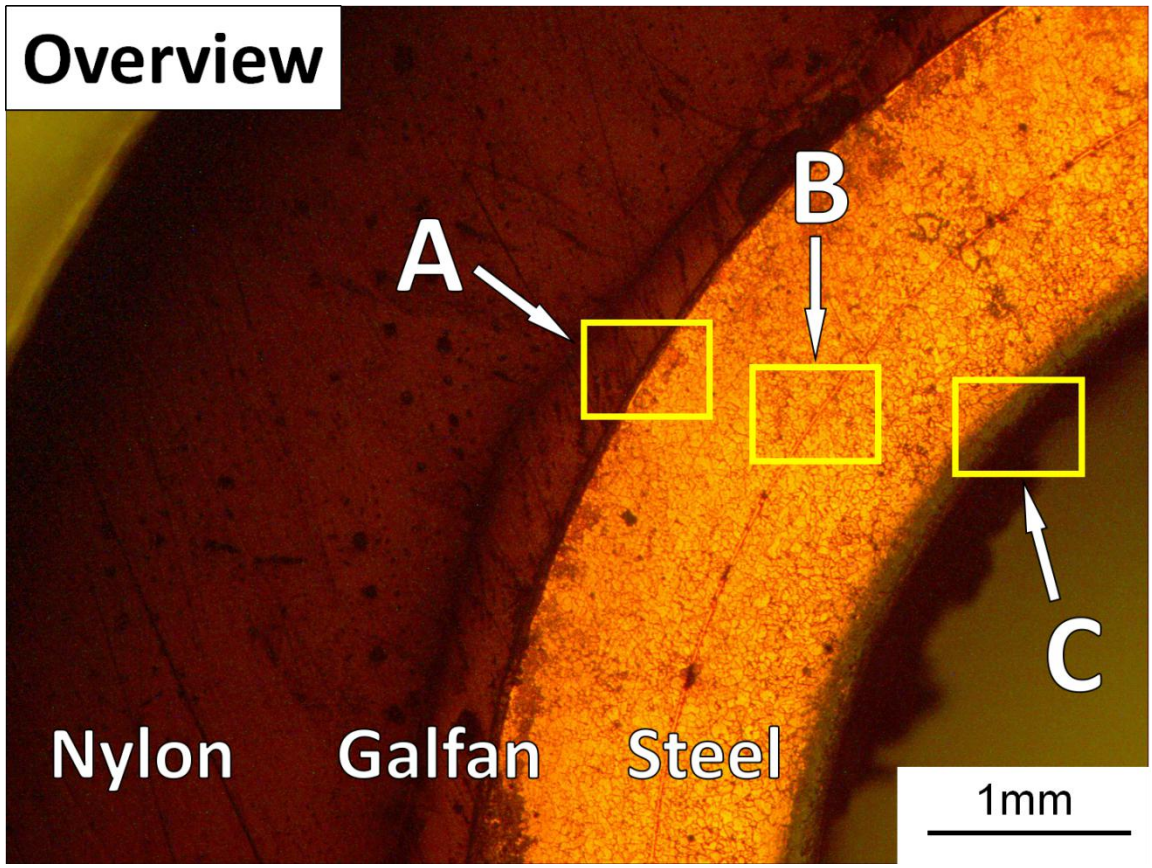

(a)

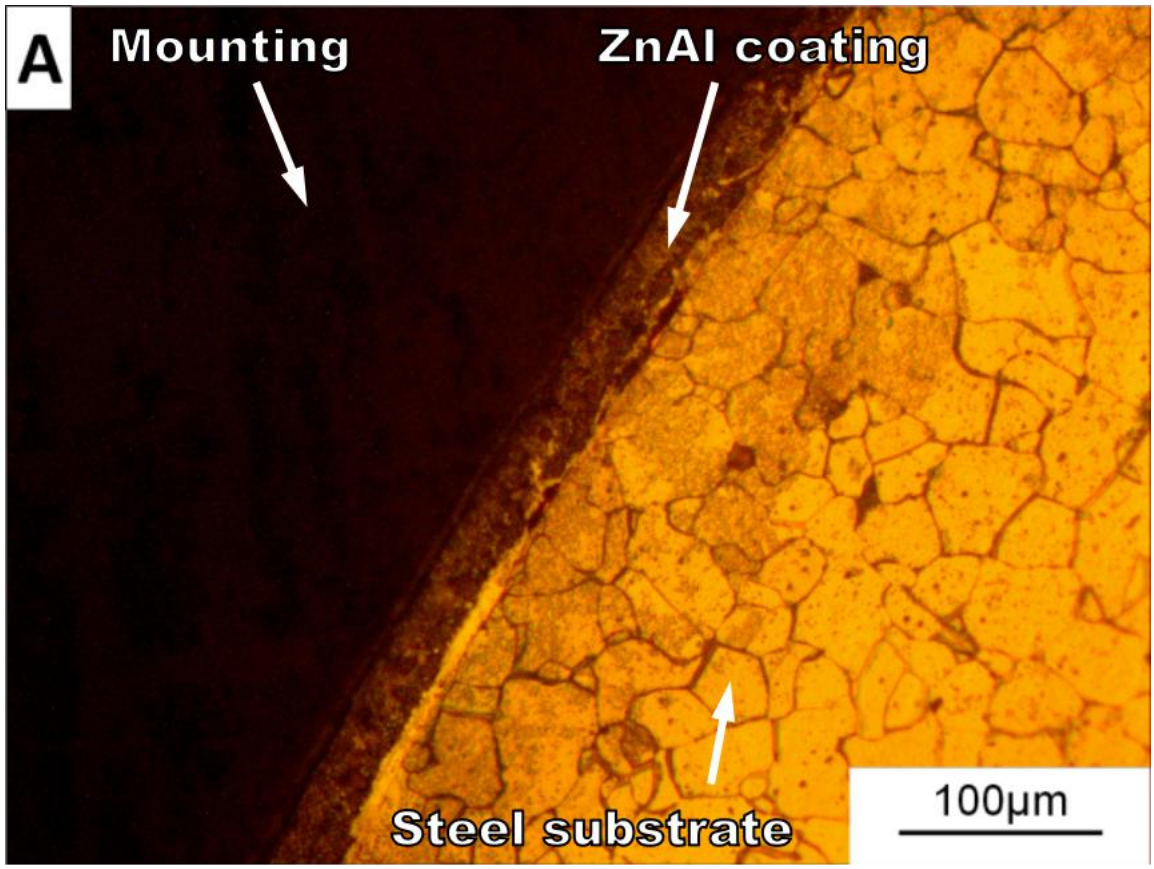

(b)

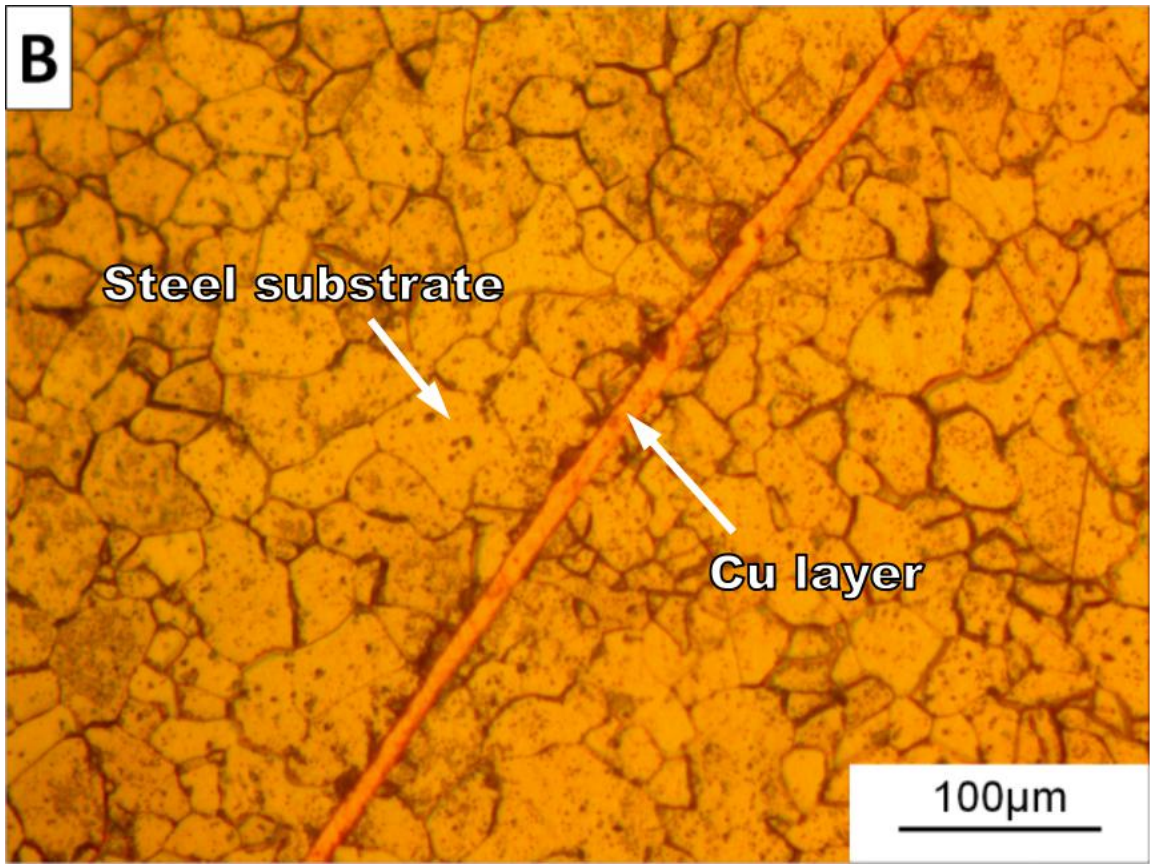

(c)

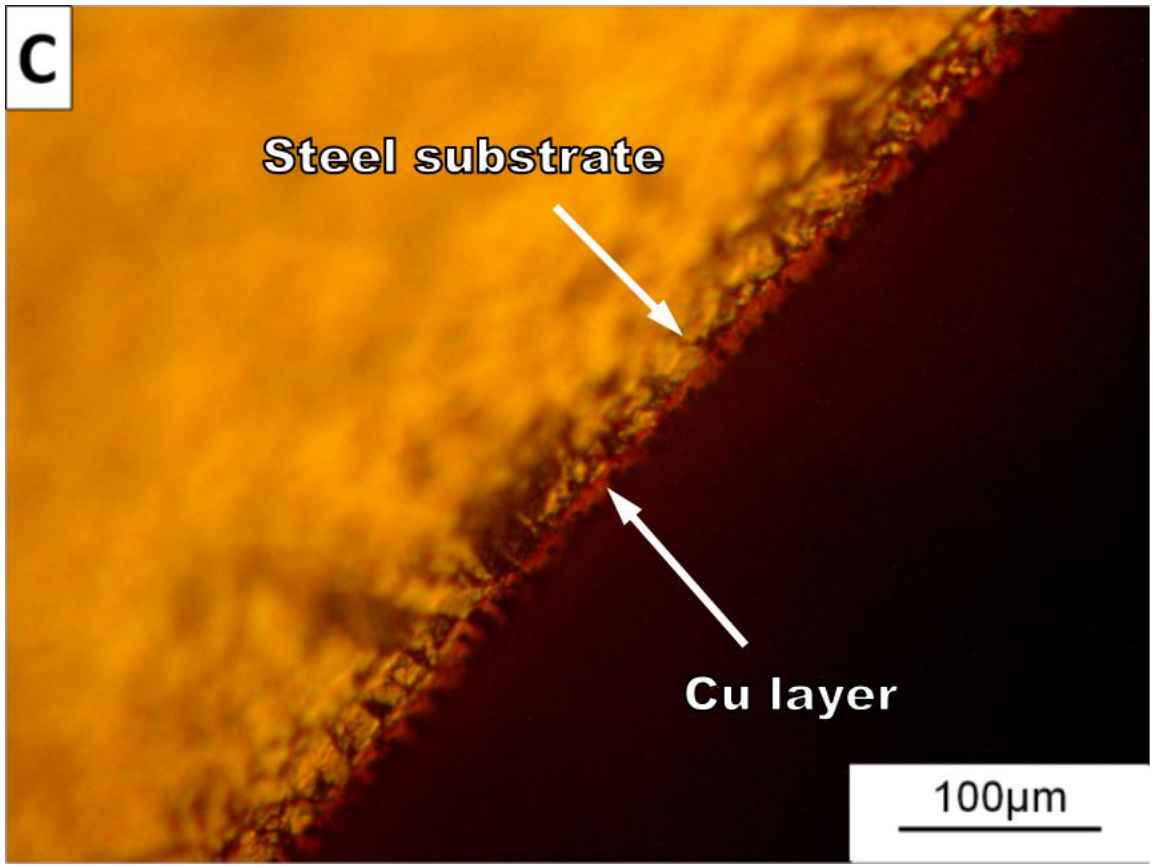

(d)

Figure A. 1 OM pictures of the intersection of a commercial brake line showing the microstructure of (a) overall (b) outer layer (c) middle layer and (d) inner layer.

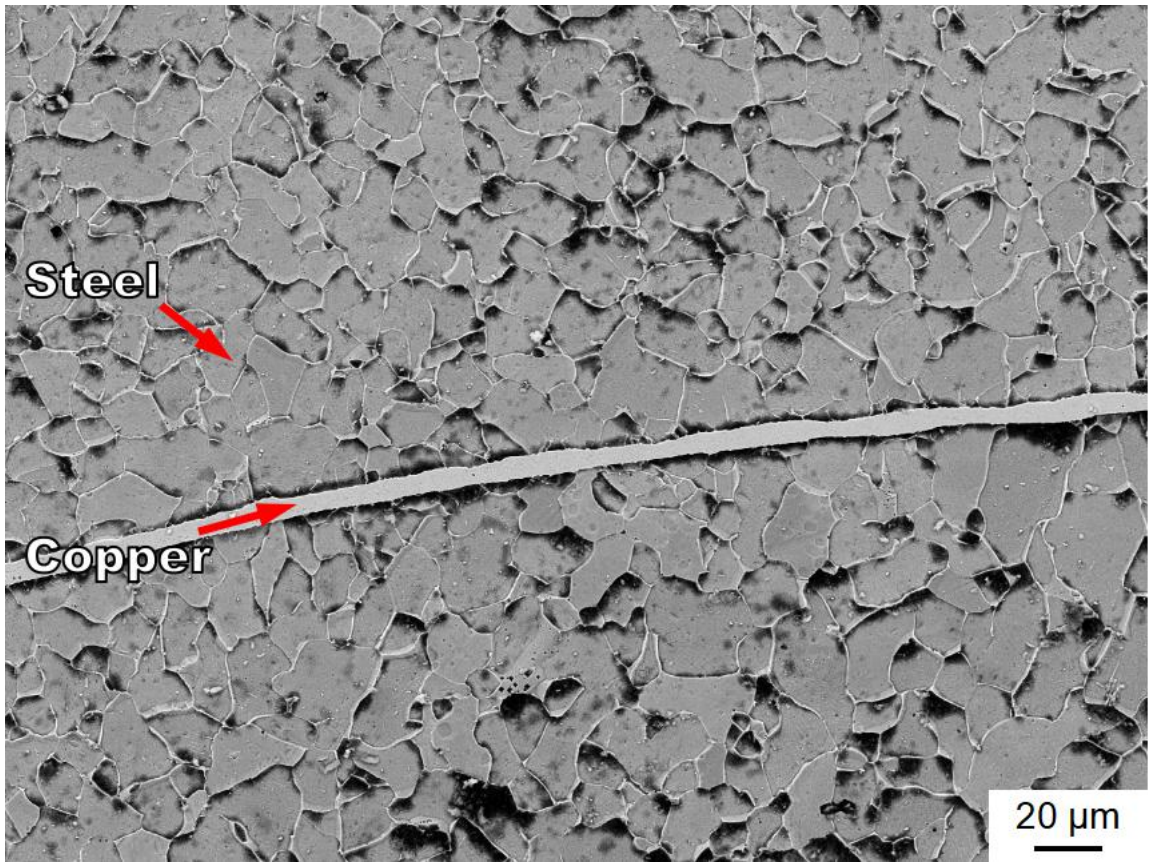

(a)

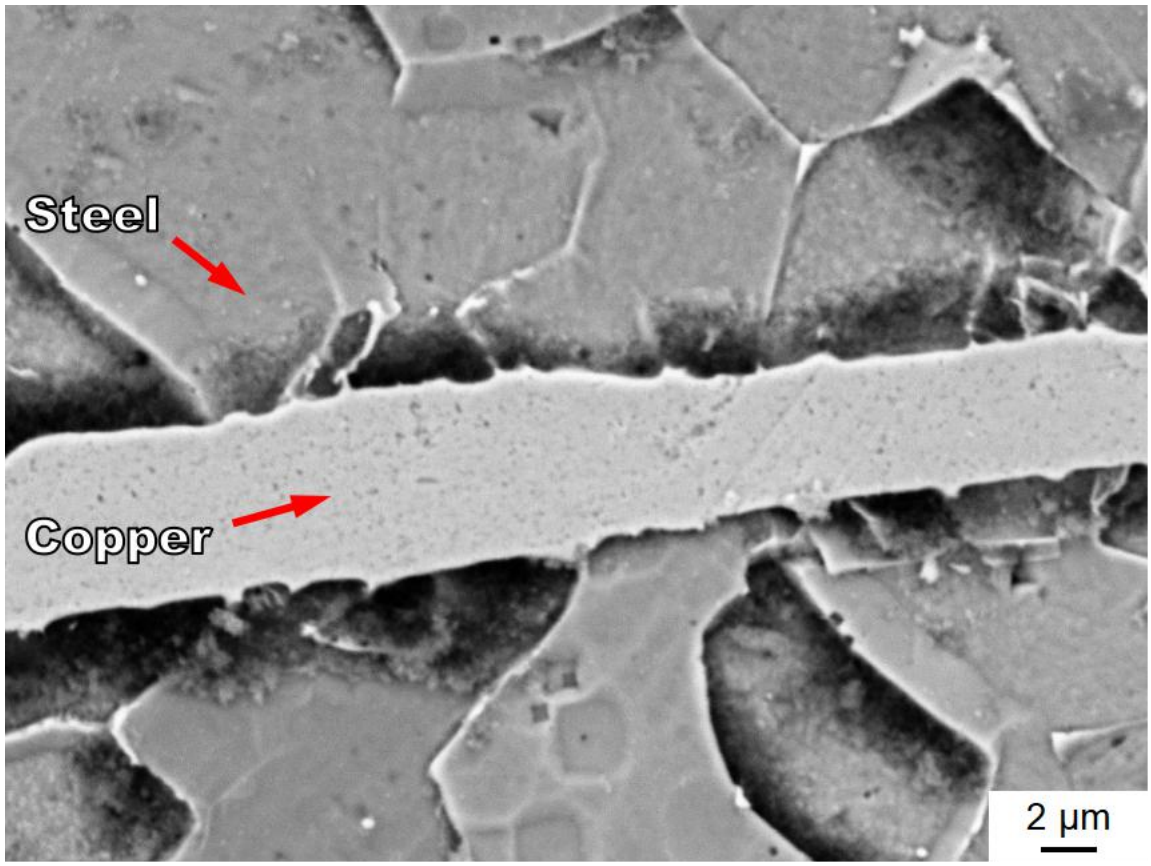

(b)

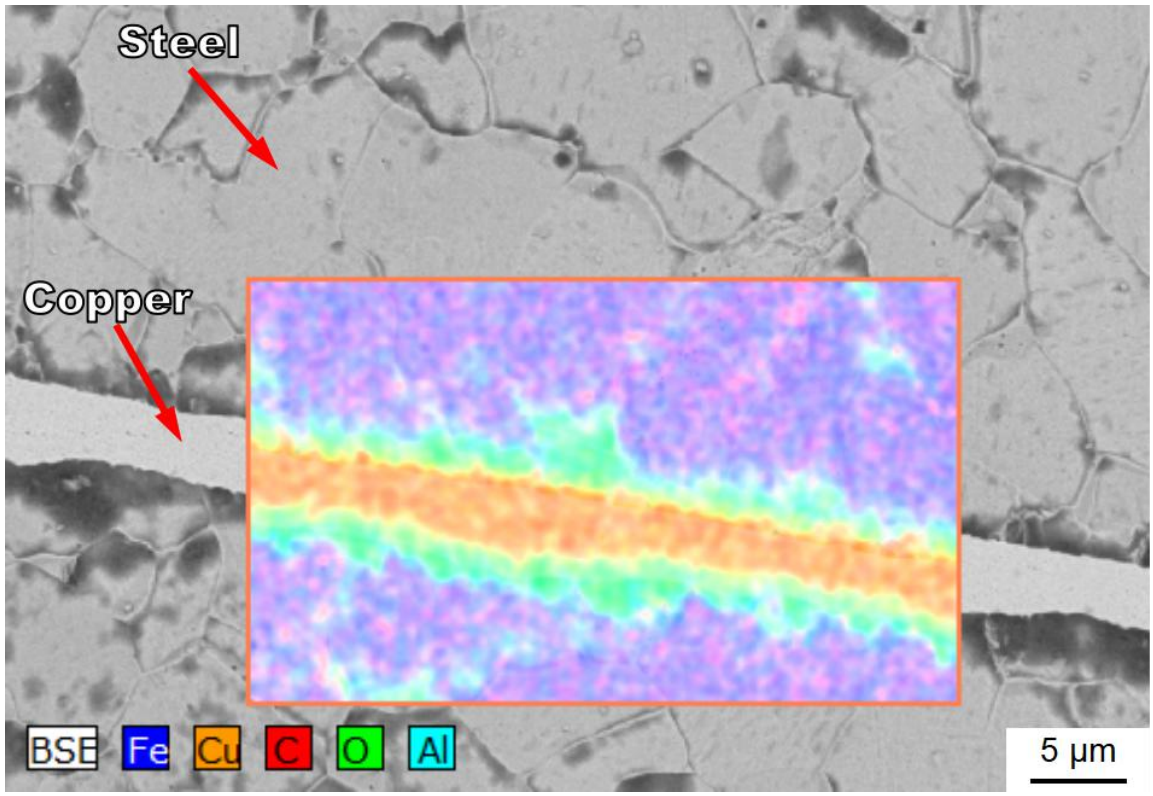
Steel
Copper
BSE
Fe
Cu
C
O
Al
5 µm

(c)

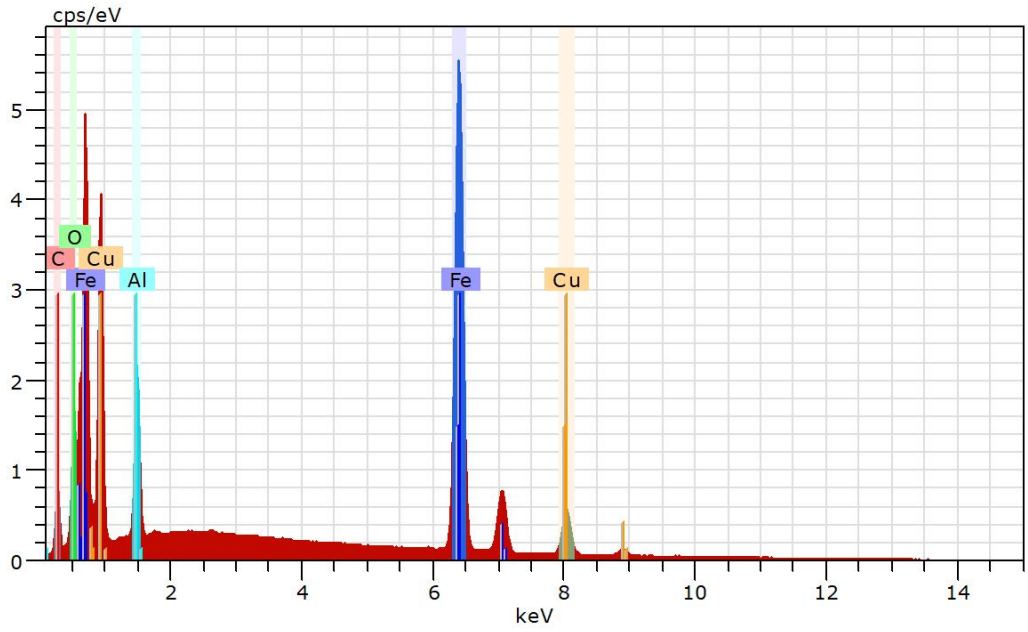
cps/eV
5
4
3
2
1
0
O
C
Cu
Fe
Al
Fe
Cu
2
4
6
8
10
12
14
keV

(d)

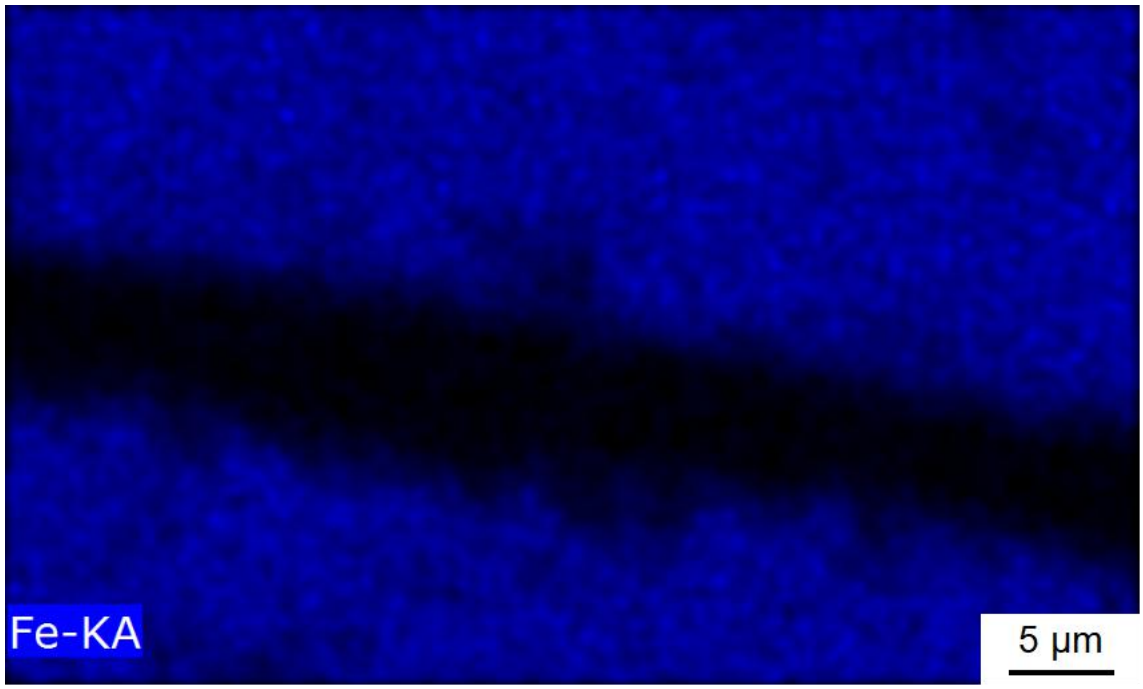

(e)

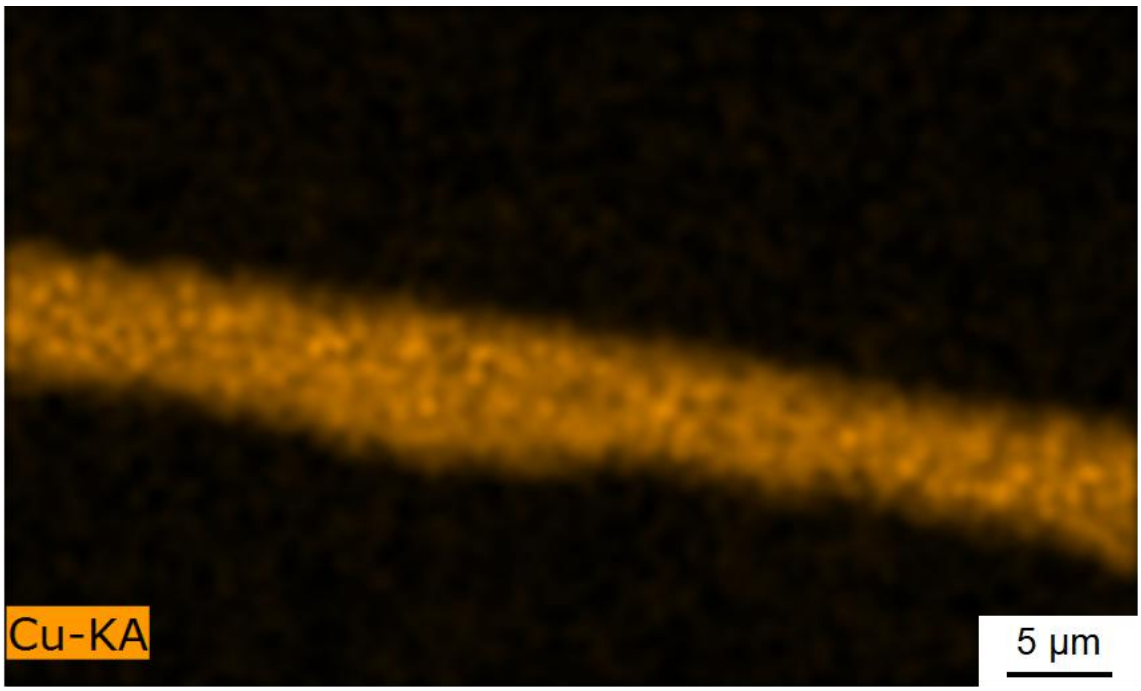

(f)

Figure A. 2 (a) low magnification and (b) high magnification SEM picture (c) element distribution (d) EDS spectrum of the scanned area (e) distribution diagram of Fe (f)

distribution diagram of Cu of copper layer in the middle commercial brake line showing the sample was produced through double rolling.

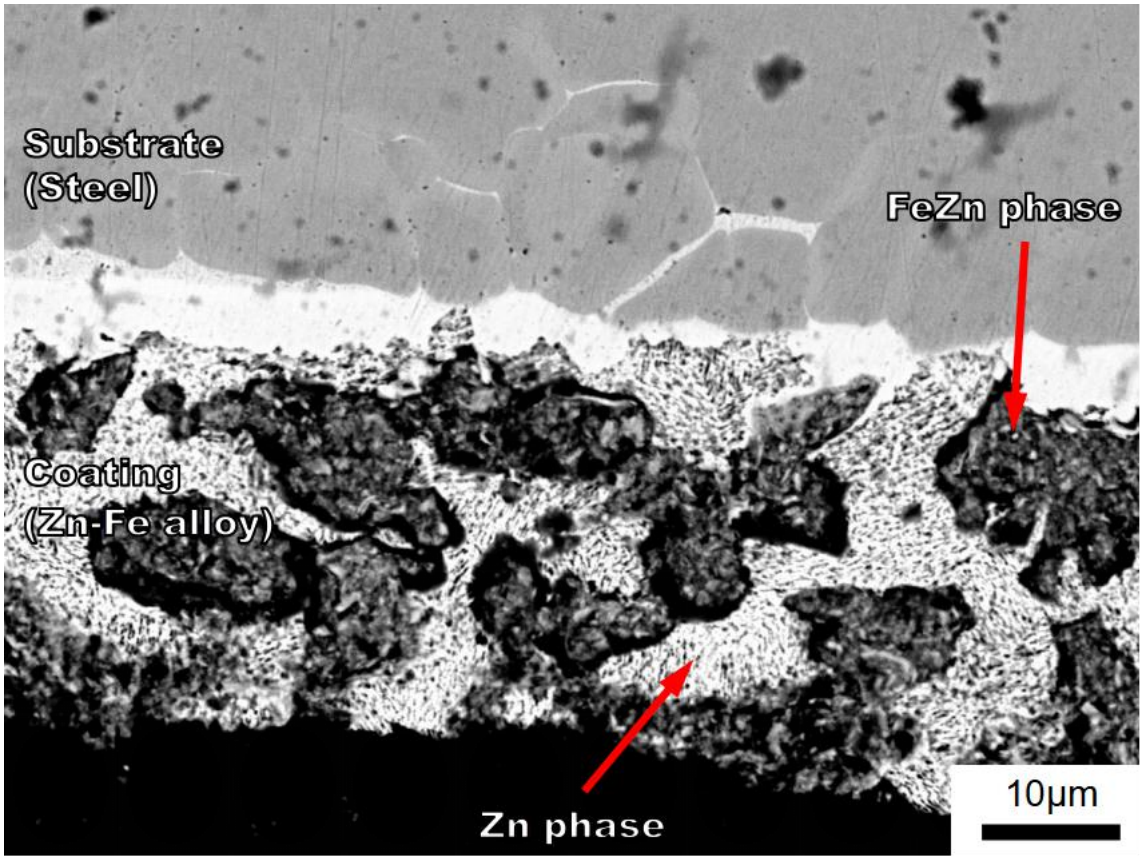

(a)

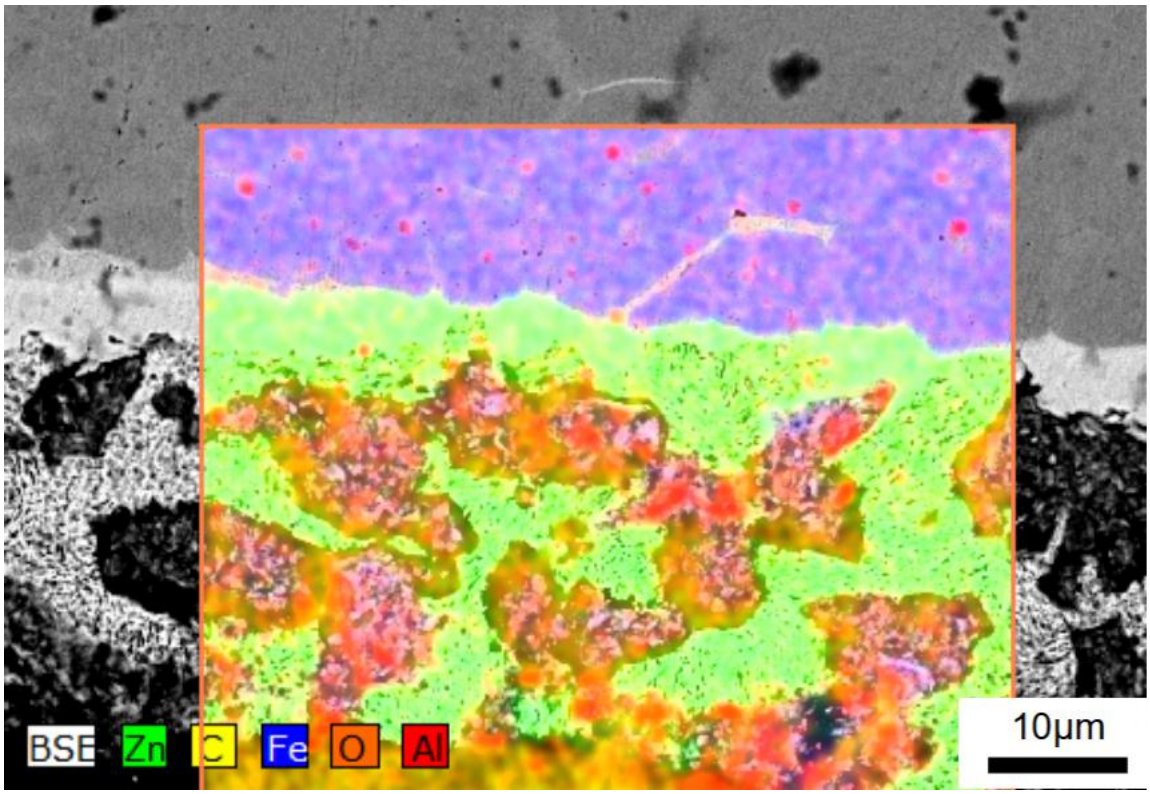
BSE
Zn
C
Fe
O
Al
10μm

(b)

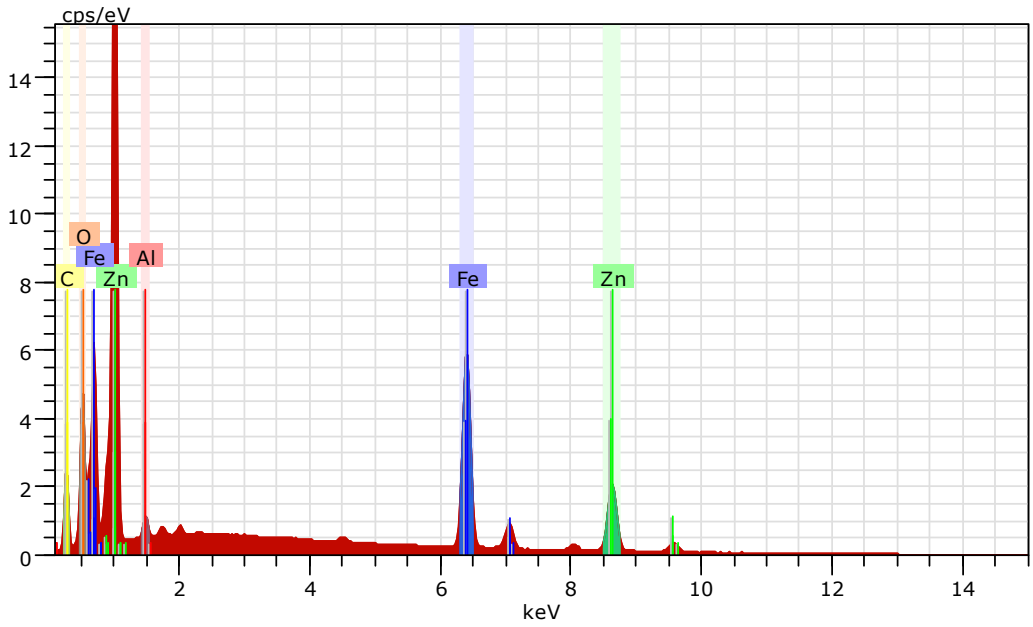
cps/eV
14
12
10
8
6
4
2
0
O
Fe
Al
C
Zn
Fe
Zn
2
4
6
8
10
12
14
keV

(c)

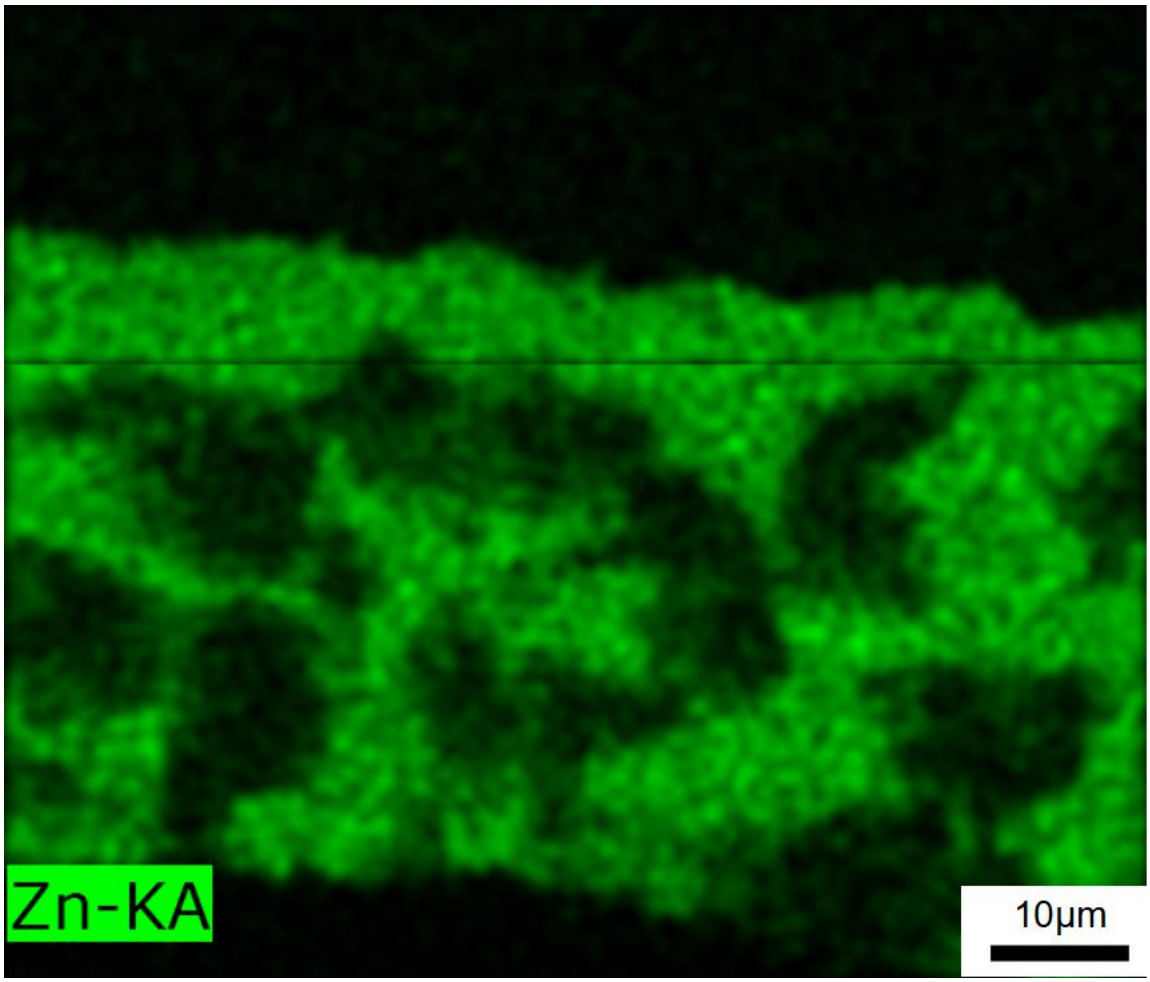

(d)

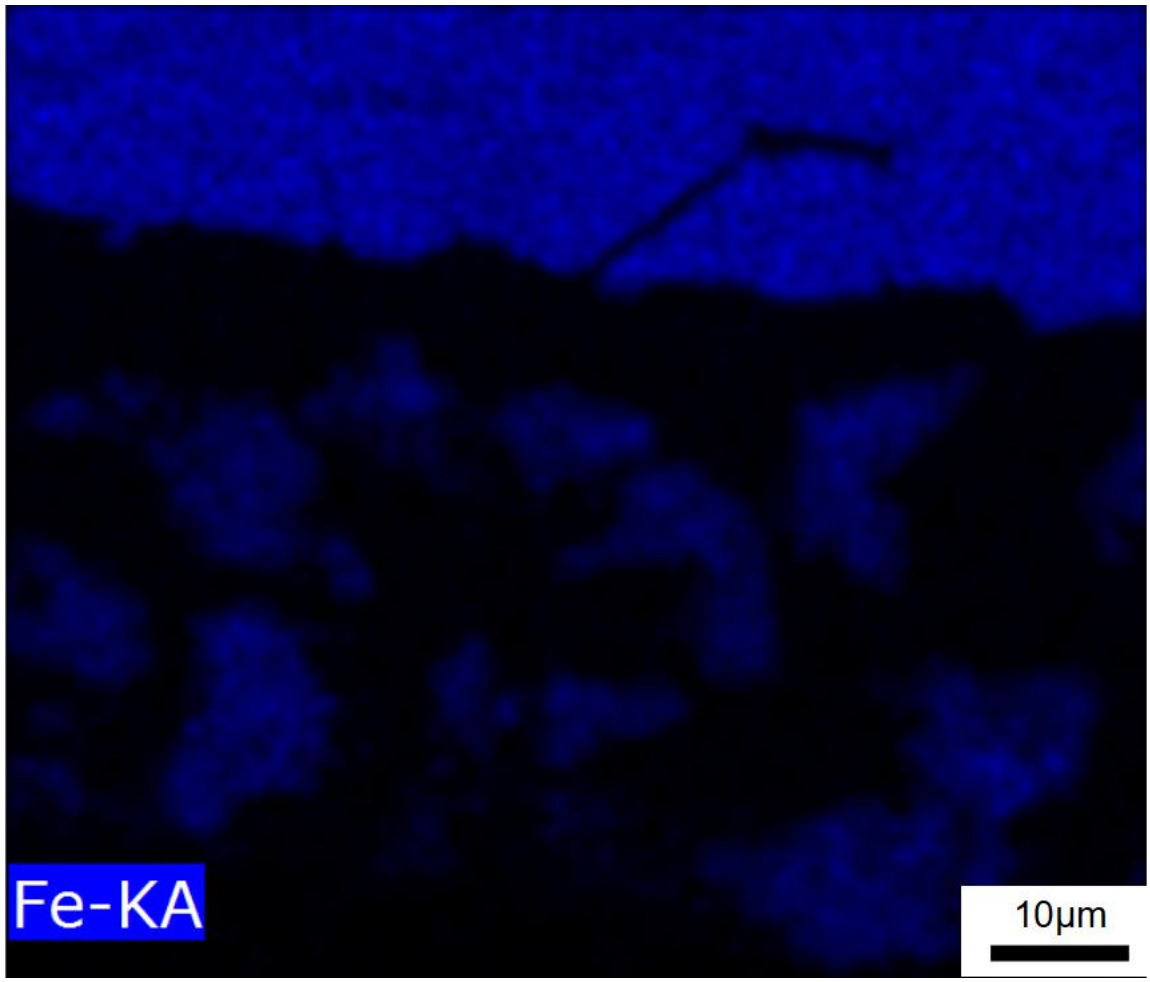

(e)

Figure A. 3 (a) SEM micrograph (b) element distribution (c) EDS spectrum of scanned area (d) distribution of Zn (e) distribution of Fe of the brake line from Toyota Corolla 2017.

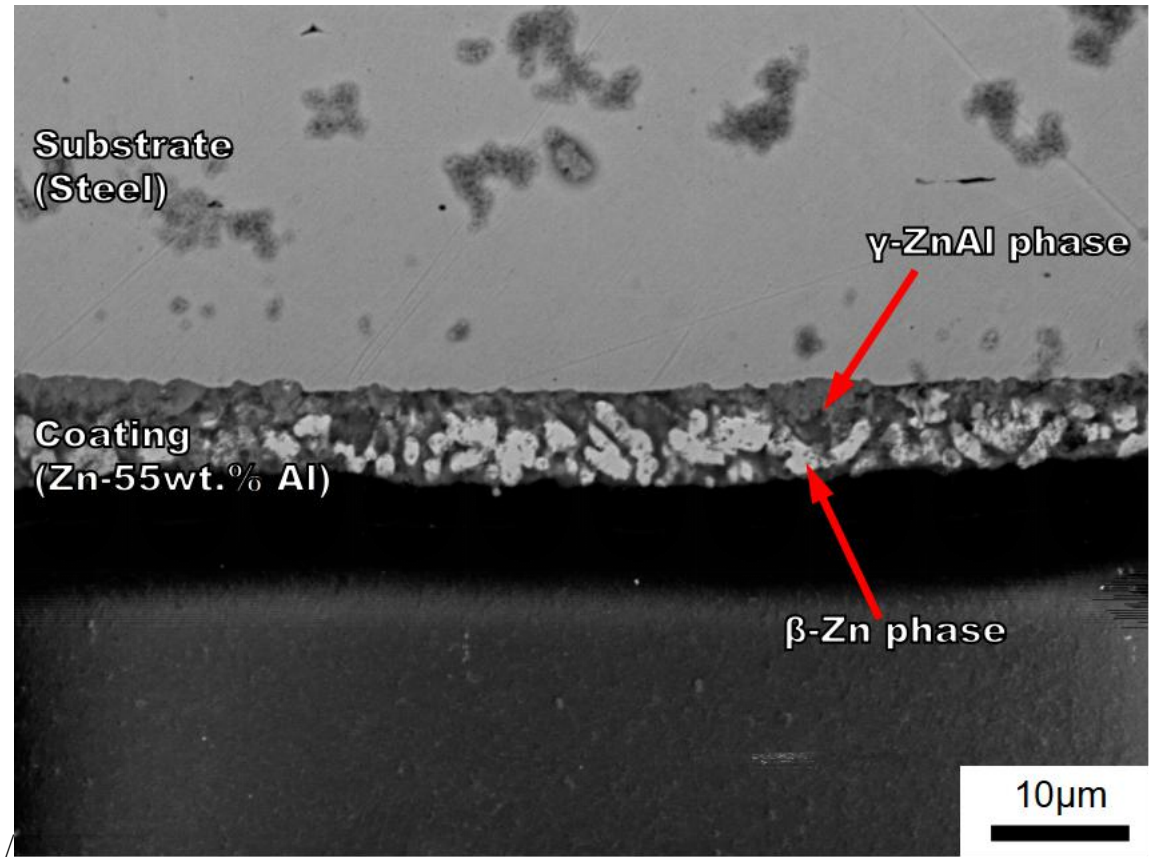
Substrate
(Steel)
γ-ZnAl phase
Coating
(Zn-55wt.% Al)
β-Zn phase
10μm

(a)

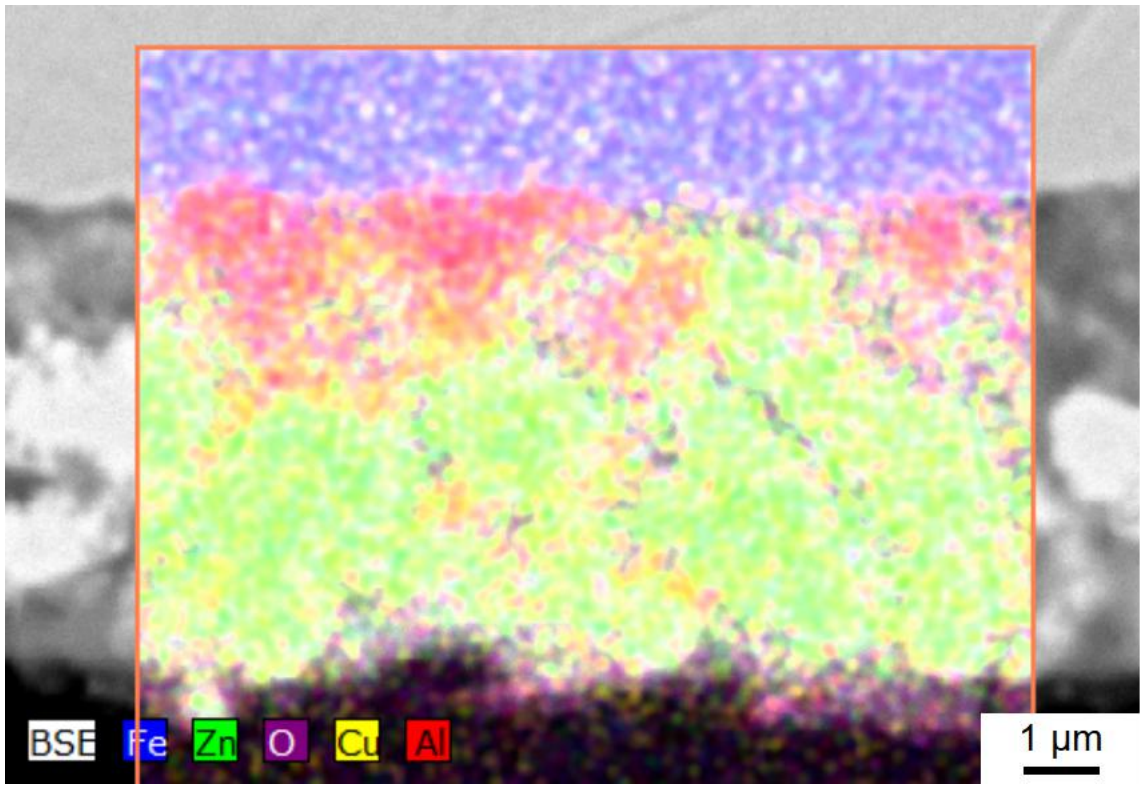
BSE
Fe
Zn
O
Cu
Al
1 µm

(b)

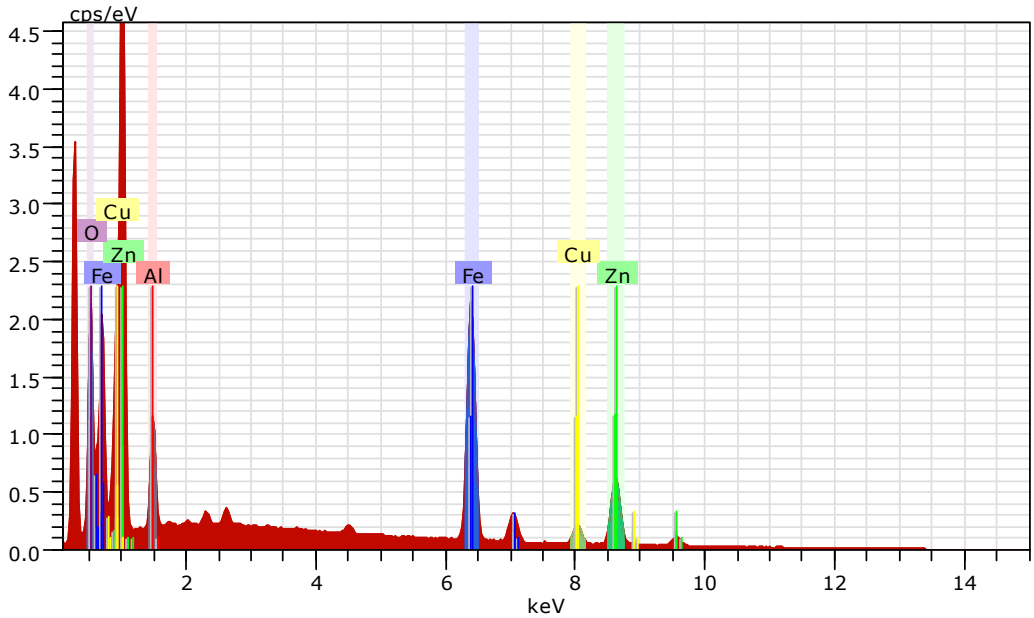
cps/eV
4.5
4.0
3.5
3.0
2.5
2.0
1.5
1.0
0.5
0.0
Cu
O
Zn
Fe
Al
Fe
Cu
Zn
2
4
6
8
10
12
14
keV

(c)

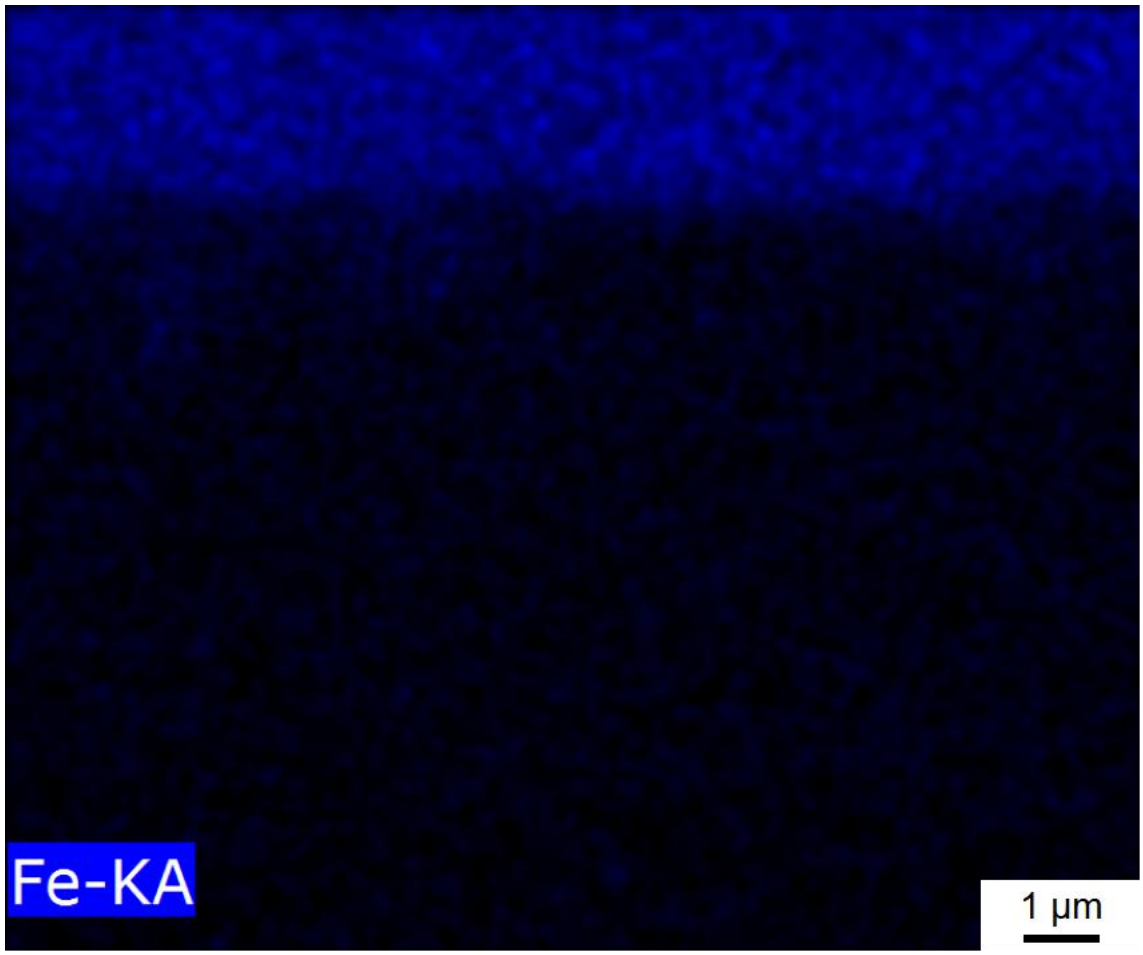

(d)

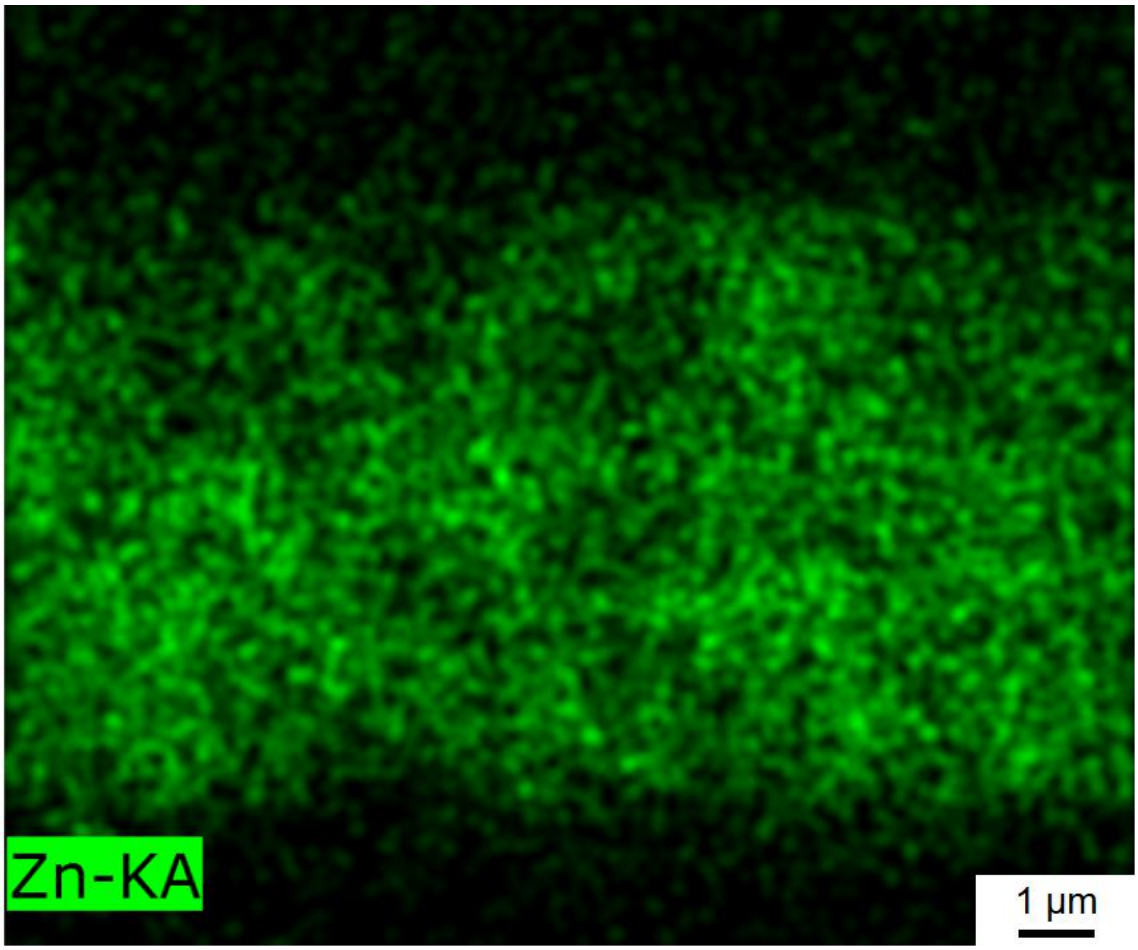

(e)

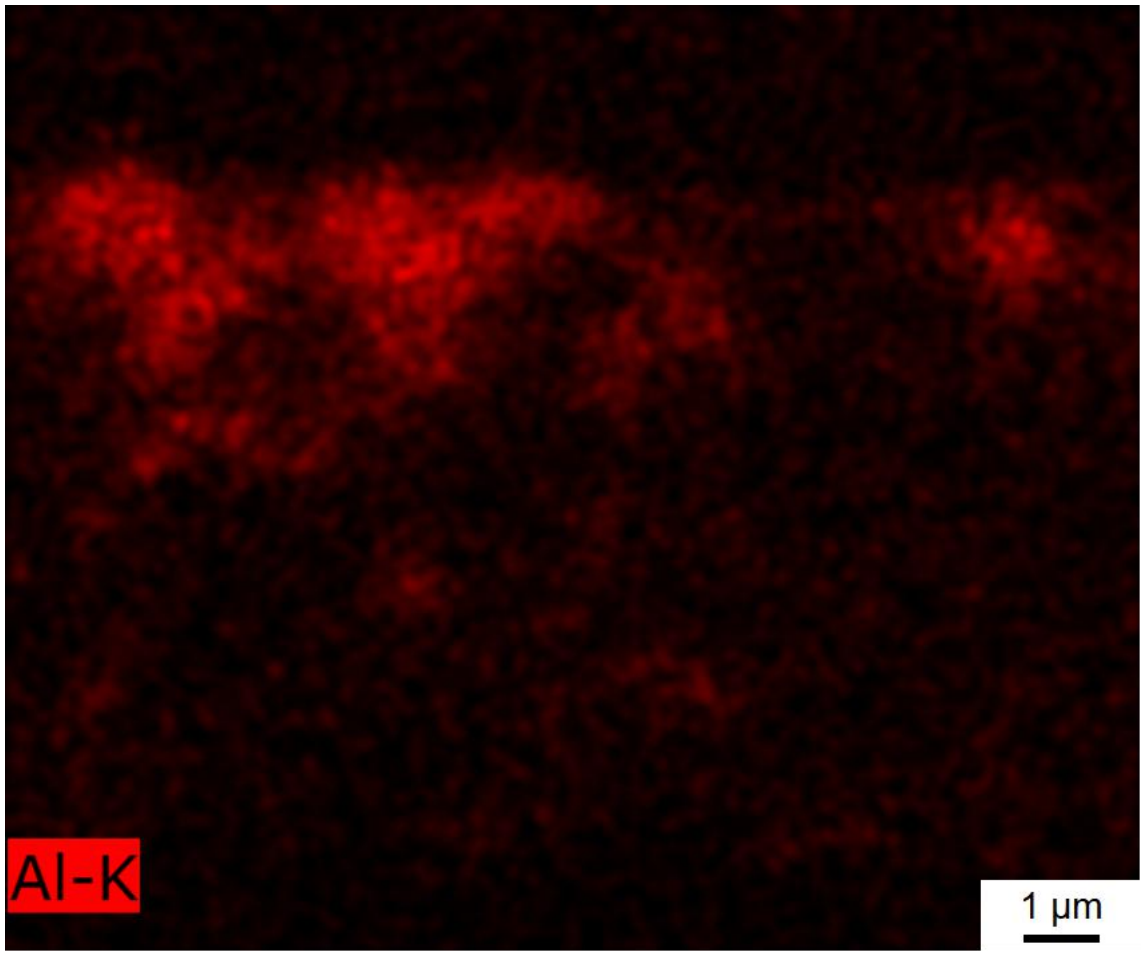

(f)

Figure A. 4 (a) SEM micrograph (b) element distribution (c) EDS spectrum of scanned area (d) distribution of Fe (e) distribution of Zn (f) distribution of Al of the brake line from Honda Civic 2017.

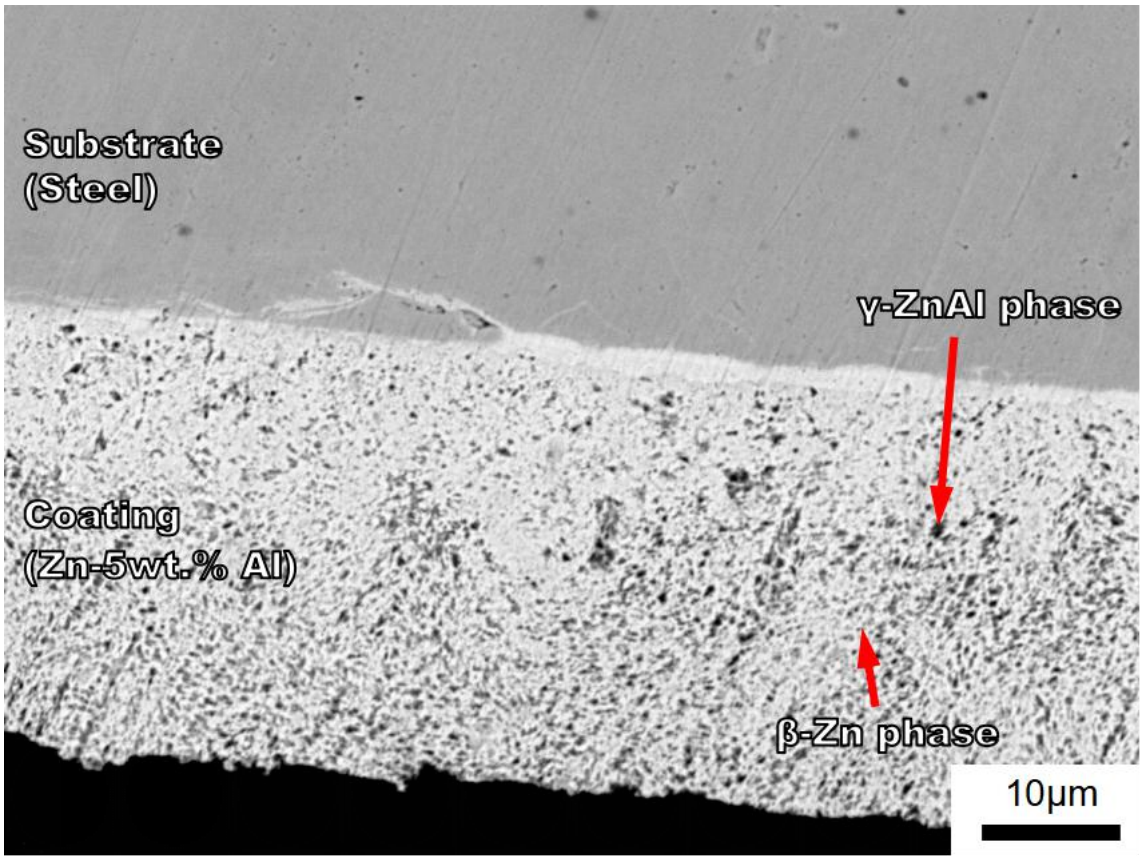
Substrate
(Steel)
γ-ZnAl phase
Coating
(Zn-5wt.% Al)
β-Zn phase
10μm

(a)

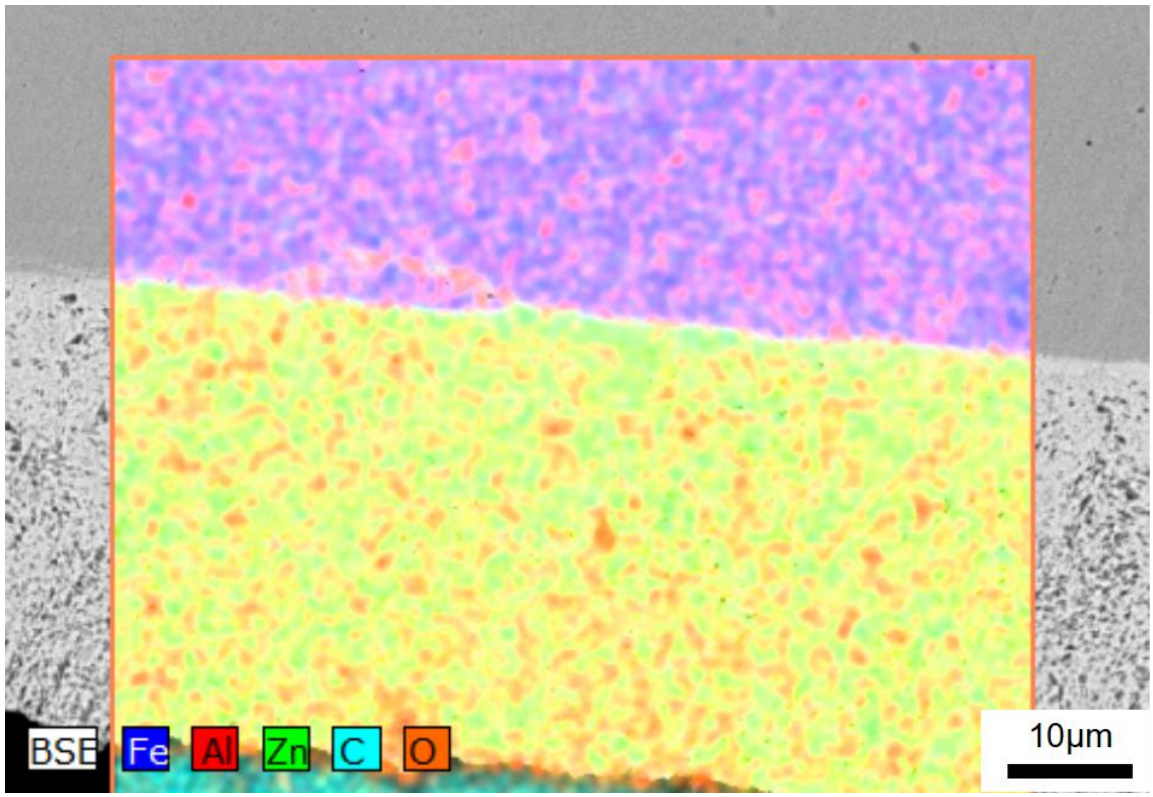
BSE
Fe
Al
Zn
C
O
10µm

(b)

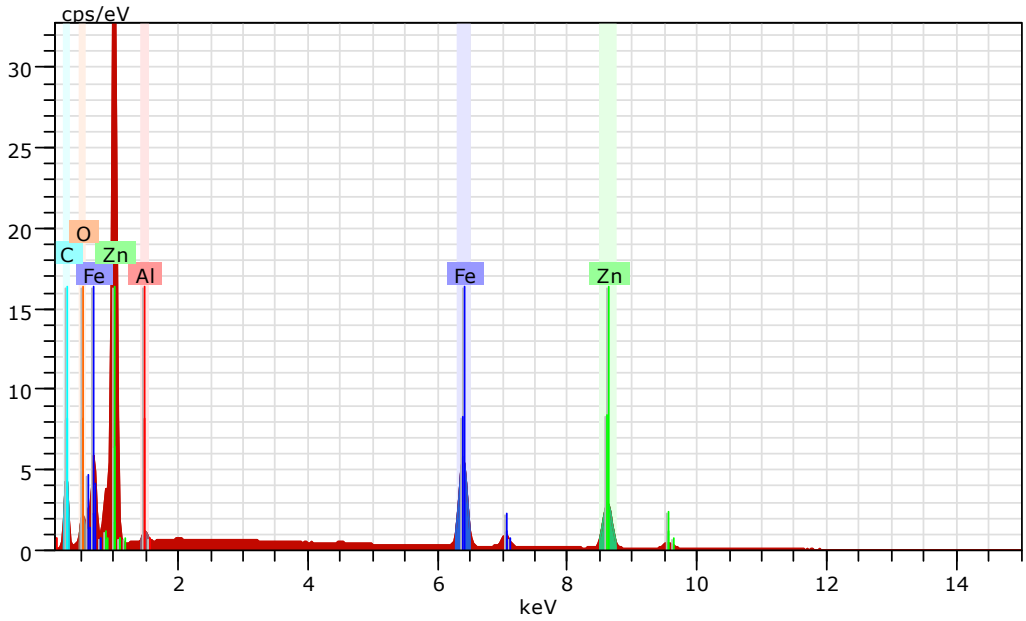
cps/eV
30
25
20
15
10
5
0
O
C
Zn
Fe
Al
Fe
Zn
2
4
6
8
10
12
14
keV

(c)

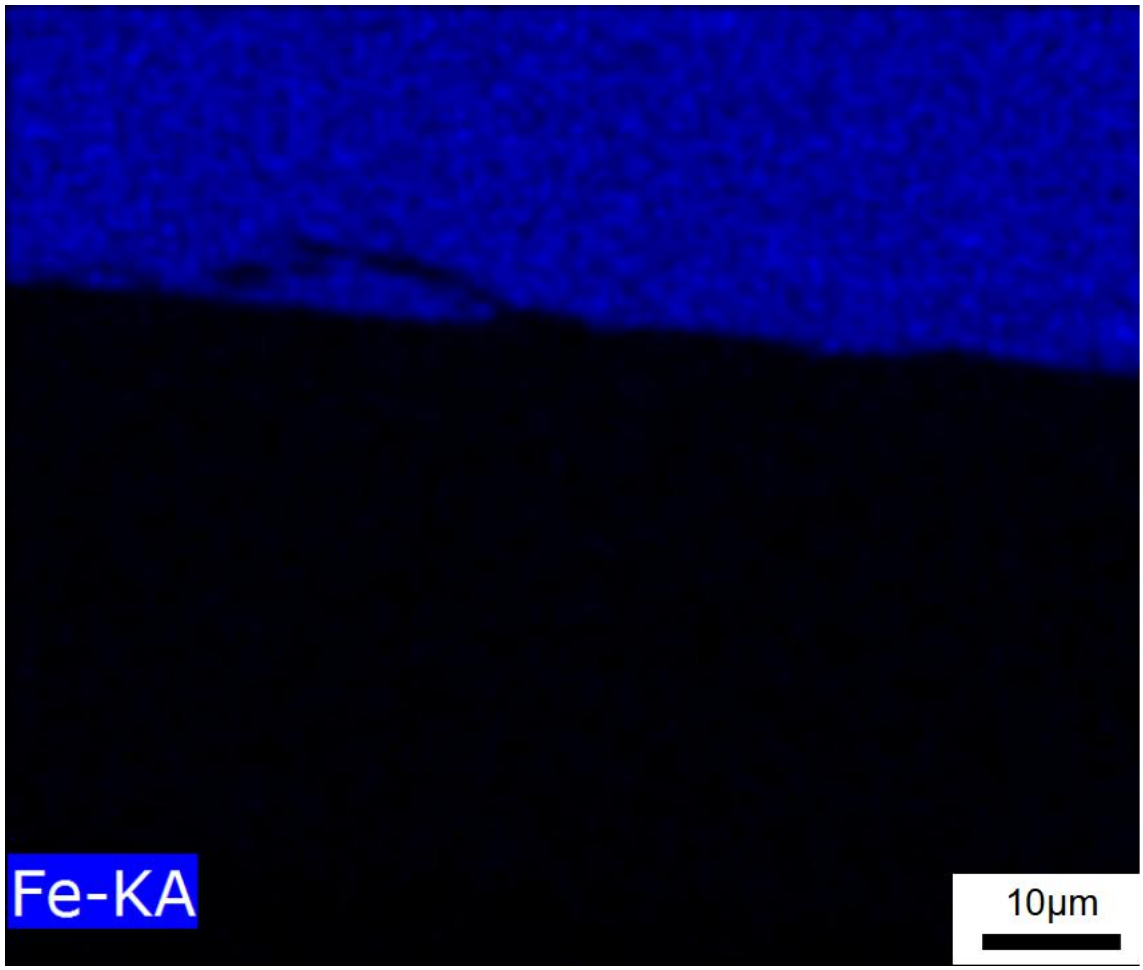

(d)

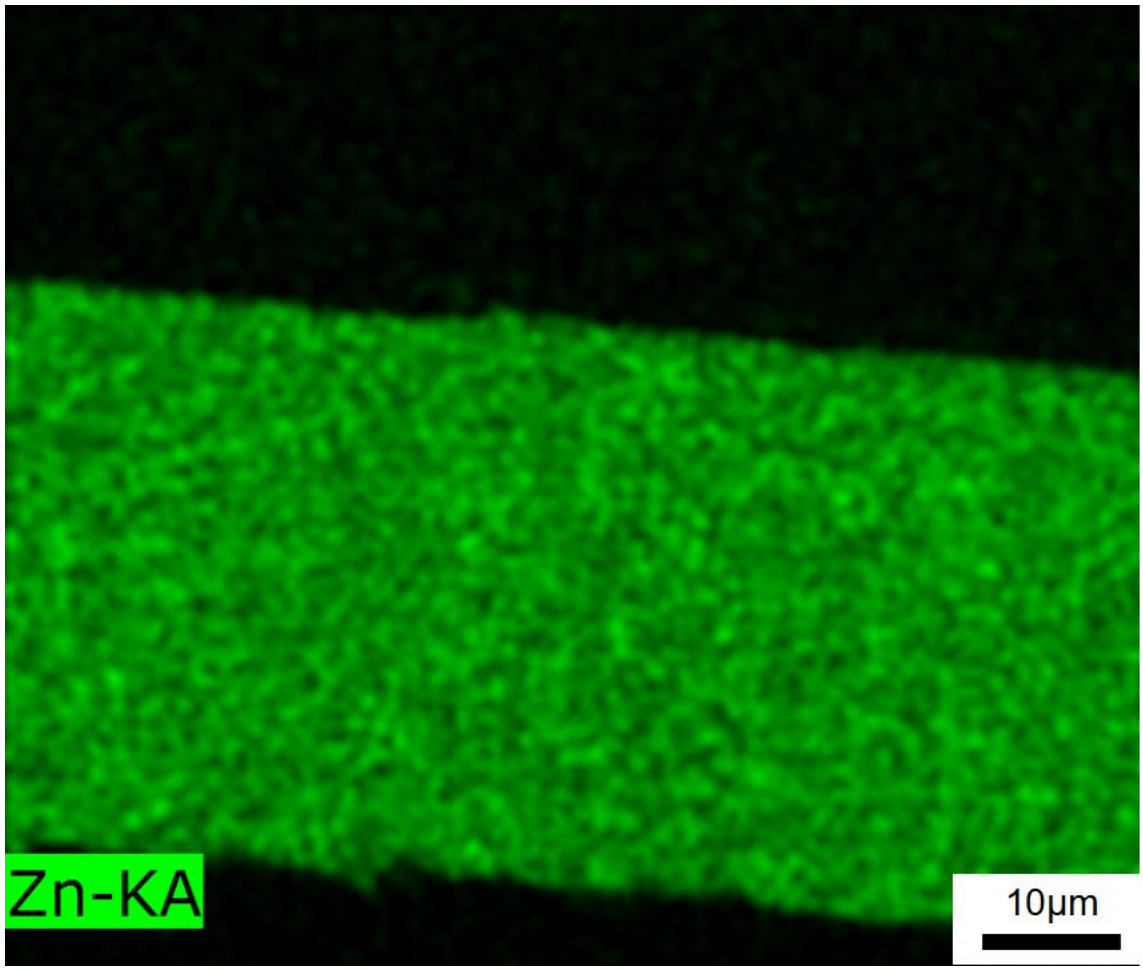

(e)

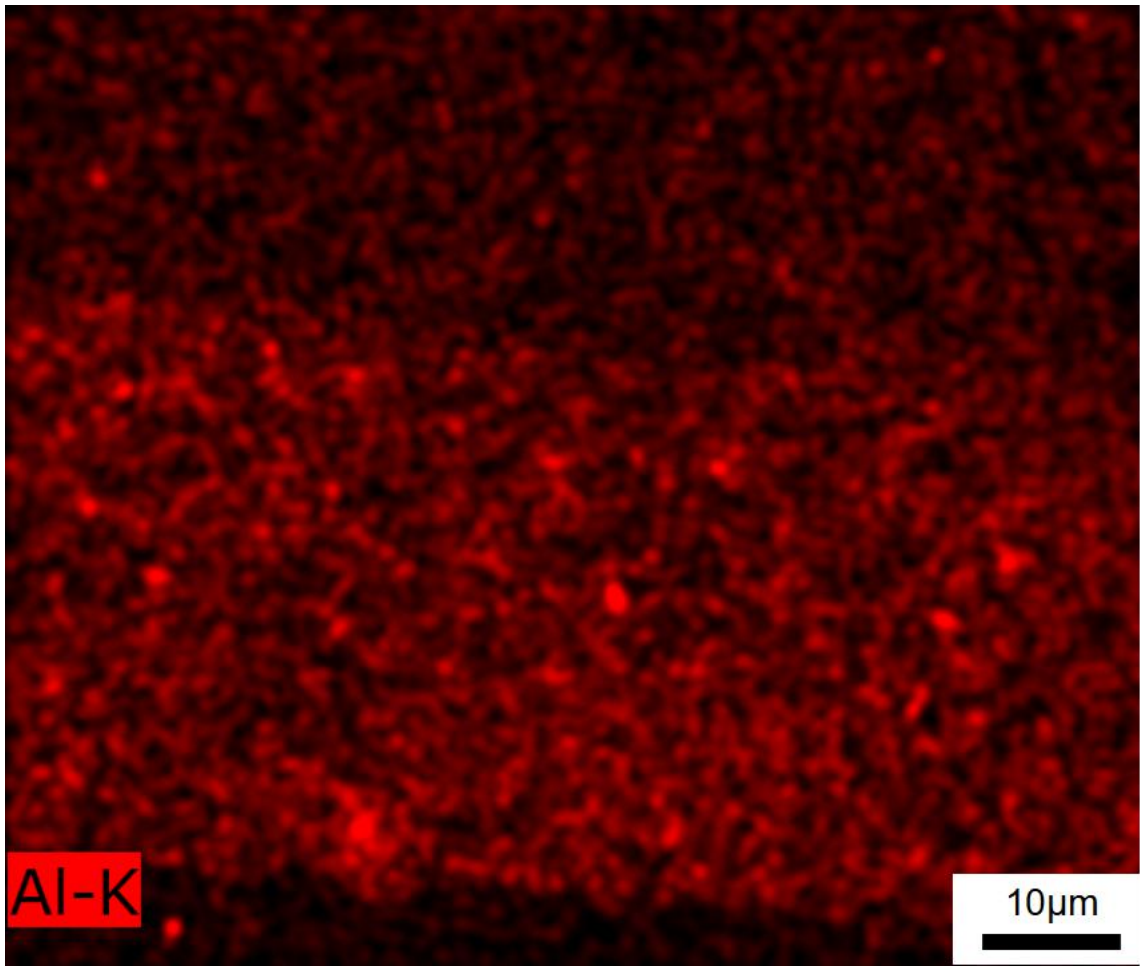

(f)

Figure A. 5 (a) SEM micrograph (b) element distribution (c) EDS spectrum of scanned area (d) distribution of Fe (e) distribution of Zn (f) distribution of Al of the brake line from Mazda 3 2017.

.

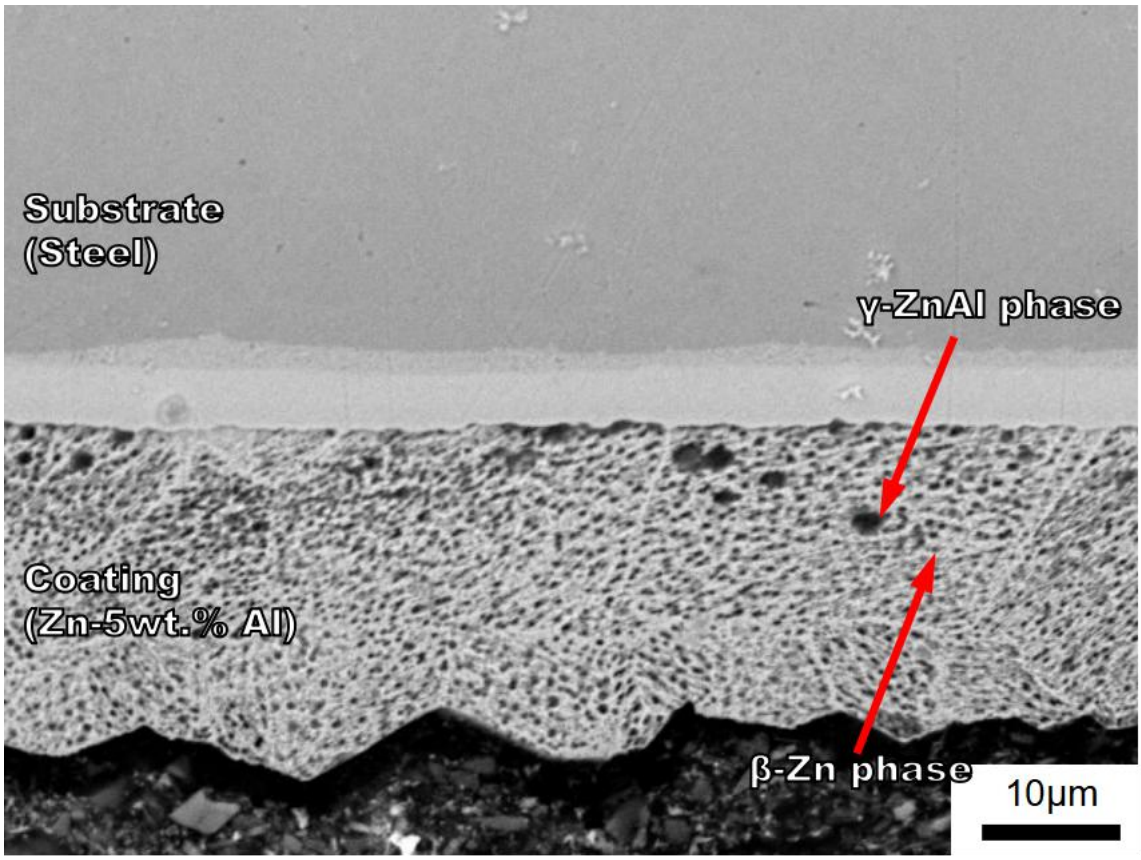
Substrate
(Steel)
γ-ZnAl phase
Coating
(Zn-5wt.% Al)
β-Zn phase
10μm

(a)

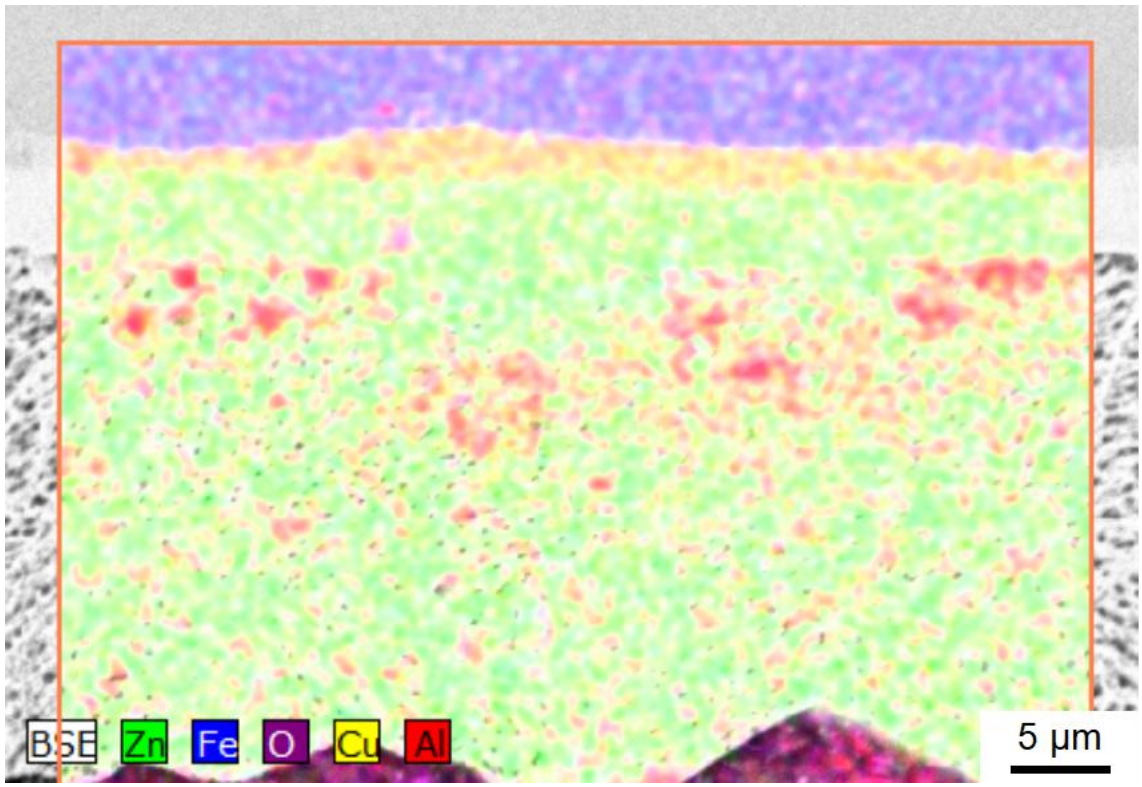
BSE
Zn
Fe
O
Cu
Al
5 µm

(b)

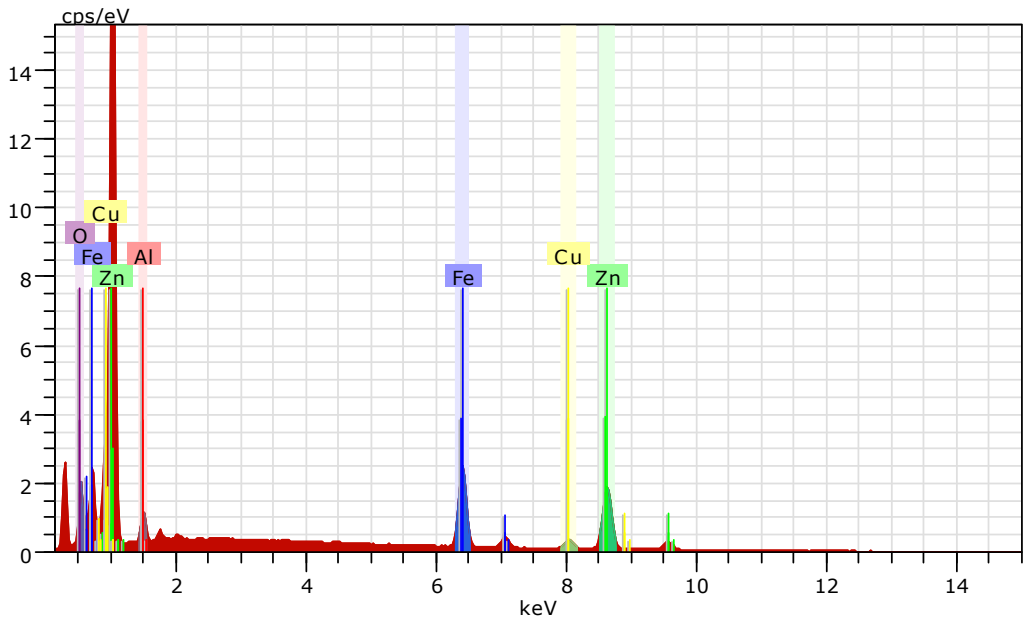
cps/eV
14
12
10
8
6
4
2
0
Cu
O
Fe
Al
Zn
Fe
Cu
Zn
2
4
6
8
10
12
14
keV

(c)

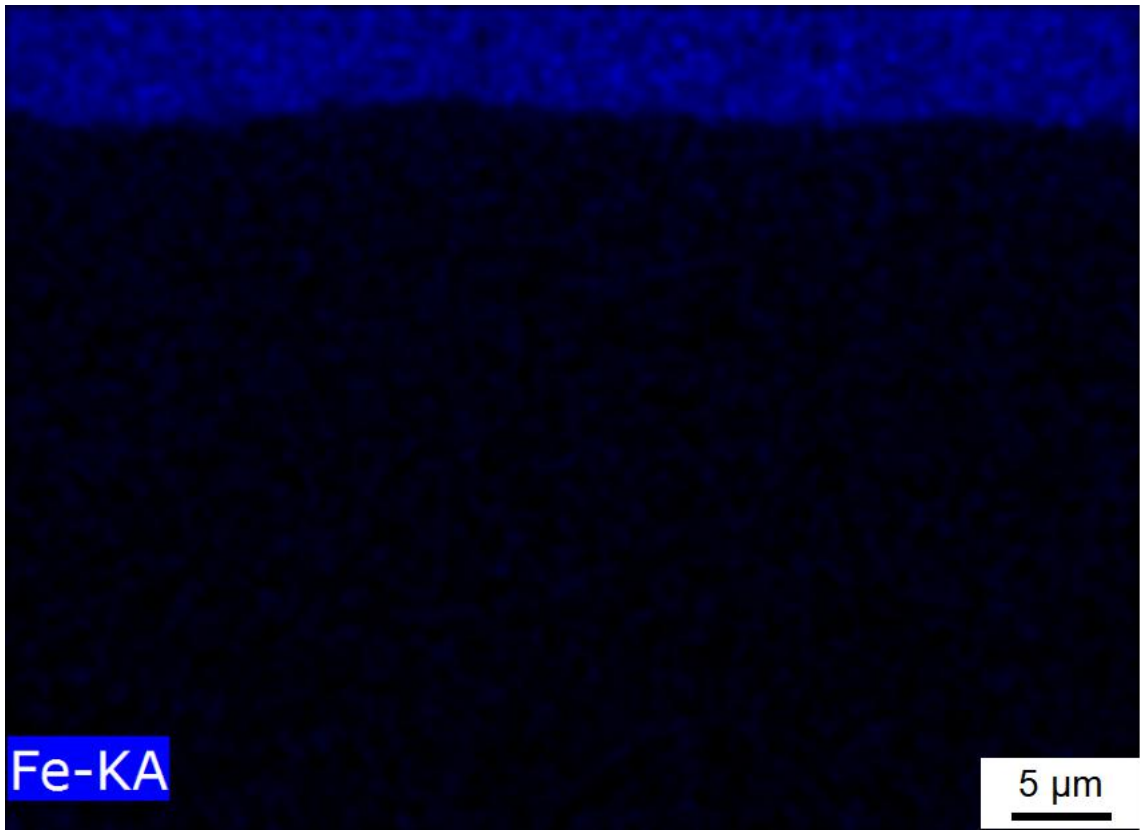

(d)

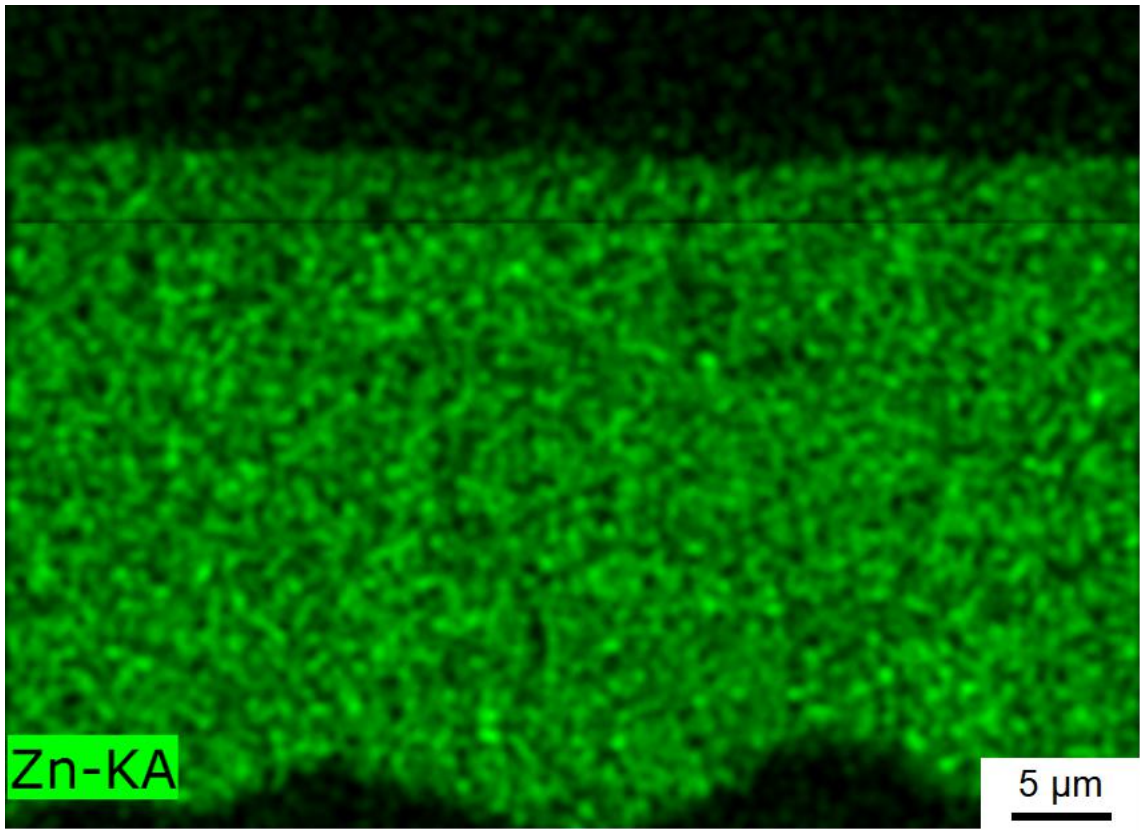

(e)

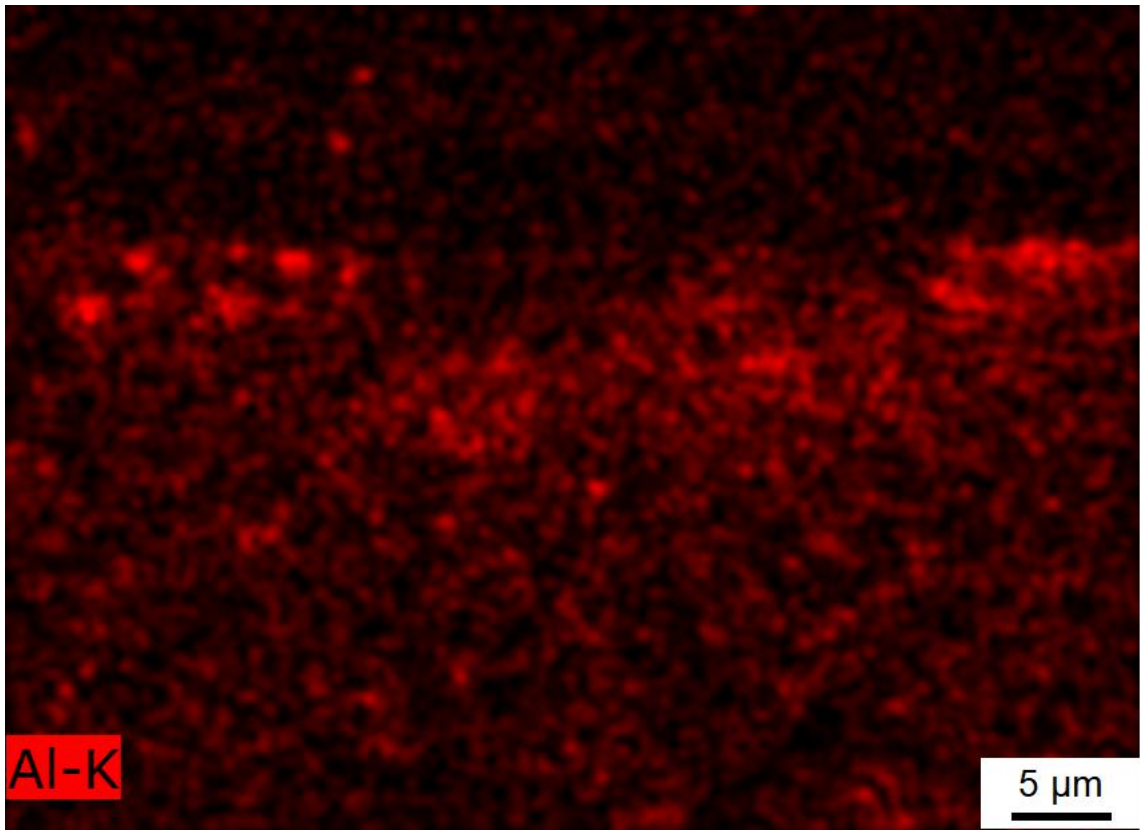

(f)

Figure A. 6 (a) SEM micrograph (b) element distribution (c) EDS spectrum of scanned area (d) distribution of Fe (e) distribution of Zn (f) distribution of Al of the brake line from Nissan Sentra 2017.

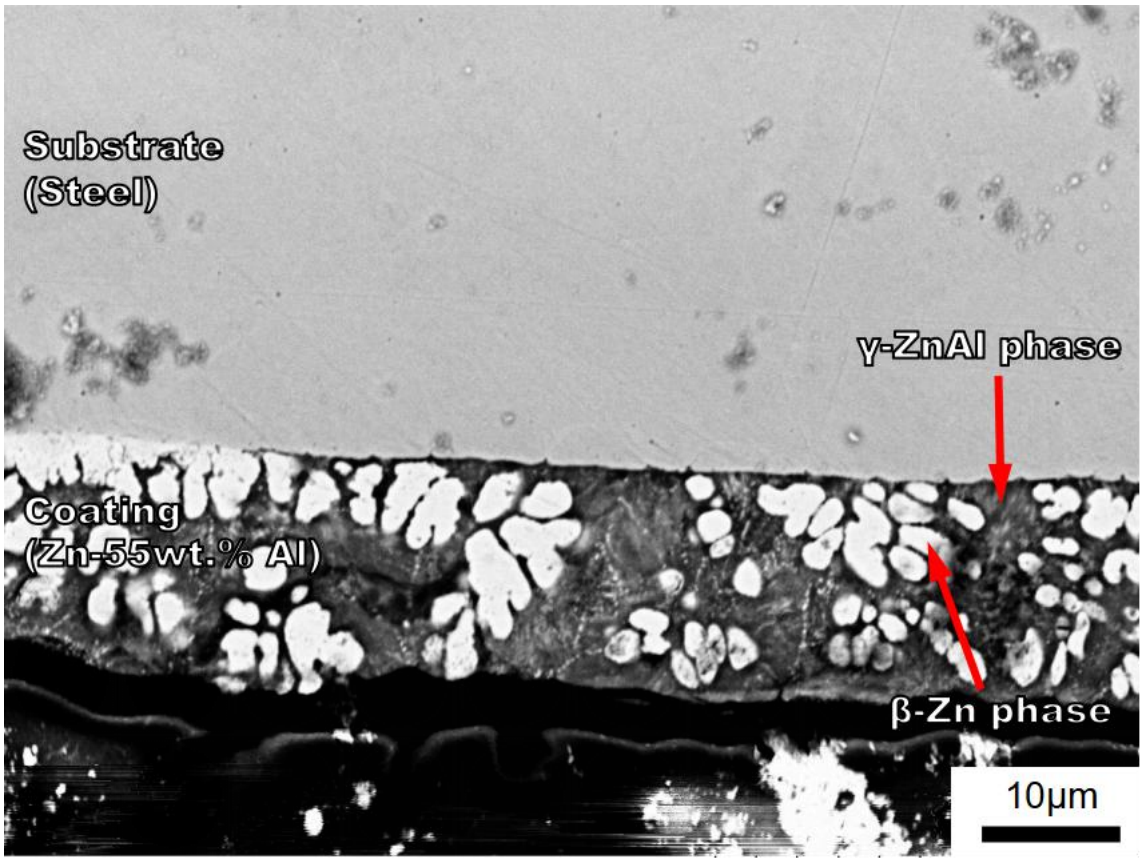
Substrate
(Steel)
γ-ZnAl phase
Coating
(Zn-55wt.% Al)
β-Zn phase
10μm

(a)

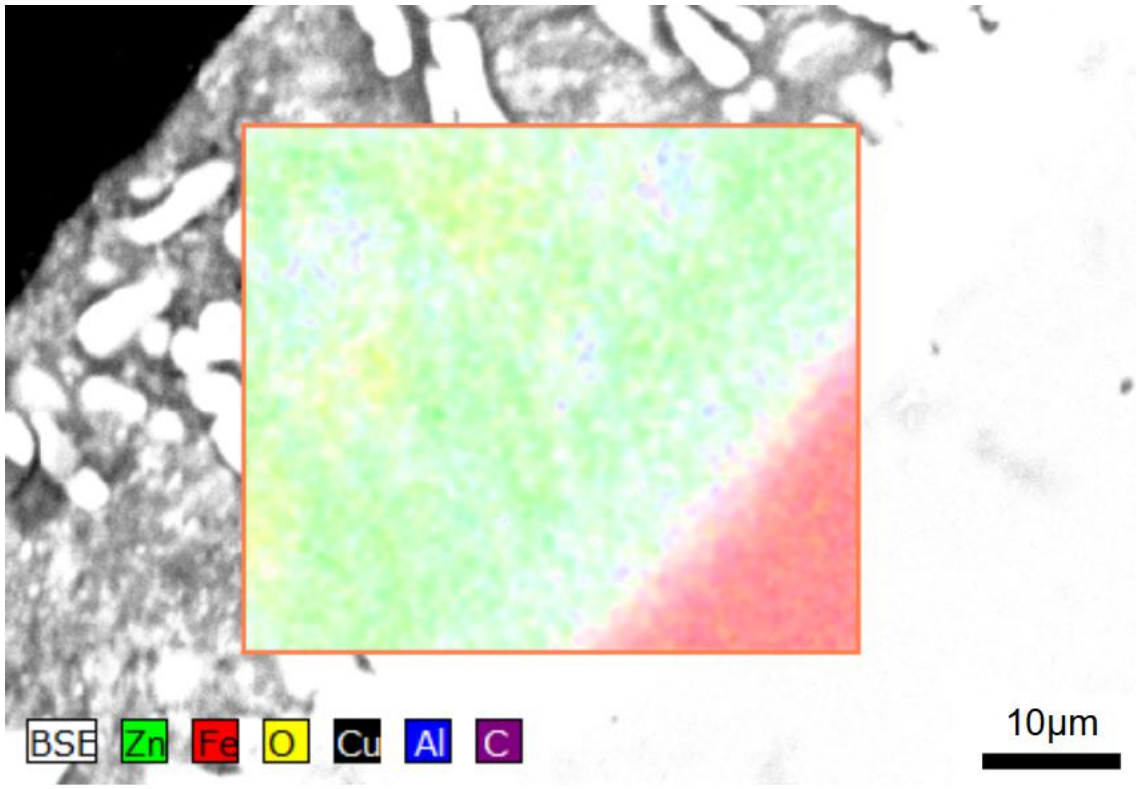
BSE
Zn
Fe
O
Cu
Al
C
10µm

(b)

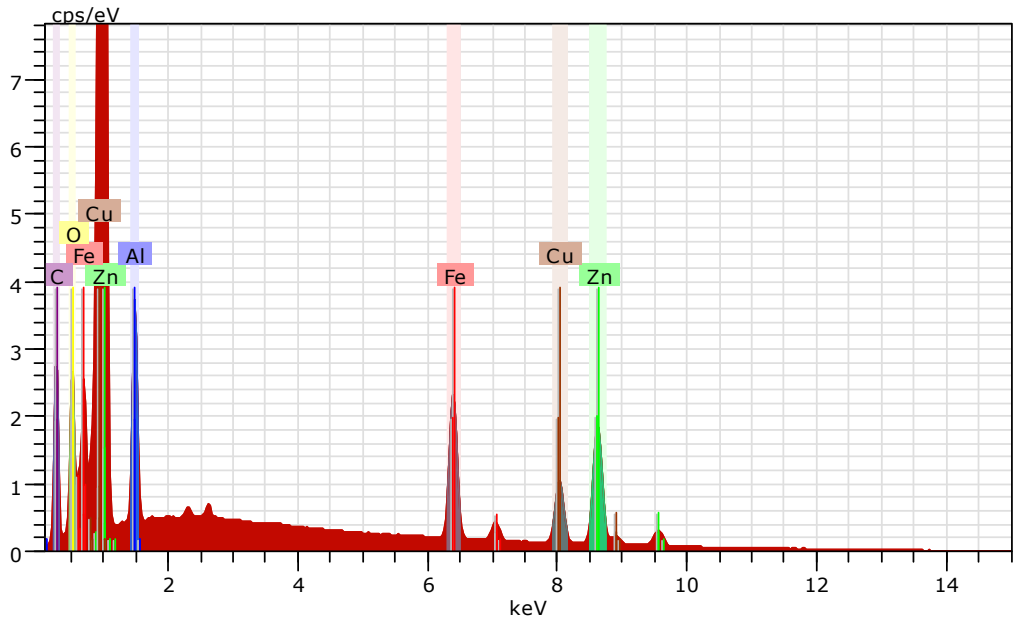
cps/eV
0
1
2
3
4
5
6
7
Cu
O
Fe
Al
C
Zn
Fe
Cu
Zn
2
4
6
8
10
12
14
keV

(c)

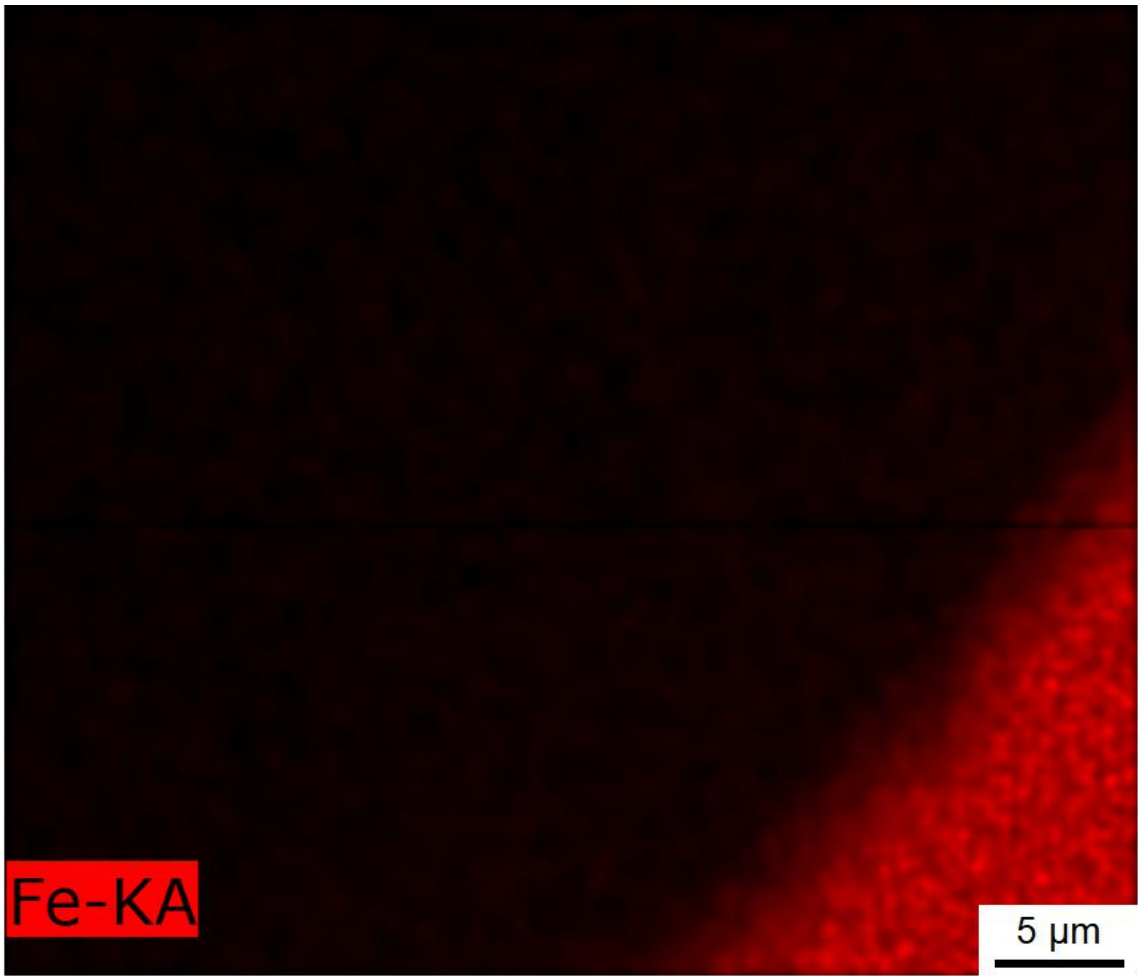

(d)

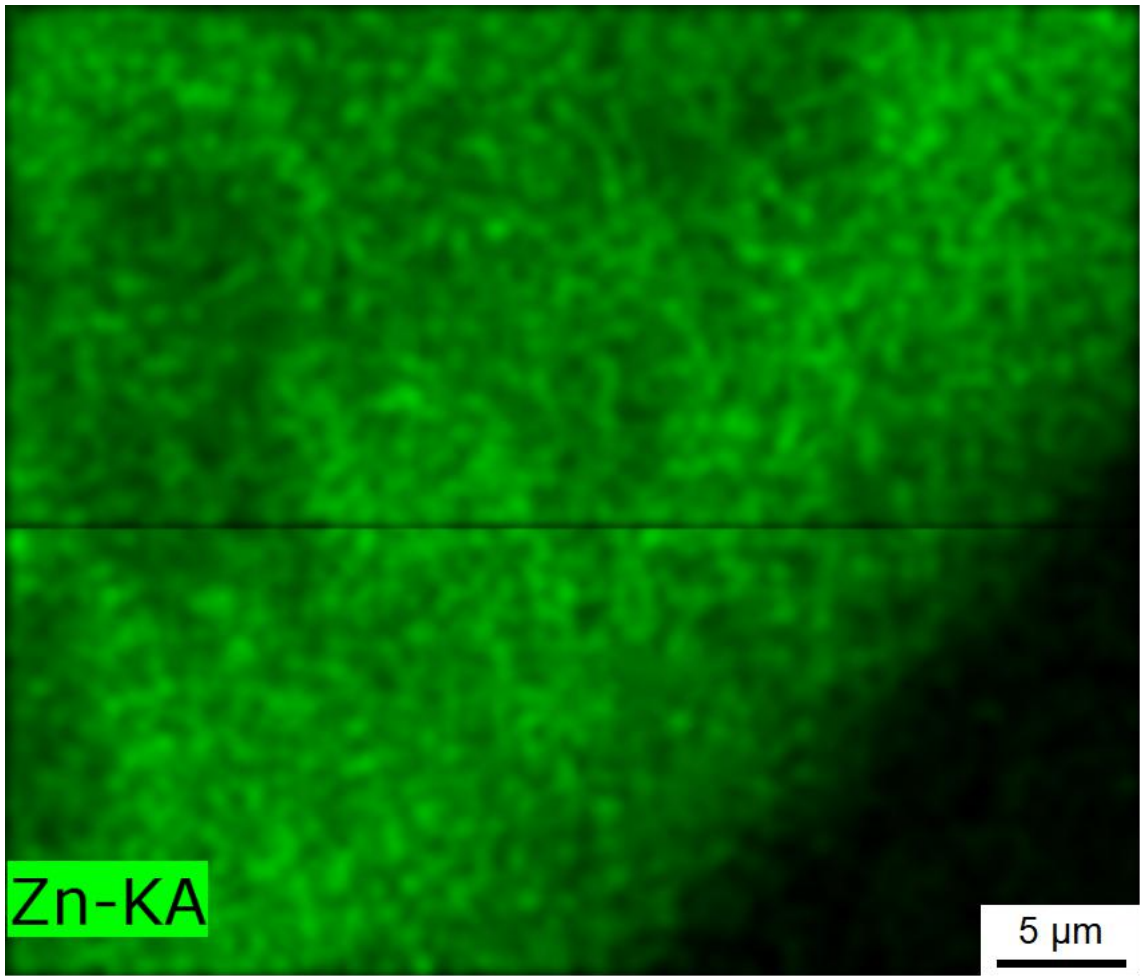

(e)

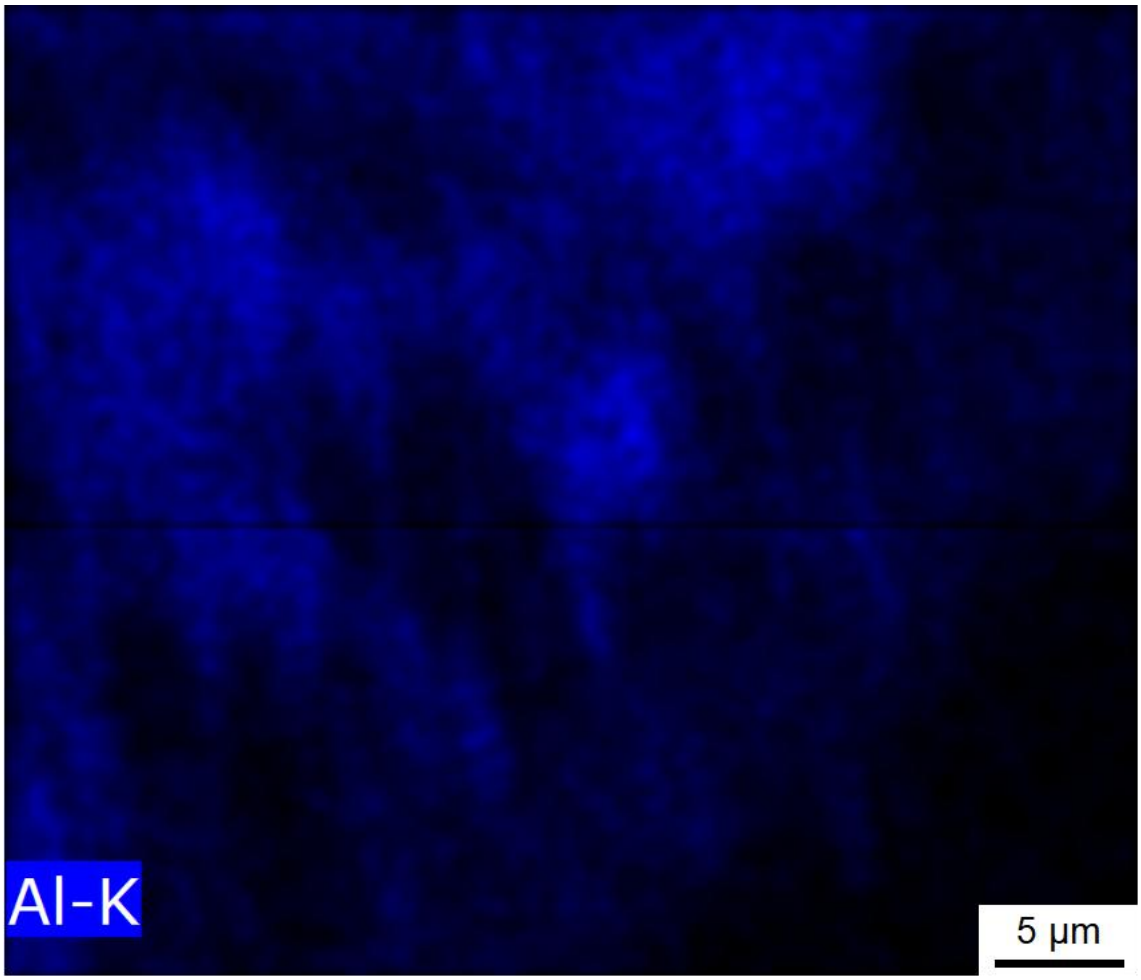

(f)

Figure A. 7 (a) SEM micrograph (b) element distribution (c) EDS spectrum of scanned area (d) distribution of Fe (e) distribution of Zn (f) distribution of Al of the brake line from Ford Fusion 2017.

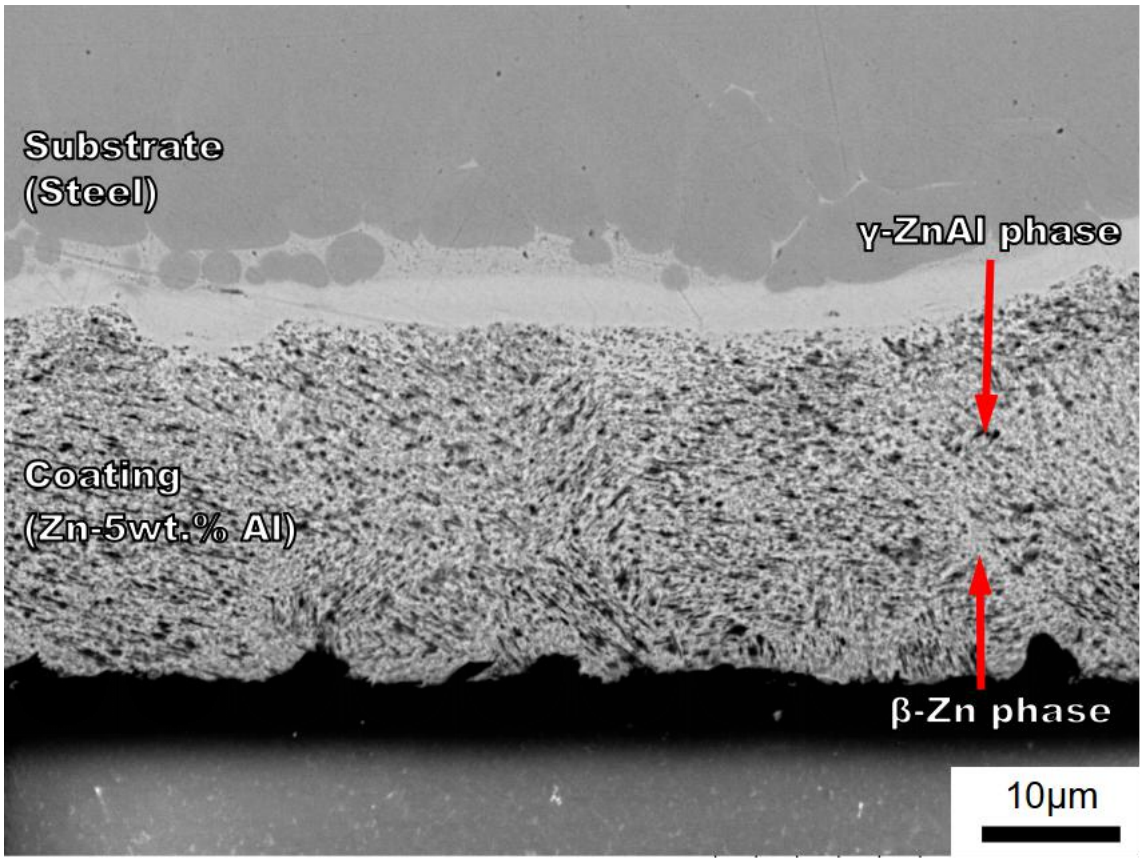
Substrate
(Steel)
γ-ZnAl phase
Coating
(Zn-5wt.% Al)
β-Zn phase
10μm

(a)

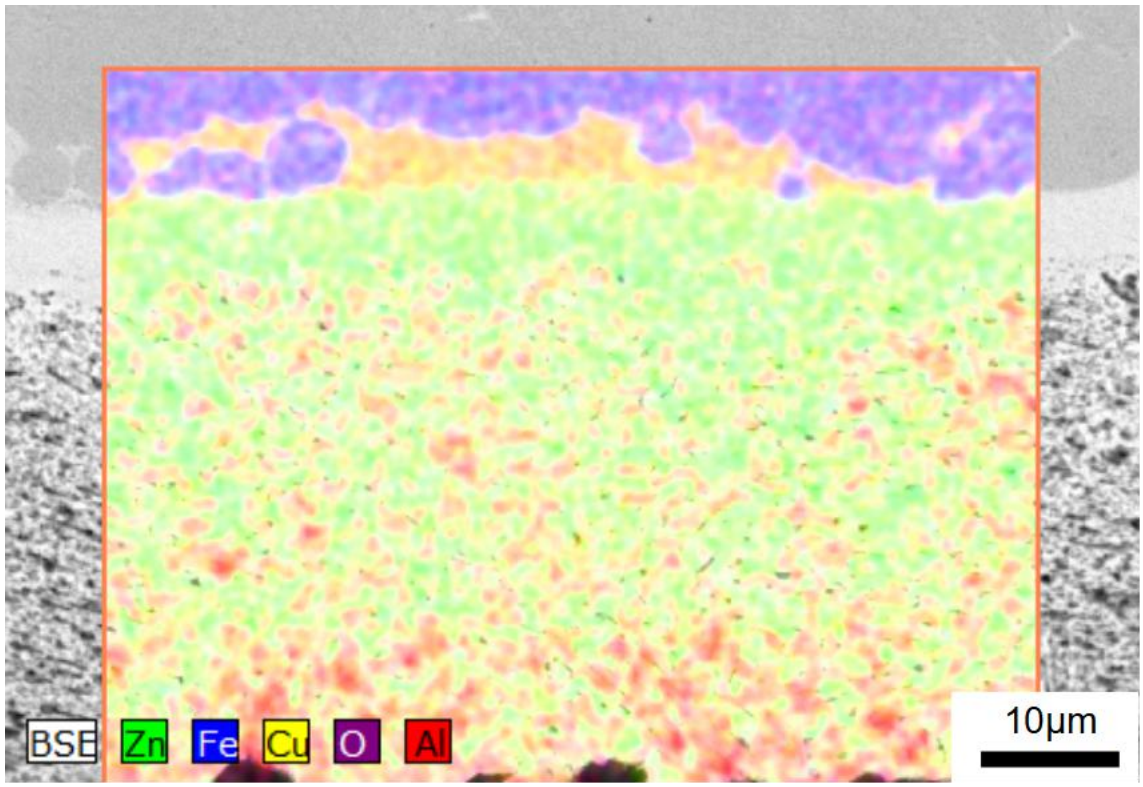
BSE
Zn
Fe
Cu
O
Al
10µm

(b)

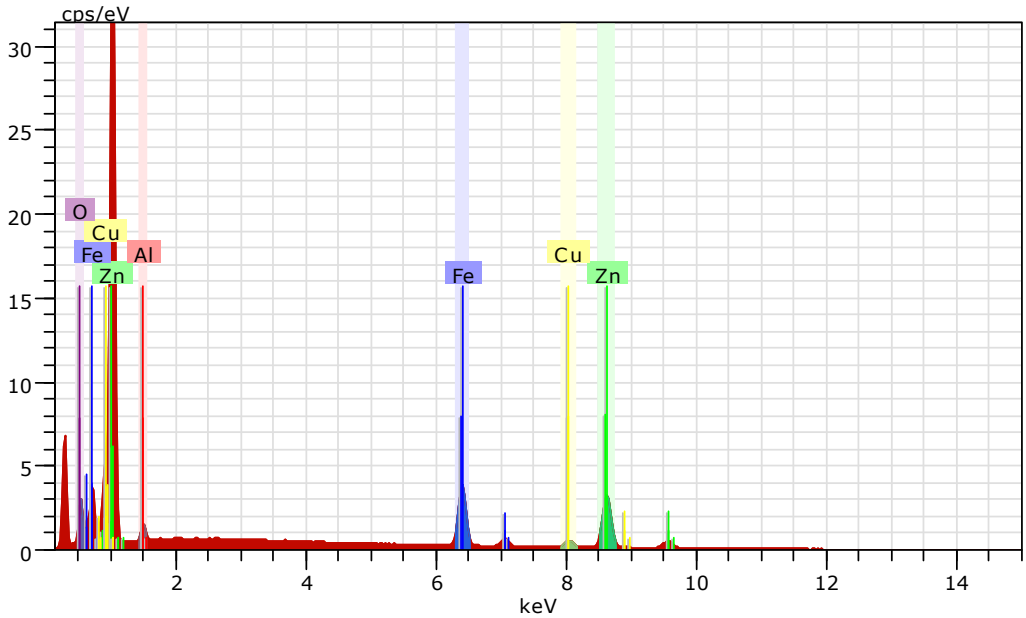
cps/eV
30
25
20
15
10
5
0
O
Cu
Fe
Al
Zn
Fe
Cu
Zn
2
4
6
8
10
12
14
keV

(c)

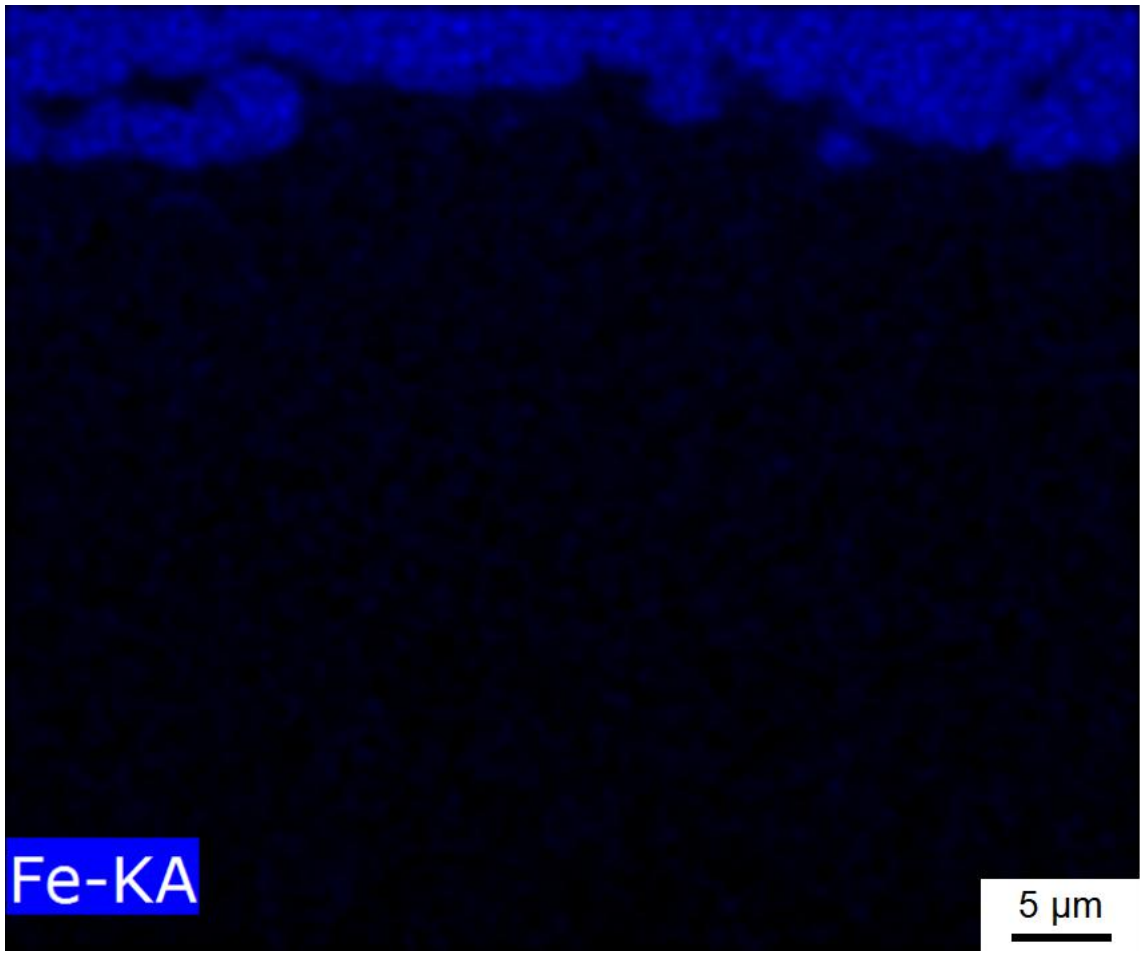

(d)

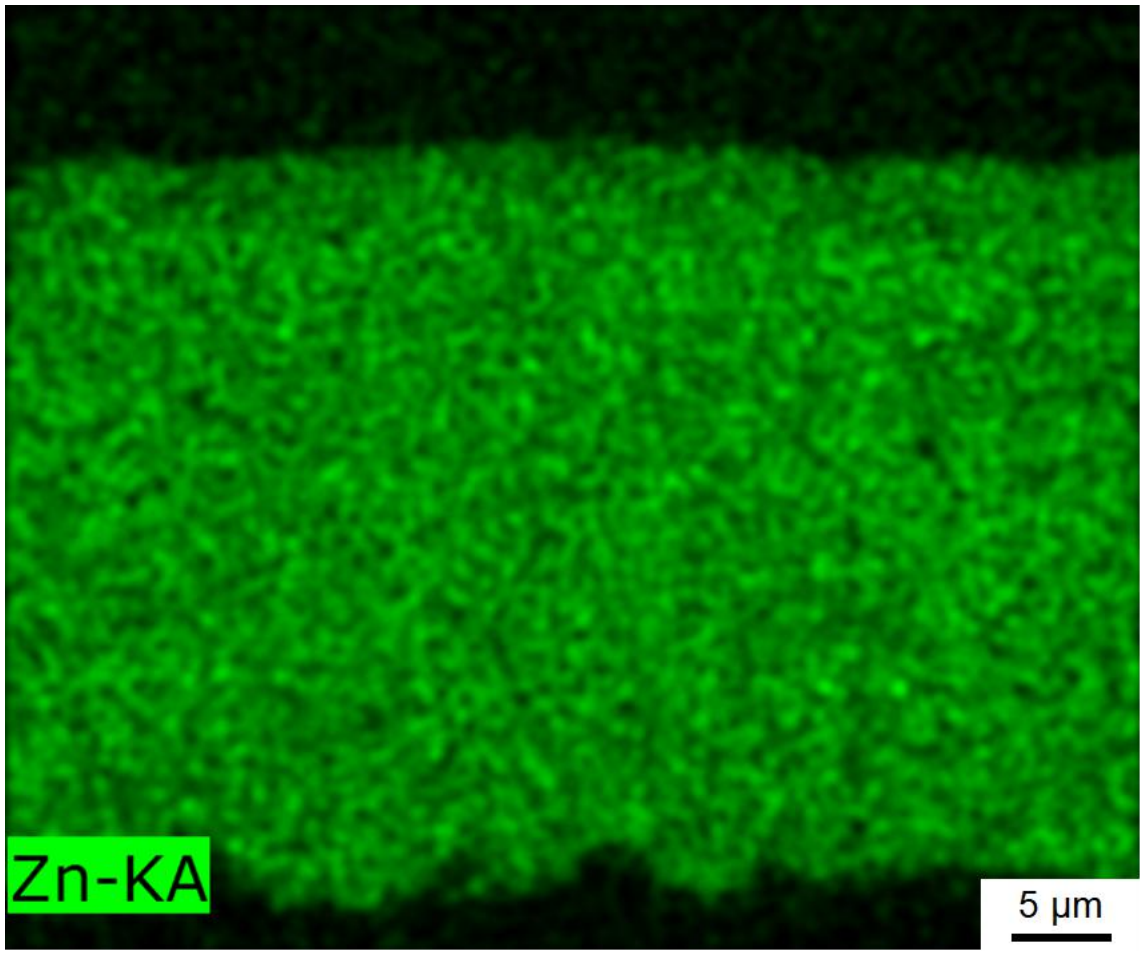

(e)

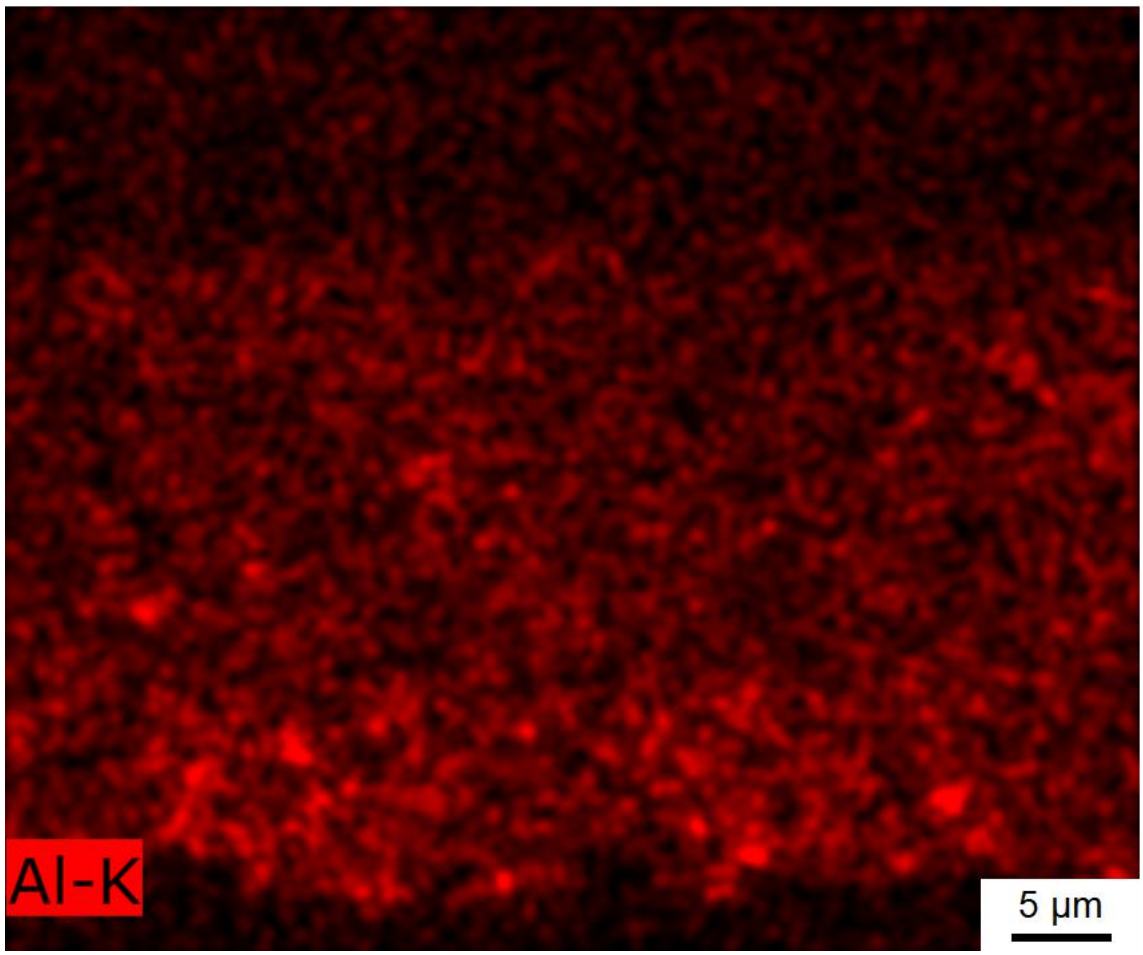

(f)

Figure A. 8 (a) SEM micrograph (b) element distribution (c) EDS spectrum of scanned area (d) distribution of Fe (e) distribution of Zn (f) distribution of Al of the brake line from Chrysler 300 2017.

.

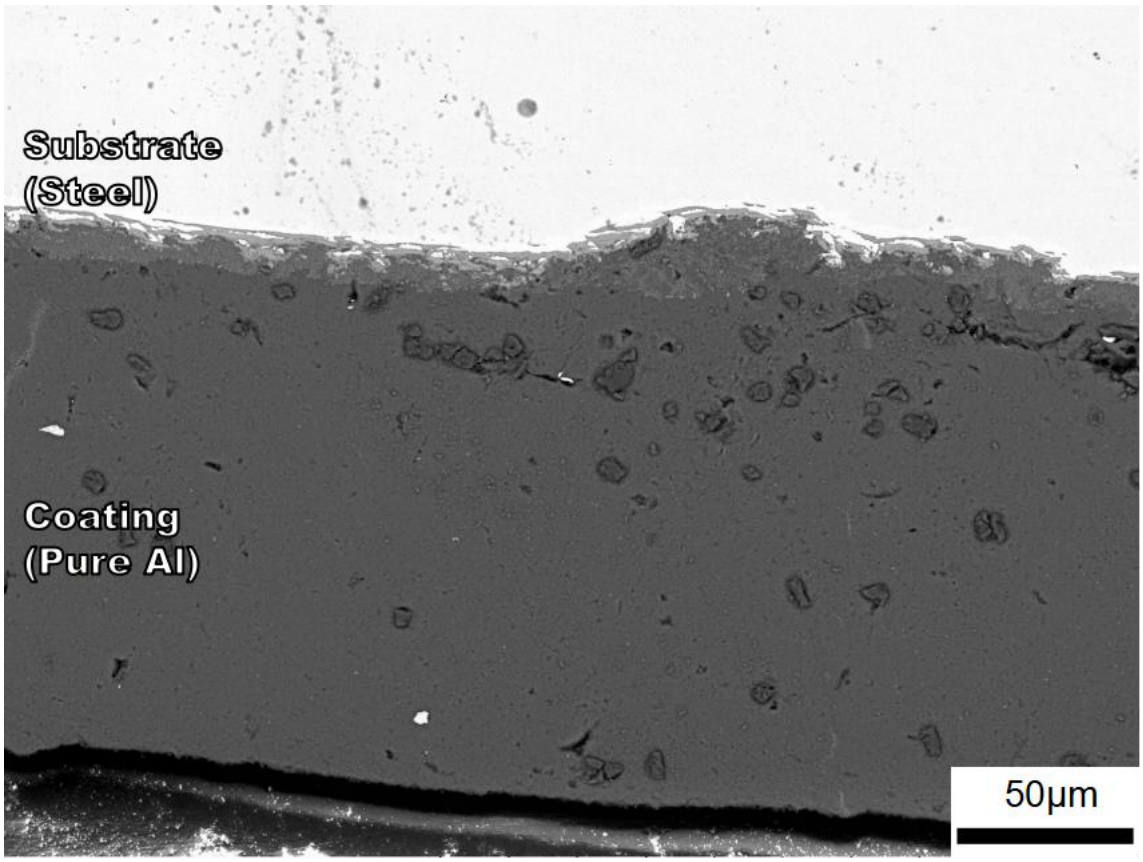

(a)

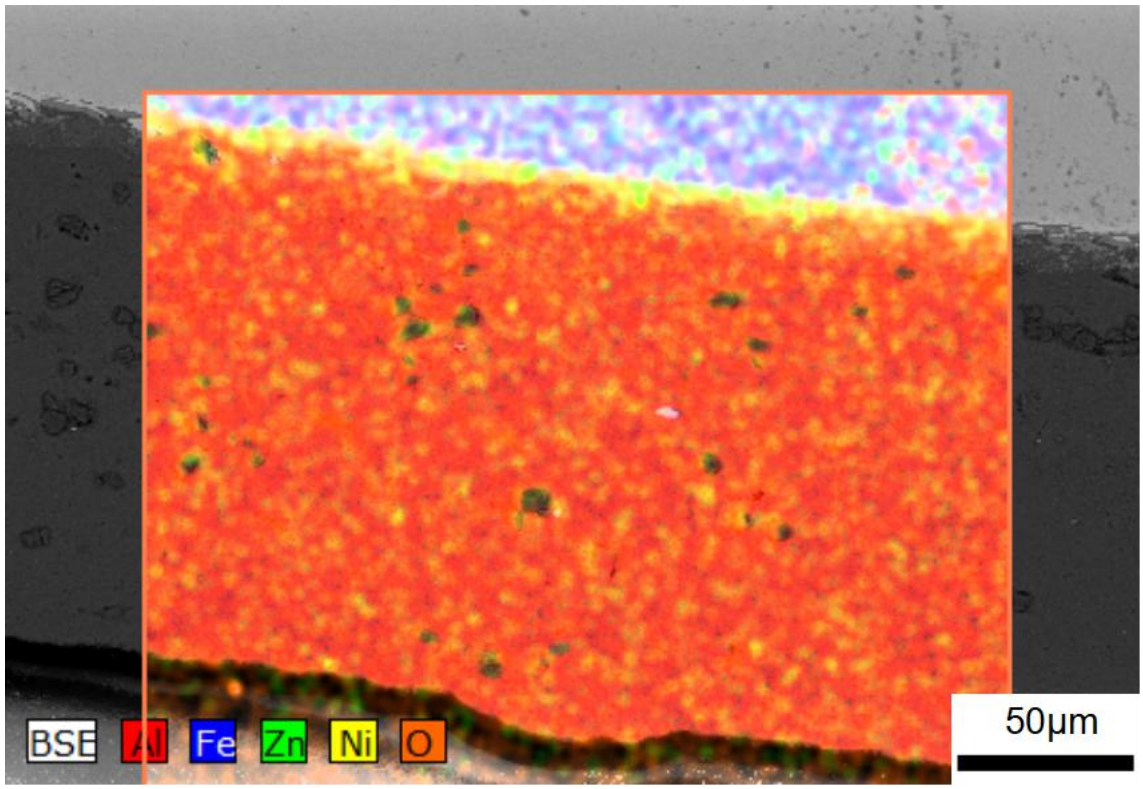
BSE
Al
Fe
Zn
Ni
O
50µm

(b)

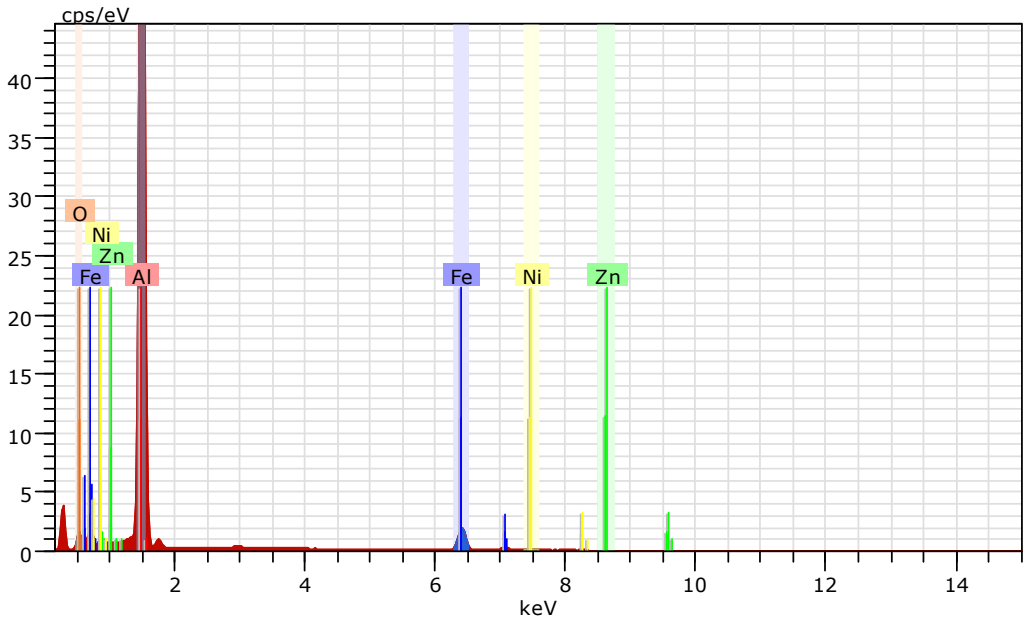
cps/eV
40
35
30
25
20
15
10
5
0
O
Ni
Zn
Fe
Al
Fe
Ni
Zn
2
4
6
8
10
12
14
keV

(c)

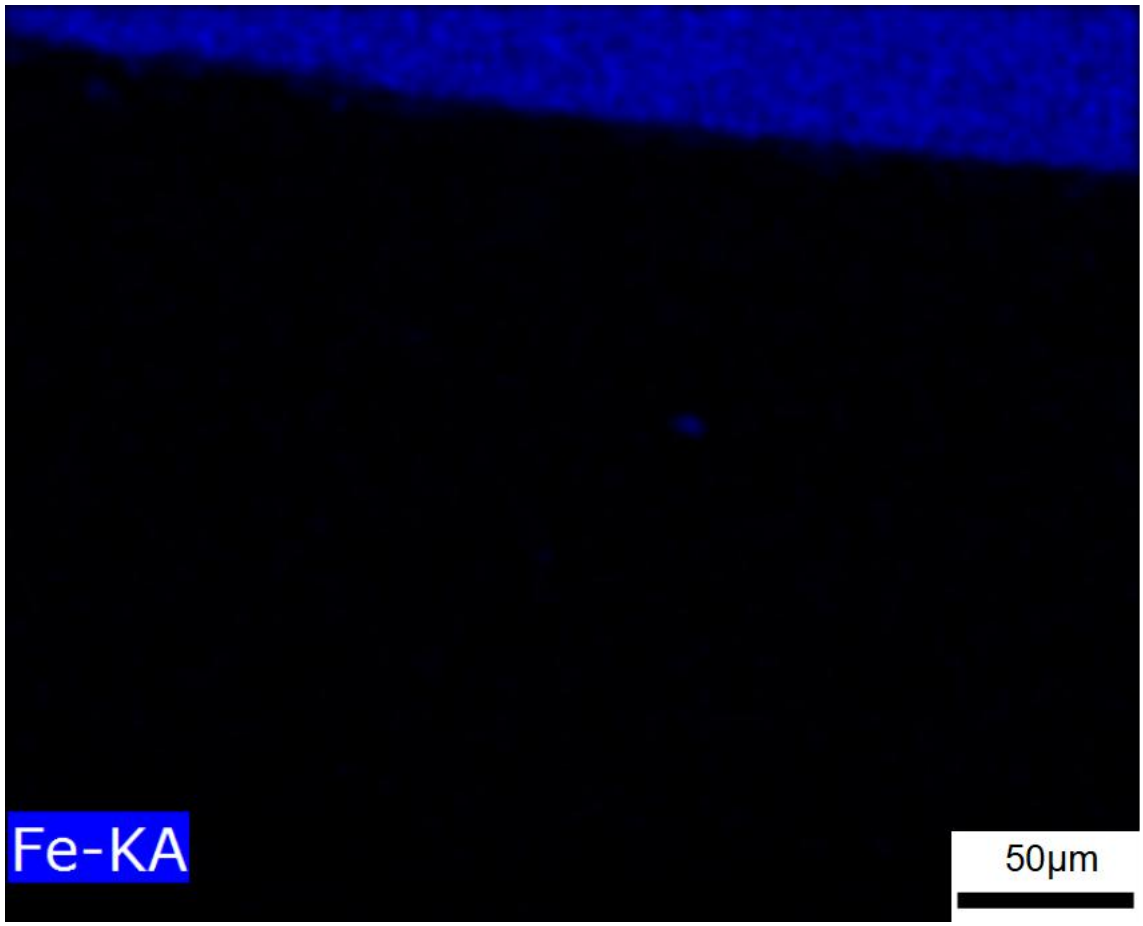

(d)

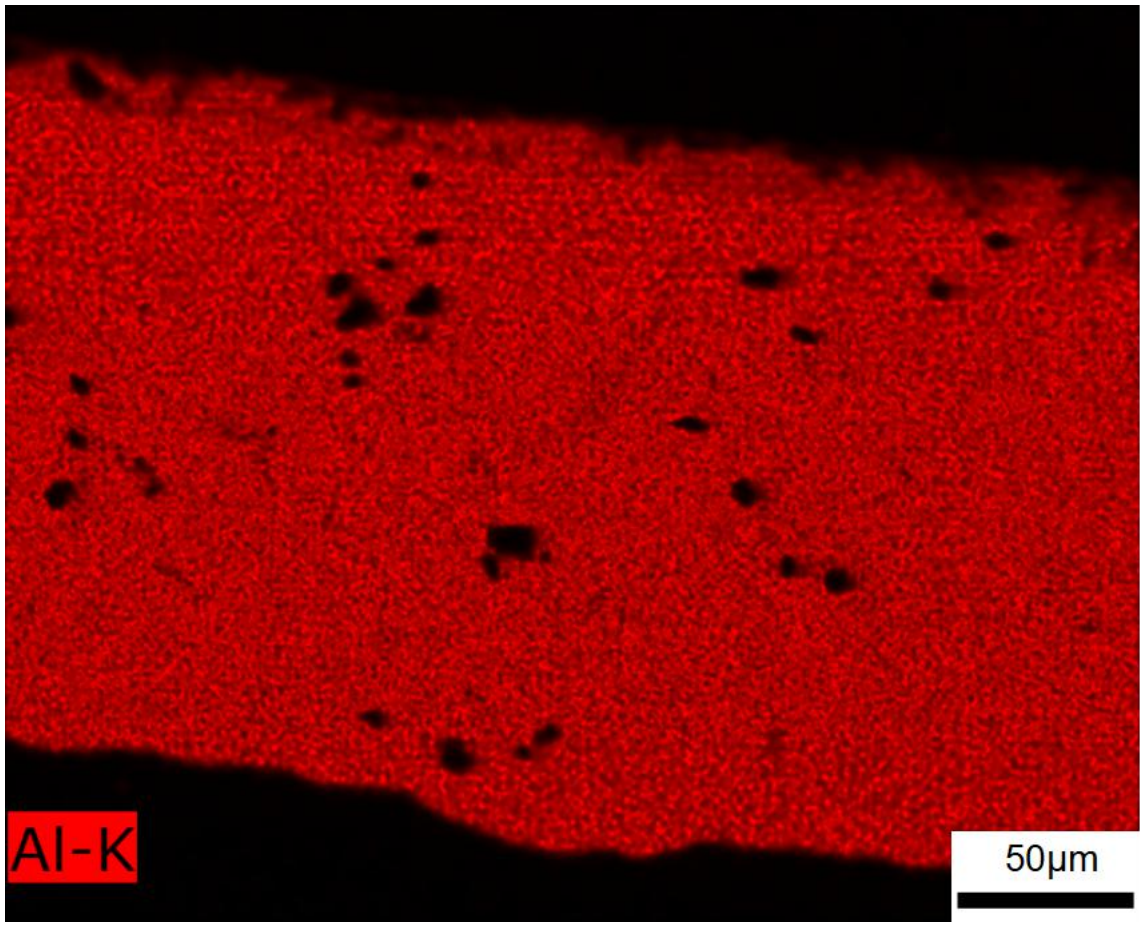

(e)

Figure A. 9 (a) SEM micrograph (b) element distribution (c) EDS spectrum of scanned area (d) distribution of Fe (e) distribution of Al of the brake line from VW Jetta 2017.

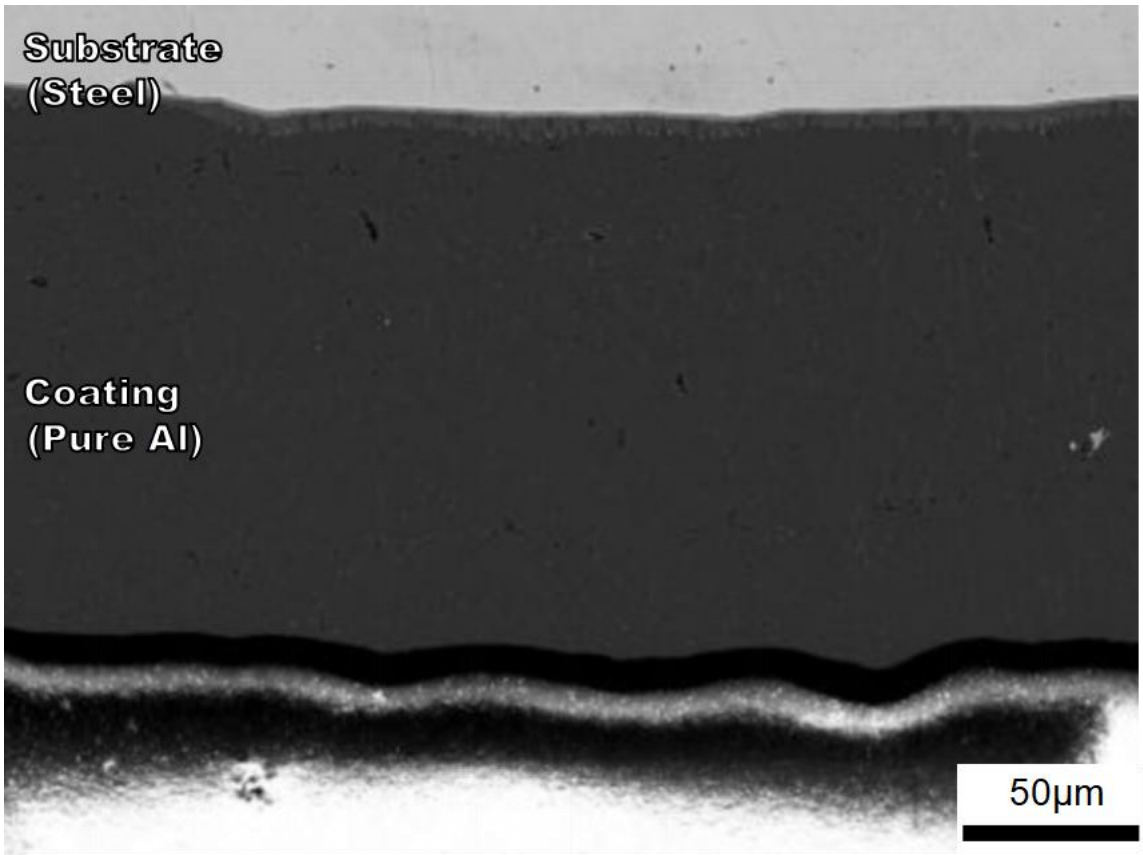

(a)

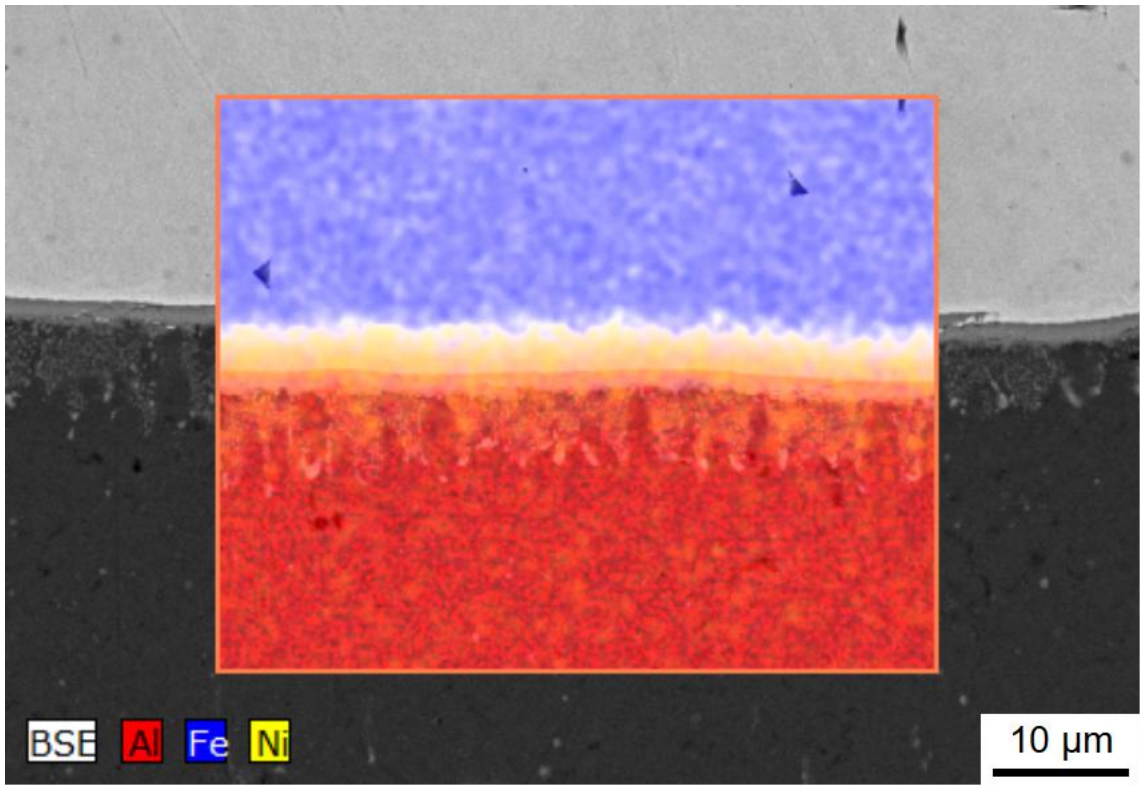
BSE
Al
Fe
Ni
10 µm

(b)

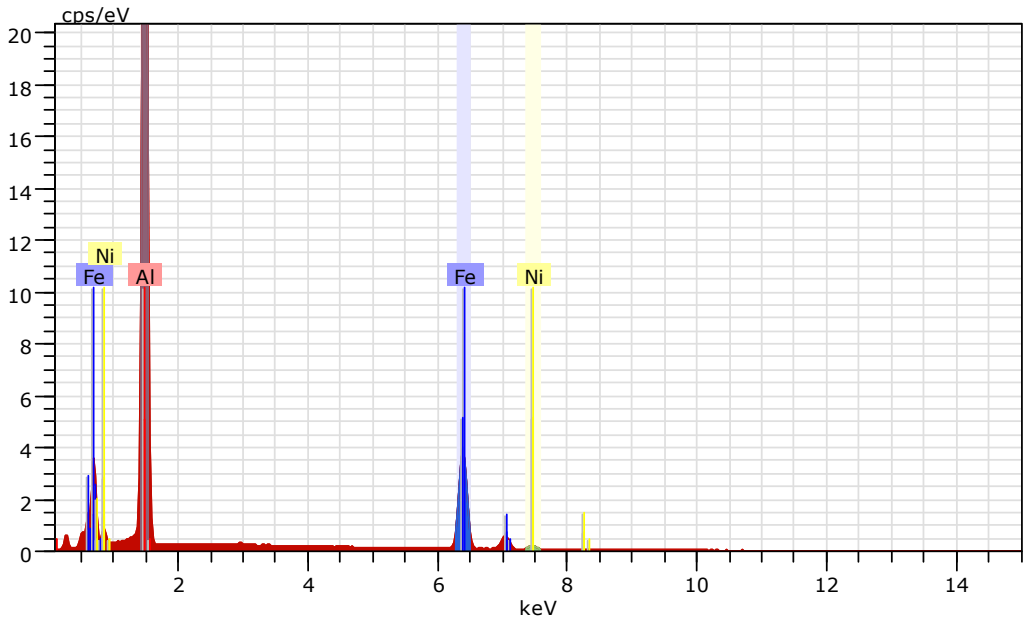
cps/eV
20
18
16
14
12
10
8
6
4
2
0
Ni
Fe
Al
Fe
Ni
2
4
6
8
10
12
14
keV

(c)

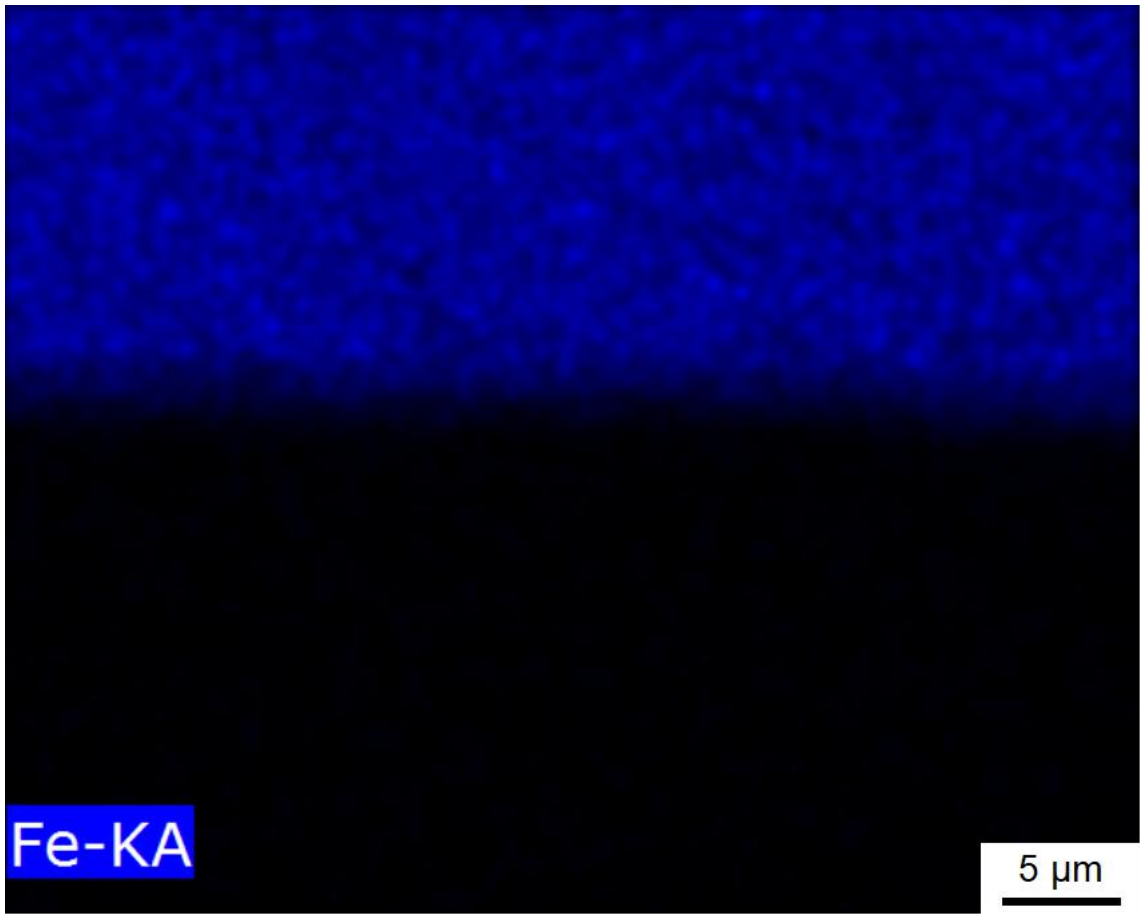

(d)

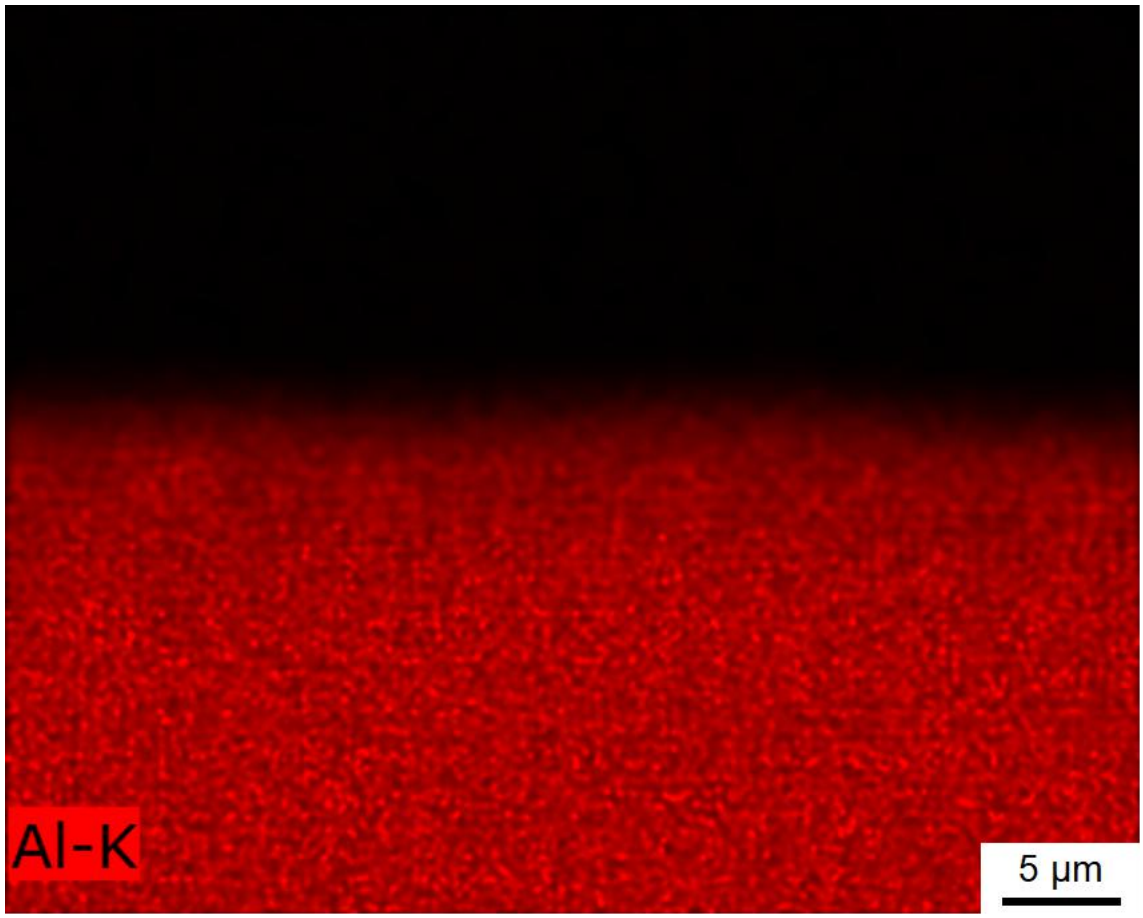

(e)

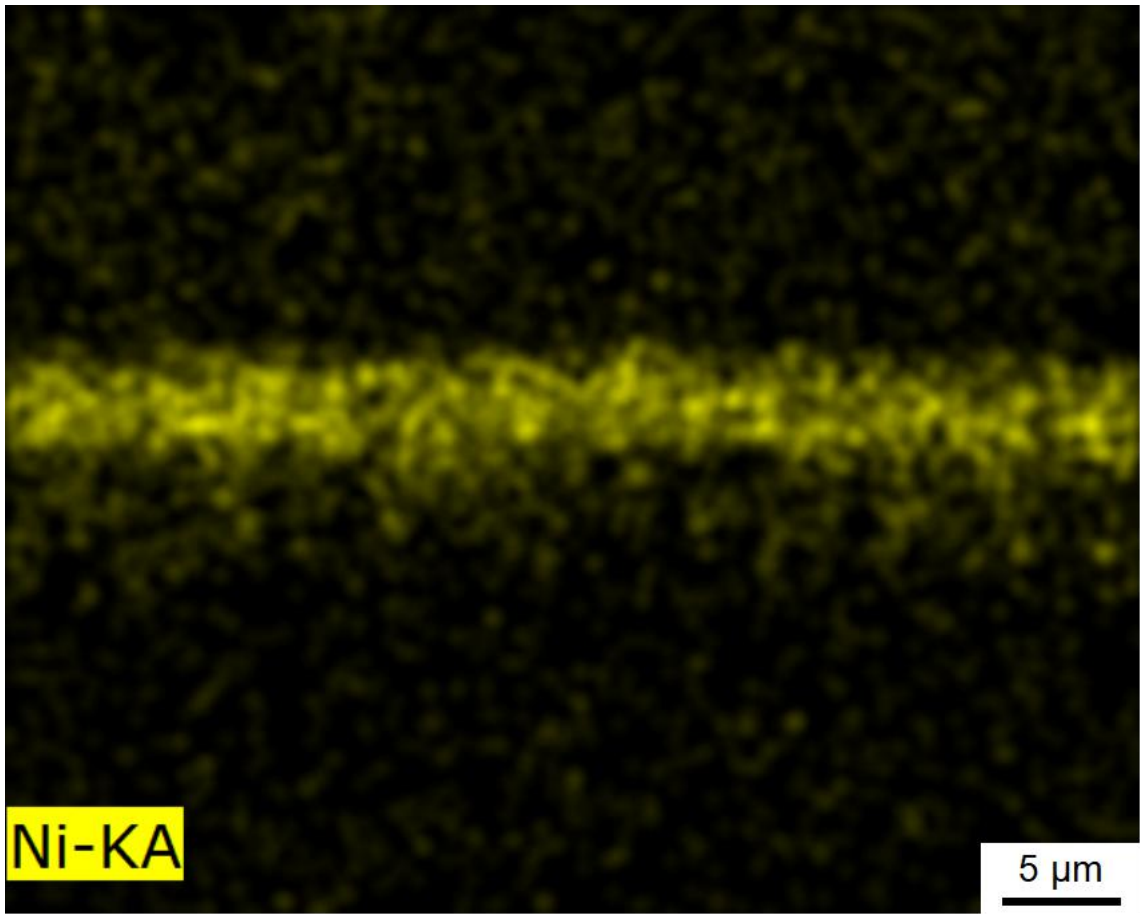

(f)

Figure A. 10 (a) SEM micrograph (b) element distribution (c) EDS spectrum of scanned area (d) distribution of Al (e) distribution of Ni of the brake line from BMW 320 2017

Table A. 1 Thickness and phases of coatings in various brake lines

Type	Coating Thickness (µm)	Phase Detected
Mazda 3 SE 2017	20	Zn, Zn-Fe
Toyota Carolla CE 2017	8	Zn, Zn-Al
Honda Civic LX 2017	25	Zn, Zn-Al
Nissan Sentra SA 2017	21	Zn, Zn-Al
Ford Fusion S 2017	12	Zn, Zn-Al
Chrysler 300 Touring 2017	20	Zn, Zn-Al
Volkswagen Jetta 2017	120	Al
BMW 320I 2017	130	Al

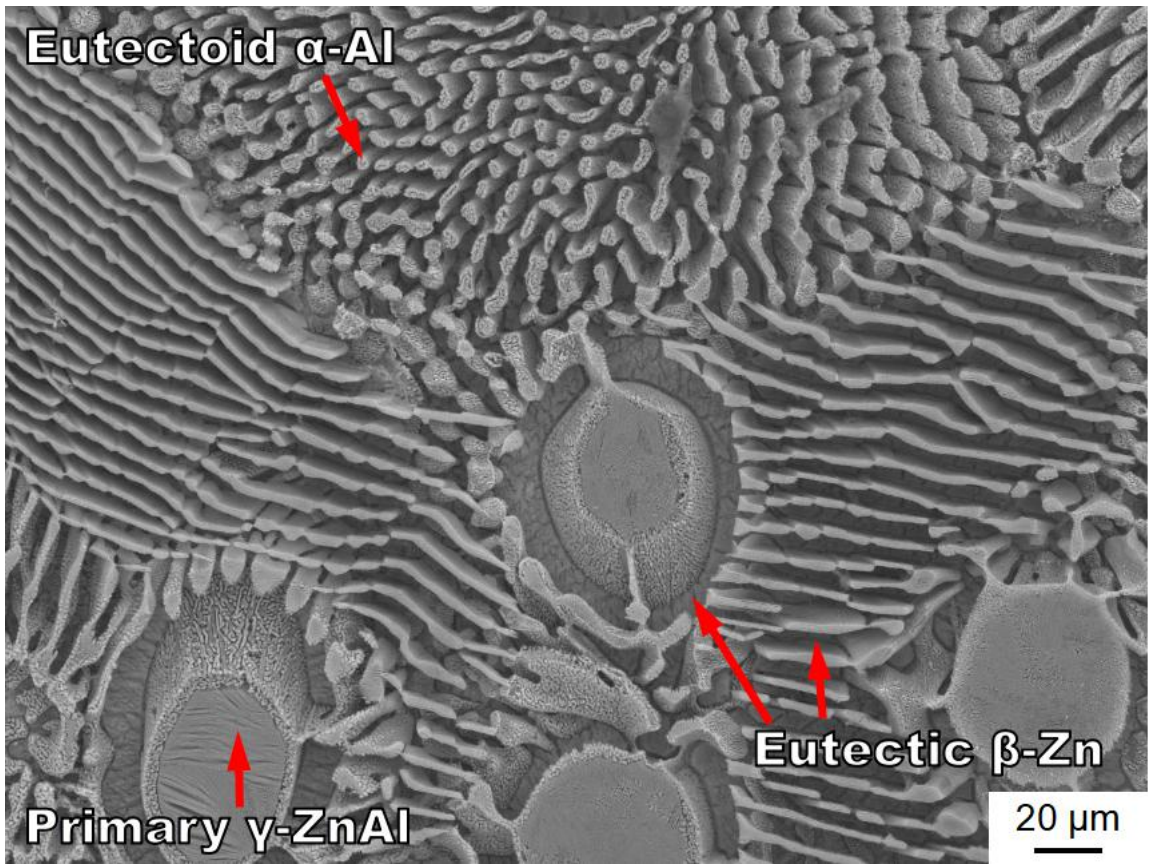

(a)

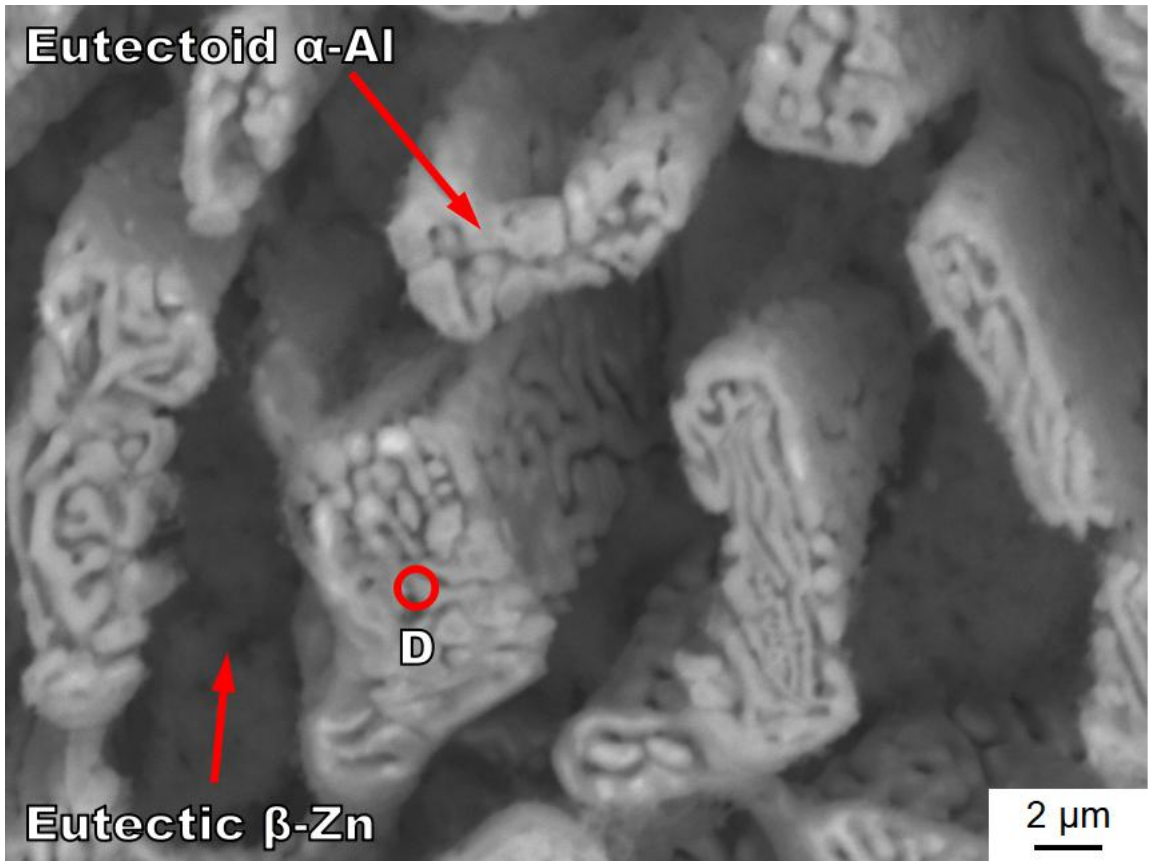

(b)

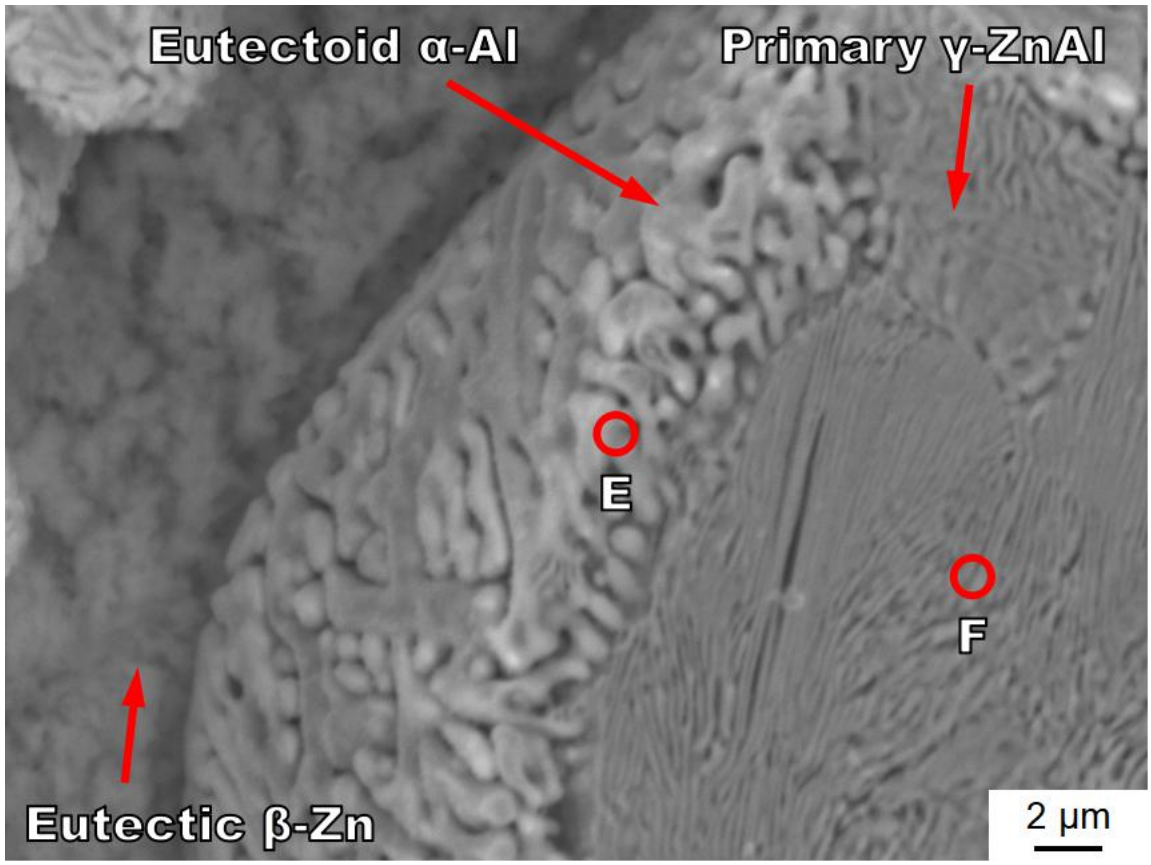
Eutectoid α-Al
Primary γ-ZnAl
E
F
Eutectic β-Zn
2 μm

(c)

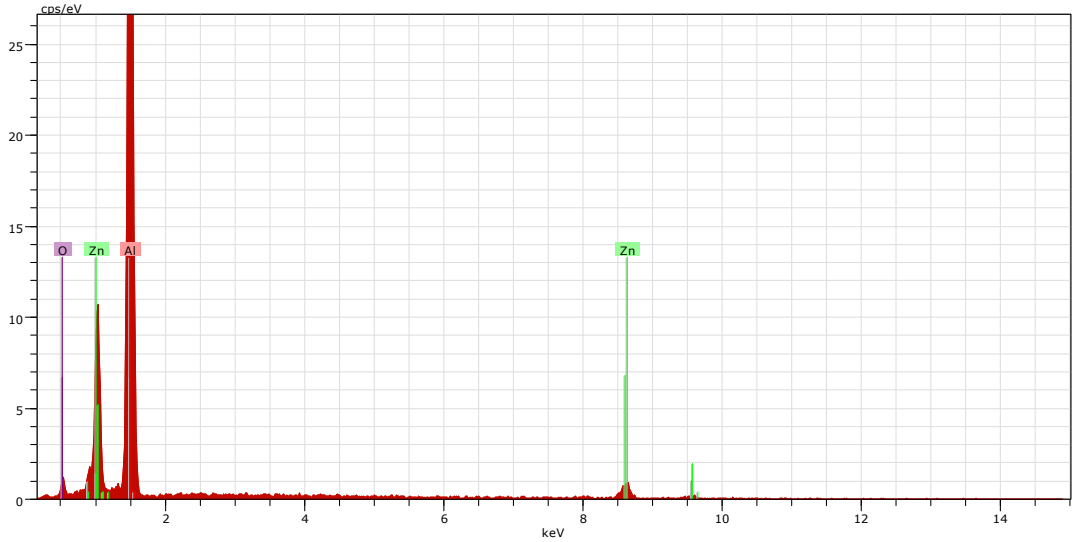
cps/eV
25
20
15
10
5
0
O
Zn
Al
Zn
2
4
6
8
10
12
14
keV

(d)

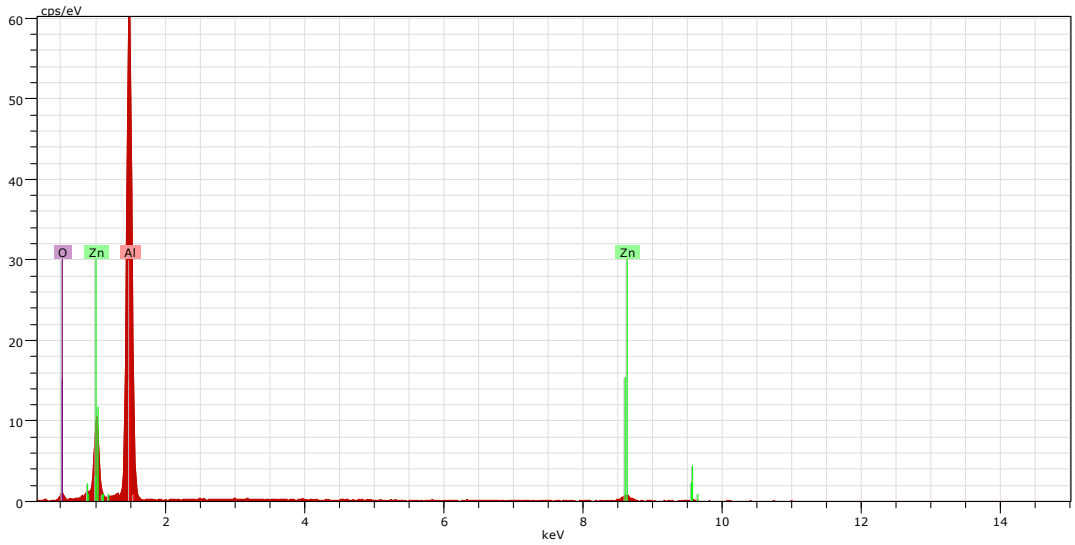

(e)

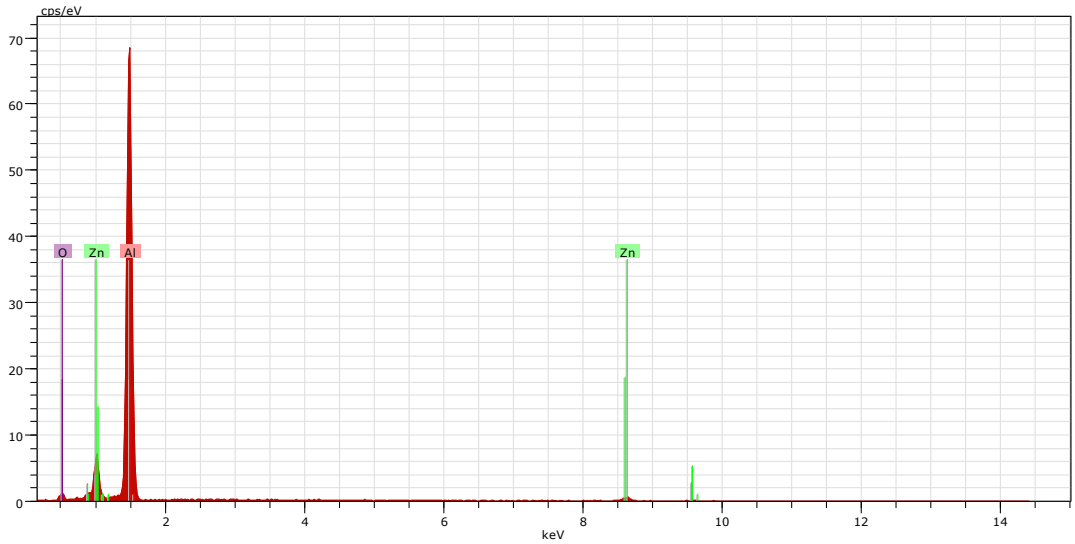

(f)

Figure A. 11 SEM pictures of deep etched Zn- 6wt.% Al under furnace cooling condition showing the detail of (a) overall mophorogy (b) eutectic α-Al phase and (c) primary γ-ZnAl phase (d) EDS spectrum of point D (e) EDS spectrum of point E (f) EDS spectrum of point F.

Table A. 2 EDS results of the point D, E, and F in Figure A. 11 showing the weight and atomic percentage of each pint

Point	Al wt.%	Zn wt.%	Al at.%	Zn at.%
D	72.33	23.30	80.99	10.76
E	80.66	15.33	86.04	6.75
F	79.96	14.89	84.35	6.48

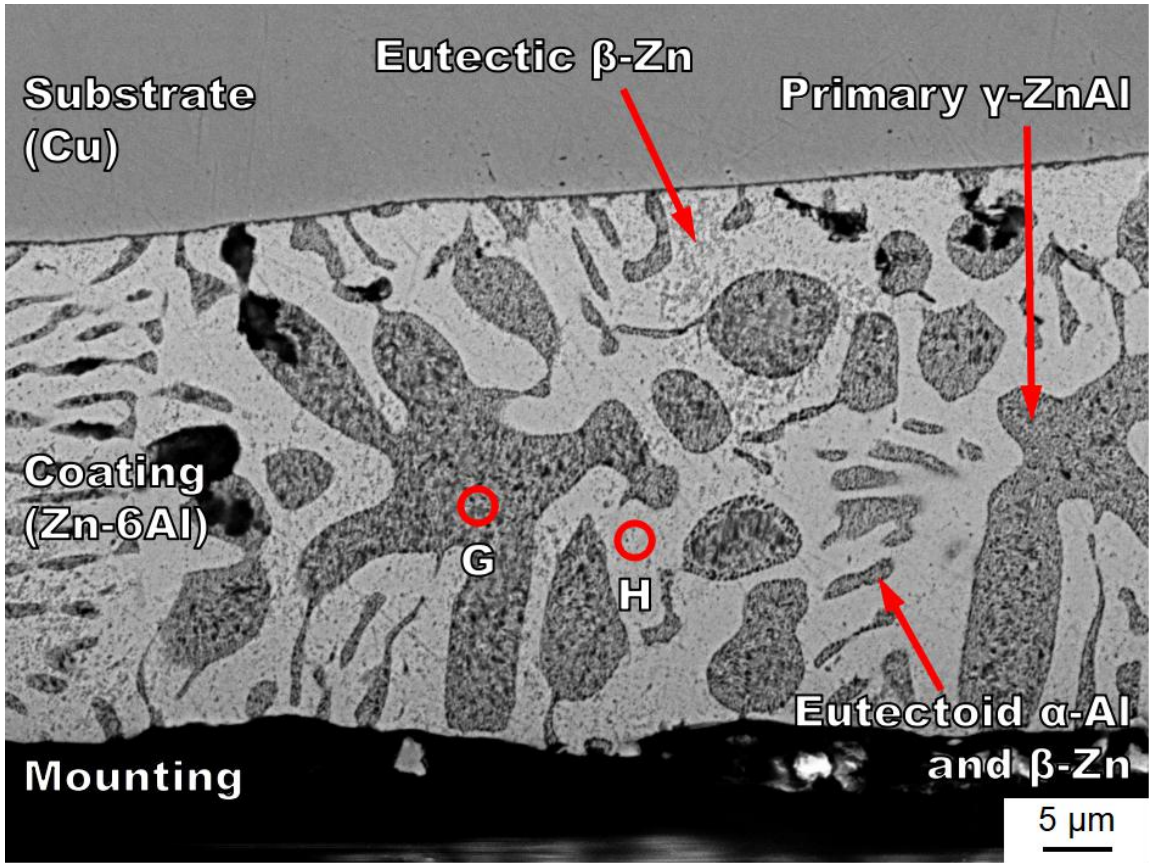

(a)

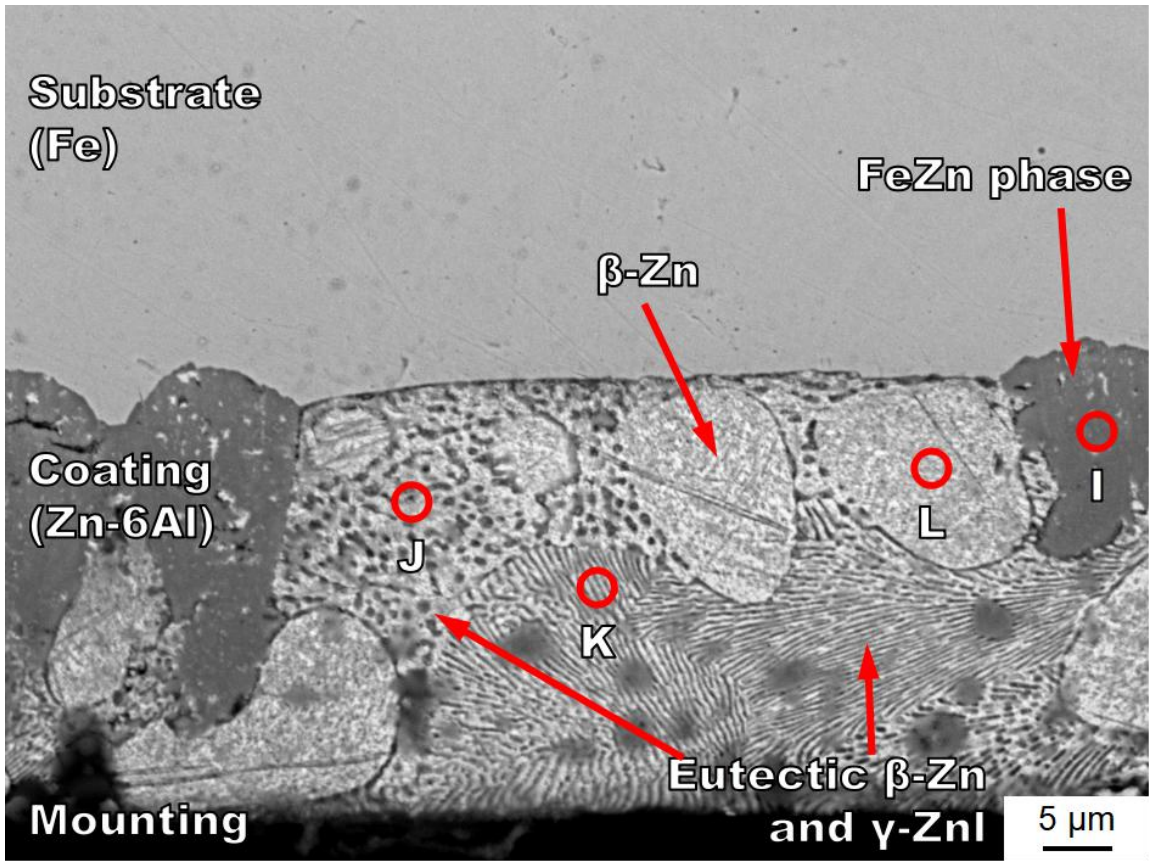
Substrate
(Fe)
FeZn phase
β-Zn
Coating
(Zn-6Al)
J
K
L
I
Eutectic β-Zn
and γ-ZnI
Mounting
5 µm

(b)

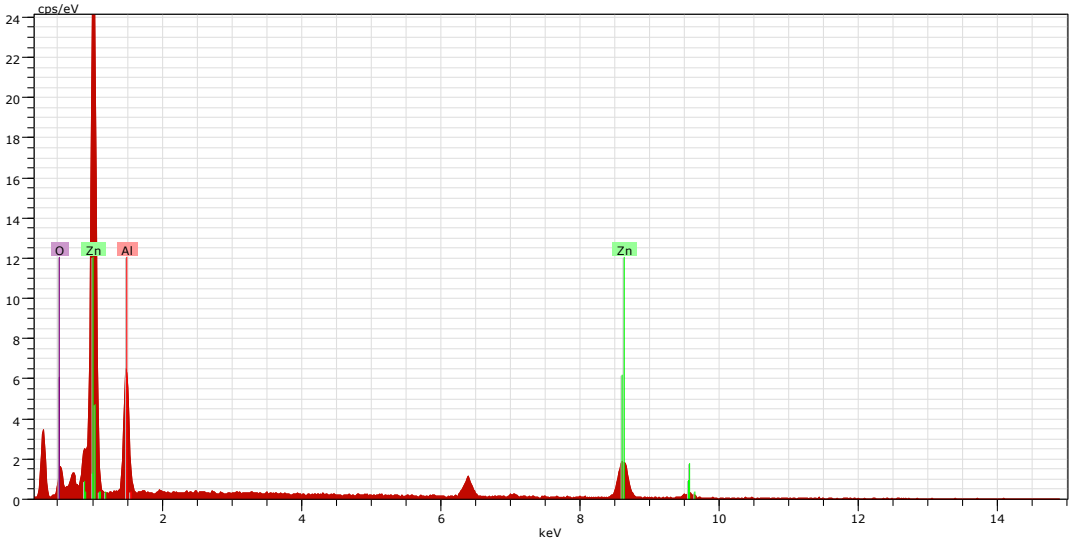
cps/eV
O
Zn
Al
Zn
keV

(c)

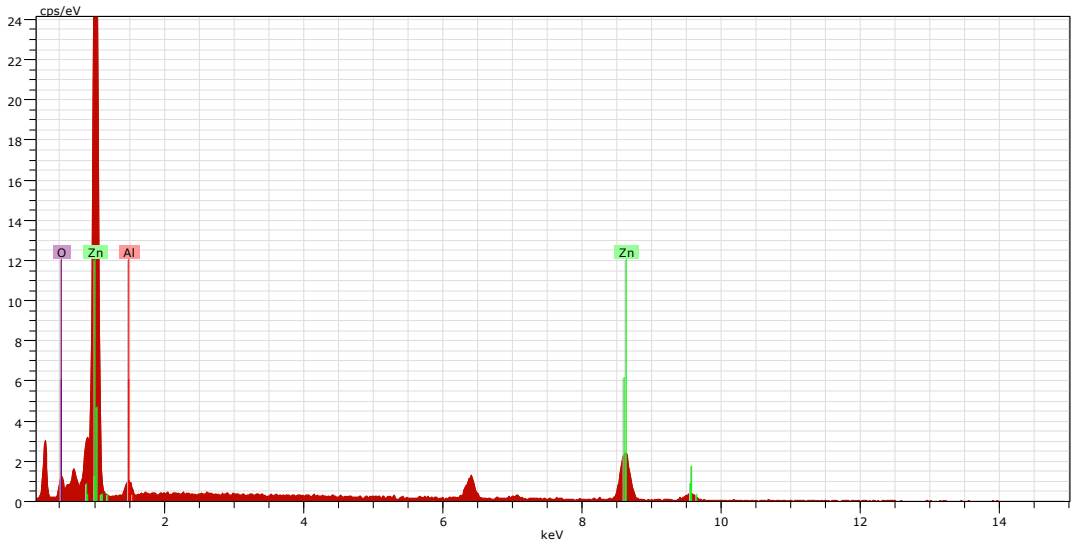

(d)

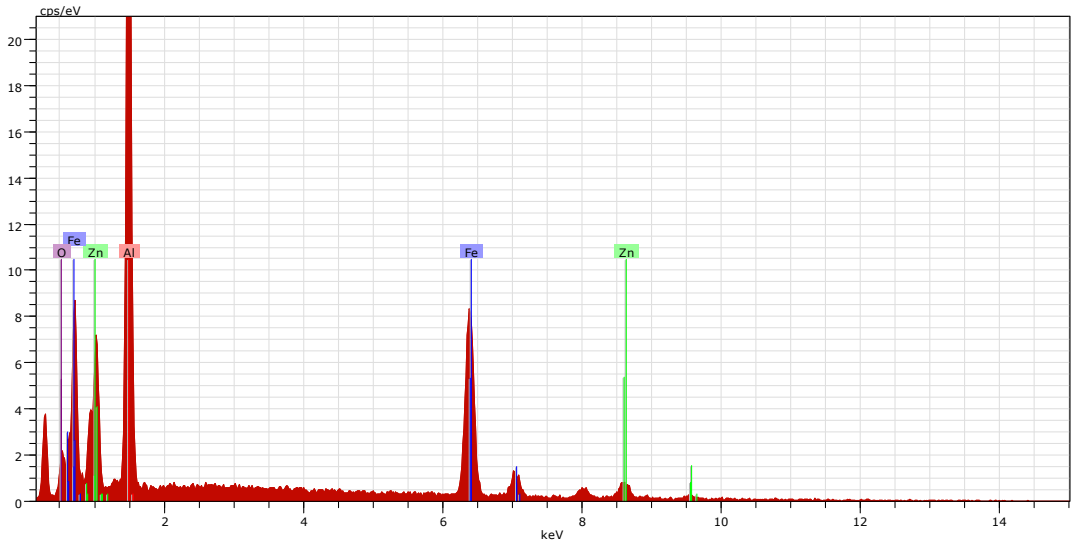

(e)

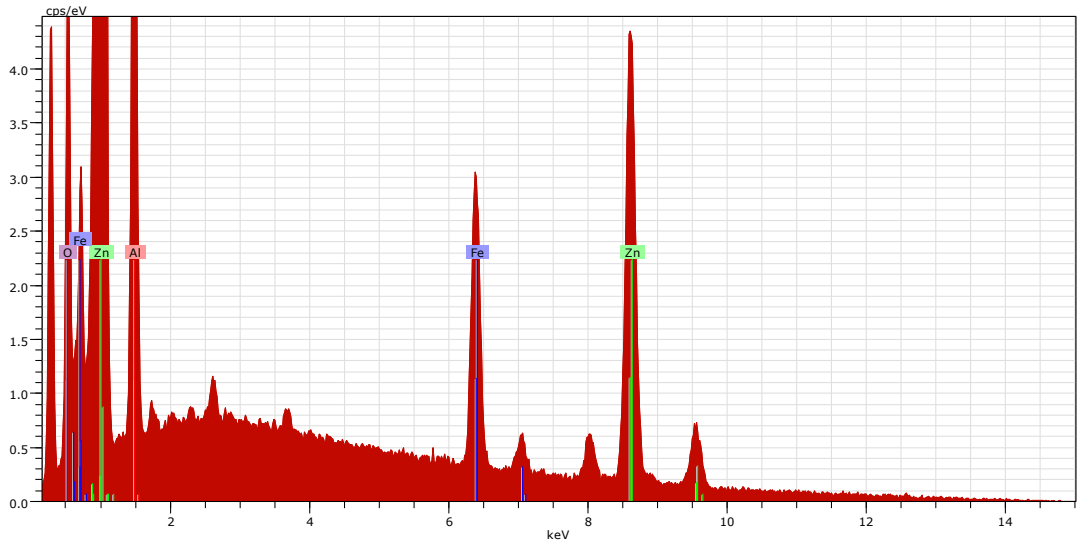
cps/eV
4.0
3.5
3.0
2.5
2.0
1.5
1.0
0.5
0.0
Fe
O
Zn
Al
Fe
Zn
2
4
6
8
10
12
14
keV

(f)

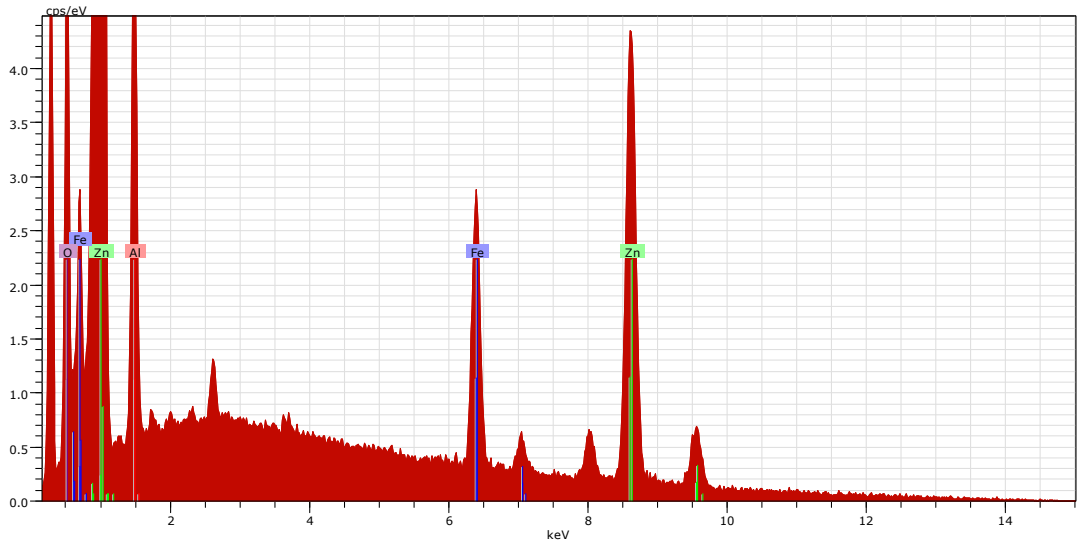
cps/eV
4.0
3.5
3.0
2.5
2.0
1.5
1.0
0.5
0.0
Fe
O
Zn
Al
Fe
Zn
2
4
6
8
10
12
14
keV

(g)

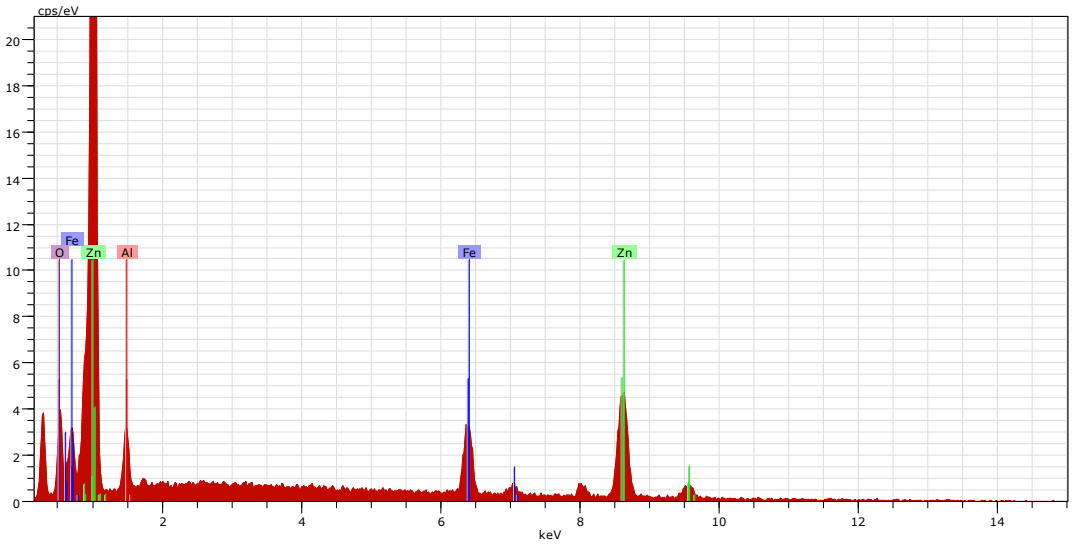

(h)

Figure A. 12 SEM pictures of Zn - 6wt.% Al coating on (a) copper substrate (b) steel substrate and EDS spectrum of (c) point G (d) point H (e) point I (f) point J (g) point K (h) point L.

Table A. 3 EDS results of the point G to L in Figure A. 12 showing the weight and atomic percentage of each pint

Point	Al wt.%	Zn wt.%	Fe wt.%	Al at.%	Zn at.%	Fe wt.%
G	20.91	71.59	-	33.13	46.82	-
H	2.97	91.27	-	5.90	74.80	-
I	41.57	10.87	43.78	56.50	6.10	28.75
J	10.38	67.36	13.08	17.31	46.34	10.54
K	8.02	68.90	12.95	13.41	47.55	10.46
L	4.80	73.05	15.09	8.86	55.67	13.47

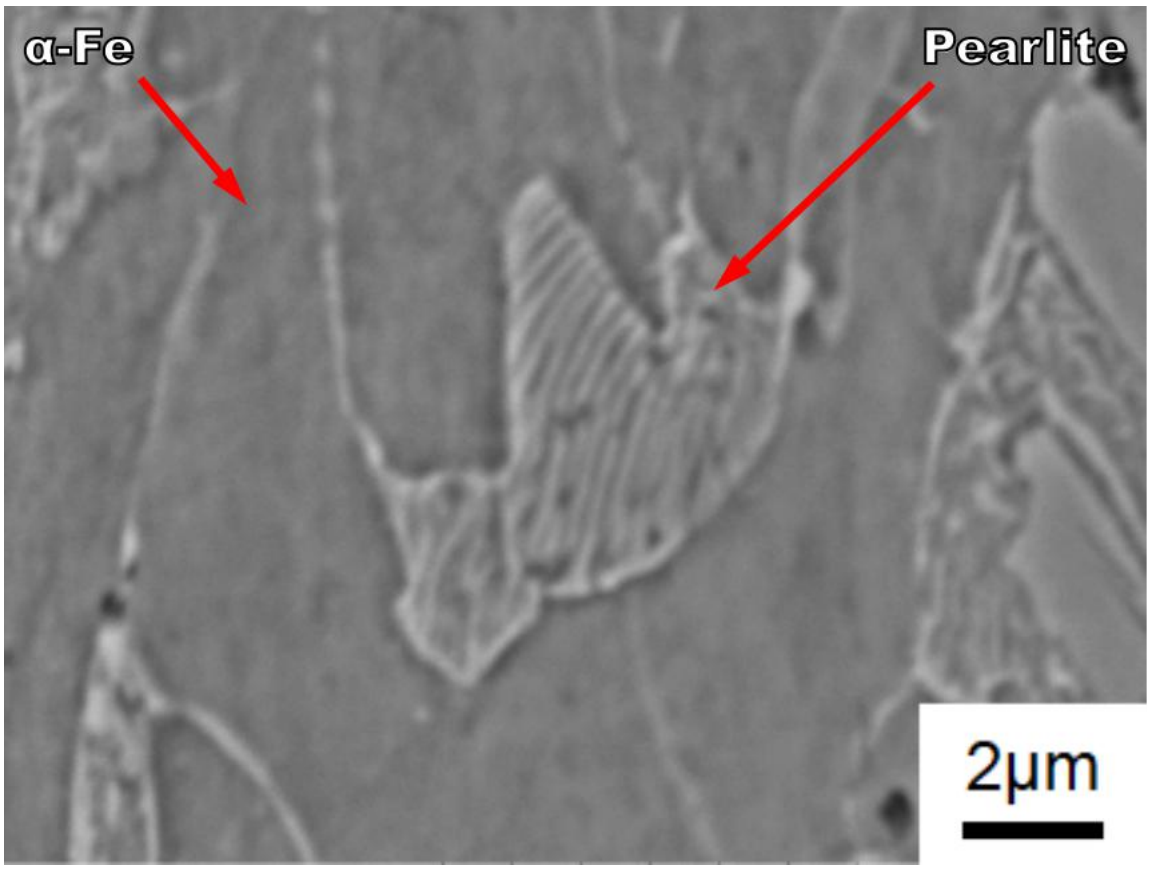

(a)

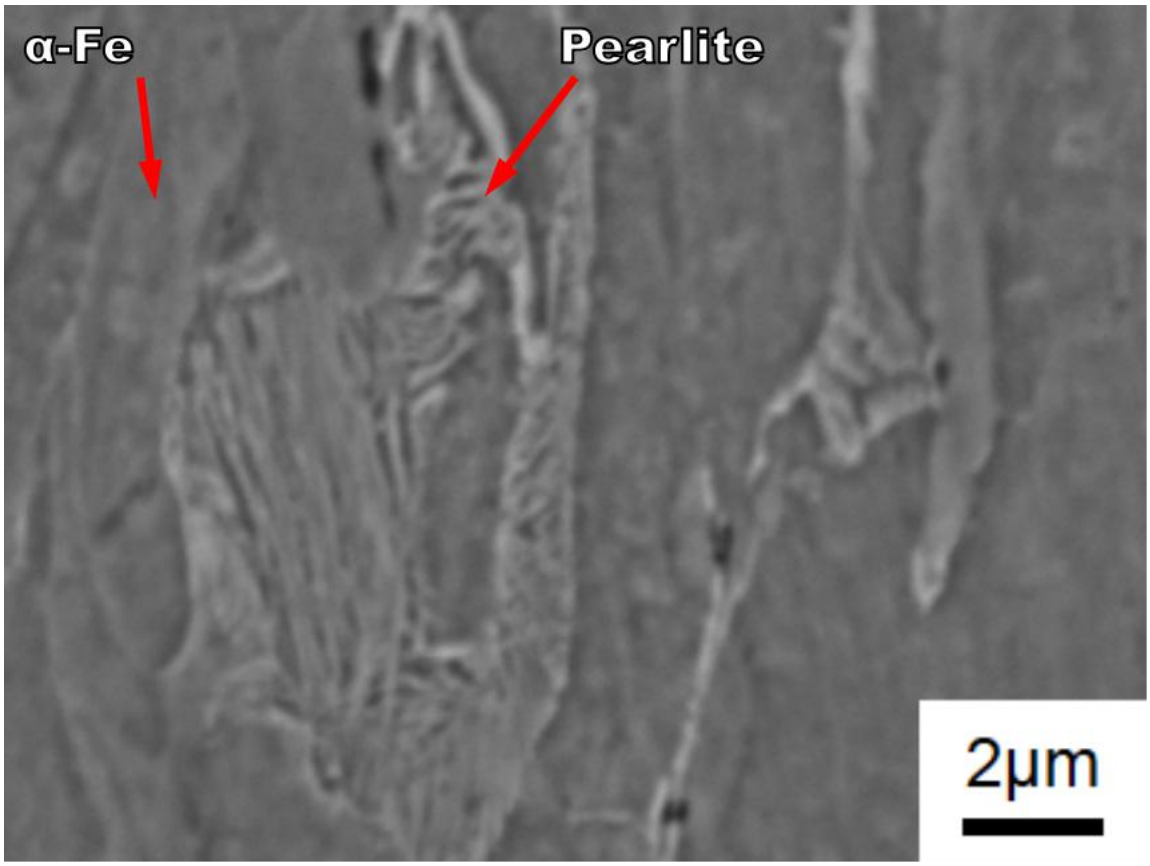

(b)

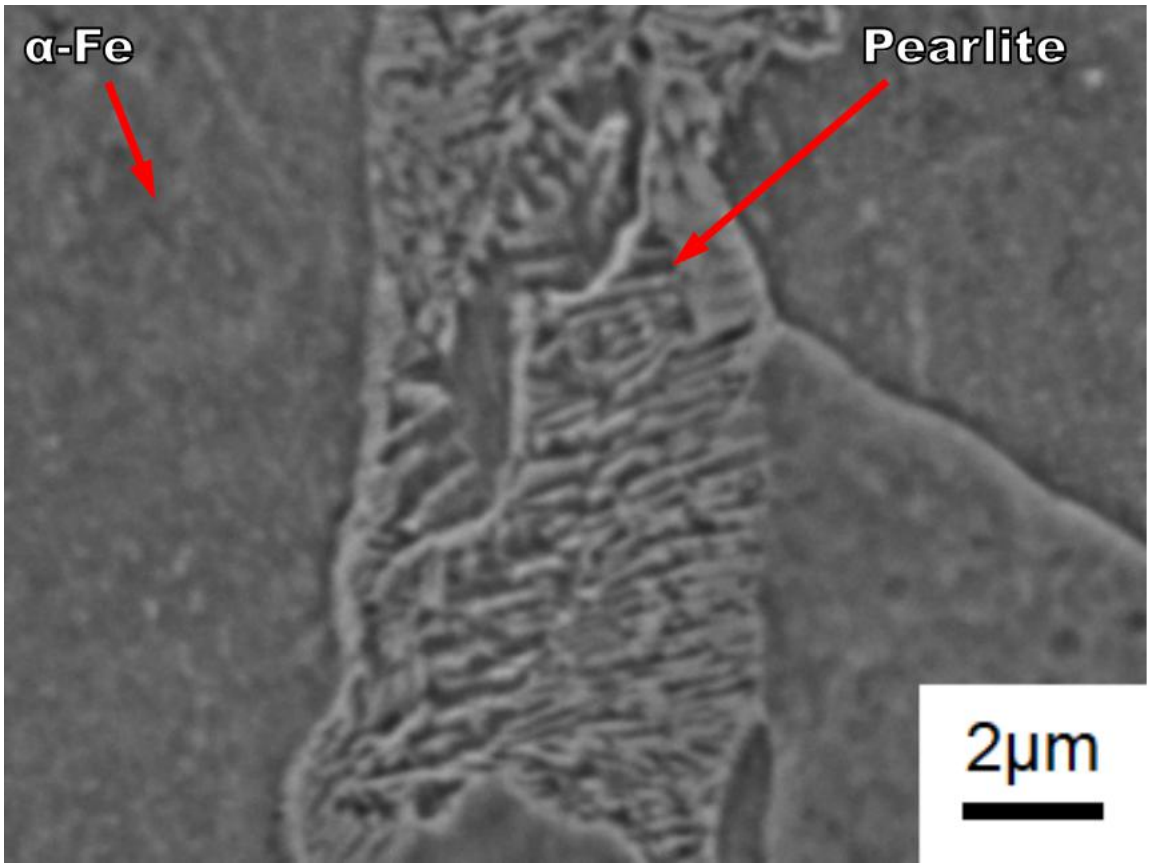

(c)

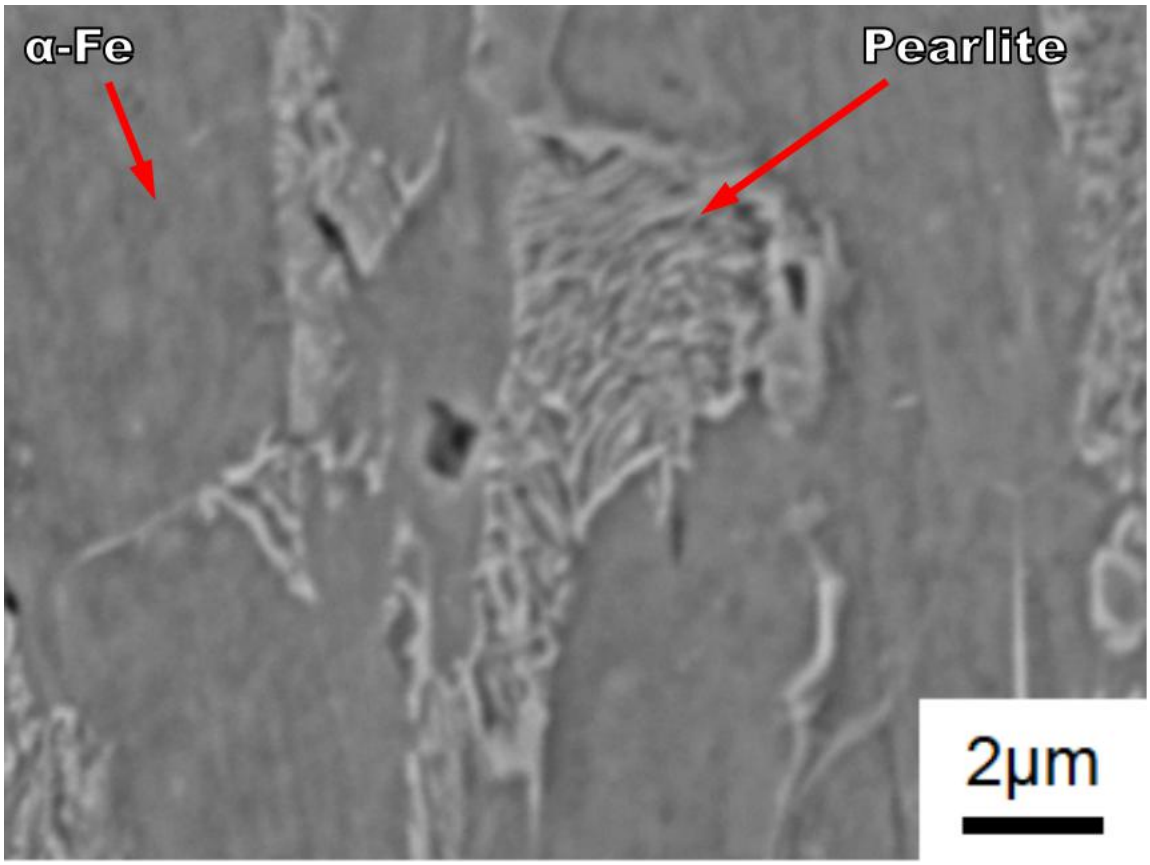

(d)

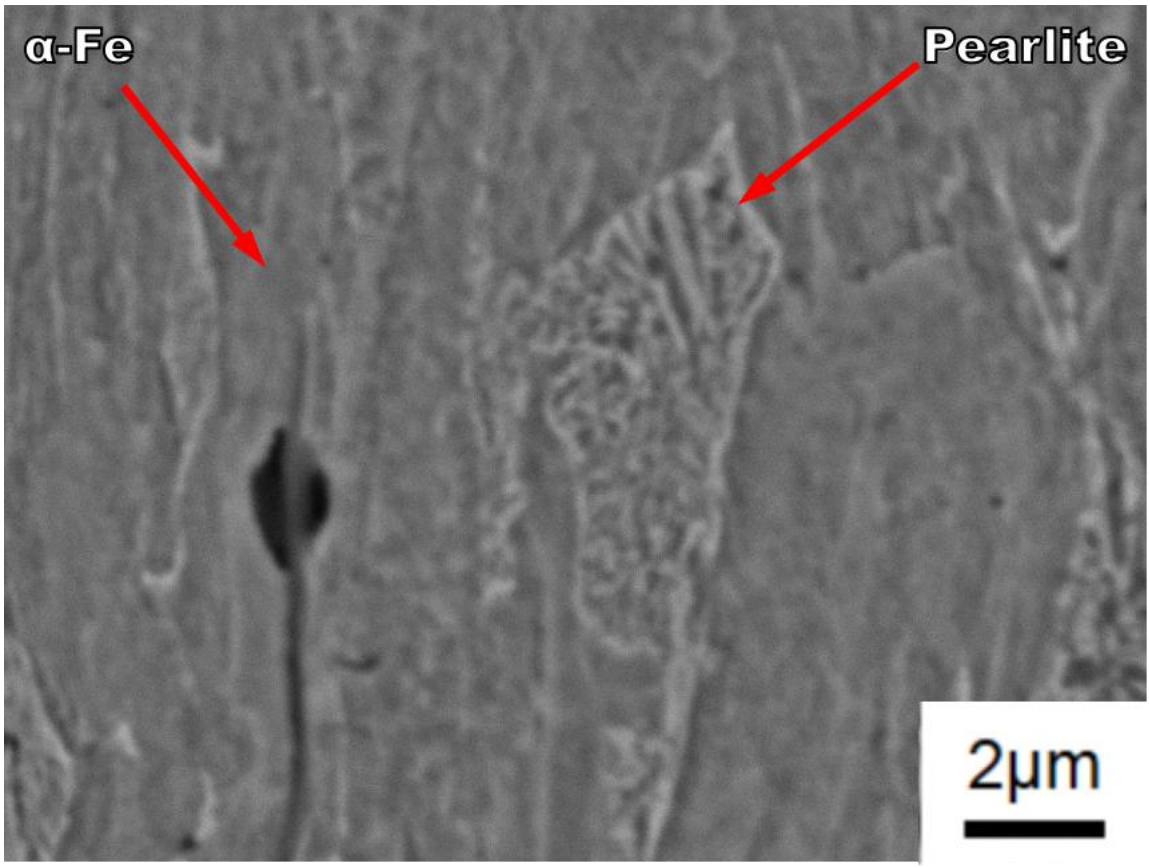

(e)

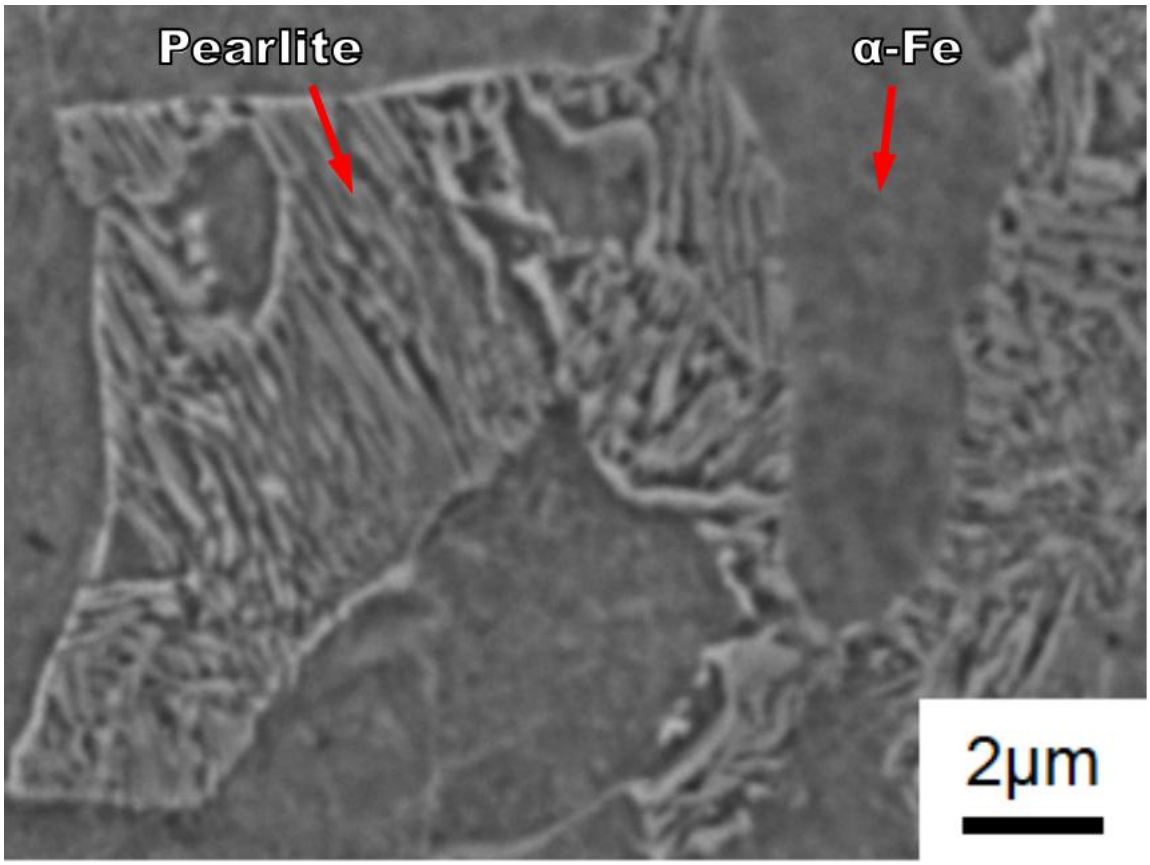

(f)

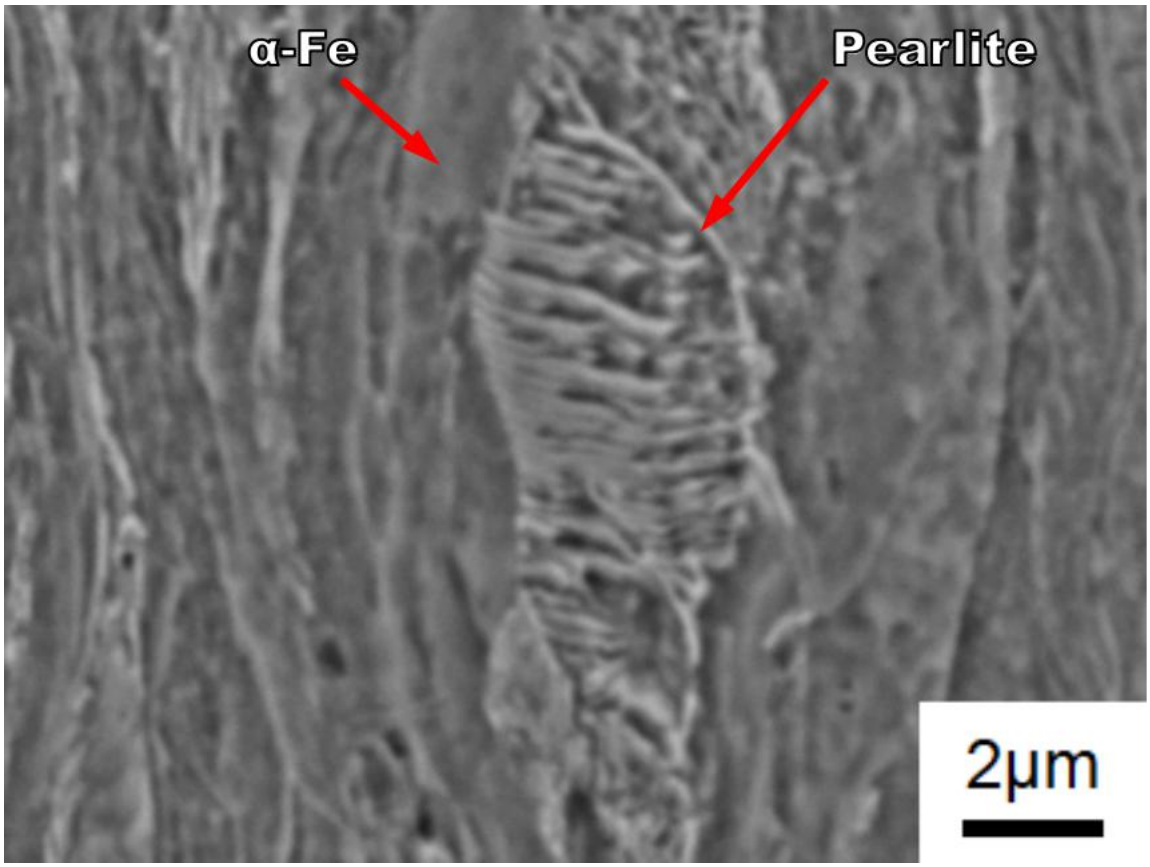

(g)

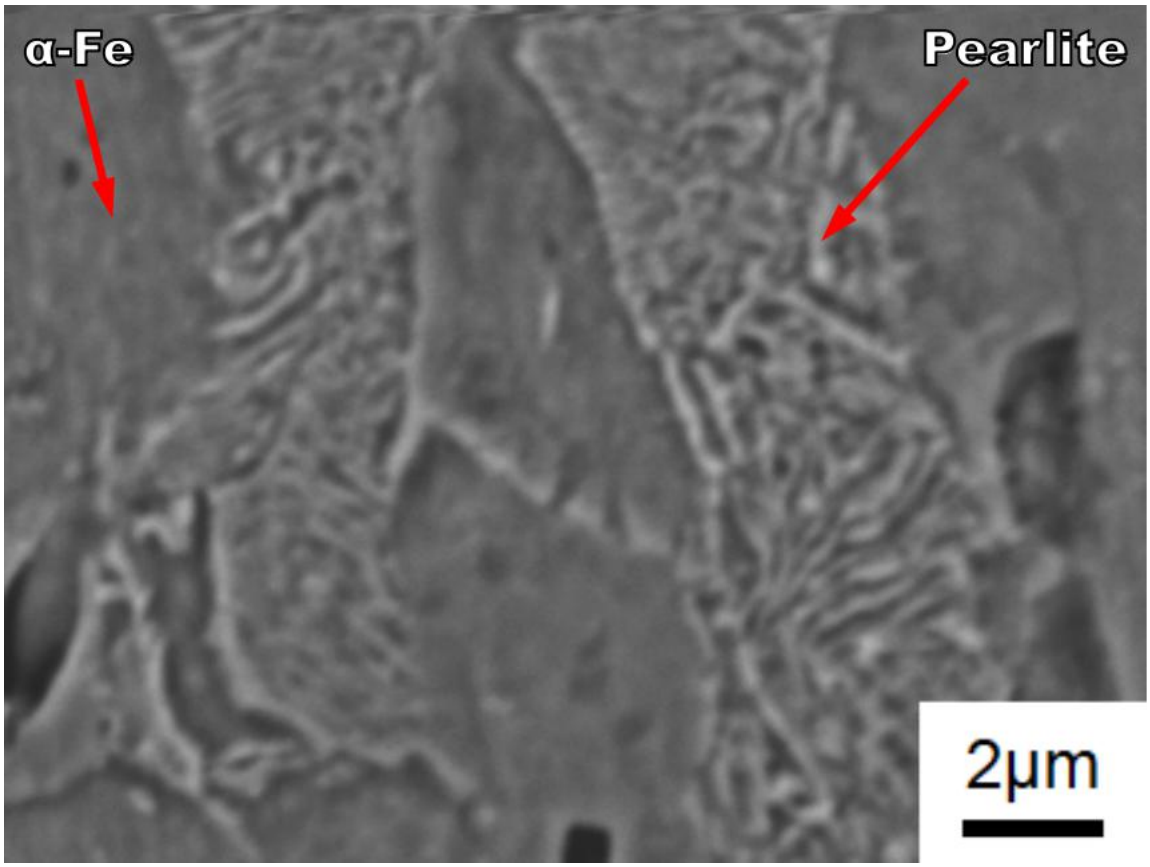

(h)

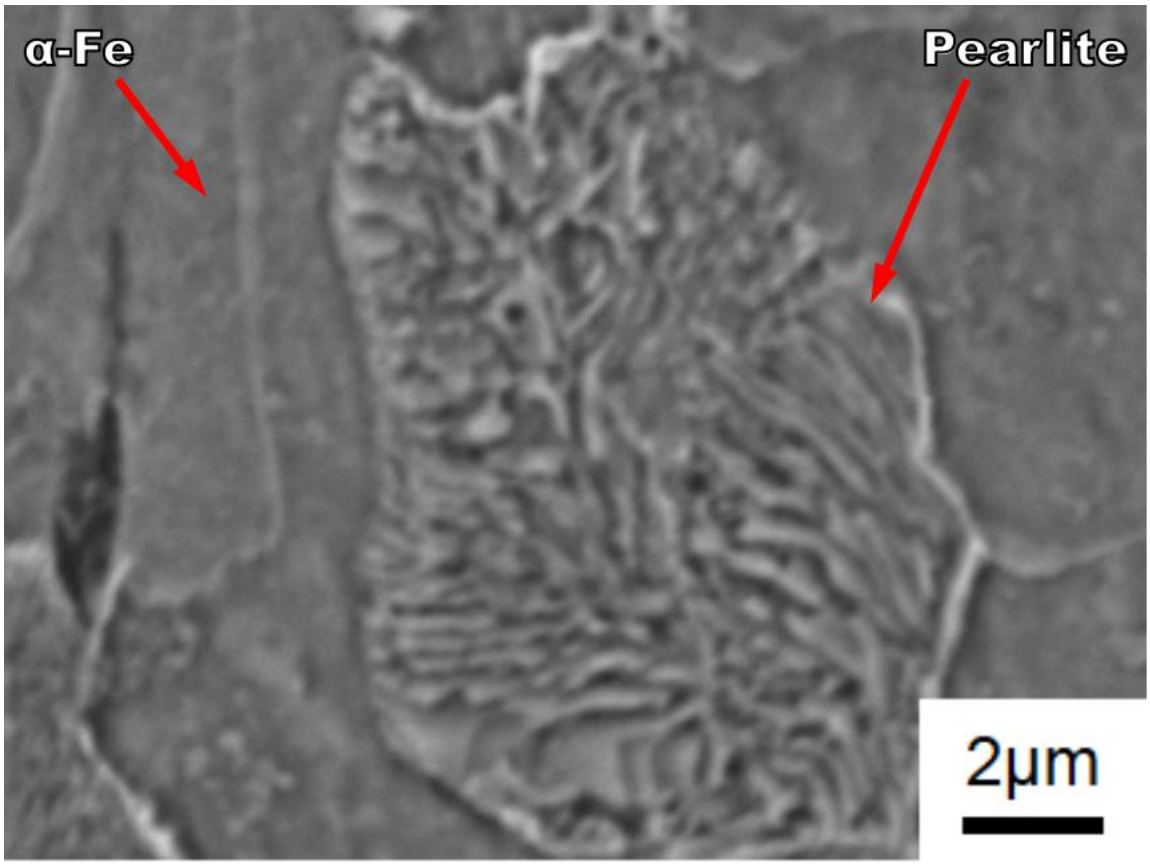

(i)

Figure A. 13 SEM pictures with high magnification showing the detail of pearlite in CRS 1018 steel tensile bars (a) S1 (as-machined) LT-ST (b) S1 (as-machined) LD-ST plane (c) S1 (as-machined) LD-LT (d) S2 (heated, uncoated) LT-ST (e) S2 (heated, uncoated) LD-ST (f) S2 (heated, uncoated) LD-LT (g) S3 (heated, coated) LT-ST (h) S3 (heated, coated) LD-ST and (i) S3 (heated, coated) LD-LT plane.

Table A. 4 Intermetalic spacing of pearlite and pearlite percentage and S1, S2, S3 in chapter 4

Sample	Plane	Intermetalic spacing of pearlite (μm)	Pearlite percentage (%)
S1	LT-ST	0.235±0.024	25.259±2.076
	LD-ST	0.232±0.021	25.209±2.585
	LD-LT	0.238±0.021	24.469±2.201
S2	LT-ST	0.235±0.025	24.610±2.288
	LD-ST	0.236±0.024	24.351±2.258
	LD-LT	0.235±0.018	25.265±2.270
S3	LT-ST	0.228±0.028	24.951±2.416
	LD-ST	0.227±0.035	24.632±2.438
	LD-LT	0.230±0.034	24.390±2.425

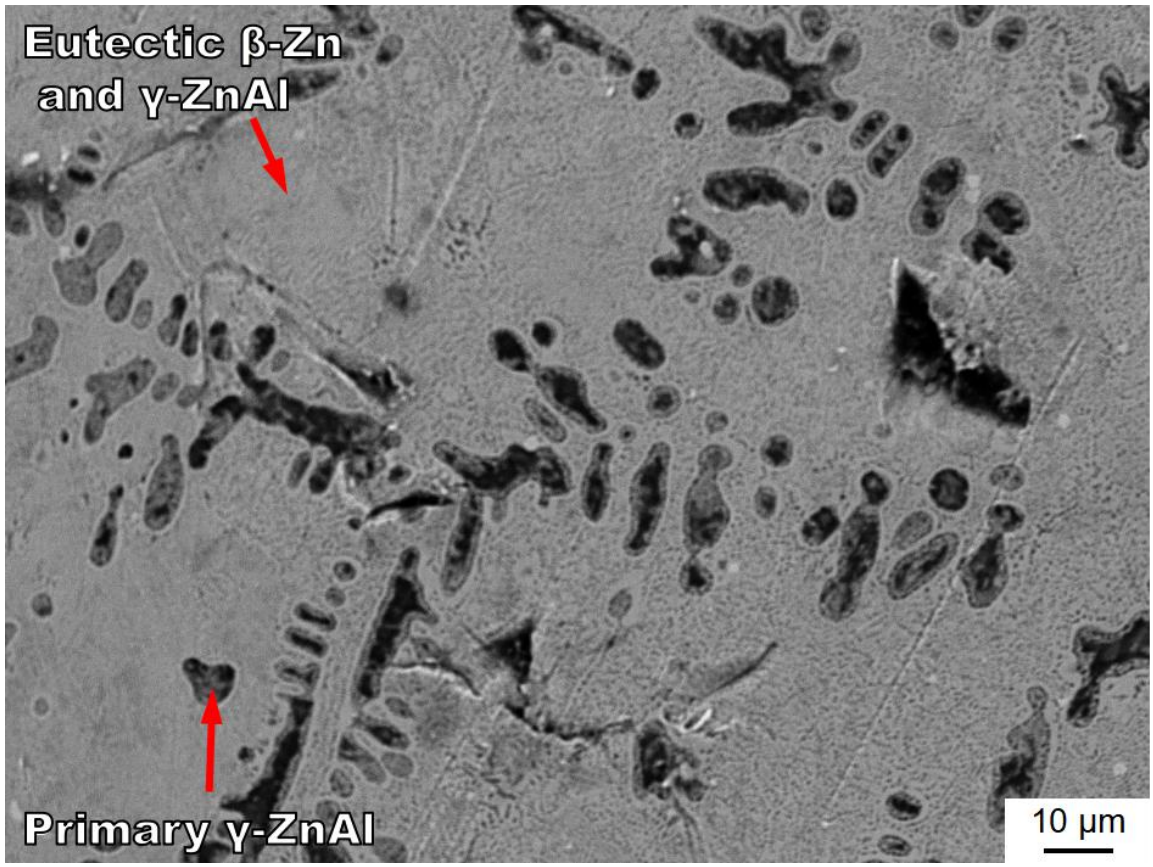

(a)

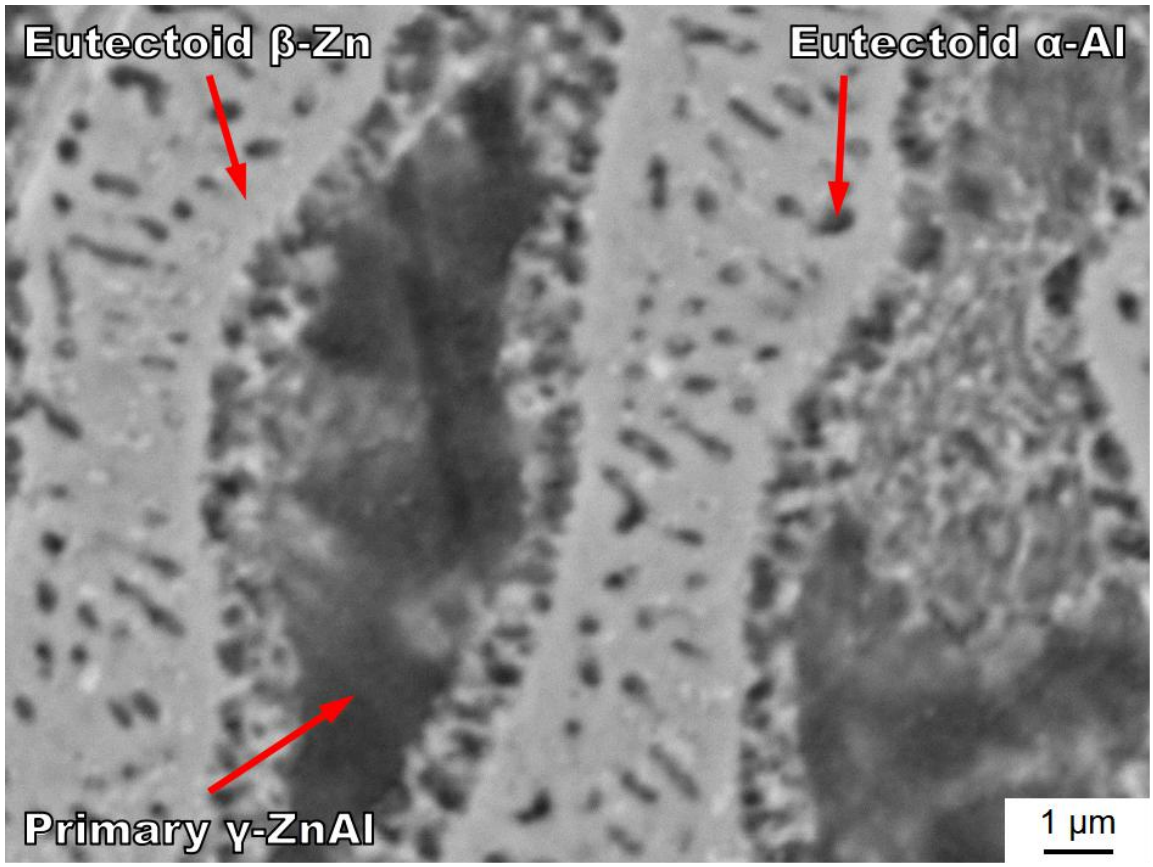

(b)

Figure A. 14 SEM pictures of polished Zn- 6wt.% Al sample been exposed in the air for 30 days with (a) low magnification and (b) high magnification.

VITA AUCTORIS

Xingyuan Wei was born in 1992 in China. He graduated from Tianjin University of Technology in 2011. He is currently a candidate for the master degree in engineering material at the University of Windsor and hopes to graduate in Winter 2019